Springer Atmospheric Sciences

Johannes Böhm
Harald Schuh *Editors*

Atmospheric Effects in Space Geodesy

Springer

Springer Atmospheric Sciences

For further volumes:
http://www.springer.com/series/10176

Johannes Böhm · Harald Schuh
Editors

Atmospheric Effects in Space Geodesy

Springer

Editors
Johannes Böhm
Department of Geodesy and Geoinformation
Vienna University of Technology
Vienna
Austria

Harald Schuh
Department 1 Geodesy and Remote Sensing
Helmholtz Centre Potsdam GFZ German Research Centre for Geosciences
Potsdam
Germany

ISSN 2194-5217 ISSN 2194-5225 (electronic)
ISBN 978-3-642-36931-5 ISBN 978-3-642-36932-2 (eBook)
DOI 10.1007/978-3-642-36932-2
Springer Heidelberg New York Dordrecht London

Library of Congress Control Number: 2013936539

Printed on acid-free paper

Springer is part of Springer Science+Business Media (www.springer.com)

Wir leben auf dem Grunde eines Meeres, des Luftmeeres

(Bretterbauer 1969)

Foreword

Geodesy is the science concerned with the figure of the Earth (geokinematics and the terrestrial reference frame), the gravity field of the Earth, and Earth rotation; the modern study of these elements requires very precise measurements. Because of this required precision, many components of the Earth must be taken into account. That the atmosphere plays an especially important role in geodesy is most remarkable because, of all the terrestrial components, it is in fact the least massive. However due to its mobility, its strong dynamic nature, and its interaction with solar radiation, the atmosphere's importance is well out of proportion to its relative size.

I am pleased to introduce some background related to the use of atmospheric information in space geodesy, the topic of which is covered here by my very able colleagues at the Vienna University of Technology. In a broad sense, we can note the overall concept of Earth system science, in which the links between all the terrestrial components can be important, including those between the atmosphere, solid Earth, ocean, hydrosphere, core, and the external near-space environment. The influence of one component may be noted in the others, and because of this connection, observations in one domain are often impacted by the presence of the other.

As an atmospheric scientist, my interest in the global scales and these interactive concepts was first inspired by working with my graduate advisors, Victor P. Starr and Edward N. Lorenz, at the Massachusetts Institute of Technology. Prof. Starr had the vision to organize a library of available observations of the global atmosphere and to examine, according to physical principles, its general circulation, with an emphasis on the separate angular momentum, hydrological, and energy cycles on a broad scale. Starr surmised, in particular, that changes in the overall angular momentum of the atmosphere can exist, and would of necessity be realized in changes in other terrestrial components, notably in the solid Earth. Prof. Lorenz's research used the overall framework of this diagnostic viewpoint, expanding its theoretical basis, and extending it to view the atmosphere prognostically. His models simulated the basic elements of the atmosphere in order to understand the underlying uncertainty in atmospheric forecasts, and by extension that of all chaotic flow.

The atmospheric influence on the Earth's rotation was beginning to be considered, and, together with Richard Rosen at Atmospheric and Environmental Research, I became involved with the space geodesy community in this context. Our first connections were through NASA's LAGEOS and Crustal Dynamics Projects, which, in addition to their study of terrestrial plate motions, produced some of the earlier measurements of Earth rotation and polar motions with high accuracy and temporal resolution. We used independent analyses of the atmosphere to calculate series of atmospheric angular momentum, and demonstrated close agreement with the then emerging series of Earth rotation (length of day) values.

The geodesy and astronomy communities quickly appreciated the importance of this connection and supported the maintenance of a database for relevant atmospheric statistics. I helped organize, at their request, a special bureau for angular momentum under the organization that has now become the International Earth Rotation and Reference Systems Service. Eventually, the broader significance of the atmosphere in geodesy led to the enhancement of this Special Bureau for the Atmosphere's mission. We now include atmospheric applications, related to gravity, loading, and tropospheric path delay. This mission could be extended to the even higher realm of the ionosphere, the region critical to the signals needed to interpret space-geodetic data.

When discussing the need for atmospheric information for geodesy, other aspects of Earth system science emerge, including the interactions between the atmosphere and ocean; an important topic here is how the ocean responds to the overlying atmospheric pressure. The role of the hydrological cycle is paramount in geodetic applications too, including the signature and variability of moisture in the atmosphere, which change the mass distribution and influence calculations of wet path delays. These effects culminate in links with the solid Earth, including also the loading and the effects on the gravity field. The importance of the changing pressure patterns, so well known in weather analysis and forecasting, in these latter applications, was striking to me. The tidal structure of the atmosphere, as is also noted in the book, has prominent importance in geodetic applications.

These days we are concerned more than ever about the consequences of potential climate change, which have been both observed and assessed by models. Important areas of concern regarding a modified climate are changes in the temperature and moisture fields. Add to this the related changes in the circulation systems, and we have ingredients that will impact a number of geodetic parameters as well.

Atmospheric science is a discipline that now uses the numerical weather prediction system as one of its major tools. This complex set of procedures is run routinely at the world's largest weather centers. Such systems include analysis of the atmosphere based on a combination of observations from radiosondes, satellites, surface, and other measurements, which are then assimilated according to their locations and error characteristics. The resulting operational fields are projected into the future according to physics and fluid dynamical equations, with short-term forecasts used in the assimilations. The meteorological community has

also produced so-called reanalysis fields, which have a more consistent set of characteristics over a lengthy period.

Geodetic scientists are now using both operational and reanalysis fields in their applications. The fact that this information is of such importance to the geodetic community will be heartening to meteorologists who see the usefulness of their data in another discipline. Indeed, a cross-discipline exchange of information about the atmosphere is of fundamental importance, and will help the overall concepts of Earth system science.

The opportunity to make regular visits to the Advanced Geodesy group at the Vienna University of Technology, with Profs. Johannes Böhm and Harald Schuh and their collaborators and students, provided me a chance to enhance the interactions with geodetic scientists in a most productive environment, particularly with those who consider the atmosphere of paramount importance in the determination of geodetic parameters. I thank the Austrian Science Fund for support of these interactions, the US National Science Foundation for research support, the US National Oceanic and Atmospheric Administration for their cooperation in setting up and running the special bureau, and the worldwide community of solid Earth, atmospheric, geodetic, and astronomical scientists, with whom I have interacted, for much inspiration and help. It has been a truly interdisciplinary journey. Many aspects of this interactive science will be evident in the chapters to follow.

Lexington, December 2012 David Salstein

Preface

Dedicated lectures on Advanced Geodesy (*Höhere Geodäsie*) at Vienna University of Technology (erstwhile *k.k. Polytechnisches Institut*) were originated in 1857 by Josef Herr, at that time Professor of Applied Geometry (*Praktische Geometrie*) and later also of Advanced Geodesy and Spherical Astronomy (*Höhere Geodäsie und Sphärische Astronomie*). Since those early days of Advanced Geodesy in Vienna, research topics have been manifold and broad, being revolutionized with the advent of computers and satellites in the second half of the twentieth century. This development certainly strengthened the value of studies dealing with atmospheric effects in geodesy. For instance, in 1969 Kurt Bretterbauer, predecessor of Harald Schuh as Chair of Advanced Geodesy, wrote his dissertation on refraction issues in Advanced Geodesy, stating in the first sentence of the introduction to the thesis that we are living at the bottom of a sea, the'air-sea' (*Wir leben auf dem Grunde eines Meeres*, *des Luftmeeres*). The substance of this quote should not be underrated, as many atmospheric effects have counterparts in the oceans, e.g., atmospheric and oceanic loading of the solid Earth, excitation of Earth rotation, or variable gravitational effects due to density variations in both fluids. While there are no antennas at the ocean bottom to receive signals from satellites or extragalactic radio sources, systems with receivers and transponders at the sea surface exist as well as sensors located at the bathymetry.

Ever since Johannes Böhm completed his Ph.D. thesis on tropospheric path delays of Very Long Baseline Interferometry (VLBI) observations in 2004 supervised by Harald Schuh, the research group on Advanced Geodesy at Vienna University of Technology has been very active in investigating atmospheric effects in space geodesy. Johannes Böhm's thesis laid the foundation for the Vienna Mapping Functions 1 (VMF1) and the Global Mapping Functions (GMF), which were published in 2006 and can be used to map tropospheric delays from the zenith to arbitrary elevations. In the wake of this work, numerous research and Ph.D. projects were stimulated by issues relating to tropospheric delays, e.g., the determination of long-term trends in zenith delays determined from VLBI observations (Ph.D. thesis by Robert Heinkelmann, finished in 2008) or the retrieval of precipitable water with Global Navigation Satellite Systems (GNSS)—a topic that has been primarily dealt with in projects led by Robert Weber with Ph.D. theses, e.g., by Elisabeth Klaffenböck in 2005 or Ana Karabatic in 2011.

Under the supervision of Harald Schuh, Thomas Hobiger completed his Ph.D. thesis on the determination of ionospheric parameters from VLBI observations in 2005. His study marks the starting point of research on ionospheric effects in space geodesy, and was continued by Sonya Todorova (Ph.D. in 2008), Mahdi Alizadeh, Nina Magnet, and Claudia Tierno Ros.

A diversification of research topics beyond the field of atmospheric delays arose when the Austrian Science Fund (FWF, *Der Wissenschaftsfond*) approved project *GGOS Atmosphere* in October 2008. GGOS is the Global Geodetic Observing System of the International Association of Geodesy (IAG), aimed at the consistent treatment of geokinematics (i.e., the shape of the Earth), the gravity field of the Earth, and Earth rotation. In accordance with those pillars, *GGOS Atmosphere* allowed funding of three scientists dealing with atmospheric loading (Dudy Wijaya), atmospheric effects on gravity (Maria Karbon), and atmospheric excitation of Earth rotation (Michael Schindelegger). Additionally, Vahab Nafisi and Matthias Madzak addressed the refinement of ray-tracing through numerical weather models. All scientists in project *GGOS Atmosphere* consistently used data from numerical weather models of the European Centre for Medium-Range Weather Forecasts (ECMWF) for the determination of the respective products.

Since 2002, Johannes Böhm has been giving these lectures on *Atmospheric effects in space geodesy* at the Vienna University of Technology. Supported by the input of the research staff of Advanced Geodesy, these lectures present both theoretical foundations as well as recent results achieved in the field. Consequently, with all the expertise available, we decided to write a book based on the contributions of various members of the research group. Instead of simply compiling numerous papers, the plan was to publish a textbook with a consistent and homogeneous description of atmospheric effects that can be used for lectures, primarily in geodesy courses.

The first chapter (Geodetic and Atmospheric Background) by Böhm et al. provides introductory information for the other chapters in the textbook, summarizing gas laws and meteorological parameters or phenomena for the troposphere, as well as ionization processes for the ionosphere. More specifically, the second chapter (Ionospheric Effects on Microwave Signals) by Alizadeh et al. discusses delays (and phase advances) of signals from space geodetic techniques in the ionosphere, and how they are treated in the analysis of the observations. Analogously, in the third chapter (Path Delays in the Neutral Atmosphere), Nilsson et al. report about signal delays in the neutral atmosphere. In both cases, ionosphere and neutral atmosphere, the emphasis of the book is on atmospheric effects on space geodetic observations and how they can be reduced or mitigated to get the best possible geodetic results in terms of station coordinates or Earth orientation parameters. However, the contributions do not deal with the reverse applications, that is the use of space geodetic observations for the determination of atmospheric parameters in the first place, e.g., maps of water vapor or Total Electron Content. "Atmospheric Pressure Loading" by Wijaya et al. describes atmospheric loading of the solid Earth by changing surface pressure and its implication on geometric space geodetic techniques, while in the fifth chapter

(Atmospheric Effects on Gravity Space Missions) Karbon et al. report about atmospheric effects on gravity missions in space. Again, atmospheric loading shows up as an indirect effect for gravity determination. Finally, Schindelegger et al. provide a detailed summary of atmospheric excitation of Earth rotation in "Atmospheric Effects on Earth Rotation".

For the sake of completeness, we want to list here the atmospheric effects in space geodesy which are not covered by the book: presently there is no review of tropospheric delays affecting Interferometric Synthetic Aperture Radar (InSAR) observations and how they can be mitigated. Furthermore, we do not deal with atmospheric drag on satellite orbits, nor do we describe thermal deformation of VLBI telescopes or other monuments that carry space geodetic antennas. However, those topics are kept in mind and will be eventually added to a new edition of the book at some time in the future.

The development of the book was quite a challenge, and we are sure that there are some bugs (hopefully not too many). Thus, we will be very happy to receive comments and feedback (positive and negative) so that we can further improve the description of atmospheric effects in space geodesy.

Vienna, December 2012

Johannes Böhm
Harald Schuh

Acknowledgments

We owe many thanks to a large number of persons and institutions who have made this book possible. We would like to acknowledge the Austrian Science Fund (FWF, *Der Wissenschaftsfond*) for funding project GGOS Atmosphere (P20902-N10) as well as many other projects, and the Austrian Weather Service (ZAMG, *Zentralanstalt für Meteorologie und Geodynamik*) for granting access to data of the European Centre for Medium-Range Weather Forecasts (ECMWF). These institutions have been very open and supportive to our research in the past years.

We would also like to thank all the reviewers of the chapter of the book. In alphabetical order, these are Jean-Paul Boy, Aleksander Brzeziński, Gunnar Elgered, Frank Flechtner, Manuel Hernandez-Pajares, and Michael Schmidt. They are acknowledged at the end of the chapters they have reviewed. In particular, we want to express our sincere gratitude to David Salstein, a very good friend and colleague of our research group, who visits our group frequently and who has provided a lot of comments and feedback on the book. He was so kind to write the foreword.

We are very grateful to all our colleagues at the research group Advanced Geodesy at the Vienna University of Technology. Without the friendly, cooperative, and inspiring environment it would not have been possible to realize so many projects and ideas, and to finally write this book on Atmospheric Effects in Space Geodesy.

Contents

Geodetic and Atmospheric Background 1
Johannes Böhm, David Salstein, Mahdi Alizadeh and Dudy D. Wijaya

Ionospheric Effects on Microwave Signals 35
M. Mahdi Alizadeh, Dudy D. Wijaya, Thomas Hobiger, Robert Weber and Harald Schuh

Path Delays in the Neutral Atmosphere 73
Tobias Nilsson, Johannes Böhm, Dudy D. Wijaya, Ana Tresch, Vahab Nafisi and Harald Schuh

Atmospheric Pressure Loading 137
Dudy D. Wijaya, Johannes Böhm, Maria Karbon, Hana Krásná and Harald Schuh

Atmospheric Effects on Gravity Space Missions 159
Maria Karbon, Johannes Böhm, Dudy D. Wijaya and Harald Schuh

Atmospheric Effects on Earth Rotation 181
Michael Schindelegger, Sigrid Böhm, Johannes Böhm and Harald Schuh

Index 233

Geodetic and Atmospheric Background

Johannes Böhm, David Salstein, Mahdi M. Alizadeh and Dudy D. Wijaya

Abstract This first part in the book on atmospheric effects in space geodesy provides a review of the basic structure, composition, and workings of the atmosphere and serves as a general background needed to help the reader understand the material in later parts. Its large diversity of topics would usually not be included in one paper, but since this work is designed as a textbook in a university geodesy course, we intentionally discuss this broad variety of topics at the outset. The reader may wish to skip this part and only revisit it as references and interest suggest. Here we cover the following topics: After an overview of atmospheric effects in space geodesy, we briefly review physical terminology and meteorological quantities. Then, we discuss gas laws and atmospheric statics, and we introduce specific topics like reference pressure, atmospheric tides, and the inverted barometer hypothesis, all of which reappear in later parts. After an overview of atmospheric layers and circulation, we concentrate on the ionosphere, highlighting ionization and recombination processes and introducing the concept of Chapman layer profiles. Finally, we discuss height-

J. Böhm (✉)
Department of Geodesy and Geoinformation, Vienna University of Technology,
Gußhausstraße 27-29, 1040 Vienna, Austria
e-mail: johannes.boehm@tuwien.ac.at

D. Salstein
Atmospheric and Environmental Research,
131 Hartwell Ave, Lexington, MA 02421, USA
e-mail: salstein@aer.com

M. M. Alizadeh
Department for Geodesy and Geoinformation Science,
Technical University of Berlin, Strasse des 17. Juni, 135, 10623Berlin, Germany
e-mail: mahdi.alizadeh@mail.tu-berlin.de

D. D. Wijaya
Geodesy Research Group, Institute of Technology Bandung,
Ganesha 10, Bandung-West Java, Indonesia
e-mail: dudy@gd.itb.ac.id

J. Böhm and H. Schuh (eds.), *Atmospheric Effects in Space Geodesy*,
Springer Atmospheric Sciences, DOI: 10.1007/978-3-642-36932-2_1,

and latitude-dependent spatial variations as well as regular and non-regular temporal variations in the ionosphere.

1 Setting the Stage: Geodetic Motivation

Space geodesy refers to observations that are transmitted or received by natural or artificial objects outside the lower portions of the atmosphere, i.e., in space where the density of the atmosphere is sufficiently small to allow stable satellite orbits. We do not consider airborne instruments as space geodesy but we restrict the term *space geodesy* to extragalactic radio sources in the case of Very Long Baseline Interferometry (VLBI) and to satellites. VLBI is a microwave-based technique that measures the difference in arrival times at pairs of locations of signals from a radio source by cross correlation (Schuh and Böhm 2012). The observed radio sources are principally extragalactic objects but signals from satellites can also be used. Geodetic VLBI is the only technique for the realization of the Celestial Reference Frame (CRF) and for the estimation of Universal Time (UT1) and nutation over longer time spans. Furthermore, VLBI is a primary technique for the determination of the scale of the terrestrial reference frame due to the accurate determination of very long baseline lengths.

Global Navigation Satellite Systems (GNSS), including the United States Global Positioning System (GPS), the Russian GLONASS (Globalnaja Nawigazionnaja Sputnikowaja Sistema), the European Galileo, and others use satellites at orbital heights of about 20000 km that transmit microwave signals received by antennas at the Earth surface or onboard other satellites like Low Earth Orbiters (LEO). The strategy of the French system called Doppler Orbitography by Radiopositioning Integrated on Satellite (DORIS) is different, with the microwave signals being transmitted by antennas on the ground and received onboard the satellites.

All microwave-based space geodetic techniques mentioned above (VLBI, GNSS, DORIS) as well as altimeter satellite missions are subject to propagation effects in the atmosphere. With respect to propagation, we divide the atmosphere into the neutral atmosphere up to about 100 km (see Sect. 2 in this part of the book), and into the ionosphere where the density of free electrons and ions is large enough to influence the propagation of microwave signals, extending from about 60–2000 km depending on time and location (see Sect. 4 in this part). Microwave signals experience phase and group delays of the same size in the neutral atmosphere, but they are subject to phase advances and group delays in the ionosphere. The situation is different with Satellite and Lunar Laser Ranging (SLR/LLR), which observe in the optical regime and are only subject to delays in the neutral atmosphere.

Alizadeh et al. (2013) and Nilsson et al. (2013), both in this book, deal with the treatment of atmospheric delays in the analysis of space geodetic observations in the neutral atmosphere and the ionosphere, respectively. While ionospheric delays can be determined and eliminated by observing at more than one frequency, dedicated

models like mapping functions and gradients need to be applied in the case of the neutral atmosphere which is non-dispersive for microwaves.

Space geodetic techniques like VLBI, GNSS, DORIS, or SLR are not only affected by propagation delays or phase advances of the signals, but geodetic estimates are also influenced by other atmospheric effects. Satellites at low orbits are subject to atmospheric drag, which causes decreasing orbit altitudes and the destruction during re-entry into the atmosphere starting at about 100 km. In any case atmospheric drag has to be modelled very carefully to achieve highest accuracy for satellite ephemerides. Moreover, it is not just the direct interaction with atmospheric particles, but also the gravitational effect on satellite orbits that need to be considered. Karbon et al. (2013) in this book describe the determination of atmospheric gravity from data of numerical weather models, e.g., from the European Centre for Medium-range Weather Forecasts (ECMWF). These gravity changes due to atmospheric variability are also of great importance for gravity missions like the Gravity Recovery and Climate Experiment (GRACE) or the Gravity Field and Steady-State Ocean Circulation Explorer (GOCE) because the accurate correction of the observations prevents aliased errors in static or time-varying gravity field models.

Rigorously, atmospheric gravity is determined from the three-dimensional density distribution in the atmosphere, but it can also be approximated by calculations based on surface pressure. Surface pressure is also the meteorological input parameter to determine the displacement of the solid Earth due to atmospheric loading which is described in detail by Wijaya et al. (2013) in this book. Atmospheric loading displacements can be as large as 2–3 cm with respect to a mean state which goes along with a mean reference pressure. This reference pressure, which has dependence on the orography within an atmospheric analysis, is also of importance for hydrostatic zenith delays (Nilsson et al. 2013) and atmospheric gravity variations (Karbon et al. 2013), and it will be discussed in Sect. 2.6.

For the rigorous determination of atmospheric loading corrections, we need the surface pressure not only at the site of interest, but—theoretically—over the whole globe (see (Wijaya et al. 2013)). The surface pressure variations (w.r.t. the reference pressure) are weighted by the Green's functions which also account for geophysical properties of the Earth via the load Love numbers. Things get complicated for sites close to the ocean, because the ocean surface responds in a complex way to overlying atmospheric pressure variations. In the lack of real ocean models, we need to apply simple models like the inverted barometer hypothesis (IB) as described in Sect. 2.8.

Other interesting phenomena are atmospheric tides, the most important of which are thermally induced pressure variations at the 1–2 hPa level occurring with periods of 24 h (S1) and 12 h (S2). When using data from numerical weather models with a 6-hour time resolution, it is not possible to properly account for S2 because it is exactly at the Nyquist frequency of the underlying data. More information on atmospheric tides is provided in Sect. 2.7.

Space geodetic techniques like VLBI, GNSS, SLR, or DORIS are used to observe Earth rotation variations, a large part of which is caused by atmospheric effects. Schindelegger et al. (2013) in this book focus on atmospheric excitation of Earth rotation, e.g., how it can be determined from density variations (approximated by

surface pressure variations) and wind fields. The determination is again affected by the oceanic response to atmospheric pressure variations (Sect. 2.8) and atmospheric tides (Sect. 2.7).

2 Neutral Atmosphere

The first subsections here are meant as review and summary of basic physical and meteorological relations which should serve as introduction for students in geodesy who are not very familiar with those aspects but can be skipped by more experienced readers in that field.

2.1 Physical Terminology

To conclude from the mechanical properties, which describe the behavior of single molecules and atoms of a gas or gas mixture, to the behavior of a macroscopic quantity of fluid, it would be necessary to count the number of particles. However, this is not possible, and the total amount of substance n is used instead of the number of particles. This amount of substance n is proportional to the number of particles N, independent of the substance, and it can be measured with methods of continuum physics. It holds that $n = N/N_A$ when $\mathrm{N_A} = 6.02252 \cdot 10^{23}/\mathrm{mol}$ is Avogadro's number. The unit of the amount of substance is 1 mol, and it is defined as the amount of carbon of pure nuclide C_6^{12} of the exact mass 12 g, 12 being the molecular weight of this form of carbon.

Several relations can be introduced here: If the proportion of the amount of substance n to the unit amount of substance n_p of a prototype is known, then the proportion of the number of particles N and N_p is known as well with $N/N_p = n/n_p$. If m is the mass of an amount of substance n, then $M_m = m/n$ is the molar mass with the unit g/mol or kg/kmol. If μ is the mass of a single particle of an amount of substance and N is the number of particles, then $m = N \cdot \mu$ is the mass of the amount of substance and $\mu = M_m/N_A$.

The numbers of the molar masses of various substances are the relative masses of the molecules and atoms of the substances related to that of the fictitious substance with $\mu/\mu' = M_m/M_m'$. They are only proportions, and they are identical to those numbers in the periodic table, which are called *weight of the molecules and atoms*. 1 mol is the amount of substance which has that mass in grams that is shown by the atomic or molecular weight.

If V is the volume of an amount of substance, then $V_m = V/n$ is the molar volume with units, e.g., $\mathrm{cm}^3/\mathrm{mol}$, and it is dependent on pressure and temperature. The Loschmidt's number $\mathrm{N_S^0} = 2.687 \cdot 10^{25}/\mathrm{m}^3$ is the specific number of molecules of ideal gases at 0 °C and 1013.25 hPa. At this pressure and temperature, 1 mol of a gas takes a volume of 22414 cm^3.

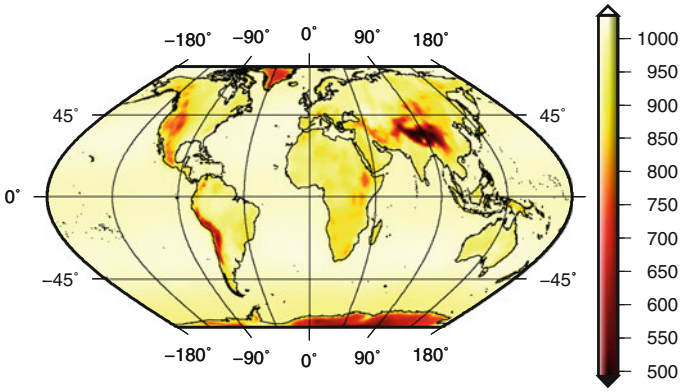

Fig. 1 Mean surface pressure in hPa as determined from 36 epochs in 2005

2.2 Meteorological Quantities

Pressure is defined as force per area. At mean sea level, the pressure p is about 1013.25 hPa (old: 1013.25 mbar). It holds that $1\,\mathrm{Pa} = 1\,\mathrm{N/m^2} = 1\,\mathrm{kg \cdot m/s^2/m^2}$. Figure 1 shows the mean (reference) pressure as derived from reanalysis pressure level data of the ECMWF.

In thermodynamics the temperature is related to the mean kinetic energy of the molecules of a gas. The term temperature can only be applied to a large number of molecules. The scientific temperature scale is the thermodynamic Kelvin scale. The absolute zero point is 0 K, and the unit Kelvin is defined in a way that the triple point of pure water is at $\mathrm{T_{tr}} = 273.16\,\mathrm{K}$. At this temperature and at 6.11 hPa water can exist in all three states, i.e., as ice, in liquid, and in gaseous form. At 1013.25 hPa, liquid water turns to ice at $\mathrm{T_0} = 273.15\,\mathrm{K}$, and the boiling point is at 373.15 K. If T is the temperature in Kelvin and t in Celsius we find

$$\frac{T}{T_0} = 1 + \frac{t}{273.15} = 1 + \alpha \cdot t \tag{1}$$

with $\alpha = 0.003661$. Figure 2 illustrates that the mean temperature at the Earth surface is between −40 and +30 °C. The global mean temperature is about 15 °C.

The quantity of water vapor in air cannot exceed a certain value, which is dependent on temperature and pressure. If this temperature is reached for a given pressure then the air is *saturated* with water vapor. There are several possibilities to characterize the amount of water vapor as listed below:

- Water vapor pressure: The sum of the pressure of the dry constituents of air p_d and the water vapor pressure e is the total pressure $\mathrm{p = p_d + e}$. Similar to the

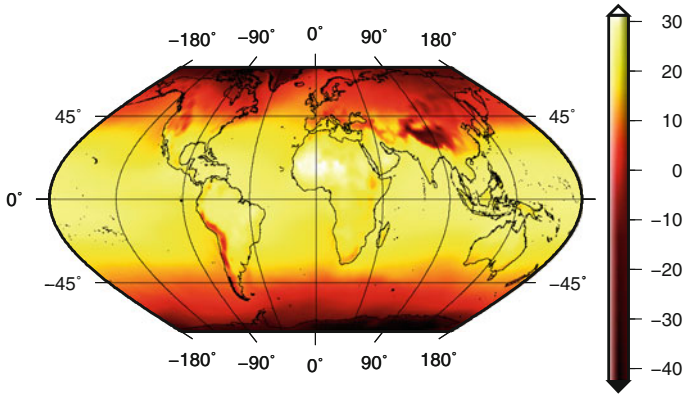

Fig. 2 Mean surface temperature in degree Celsius as determined from 36 epochs in 2005

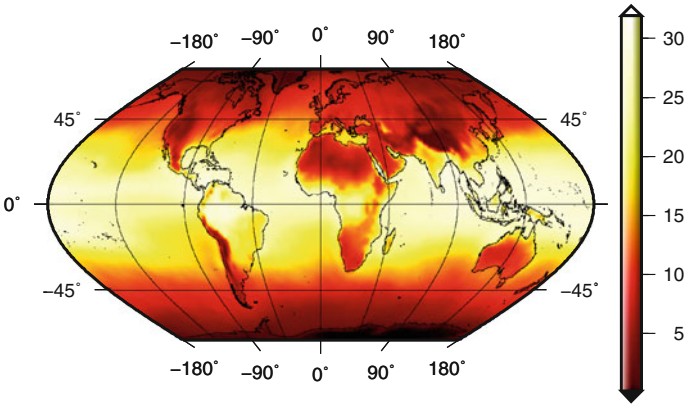

Fig. 3 Mean water vapor pressure in hPa as determined from 36 epochs in 2005

temperature, there is a clear correlation with latitude and height as illustrated in Fig. 3.

The pressure E of saturated water vapor in hPa can be determined with, e.g., the formula by Magnus (see (Kraus 2004)) when t is the temperature in degree Celsius (°C):

$$E = 6.1078 \cdot e^{\frac{17.1 \cdot t}{235+t}} \tag{2}$$

- Absolute humidity a is the amount of water vapor in air, e.g. expressed in g/m^3 with e in hPa:

$$a = \frac{0.622 \cdot 1293}{1013.25\,(1+\alpha \cdot t)} e = \frac{0.794}{1+\alpha \cdot t} \tag{3}$$

- Specific humidity s is the ratio of the density of water vapor and the density of wet air. Units are g/g:

$$s = \frac{0.622 \cdot e}{p - 0.378 \cdot e}. \tag{4}$$

- The mixing ratio m is the ratio of the density of water vapor and dry air:

$$m = \frac{0.622 \cdot e}{p - e}. \tag{5}$$

- The relative humidity f in % is often used to characterize humidity:

$$f = \frac{e}{E} \cdot 100. \tag{6}$$

  The saturated water vapor pressure can be determined with the formula by Magnus (Eq. 2).
- The dew point τ is the temperature at which enough water vapor is in the air to have saturation (equilibrium). The dew point is found by inverting the formula by Magnus (Eq. 2).
- Virtual temperature: The explanation of the virtual temperature follows later (see Sect. 2.3). For the sake of completeness, the equation is provided here:

$$T_v = T \cdot \left(1 + 0.378 \frac{e}{p}\right). \tag{7}$$

2.3 Gas Laws

The most important properties of gases are understandable if we are aware that these molecules are in constant motion. The statistical averages of these movements determine the macroscopic state quantities, which are volume V, pressure p, and temperature T. The consequences of the molecular movements are temperature and diffusion, the latter referring to the adjustment of density differences when the gases try to uniformly fill the whole space. For the investigations here, we consider ideal gases: Molecules are considered as mass points (without volume), and the van der Waals forces are neglected. These assumptions are generally reasonable.

The pressure p of a gas is based on the impact of the gas molecules. If a gas is the mixture of several gases, then each exerts that pressure as if it were alone. The total pressure is the sum of the partial pressures of the individual constituents (Dalton's law):

$$p = \sum_i p_i. \tag{8}$$

As mentioned above, the state of a gas is determined by p, T, and V. With a given amount of gas, two quantities can be varied whereas the third quantity is determined by the other two. In thermodynamics the gas law

$$p = \rho \frac{R \cdot T}{M_m} \tag{9}$$

has been found, when ρ is density, and the universal gas constant $\mathrm{R} = \mathrm{N_A} \cdot k = 8.3143\,\mathrm{J/K/mol}$ with the Boltzmann constant $\mathrm{k} = 1.3806 \cdot 10^{-23}\mathrm{J/K/mol}$. The state equation (Eq. 9) also holds for mixtures of gases, e.g., for wet air if density and molecular weight of wet air are introduced. A simpler form can be found with the specific gas constant $R' = R/M_m$, so that

$$\frac{p}{\rho} = R'T. \tag{10}$$

We apply this equation on wet air (no index), dry air (index d), and water vapor (index w). The gas laws read for the dry and wet part

$$\frac{p_d}{\rho_d} = R'_d \cdot T \tag{11}$$

$$\frac{p_w}{\rho_w} = R'_w \cdot T, \tag{12}$$

and applying Dalton's law (Eq. 8), we get

$$R'T = T\left(\frac{\rho_d}{\rho} R'_d + \frac{\rho_w}{\rho} R'_w\right). \tag{13}$$

Introducing specific humidity $s = \rho_w/\rho$ and $l = \rho_d/\rho = 1 - s$ we get

$$R' = l \cdot R'_d + s \cdot R'_w = R'_d \left[1 + s\left(\frac{R'_w}{R'_d} - 1\right)\right]. \tag{14}$$

with the molecular weight of water $M_w = 2 \cdot 1.008 + 16 = 18.016\,\mathrm{g/mol}$ and the molecular weight of dry air $M_d = 28.965\,\mathrm{g/mol}$ we find $R'_d/R'_w = 1.608$ and

$$R' = R'_d\,(1 + 0.608 \cdot s)\,. \tag{15}$$

Consequently, the gas law for wet air can be written as

$$\frac{p}{\rho} = R'T = R'_d\,(1 + 0.608 \cdot s) \cdot T = R'_d \cdot T_v \tag{16}$$

with $T_v = (1 + 0.608 \cdot s) \cdot T$ (see also Eq. 7). T_v is called virtual temperature, and it is the temperature of dry air that has the same density at the same pressure as wet air of temperature T and specific humidity s. All relationships for dry air are valid for wet air if we replace temperature T by the virtual temperature T_v.

2.4 Statics of the Atmosphere

We assume a spherical, concentric Earth. The mutual attraction of the particles is neglected as well as the thermodynamics. Thus, each gas is subject to only two influences of opposite tendency:

- the movement of the molecules, which tends to distribute the gases uniformly in space (diffusion);
- gravity, which tends to condense the particles close to the Earth surface.

If there are no effects like, e.g., turbulence, a stationary state will be reached where the density of the gases decreases with height. Then, the gases are in hydrostatic equilibrium and the sum of external and internal forces is equal to zero. The gases have a pressure p, and the partial derivatives of the scalar function p are force components per unit volume:

$$\mathbf{f} = -grad\ p \tag{17}$$

or $f_x = -dp/dx$, $f_y = -dp/dy$, and $f_z = -dp/dz$. In addition to the pressure, we only have gravity. Equilibrium is reached if the sum of all forces acting on the particles vanishes. If $\mathbf{g}$ is the vector of gravity, we get

$$\mathbf{f} + \rho\mathbf{g} = 0 \tag{18}$$

or when U denotes the gravity potential

$$grad\ p = \rho \cdot grad\ U. \tag{19}$$

Multiplying Eq. 19 with the vector $dr = (dx, dy, dz)$, we get the equation for hydrostatic equilibrium:

$$dp = \rho \cdot dU. \tag{20}$$

Since equipotential surfaces are characterized by $dU = 0$, these surfaces are also surfaces of constant pressure and density. From potential theory we know that the relation between potential, gravity and height is:

$$dU = -g \cdot dh \tag{21}$$

so that

$$dp = -\rho \cdot g \cdot dh. \tag{22}$$

This equation holds if the air moves along straight horizontal lines without acceleration. In the following case for wet air, we eliminate density with the gas law using the virtual temperature (Eq. 9) and get with Eq. 22:

$$\frac{dp}{p} = -\frac{g}{R'_d \cdot T_v} dh. \tag{23}$$

This is the basic equation for barometric height measurements, and it also holds for density:

$$\frac{d\rho}{\rho} = -\frac{g}{R'_d \cdot T_v} dh. \tag{24}$$

Strictly speaking, gravity and temperature are also dependent on height, but considering only small height changes, we can assume them to be constant. Integration between Earth surface (index B) and height h yields:

$$p = p_B \cdot e^{-\frac{g}{R'_d \cdot T_v} dh}, \tag{25}$$

$$\rho = \rho_B \cdot e^{-\frac{g}{R'_d \cdot T_v} dh}. \tag{26}$$

The factor of dh deserves a closer look. Since the exponent has to be dimensionless, the factor has the dimension 1/m. Thus, we use

$$\frac{g}{R'_d \cdot T_v} = \frac{1}{H} \tag{27}$$

where H is the barometric scale height, and it can be considered as the height of an atmosphere with constant density. Since in a homogeneous atmosphere $\rho = \rho_B$, Eq. 22 can be integrated easily. The limits for the integration are p_B and zero for p, as well as zero and H for h:

$$p_B = g \cdot \rho_B \cdot H. \tag{28}$$

With the gas law we get the height of the homogeneous atmosphere:

$$H = \frac{R'_d \cdot T_{v,B}}{g} \tag{29}$$

or

$$H = H_0 \, (1 + \alpha \cdot t) \left(1 + \frac{3e}{8p}\right) \tag{30}$$

where H_0 is the height of a homogeneous atmosphere of dry air at 0 °C. Table 1 shows the homogeneous heights at various surface temperatures for dry and saturated air. Note that if the atmosphere would consist of pure oxygen only, then H would be 8.250 km at 0 °C, for helium 57.7 km, and for hydrogen 114.6 km.

Table 1 Values of Scale Height H in km for different surface temperatures and dry or saturated air ($g = 9.806\,\mathrm{m/s^{-2}}$)

t_B in ° C	H in km for dry air	H for saturated air
−10	7.686	7.703
0	7.979	7.997
10	8.272	8.310
20	8.565	8.640
30	8.858	9.000

Using the homogeneous atmosphere we can easily determine the mass of the atmosphere. It follows from the volume of a spherical shell with height H at constant density.

$$m = V \cdot \rho = \frac{4\pi}{3}\left[(r+H)^3 - r^3\right]\rho \approx 4\pi r^2 H\rho \tag{31}$$

with $r = 6371\,\text{km}$, $H = 8\,\text{km}$, $\rho = 1.293\,\text{kg/m}^3$, we get $m = 5.27 \cdot 10^{18}\text{kg}$, i.e. about 1 ppm of the Earth mass. More sophisticated calculations of the mass of the atmosphere are shown by Karbon et al. (2013) in this book.

The actual density of air at the Earth surface is larger close to the poles than at the equator. The reason is the combination of lower temperature and the larger gravity at the poles. The extension of the atmosphere is smaller at the poles than at the equator, so the density gradient is larger in higher latitudes.

The decrease of temperature with height, known as its lapse rate, is nearly linear and $-0.65\,°\text{C}$ per 100 m. Thus, we can set the temperature to t_m which is the mean temperature of the upper and lower limit of the layer. With Eq. 30 we get for Eq. 23:

$$\frac{dp}{p} = -\frac{dh}{H_0\,(1+\alpha\cdot t_m)\left(1+\frac{3e}{8p}\right)} \tag{32}$$

Integration between the heights h_1 and h_2 yields (in logarithmic form):

$$lnp_2 = lnp_1 - \frac{h_2 - h_1}{7979\,(1+\alpha\cdot t_m)\left(1+\frac{3e}{8p}\right)} \tag{33}$$

This is the equation for barometric height measurements. For many practical purposes this equation has to be inverted. We often need the pressure gradient dp/dh or its inverse dh/dp and we express it in m/hPa (Table 2).

Although only a small fraction of the total volume of air, water vapor plays important roles in the latent heat it holds, roles in energy releases during changes of phase, roles in cloud formations and precipitation, as well as the radiative effects it has in its interaction with electromagnetic waves. Its horizontal distribution relates to the characteristics of the air masses in which it resides, but its vertical distribution generally decreases with height. Although evaporation occurs at the Earth's surface, air at higher altitudes with its lower temperatures cannot hold as much water vapor. Whereas the total pressure decreases with height according to strict equations of

Table 2 Height difference Δh in meter per 1 hPa (dry air)

t_B in °C, p in hPa	−20°C	0°C	20°C	30°C
1013	7.30	7.88	8.45	8.74
933	7.92	8.55	9.18	9.49
853	8.67	9.35	10.04	10.38
813	9.09	9.81	10.53	10.90

hydrostatic balance, no such exact formulation holds for the water vapor pressure. Its distribution is very variable temporally and spatially.

2.5 Increasing the Vertical Resolution of Meteorological Data

If not equipped with a GNSS receiver, radiosonde data do not include information about the height, but the geopotential is determined by the equations shown in Sect. 2.4. Meteorologists usually divide the geopotential C by a constant gravity value ($g_n = 9.80665\,\mathrm{m/s^2}$) to get the so-called geopotential heights h_d known in geodesy as dynamic heights. These heights can be converted to geometric heights h (orthometric or sea level heights) if realistic gravity values are available which depend mainly on height h and latitude φ.

$$h_d = \frac{C}{g_n} = \frac{1}{g_n} \cdot \int_0^h g(\varphi, h) \cdot dh \approx \frac{1}{g_n} \cdot g\left(\varphi, \frac{h}{2}\right) \cdot h \tag{34}$$

$$h = \frac{h_d \cdot g_n}{g\left(\varphi, \frac{h}{2}\right)} \tag{35}$$

Applying the normal gravity in Eq. 36 suggested by Kraus (2004)

$$g\,(\varphi, h) = g_n \left(1 - 0.0026373 \cos\left(2\varphi\right) + 0.0000059 \cos^2\left(2\varphi\right)\right) \cdot \left(1 - 3.14 \cdot 10^{-7} \cdot h\right) \tag{36}$$

the geometric heights can be derived. Theoretically, this has to be done in an iterative approach, but practically one application of Eq. 35 is sufficient. Note that the description of the height-dependence of $g\,(\varphi, h)$ which is given by $\left(1 - 3.14 \cdot 10^{-7} h\right)$ is an approximation to the more accurate expression $1/(1+h/R_E)^2$ when R_E is the Earth radius.

Let's assume we have pressure values p in hPa, temperatures in Kelvin, and water vapor pressure values e in hPa at a set of geometric heights h. Typically these data are available up to 10 hPa (30 km) or 1 hPa (50 km), but to get highest accuracy for some applications as described in the later parts of the book, the meteorological data have to be extended up to about 100 km. Hobiger et al. (2008) use an upper limit of 86 km, Rocken et al. (2001) use 136 km. For example, the temperatures in Table 3 can be used, and the pressure can be extrapolated assuming an exponential decrease from the uppermost level.

Additionally, the increments for the numerical integration of refractivity need to be reduced. Following Rocken et al. (2001) height dependent increments can be

Table 3 Standard model for the temperature at certain heights up to 130 km

height in km	25	50	80	100	130
temperature in K	220	268	200	210	533

Table 4 Increments for ray-tracing following Rocken et al. (2001)

between (km)	0–2	2–6	6–16	16–36	36–136
increment (m)	10	20	50	100	500

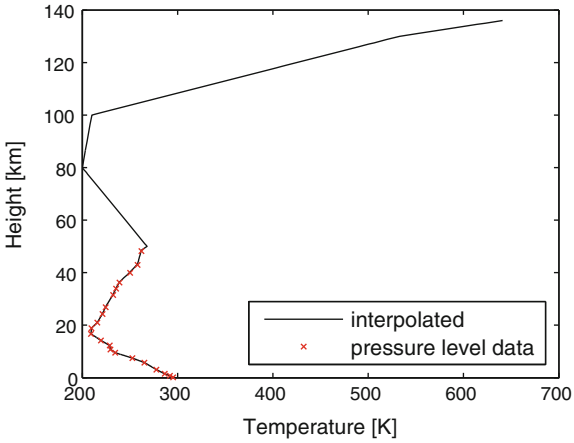

Fig. 4 Temperature versus height of the meteorological values provided with pressure level data (*red crosses*) and from inter- and extrapolation (*black line*)

applied. If the station height is at sea level, approximately 1000 layers are to be deployed (Table 4).

Temperature can be interpolated linearly but it should be extrapolated according to a standard model for the temperature (Table 3). An example is shown in Fig. 4. The water vapor pressure e can be interpolated with an exponential approach

$$e = e_0 \cdot e^{(h-h_0)/c} \tag{37}$$

where e_0 and h_0 denote the water vapor pressure and the height of the lower-next level where e is provided. The coefficient c can be determined from the water vapor pressure at two adjacent levels (compare Fig. 5). Other authors like Hobiger et al. (2008) use linear interpolation of relative humidity. The total pressure p can be determined with the hypsometric equation

$$h - h_0 = \frac{R'_d \cdot T_v}{g} \frac{p_0}{p} \tag{38}$$

which is based on Eq. 25 and where the index 0 refers to the closest level where meteorological data are available, and the virtual temperature T_v and gravity g are determined at the mean height $(h + h_0)/2$ (see Fig. 6).

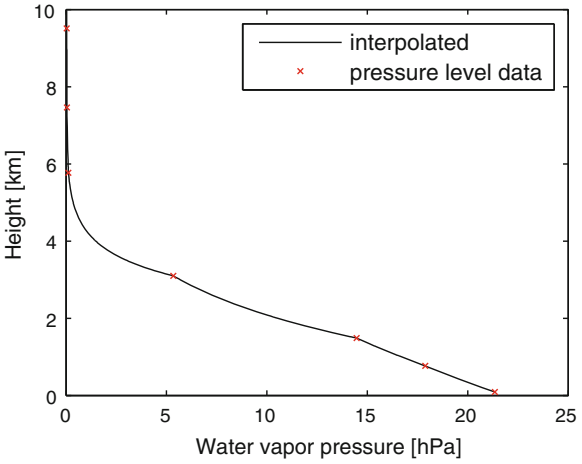

Fig. 5 Water vapor pressure versus height of the meteorological values provided with pressure level data (*red crosses*) and from interpolation (*black line*)

Fig. 6 Pressure versus height of the meteorological values provided with pressure level data (*red crosses*) and from inter- and extrapolation (*black line*)

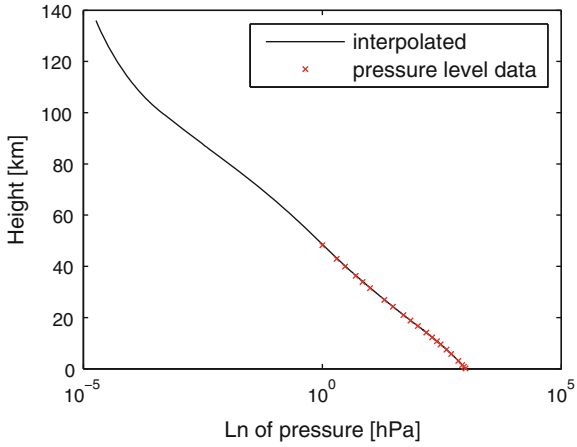

2.6 Reference Pressure

The reference pressure is a mean pressure value often realized at the topography by calculating the long-term average of surface pressure. It is required because many applications are more accurate when using deviations from the mean pressure rather than the full values themselves. The reference pressure is needed in various space geodetic applications, and it is related to other investigations of the Earth system. Examples are the determination of the atmospheric pressure loading displacements (Rabbel and Zschau 1985; Rabbel and Schuh 1986; van Dam and Wahr 1987; van

Dam and Herring 1994; Petrov and Boy 2004; Wijaya et al. 2013 in this book), the precise calculation of the Earth time-variable gravity field due to atmospheric mass redistribution (Boy and Chao 2005) and the de-aliasing of gravity mission satellite data (Flechtner 2007; Karbon et al. 2013), the determination of the centre of mass of the atmosphere with respect to the centre of mass of the total Earth (including oceans and atmosphere) (Chen et al. 1999), and the determination of the total atmospheric mass (Trenberth and Smith 2005) as well as its seasonal variations (Hoinka 1998).

With respect to atmospheric loading corrections in particular, the following requirements for the reference pressure can be identified:

- The reference pressure should be unambiguously determinable now, and the same pressure values should be obtained at any time in future.
- Any method for a reference pressure determination should be straightforward but accurate enough for present day requirements defined within the Global Geodetic Observing System (GGOS) of the International Association of Geodesy (IAG), i.e., 1 mm position accuracy and 0.1 mm/year velocity accuracy (Rothacher et al. 2009).
- The reference pressure should be accompanied by information about its corresponding height.
- The reference pressure should cause no (or minimal) biases compared to previous results, i.e. to analyses which did not refer to a reference pressure. For instance, if the reference pressure is, in an absolute sense, more accurate than 2 hPa, the resulting height bias would be less than 0.6 mm, which is certainly acceptable in all areas. The value of 0.6 mm is derived by assuming an average value for the regression coefficient of 0.3 mm/hPa (Rabbel and Zschau 1985).

2.7 Atmospheric Tides

Atmospheric tides are global-scale waves. They are excited by regular external influences, in particular by the differential heating of the Sun (the regular day/night cycle in the insolation of the atmosphere) and—to a lesser extent—by the gravitational lunisolar tidal force. For detailed descriptions we refer to Chapman and Lindzen (1970) and Volland (1997, 1988). The dominant regular daily and seasonal variations of atmospheric parameters like surface pressure, wind velocity or temperature, are of thermal origin, depending on differential solar radiation due to the Earth's rotation and the geometry of the Sun-Earth system. With the mean angular velocity of Earth rotation $\Omega = 7.292115 \cdot 10^{-5}$ rad/sec, the basic frequencies are $\Omega_s = -\Omega\,(1 - 1/366.26)$ and $\Omega_a = \Omega/366.26$ corresponding to the periods of one solar day and one tropical year, respectively (Brzezinski et al. 2002). But since the heating does not follow a simple sinusoidal pattern (the diurnal cycle is close to a slightly smoothed two-valued step function), and since there are orographic and meteorological differences near the ground, harmonics are generated with frequencies $k\Omega_s$ and $k\Omega_a$ which are positive or negative multiples of the two fundamental frequencies. These thermal waves are coherent with the gravitational tides, and thus

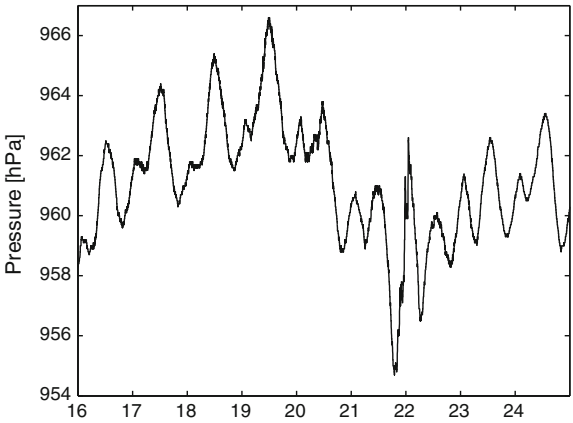

Fig. 7 Pressure time series in November 2011 at station PPTE in Presidente Prudente, Brazil

they are labelled in the same way, e.g. S_1 and S_2 (Brzezinski et al. 2002). Exemplarily, Fig. 7 shows the pressure measured at Presidente Prudente in November 2011, and the S_1 and S_2 pressure variations are clearly visible.

2.8 Inverted Barometer Hypothesis

For this section, we mainly follow Schuh et al. (2003). The oceanic response to atmospheric pressure variations is often considered to be static, causing an immediate and compensating local deformation of the sea surface. This vertical change in sea level ζ_{IB} is related to the atmospheric pressure variation δp_a with

$$\zeta_{IB} = -\frac{\delta p_a}{\rho_0 \cdot g} \tag{39}$$

applying a hydrostatic approximation (Gill 1982). As can be seen in Eq. 39 a positive pressure anomaly is accompanied by a decrease of sea surface height; thus there is an *inverted barometric* (IB) effect. For example, 1 hPa corresponds to 1 cm.

Considering time spans long enough compared to the response time of the ocean due to inertia, the IB hypothesis assumes a complete compensation of horizontal gradients of pressure by ocean height ζ without impacting the dynamics of the ocean or the ocean bottom pressure. At every depth h the pressure stays constant considering the atmospheric pressure change δp_a:

$$-\int_{\zeta}^{h} \rho \cdot g \cdot dz = -\int_{\zeta+\zeta_{IB}}^{h} \rho \cdot g \cdot dz + \delta p_a \tag{40}$$

Assuming IB behavior with its static approximation, all processes like currents caused by the isostatic compensation are neglected. The effects can be triggered

by horizontal gradients of atmospheric pressure. These barotropic components of currents vanish when the pressure anomalies have been compensated by the sea surface heights. Thus, neglecting the dynamic component of the IB correction is only justified for processes slow enough compared to the isostatic compensation (Schuh et al. 2003).

3 Atmospheric Layers and Circulation

Large-scale features of the atmosphere impact geodetic properties also because of its motions. To understand the overall structure, related to the dynamic impact of the atmosphere on the solid Earth in the form of changes in the rotational motions of the solid planet, it is necessary to understand the structure of the atmosphere and the circulations within important layers. Then interactions at the interfaces between the atmosphere, land and ocean below will be understood better.

The lowest layer, known as the troposphere, has most atmospheric mass. It extends from the surface to roughly 10 km, around the 200 hPa level, but these limits change somewhat with latitude and season, and it contains approximately 80 % of the atmospheric mass. The temperature decreases with height there, and it is typically an unstable layer. The general instability of the troposphere means that active weather phenomena occur there, with most of the water vapor residing there too. Clouds are formed when water vapor condenses on particles in the atmosphere. In addition, the wind circulation in the troposphere is quite complex.

The stratosphere is the layer above the troposphere, with the tropopause the surface boundary between these two layers of markedly different characteristics. The stratosphere is characterized by temperature increase with altitude, and so is a more stable layer. Its upper limit, the stratopause, at roughly 30 km in altitude, is a transition to another region, the mesosphere where temperature again decreases with altitude (see Fig. 2.2 by Salstein (1995)). Finally, the thermosphere, above roughly 85 km is a layer of again increasing temperature, due in large part by the strong absorption of solar radiation by gases there. Table 3 gives some standard values of temperatures at different altitudes, particular in these regions. Gases from the thermosphere in that region are more easily ionized, and so the regions above are known as the ionosphere, with details covered in later sections of this part.

The general circulation of the atmosphere includes the mean wind patterns and anomalies about the mean. Near the surface, prevailing winds in the tropics are the easterlies (from the east), also known as the trade winds, especially across regions above the ocean, and these are fairly shallow. In the middle latitudes are westerly winds, typically increasing with elevation, which achieve maximum values near the top of the troposphere, culminating in a largely zonal (east-west) jet structure in the mean in middle latitudes. This increase with height of the strength of the zonal winds is related physically to the meridional gradients of temperature, and this balanced portion is known as the thermal wind. In polar latitudes easterlies again occur, but the overall mass of the atmosphere in the polar regions carrying this momentum is

small. The overall sense of the mean circulation is westerly, positive with respect to the Earth's rotation, so that the atmosphere is in the mean in superrotation about the solid Earth. The strength of the superrotation varies strongly with the season, because of the high difference between the winds in winter and those in summer over the northern hemisphere, much of which has a so-called continental climate (see Schindelegger et al. (2013) in this book).

In addition, winds have northerly and southerly components, so that the air masses travel in waves around the planet. Large-scale waves are generally baroclinic in effect and are part of the patterns of migrating weather systems. In the northern hemisphere middle latitudes, we generally have weather moving from the west to the east, though whether they come from the northwest or southwest often depends on which phase of a planetary wave the region is in at that time.

Variability in the winds may indicate a total change in the angular momentum of the atmosphere, which in the closed Earth system is transferred to either the ocean or solid Earth below. In fact, most of the transfers to the ocean are then quickly transferred to the solid Earth itself, and impacts the changes in the Earth's rotation rate and vector. These torques happen because of a variety of tangential forces from surface winds, normal forces of atmospheric pressure against mountains, and gravitational forces. The atmospheric angular momentum and torques are covered by Schindelegger et al. (2013) in this book.

The atmosphere has been modeled for the purpose of analysis, short-term weather forecasts, and climate projections. Such models, which are produced and used by the world's major research and weather forecast centers, are based on the principles of atmospheric physics which frame an analysis of the weather and climate system.

Physical equations for the atmosphere include the equation of motion, a form of Newton's second law, the equation of total mass continuity, and of continuity of its constituents, particularly water substance and the equation of thermodynamics (reviewed by Salstein (1995)). These may be thought of as representing the conservation laws of momentum, mass, and energy, respectively. Together with information about gas physics, chemistry, and radiative transfer, these equations are the basis of numerical weather prediction. To analyze the basic meteorological quantities, namely temperature, pressure or geopotential height, wind, and moisture, and to use these meteorological fields as initial conditions for forecasts, a variety of observational data concerning the atmosphere are assimilated into an analysis-forecast system. Such data are derived from weather observations on the surface, and upon the radiosonde network, from aircraft-based measurements, and from both geostationary and polar orbiting satellites.

The atmosphere has been thought of as a heat engine, in which solar energy in different forms is applied to the air to first provide heating for the atmosphere. These forms are sensible heating of direct contact, say from the warm land or warmer air layers, below, latent heating from the condensation of water vapor (reduced by its opposite, latent cooling from evaporation), and the form of heating by radiational transfer through gases, mostly from the near infrared, visible, and near ultraviolet parts of the spectrum. When these forms of heating are applied, overturning circulations of the atmosphere result, creating vertical motions and horizontal wind

motions of the air. However, the Earth and atmosphere then radiate out the energy in the form of longwave radiation in the infrared. The overturning of the atmosphere relates to the prevailing meridional circulation. The fundamental physical elements of the atmospheric climate system are thus the momentum, heat and moisture cycles (see Peixoto and Oort (1992)). The differential heating in the troposphere, because of latitude, cloud effects, and the irregular distribution of land and ocean, and land surface characteristics, leads to patterns of atmospheric mass, along with the changes in temperature and circulation structure. The total atmospheric mass patterns have distinct climatological distribution, such as the strong prevailing high pressures over Siberia in the cold winter. These patterns, and changes in them on daily to weekly weather time scales and more seasonal time scales, also is a cause of angular momentum variation, leading in particular to exchanges from the Earth causing changes in positions of the pole, and to a lesser extent, changes in the speed of the Earth's rotation.

4 The Ionosphere

The ionosphere is an upper part of the Earth's atmosphere, extending from about 60–2000 km, with the main concentration of its particles between 300 and 400 km (Rishbeth and Garriott 1969; Hargreaves 1995). Solar Extreme Ultra Violet (EUV) radiation at wave lengths <130 nm significantly ionizes the neutral gas. In addition to photo-ionization by electromagnetic radiation, energetic particles from the solar wind and cosmic rays contribute to the ionization but to a much lesser extent (Hunsucker and Hargreaves 2002). The electron production in the ionosphere is a direct consequence of the interaction of the solar radiation with atoms and molecules in the Earth's upper atmosphere. These free electrons and ions affect the propagation of electromagnetic waves. This effect is called ionosphere refraction and has to be considered when determining the propagation velocity of signals of all space geodetic techniques operating in the microwave band.

4.1 Ionization and Recombination

Within the ionosphere, solar radiation hits the atmosphere with a power density of 1370 W/m^2, a value known as the solar constant. The intense level of solar radiation is spread over a wide spectrum, ranging from radio frequency through infrared (IR) radiation and visible light to X-ray. Due to the fact that the photons of energy at ultraviolet (UV) or shorter wavelengths are capable of separating an electron from a neutral gas atom or molecule during a collision, they are considered as ionizing. During a strike, the incoming solar radiation hits a gas atom (or molecule); the atom absorbs part of this radiation and produces a free electron and a positively charged ion.

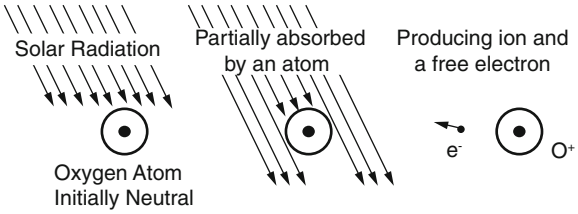

Fig. 8 Ionization of an Oxygen molecule due to solar radiation (modified from http://www.haarp.aloska.edu/harp/ion1.html)

4.1.1 Ionization

There are three different sources for ionization within the ionosphere, which are extreme UV and X-ray radiation, high-energy particles, and cosmic rays.

Extreme UV and X-ray radiation: At the highest altitudes of the Earth's atmosphere, solar radiation is very strong but a smaller number of atoms exist to interact with, and so the amount of ionization is limited. At somewhat lower altitudes, more gas atoms are present, increasing the ionization process. In the ionizating process, a neutral atom X absorbs energy hf, to produce a positive ion X^+ and a free electron e^- (Fig. 8)

$$X + hf \rightarrow X^+ + e^- \,. \tag{41}$$

High-energy particles: Those particles could reach up to several thousands of electron volts (eV) in the auroral zone due to magnetosphere activities.

Cosmic rays: The Ultra-high energy particles with cosmic origin can penetrate deep into the atmosphere and cause ionization within the lower ionosphere.

4.1.2 Recombination

Meanwhile an opposing process begins to take place in which a free electron moves close enough to a positive ion to be captured by it. This recombination process also accelerates at lower altitudes as the density of gas molecules and ions increases and they are closer to each other. The balance between ionization and recombination determines the degree of ionization present at any time.

If ionization was undone by recombination, the atmosphere would become fully ionized. However, instead, the production and destruction of ions reach an equilibrium. In this recombination process, negative electrons e^-, and positive ions X^+, combine to produce neutral particles. There are two basic types of recombination.

Radiative recombination: An electron combines with an atomic ion producing a neutral atom and a photon $h\nu$:

$$e^- + X^+ \rightarrow X + h\nu \,. \tag{42}$$

Dissociative recombination: An electron combines with a molecular ion XY^+ and produces two neutral atoms X and Y:

$$e^- + XY^+ \rightarrow X + Y \ . \tag{43}$$

With decreasing altitude and increasing numbers of gas atoms and molecules, there should be more opportunity for energy absorption. But the energy from the solar UV radiation is already absorbed at higher altitudes, and the intensity of radiation is less lower down. At certain points with a balance of lower radiation and greater gas density, recombination rates balance the ionization rate, leading to formation of ionization peaks at different layers, known as the Chapman layers.

4.2 Chapman Layer Profile

It is known that the density of the atmosphere decreases exponentially with altitude (neglecting, for the moment, variations caused by the temporal structure or the diffusive separation of species). Also, monochromatic radiation is attenuated exponentially by an absorbing medium (Aghanajafi 2000). Using these two facts, we can conceive how solar radiation produces ionized layers. At the outer fringes of the atmosphere, the density is low and radiation is absorbed only slightly; but deeper in the atmosphere, both the density and the absorption of radiation increase exponentially. At a certain region, this process produces very rapid attenuation of radiation at a particular wavelength, with virtually no penetration below. If the absorption is caused by ionization processes, an ionized layer will result. This phenomenon is represented schematically by Fig. 9 (Whitten and Poppoff 1971).

This layer formation theory was put in good quantitative form by Sydney Chapman in 1931. The Chapman law describes the direct relation of the density of free electrons and ions to height and daily solar motion. The production rate of ion pairs is given by

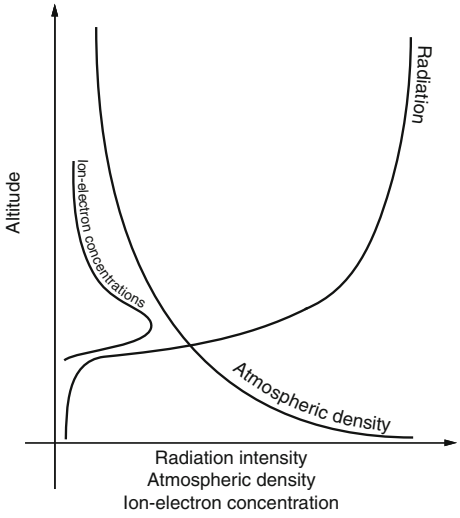

Fig. 9 Schematic representation of layer formation (modified from Whitten and Poppoff 1971)

the Chapman function under the following simplifying assumptions as e.g. described by Todorova (2008):

- only the solar radiation is taken into account, i.e. the impact of the cosmic rays, which are the second main (but less strong) cause of ionization, is neglected;
- the atmosphere consists of a one-component isothermal gas distributed in horizontally stratified shells with constant scale height;
- the solar radiation is monochromatic and absorbed proportionally to the concentration of gas particles.

To describe the vertical structure of electron density in the ionosphere, a Chapman profile function can be derived. Taking the hydrostatic equilibrium assumption of the upper atmosphere into account (compare Sect. 2.4) one can approximate the scale height H as a linear function of ion altitude.

Now we introduce the ion production rate under simplifying assumptions mentioned in Sect. 4.2. Following Schaer (1999), the ion production rate is given by the Chapman function

$$q(h, \chi) = q_0 \, e^{(1 - z - \sec \chi \, e^{-z})} \qquad \text{and} \qquad z = \frac{h - h_0}{H} \, , \tag{44}$$

where

$q(h, \chi)$ ion production rate,
z scaled altitude,
q_0 maximum ion production rate at $\chi = 0$,
h_0 reference height of maximum ion production at $\chi = 0$, i.e. the Sun at zenith,
H scale height, and
χ Sun zenith angle.

The maximum ion production rate is defined as

$$q_0 = \frac{\phi(\infty)\eta}{He} \, , \tag{45}$$

where

$\phi(\infty)$ solar flux density outside the atmosphere (in photons/area),
η number of ion pairs produced per proton,
e base of natural exponential function.

To obtain the altitude of maximum ion production rate h_{max}, the Chapman function Eq. (44) is differentiated. This yields

$$h_{max} = h_0 + H \, z_{max} \qquad \text{with} \qquad z_{max} = \ln \sec \chi \, . \tag{46}$$

The maximum of the ion production is obtained from

$$q_{max} = q_0 \cos \chi \, . \tag{47}$$

Within the ionosphere, ions and electrons recombine proportionally to the electron density. Neglecting the electron transportation processes, the following equation holds

$$\frac{dN_e}{dt} = q - aN_e^{\frac{1}{\alpha}}\,, \tag{48}$$

where a is the mean recombination coefficient for molecular ions and α is a constant depending on the ionospheric altitude. Using Eqs. (44) and (48) in the photochemical equilibrium condition, where $dN_e/dt = 0$, the electron density is given by

$$N_e(h, \chi) = N_0\, e^{\alpha(1-z-\sec\chi e^{-z})} \qquad \text{with} \qquad N_0 = \left(\frac{q_0}{a}\right)^{\alpha}. \tag{49}$$

N_0 is the maximum electron density at $\chi = 0$. This distribution is called the simple Chapman function (Rishbeth and Garriott 1969).

According to Ratcliffe (1972) the maximum electron density N_m and its corresponding height h_m vary with the Sun zenith angle χ, i.e. with day time. At noon, (where $\chi = 0$) N_m reaches its maximum and h_m its minimum. During the time of sunset and sunrise h_m has its maximum and N_m its minimum. The relation between the electron density maximum N_m and its corresponding value at $\chi = 0$, i.e. N_0 can be simply derived by

$$N_m = N_0 \cos\chi\,. \tag{50}$$

Substituting N_0 with the more general quantity N_m leads to

$$N_e(h) = N_m\, e^{\alpha(1-z-e^{-z})}. \tag{51}$$

Figure 10 shows the electron density profile using Eq. (49) for different solar zenith angles. Though at lower latitudes there is a large amount of ionizable molecules, the

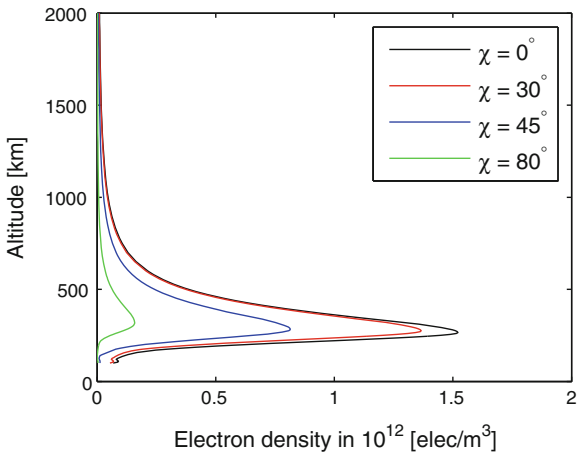

Fig. 10 Electron density profile for different solar zenith angles (modified from Todorova 2008)

ion production rate decreases due to the ionization of the high atmospheric layers and the reduction of photons. The potential of the increased quantity of photons at higher latitudes, however, is limited by the low molecular density. Therefore, the altitude of maximum ion production is found at heights of about 200–700 km.

In spite of the simplifying assumptions under which the Chapman theory is derived, it is able to explain the main characteristics of the ionosphere and provides a reliable reference for the basics in the ionosphere modeling (Kelly 1989). As shown by the altitude profiles, the maximum electron density is concentrated in a relatively thin layer, typically located at a height between 300 and 500 km above the Earth's surface. Based on that result, the Single Layer Model (*SLM*) has been introduced (see Alizadeh et al. (2013) for more details). In *SLM* it is assumed that all free electrons are concentrated in an infinitesimally thin layer at a fixed height. Usually, this height slightly exceeds the altitude of maximum electron density in order to balance the effect of the more extended topside ionosphere.

4.3 Variations in the Ionosphere

The ionosphere is a complicated medium. It varies with a number of different parameters, which cause variations in spatial and temporal structure of electron density and so in the ionospheric layers. The main parameters driving the ionosphere are the solar activity and the behavior of the geomagnetic field, so when studying the electron density it will be beneficial to introduce two additional coordinate systems besides the geographical coordinate system, which take the characteristics of the medium into account.

The Sun-fixed coordinate system is used to keep the change in the Sun position minimal. The coordinate system should co-rotate with the Sun, so the temporal variation of the electron content is slow and can be averaged for a short period, e.g. 1–2 h. The origin of this Sun-fixed coordinate system is set at the center of mass of the Earth, the terrestrial rotation axis is chosen for Z-axis and the X-axis is defined by the mean solar meridian; the Y-axis completes the coordinate system to a right-handed one. In that way the geographical longitude and latitude (λ_g, φ_g) can be transformed into sun-fixed latitude and longitude (λ_s, φ_s) as follows:

$$\varphi_s = \varphi_g \ , \tag{52}$$

$$\lambda_s = s = \lambda_g + UT - \pi = \lambda_g + (UT - 12)^{hours} \ , \tag{53}$$

where φ_s and λ_s are in degrees and UT is the Universal Time in hours. In order to unify the units in Eq. (53), $(UT - 12)$ should be multiplied by 15°/h. After the transformation, the latitude remains unchanged (Eq. 52) and the sun-fixed longitude Eq. (53) matches the hour angle of the Sun.

The geomagnetic coordinate system is defined by its Z-axis parallel to the axis of magnetic dipole, and its Y-axis perpendicular to the geographic poles. So if $\overrightarrow{DP}$

would be the dipole position and $\overrightarrow{SP}$ the south pole, we have $\overrightarrow{Y} = \overrightarrow{DP} \times \overrightarrow{SP}$. Finally, the X-axis of the system completes an orthogonal right-handed set. The relation between the geomagnetic coordinates (λ_m, φ_m) and the geographic coordinates (λ_g, φ_g) follows:

$$\sin \varphi_m = \sin \varphi_g \sin \varphi_0 + \cos \varphi_g \cos \varphi_0 \cos(\lambda_g - \lambda_0) \tag{54}$$

$$\sin \lambda_m = \frac{\cos \varphi_g \sin(\lambda_g - \lambda_0)}{\cos \varphi_m} \tag{55}$$

where φ_0 and λ_0 are the geographical coordinates of the geomagnetic north pole. According to the International Geomagnetic Reference Field (IGRF), the coordinates of the north magnetic pole for the year 2010 are $\varphi_0 = 80.0°$ (N) and $\lambda_0 = 72.2°$ (W) (IGRF 2011). According to Schaer (1999) the geomagnetic north pole is moving about $+0.03°$ in the south-north direction and $-0.07°$ in the west-east direction per year.

4.3.1 Height Dependent Spatial Variations

The ionosphere is subdivided into different height-dependent layers, based on the solar radiation wavelength which is most absorbed in that layer or the level of radiation which is required to photo dissociate the molecules within these individual regions. The main layers are known as D, E, F1 and F2.

The D layer is the part from approximately 60–90 km, which absorbs the most energetic part of solar radiation. This layer reflects long wavelength radio waves transmitted from Earth's surface back to the Earth. This phenomenon makes long distance radio communication possible. The D region is the most complex part of the ionosphere from the chemical point of view. Several different sources cause the ion production within this layer. The most important are: Lyman-α (Rhoads et al. 2000) that ionizes the *NO* molecule, ultraviolet radiation that ionizes O_2 and N_2, hard X-rays that depend strongly on the solar activity and are not significant at sunspot minima, and galactic cosmic rays that affect mainly the lower parts of the D region. The D region shows sudden changes in the electron concentration near sunrise and sunset and remains almost constant during the day. During the nighttime at mid latitudes this layer vanishes.

The E Layer is the part from about 85–140 km, although the production peak is at 110–115 km. Since at this height different molecular gases are present, molecular ions are produced directly and the loss rate is dominated by dissociative recombination. As this is not height-dependent, the resulting electron concentration in this region closely follows the production profile. The E layer absorbs soft X-rays, and it reflects standard AM radio waves, which are transmitted from the Earth, back to its surface. The variations are regular and are mainly controlled by the Sun and may be described by a Chapman law (see (Alizadeh et al. 2013) in this book). The E layer does not vanish at night, but a weakly ionized layer remains with an electron density of approximately $2 \cdot 10^9$ electrons/m^3.

In addition to the regular E layer of the ionosphere, there exist other irregular layers known as the sporadic E layers (Es). Depending on the mechanism of formation, there are different sporadic E layers. In the equatorial zone, the sporadic E layer may be interpreted in terms of the two-stream ion wave instability in the plasma (Feltens et al. 2009). In the polar ionosphere, the same mechanism may sometimes apply as well as ionization due to penetration of charged particles. In other cases, turbulence may also play a role in the formation of the sporadic E layer. Auroral sporadic E is produced by energetic electrons from the magnetosphere. Furthermore, in the auroral zone, nighttime ionization is produced by particles from the magnetosphere (Mayer and Jakowski 2009). Sporadic E layer can occur over a range of heights from about 90–120 km or even more. In some cases the Es is a relatively thick layer with a well-defined maximum of electron density whereas in other cases it is extremely thin. In some cases the Es layer is opaque and blankets the upper layers; in other cases the upper layers can be seen through the Es, which suggests that the radio waves are penetrating through the gaps.

In the F layer the peak production height is at 150–160 km. But the electron concentration peak is well above this height at around 250–300 km. Among the solar radiation the F layer absorbs EUV radiation. The F region reflects radio waves with shorter lengths transmitted from Earth's surface. Visible light, radar, television and FM wavelengths are all too short to be reflected by the ionosphere and they penetrate through this medium. So these wavelengths are suitable for satellite communications. Through the F layer, by increase in height, the loss rate gradually becomes dominated by the ion-atom exchange rate and starts to decrease. In fact the loss rate drops down faster than the rate of production, resulting in an actual increase in electron concentration. As the plasma diffusion takes over, the electron concentration becomes distributed similar to the neutral gas concentration, and a maximum is reached. The height where the loss rate transits from dissociative to ion-atom exchange can vary. If this height is above the peak production, a reduction in the actual electron concentration happens. This results in a secondary peak in the electron concentration profile at the peak of production called the F1 peak. Therefore the F layer is subdivided into two layers, the F1 layer extending from about 140–200 km and the F2 layer from 200–1000 km. Table 5 designates the four principal layers of the ionosphere.

From altitudes of about 1000 km the density of O^+ ions starts to fade and the H^+ ion turns into the dominate particle. This height is known as the transition height. This layer of the upper atmosphere is called the plasmasphere. The plasmasphere is bounded on the upper side by the plasmapause where plasma density drops by one or two orders of magnitude. Due to the fact that neutral densities are very low in this region, the plasma profiles are determined by transport of electrons and ions. The

Table 5 Characteristics of the main ionospheric layers

Layer		D	E	F1	F2
Height domain (km)		60–90	85–140	140–200	200–1000
Electron density (elec/m^3)	Day	10^8–10^{10}	10^{11}	$5 \cdot 10^{11}$	10^{12}
	Night	–	$2 \cdot 10^9$	10^9	$3 \cdot 10^{11}$

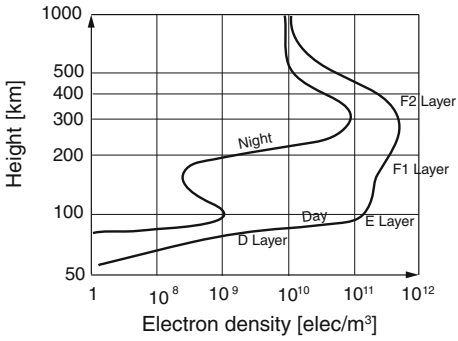

Fig. 11 Chapman electron density profile and the ionospheric layers D, E, and F for both night and day conditions at mid-latitudes (Cravens 1997)

position of the transition height (at which the concentration of O^+ and H^+ are equal) varies from around 800 km on a winter night at low solar activity to around 4000 km during a summer day at high solar activity (Feltens et al. 2009). Since there is almost no plasma production in the plasmasphere, the ionized particles diffuse up from the ionosphere to plasmasphere. The plasmasphere takes ionized particles from the ionosphere by day, acting like a reservoir and stores them in a loss-free environment. At nighttime this procedure gets inversed and the plasmasphere returns the ions back to the ionosphere. Thus the nighttime F layer is maintained in the ionosphere (Fig. 11).

4.3.2 Latitude Dependent Spatial Variations

Due to the Earth's magnetic field the behavior of the ionosphere can be divided into three latitudinal regions: low latitude (equatorial), mid latitude and high latitude regions (Fig. 12). The boundaries between the regions are not constant, but vary according to local time, geomagnetic condition and solar activity.

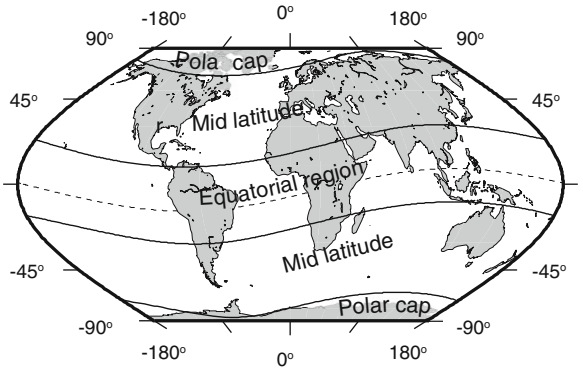

Fig. 12 Latitude dependent regions of the ionosphere (modified from Hobiger 2005)

The low latitude region contains the highest values of the Total Electron Content (TEC) and the peak electron density. The scintillation effect (see Sect. 4.3.3) has its greatest amplitude at these latitudes. The distribution of the peak electron density at the F2 layer depicts a minimum at the geomagnetic equator with two maximum peaks on both sides of the equator, at the magnetic latitudes of 15°–20° north and south. This phenomenon is called equatorial (or Appelton) anomaly and this region is also called the equatorial region. Investigations by several authors (e.g. Hoque and Jakowski (2012)) show that the peak over the geomagnetic equator extends during daytime, but becomes weaker during nighttime. Various processes significantly disturb these areas, which display a strong diurnal dependence.

The mid latitude region is the least variable region of the ionosphere. It shows the most regular and predictable variations of TEC. There are several ionospheric models that estimate the mean ionosphere in this region with a high degree of accuracy. Nevertheless, the daily variations of TEC in this region reveal a root mean square (r.m.s.) variations of 20–30 % from the average value. Within this region there are zones of low electron densities lying between 50°–70° geomagnetic latitude called the mid latitude troughs (Muldrew 1965). The electron density inside the trough is drastically reduced by as much as a factor of 2 at 1000 km altitude and as much as an order of magnitude at the F2 peak (Timleck and Nelms 1969).

In the high latitude region photo-ionization is the main source of ionization. Another important driver in this region is the high energy particles. Geomagnetic field lines guide energetic protons and electrons from the magnetosphere down to the Earth's atmosphere. Accelerating particles lose their energy after colliding with the neutral particles and ionize them at the same altitude where solar UV radiation is absorbed by the atmosphere. Precipitating particles also lose their energy before collisions with the neutral particles through the particle-wave interaction, which finally generates intense electromagnetic waves named auroral kilometric radiation (AKR) with a frequency between 100 and 500 kHz. Additionally, some of the atmospheric elements are excited to higher energy levels. This leads to emission of visible lights, called the auroral lights. This activity occurs mainly within the auroral oval. The maximum is near 67°N at midnight, increasing to about 77°N at noon. They tend to occur in bursts, each lasting about 30–60 min, separated by intervals of several hours.

4.3.3 Regular Temporal Variations

Variations within the solar radiation and the solar zenith angle causes temporal variations of the ionosphere. These variations could be classified into regular and irregular variations. The ionosphere exhibits daily, seasonal and longer variations controlled by the solar activity. Over the course of the day, season, and sunspot cycle the ionosphere parameters might change by several orders of magnitude. However, during irregular variations, the change can happen within a few minutes up to several days.

The solar cycle variations are long-period in the ionosphere depending on the solar activity. A basic indicator for the level of solar activity is the sunspot number. Due to their relatively low temperature, the sunspots are visible on the solar surface

as darker regions and are usually located between 5° and 30° solar latitude (Hobiger 2005). A widely used quantity is the Wolf sunspot number R:

$$R = k(f + 10g) \tag{56}$$

where

f total number of the observed single spots,
g number of sunspot groups,
k constant, depending on the instrumental sensitivity.

Sunspots were first noticed around 325 BC and have been recorded for several centuries. The spectral analysis of sunspot number time series shows a very prominent period of about 11.1 years. However the typical cycle is not symmetric, the time from minimum to maximum is about 4.3 years and the time from maximum to minimum is 6.6 years on average. The latest solar minimum was recorded in the period 2005–2006. The next solar maximum is expected to occur in 2013. The solar activity level is also measured by the F10.7 cm solar radio flux which is a proxy for the solar EUV radiation.

Seasonal variations. In general, the maximum electron density and the total electron content of the nighttime F region are higher in summer than in winter. However, in mid latitudes, the peak density of noon profiles is considerably greater in winter than in summer; this is called winter anomaly. This anomaly is more evident in mid-latitudes than in low and high latitudes (Feltens et al. 2009). The winter anomaly occurs in the daytime only and is thought to be due to a large summer electron loss rate caused by an increase in the molecular-to-atomic composition of the neutral atmosphere (Davies 1990). The night time F2 layer tends to be at higher altitudes in summer than in winter, the tendency being accentuated in lower latitudes. The night time F2 layer tends to be thicker when higher. In the summer months, in mid latitudes, the F layer bifurcates into the F1 and F2 layers. Under these conditions the F2 peak density is fairly small and is located at a relatively high altitude. The F1 layer is not so much a distinct layer but rather a minor inflection in the profile at about 180–220 km. However, in the summer or around noon time, it is more liable to see the F1 layer as an individual layer comparing to winter time or in the sunrise and sunset.

Diurnal variations. The most apparent effect is seen within the ionosphere as the Earth rotates around its axis. The ionization increases in the sunlit hemisphere, reaching a peak shortly after local noon time, and decreases on the shadowed side. In general, the electron densities are greater at all heights by day than by night and large diurnal changes occur particularly in the lower ionosphere. While the D layer causes the weakening of propagated radio waves through the ionosphere during the day, it almost disappears during the night. The E layer appears promptly at sunrise and essentially disappears at sunset, except for the residual ionization at night.

4.3.4 Irregular Temporal Variations

Ionospheric storms are large scale disturbances of the ionospheric structure and dynamics caused by a Coronal Mass Ejection (CME) from the sun. The storm is usually initiated by a huge solar flare followed by several coronal mass ejections on the subsequent days. The strong enhancements of the solar wind energy generate large perturbations in the high-latitude ionosphere and thermosphere, resulting in significant variability of the plasma density, which commonly propagates towards lower latitudes (e.g. Förster and Jakowski (2000), and Ho et al. (1996)). The ionospheric storm can increase the TEC by more than 10 Total Electron Content Units (TECU) (Feltens et al. 2009).

Traveling ionospheric disturbances (TID) are wave shape plasma density fluctuations propagating through the ionosphere at different range of velocities and frequencies. TID are observable in most of the ionospheric measurements (e.g. Faraday rotation, VLBI, GPS, and Incoherent Scatter-Radar). TID can change the value of the TEC in the region of their occurrence in the range of several percent (Schaer 1999). Three types of TID are defined: large- (LSTID), medium- (MSTID) and small-scale (SSTID). LSTID present a period of 30–180 min and move at about 300 m/s. LSTID are related to geomagnetic activities and the Joule effect in high latitudes, producing thermospheric waves towards lower latitudes. MSTID move slower (50–300 m/s) and have shorter periods (ranging from 10 min to 1 h). The origin of MSTID is related to meteorological phenomena like neutral winds or solar terminators, which produce atmospheric gravity waves revealing TID at different ionospheric heights. Table 6 lists the main classifications of TID. According to Hobiger (2005), TID occur mostly in midlatitudes and are more evident close to solar maximum (Hernández-Pajares et al. 2006).

Scintillations describe the irregular variations of the amplitude or the phase of a radio signal received after passing through, or being reflected by the ionosphere. A strong scintillation can typically last for periods of up to several hours in the evening, broken up with varying intervals of time with no scintillation. The most severe scintillation effects are observed at and near the equatorial regions (Goodman and Aarons 1990). However, the times of strong scintillation effects are generally limited to approximately 1 h after local sunset to local midnight except some exceptions. The occurrence of strong scintillation is closely related to the sunspot number. During the years of maximum solar activity, strong scintillation effects can be observed in the equatorial and low-latitude regions. In the months from September through March, chances are high for significant scintillation in the American, African, and Indian longitude regions. However, in the Pacific region, scintillation effects maxi-

Table 6 Traveling ionospheric disturbances

Classification	LSTID	MSTID	SSTID
Horizontal wavelentgh (km)	>1000	>100	>10
Period (min)	30–180	10–60	>1
Phase velocity (ms^{-1})	300–1000	100–300	–

mize during April to August. In the auroral and polar cap latitudes, any significant magnetic storm activity can produce scintillation effects. Although the high-latitude scintillations are not as strong as those measured in the near-equatorial belt, they can last for many hours, even days, and are not limited to the local late evening hours, as the near equatorial scintillation effects (Feltens et al. 2009).

Solar flare effects. Solar radiation bursts known as solar flares may cause a rapid and severe increase of ionization in the ionosphere. Sudden Increase of TEC (SITEC) are caused by enhanced photoionization due to solar radiation bursts at wavelengths less than 130 nm. SITEC can effect TEC values in the range from less than 1 TECU up to 20 TECU or even more (Jakowski and Lazo 1977). These TEC jumps are within few minutes and may seriously limit the accuracy and reliability of GNSS applications.

Acknowledgments The authors would like to thank the Austrian Science Fund for supporting their work within project GGOS Atmosphere (P20902-N10). Support to David Salstein was also provided by the US National Science Foundation, under a series of grants, most recently ATM-0913780.

References

C. Aghanajafi. *Aeronomy*. KNToosi University of Technology Academic Press, 2000.

M. Alizadeh, D.D. Wijaya, T. Hobiger, R. Weber, and H. Schuh. Ionospheric effects on microwave signals. In J. Böhm and H. Schuh, editors, *Atmospheric effects in space geodesy*. Springer-Verlag, 2013. this book.

J.-P. Boy and B.F. Chao. Precise evaluation of atmospheric loading effects on Earth's time-variable gravity field. *J. Geophys. Res., 110*, B08412, 2005.

A. Brzeziński, C. Bizouard, and S.D. Petrov. Influence of the atmosphere on Earth rotation: what new can be learned from the recent atmospheric angular momentum estimates? *Surveys in Geophysics 23:33–69*, 2002.

S. Chapman and R.S. Lindzen. *Atmospheric Tides: Thermal and Gravitational*. Reidel, Dordrecht, The Netherlands, 1970.

J.L. Chen, C.R. Wilson, R.J. Eanes, and R.S. Nerem. Geophysical interpretation of observed geocenter variations. *J. Geophys. Res., 104, B2:2683–2690*, 1999.

T.E. Cravens. Ionosphere. In *Encyclopedia of Planetary Science*, pages 354–359, Springer-Verlag, 1997.

K. Davies. *Ionospheric Radio*, Volume 31 of IEE Electromagnetic Waves Series. Peter Peregrinus Ltd, London, 1990.

J. Feltens, M. Angling, N. Jakowski, C. Mayer, M.M. Hoque, H. Hernández-Pajares, A. García-Rigo, R. Orús-Perez, and A. Aragón-Angel. Analysis of the state of the art ionosphere modelling and observation techniques. Technical Report OPS-SYS-TN-0017-OPS-GN, Iss. 1/0, ESA/ESOC, June 2009.

F. Flechtner. Grace AOD1B product description documents, rev.3.1, Apr. 13, 2007. Technical report, Department 1: Geodesy and Remote Sensing, GeoForschungzentrum, Potsdam, 2007.

M. Förster and N. Jakowski. Geomagnetic storm effects on the topside ionosphere and plasmasphere: A compact tutorial and new results. *Surveys in Geophysics*, 21(1):47–87, 2000.

A.E. Gill. *Atmosphere-Ocean Dynamics*. Academic Press, New York, 1982.

J.M. Goodman and J. Aarons. Ionospheric effects on modern electronic systems. *Proc. IEEE*, 78(3), 1990.

J.K. Hargreaves. *The Solar-Terrestrial Environment - An Introduction To Geospace - The Science of the Terrestrial Upper Atmosphere, Ionosphere, And Magnetosphere*. Cambridge University Press, May 1995.

M. Hernández-Pajares, J.M. Juan, and J. Sanz. Medium-scale traveling ionospheric disturbances affecting GPS measurements: Spatial and temporal analysis. *J. of Geophys. Res.*, 111(A07S11), 2006.

M.C. Ho, A.J. Mannucci, U.J. Lindquister, X. Pi, and B. Tsurutani. Global ionosphere perturbations monitored by the worldwide GPS network. *Geophys. Res. Lett.*, 23:3219–3222, 1996.

T. Hobiger. *VLBI as tool to probe the ionosphere*. PhD thesis, Vienna Univ. of Technology, Austria, 2005.

T. Hobiger, R. Ichikawa, Y. Koyama, and T. Kondo. Fast and accurate ray-tracing algorithms for real-time space geodetic applications using numerical weather models. *J. Geophys. Res., 113: D20302*, 2008.

K.P. Hoinka. Mean global surface pressure series evaluated from ECMWF reanalysis data. *Q.J.R. Meteorol. Soc., 124:2291–2297*, 1998.

M.M. Hoque and N. Jakowski. A new global model for the ionospheric F2 peak height for radio wave propagation. *Ann. Geophys.*, 30:797–809, 2012.

R.D. Hunsucker and J.K. Hargreaves. *The high latitude ionosphere and its effects on radio propagation*. Cambridge University Press, 2002.

International Geomagnetic Reference Field IGRF. World data center for geomagnetism, Kyoto, 2011. http://wdc.kugi.kyoto-u.ac.jp/poles/polesexp.html

N. Jakowski and B. Lazo. Significant events in TEC measurements between 20 March and 5 May, 1976. In *Collected data reports for STIP interval II, 20 March - 5 May 1976*, Volume 61, pages 432–435. UAG, 1977.

M. Karbon, J. Böhm, D.D. Wijaya, and H. Schuh. Atmospheric effects on gravity space missions. In J. Böhm and H. Schuh, editors, *Atmospheric effects in space geodesy*. Springer-Verlag, 2013. this book.

M.C. Kelly. *The Earth ionosphere: plasma physics and electrodynamics*. Academic Press (San Diego), 1989.

H. Kraus. *Die Atmosphäre der Erde: eine Einführung in die Meteorologie*. Springer, 2004.

C. Mayer and N. Jakowski. Enhanced e-layer ionization in the auroral zones observed by radio occultation measurements onboard CHAMP and FORMOSAT-3/COSMIC. *Annales Geophysicae*, 27:1207–1212, 2009.

D.B. Muldrew. F-layer ionization trough deduced from Alouette data. *J. Geophys. Res.*, 70:2635–2650, 1965.

T. Nilsson, J. Böhm, D.D. Wijaya, A. Tresch, V. Nafisi, and H. Schuh. Path delays in the neutral atmosphere. In J. Böhm and H. Schuh, editors, *Atmospheric effects in space geodesy*. Springer-Verlag, 2013. this book.

J.P. Peixoto and A.H. Oort. *The Physics of Climate*. American Institute of Physics, New York, NY, USA, 1992.

L. Petrov and J.-P. Boy. Study of the atmospheric pressure loading signal in very long baseline interferometry observations. *J. Geophys. Res., 109, B03405*, 2004.

W. Rabbel and H. Schuh. The influence of atmospheric loading on VLBI-experiments. *J. Geophys., 59:164–170*, 1986.

W. Rabbel and J. Zschau. Static deformation and gravity changes at the Earth surface due to atmospheric loading. *J. Geophys., 56:81–99*, 1985.

J.A. Ratcliffe. *An introduction to the ionosphere and magnetosphere*. Cambridge University Press, 1972.

J. Rhoads, S. Malhotra, D. Arjun, S. Hyron, and J. Buell. First results from the large-area lyman alpha survey. *The Astrophysical Journal*, 545:85–88, 2000.

H. Rishbeth and O.K. Garriott. *Introduction to Ionospheric Physics*. New York, Academic Press, 1969.

C. Rocken, S. Sokolovskiy, J.M. Johnson, and D. Hunt. Improved mapping of tropospheric delays. *Journal of Atmospheric and Oceanic Technology, 18:1205–1213*, 2001.

M. Rothacher, G. Beutler, A. Donnellan, J. Hinderer, C. Ma, C. Noll, J. Oberst, M. Pearlman, H.-P. Plag, B. Richter, T. Schöne, G. Tavernier, and P.L. Woodworth. *The future Global Geodetic Observing System*, Chapter 9. Springer, 2009.

D. Salstein. *Mean properties of the atmosphere*, pages 19–49. Van Nostrand Reinhold, New York, NY, USA, 1995.

S. Schaer. *Mapping and predicting the Earth's ionosphere using the Global Positioning System*. PhD thesis, Bern University, Switzerland, 1999.

M. Schindelegger, S. Böhm, J. Böhm, and H. Schuh. Atmospheric effects on Earth rotation. In J. Böhm and H. Schuh, editors, *Atmospheric effects in space geodesy*. Springer-Verlag, 2013. this book.

H. Schuh and J. Böhm. Very long baseline interferometry for geodesy and astrometry. In G. Xu, editor, *Science of Geodesy II*, pages 185–227. Springer, 2012.

H. Schuh, R. Dill, H. Greiner-Mai, H.-J. Kutterer, J. Müller, A. Nothnagel, B. Richter, M. Rothacher, U. Schreiber, and M. Soffel. Erdrotation und globale dynamische Prozesse. Technical report, Verlag des Bundesamtes für Kartographie und Geodäsie, Frankfurt am Main, 2003.

P.L. Timleck and G.L. Nelms. Electron densities less than 100 electron cm^{-3} in the topside ionosphere. *Proceedings of the IEEE*, 57(6):1164–1171, 1969.

S. Todorova. *Combination of space geodetic techniques for global mapping of the ionosphere*. PhD thesis, Vienna University of Technology, Austria, 2008.

K.E. Trenberth and L. Smith. The mass of the atmosphere: A constraint on global analysis. *J. Climate, 18:864–875*, 2005.

T.M. van Dam and T.A. Herring. Detection of atmospheric pressure loading using very long baseline interferometry. *J. Geophys. Res., 99, 14505–14518*, 1994.

T.M. van Dam and J. Wahr. Displacements of the Earth's surface due to atmospheric loading. *J. Geophys. Res., 92, 1281–1286*, 1987.

H. Volland. *Atmospheric Tidal and Planetary Waves*. Kluwer Academic Publishers, Dordrecht, The Netherlands, 1988.

H. Volland. *Atmospheric Tides*. Springer-Verlag, Berlin Heidelberg, 1997.

R.C. Whitten and I.G. Poppoff. *Fundamentals of Aeronomy*. John Wiley and Sons, Inc., 1971.

D.D. Wijaya, J. Böhm, M. Karbon, and H. Schuh. Atmospheric pressure loading. In J. Böhm and H. Schuh, editors, *Atmospheric effects in space geodesy*. Springer-Verlag, 2013. this book.

Ionospheric Effects on Microwave Signals

Mahdi M. Alizadeh, Dudy D. Wijaya, Thomas Hobiger, Robert Weber and Harald Schuh

Abstract The ionosphere is a dispersive medium for space geodetic techniques operating in the microwave band. Thus, signals traveling through this medium are—to the first approximation—affected proportionally to the inverse of the square of their frequencies. This effect, on the other hand, can reveal information about the parameters of the ionosphere in terms of Total Electron Content (TEC) of the electron density. This part of the book provides an overview of ionospheric effects on microwave signals. First, the group and phase velocities are defined along with the refractive index in the ionosphere and the ionospheric delay. Then, we focus mainly on the mitigation and elimination of ionospheric delays in the analysis of space

M. Mahdi Alizadeh (✉)
Department for Geodesy and Geoinformation Science, Technical University of Berlin,
Strasse des 17. Juni, 135, 10623 Berlin, Germany
e-mail: mahdi.alizadeh@mail.tu-berlin.de

D. D. Wijaya
Geodesy Research Group, Institute of Technology Bandung,
Ganesha 10, Bandung-West Java, Indonesia
e-mail: dudy@gd.itb.ac.id

T. Hobiger
Space-Time Standards Laboratory, Applied Electromagnetic Research,
National Institute of Information and Communications Technology,
4-2-1 Nukui-Kitamachi, Koganei, 184-8795 Tokyo, Japan
e-mail: hobiger@nict.go.jp

R. Weber
Department of Geodesy and Geoinformation, Vienna University of Technology,
Gußhausstraße 27-29, 1040 Vienna, Austria
e-mail: robert.weber@tuwien.ac.at

H. Schuh
Department 1 Geodesy and Remote Sensing,
Helmholtz Centre Potsdam GFZ German Research Centre for Geosciences,
Telegrafenberg A 17, 14473 Potsdam, Germany
e-mail: schuh@gfz-potsdam.de

J. Böhm and H. Schuh (eds.), *Atmospheric Effects in Space Geodesy*,
Springer Atmospheric Sciences, DOI: 10.1007/978-3-642-36932-2_2,

geodetic observations, specifically for Global Navigation Satellite Systems (GNSS) and Very Long Baseline Interferometry (VLBI) observations. In particular, we summarize existing models as well as strategies based on observations at two or more frequencies to eliminate first and higher order delays. Finally, we review various space geodetic techniques (including satellite altimetry and radio occultation data) for estimating values and maps of TEC.

1 Group and Phase Velocity

The characteristic of an electromagnetic wave propagating in space is defined by its frequency f and wavelength λ. In a dispersive medium, the propagation velocity of an electromagnetic wave is dependent on its frequency. In such a medium the propagation velocities of a sinusoidal wave and a wave group are different. The propagation velocity of a sinusoidal wave with a uniform wavelength is called the phase velocity v_{ph}, while the propagation velocity of the wave group is referred to as group velocity v_{gr}. Within the vacuum the phase and group velocities are the same, but in the real conditions, this is not the case. Following Wells (1974) the velocity of phase is

$$v_{ph} = \lambda f. \tag{1}$$

In general, the carrier waves propagate with the phase velocity. For the group velocity we have (Hofmann-Wellenhof et al. 1993)

$$v_{gr} = -\left(\frac{df}{d\lambda}\right)\lambda^2. \tag{2}$$

According to Bauer (2003) for Global Navigation Satellite Systems (GNSS), modulated code signals propagate with the group velocity.
By forming the differential of Eq. 1 we get

$$dv_{ph} = f d\lambda + \lambda df. \tag{3}$$

This equation can be re-arranged to

$$\frac{df}{d\lambda} = \frac{1}{\lambda}\frac{dv_{ph}}{d\lambda} - \frac{f}{\lambda}. \tag{4}$$

Substituting Eq. 4 into Eq. 2 yields the relation between group and phase velocities

$$v_{gr} = v_{ph} - \lambda \frac{dv_{ph}}{d\lambda}. \tag{5}$$

In a non-dispersive media phase and group velocities are the same and are equal or lower than the speed of light $c = 299792458\,\mathrm{ms}^{-1}$ in vacuum.
As we know the wave propagation velocity in a medium depends on the refractive index n of that medium. So in principle we have

$$v = \frac{c}{n}. \tag{6}$$

Implementing this equation to the phase and group velocities, the formulae for the phase and group refractive indices n_{ph} and n_{gr} read

$$v_{ph} = \frac{c}{n_{ph}}, \tag{7}$$

$$v_{gr} = \frac{c}{n_{gr}}. \tag{8}$$

Differentiating Eq. 7 with respect to λ yields

$$\frac{dv_{ph}}{d\lambda} = -\frac{c}{n_{ph}^2}\frac{dn_{ph}}{d\lambda}. \tag{9}$$

Substituting Eqs. 9, 8, and 7 into Eq. 5 yields

$$\frac{c}{n_{gr}} = \frac{c}{n_{gr}} + \lambda\frac{c}{n_{ph}^2}\frac{dn_{ph}}{d\lambda}, \tag{10}$$

or

$$\frac{1}{n_{gr}} = \frac{1}{n_{ph}}\left(1 + \lambda\frac{1}{n_{ph}}\frac{dn_{ph}}{d\lambda}\right). \tag{11}$$

Using the approximation $(1+\varepsilon)^{-1} \doteq 1-\varepsilon$, valid for small quantities of ε, Eq. 11 is inverted to

$$n_{gr} = n_{ph}\left(1 - \lambda\frac{1}{n_{ph}}\frac{dn_{ph}}{d\lambda}\right). \tag{12}$$

Thus the group refractive index follows

$$n_{gr} = n_{ph} - \lambda\frac{dn_{ph}}{d\lambda}, \tag{13}$$

Equation 13 is the modified Rayleigh equation (Hofmann-Wellenhof et al. 1993). A slightly different form is obtained by differentiating the relation $c = \lambda f$ with respect to λ and f, that is

$$\frac{d\lambda}{\lambda} = -\frac{df}{f}, \tag{14}$$

and by substituting the results into Eq. 13, the group refractive index yields

$$n_{gr} = n_{ph} + f\frac{dn_{ph}}{df}. \tag{15}$$

2 Ionosphere Refractive Index

The ionosphere is a dispersive medium with respect to microwave signals. This means that the propagation of microwave signals through the ionosphere depends on the frequency of the signals. In order to quantify these effects, the refractive index of the ionosphere must be specified. For a general derivation of the refractive index n in the ionosphere, we refer to Budden (1985). If the collision effects of the particles are ignored, the formula for the phase ionospheric refractive index can be presented as

$$n_{ph}^2 = 1 - \frac{X}{1 - \frac{\frac{1}{2}Y^2 \sin^2\theta}{1-X} \pm \frac{1}{1-X}\left(\frac{1}{4}Y^4 \sin^4\theta + Y^2\cos^2\theta(1-X)^2\right)^{1/2}}, \tag{16}$$

where

$$X = \frac{\omega_0^2}{\omega^2}, \qquad Y = \frac{\omega_H}{\omega},$$

$$\omega_0 = 2\pi f_0 = \sqrt{\frac{N_e e^2}{\varepsilon_0 m_e}}, \qquad \omega_H = 2\pi f_H = \frac{B_0|e|}{m_e},$$

n	complex refractive index	N_e	electron density
ω	$= 2\pi f$ (radial frequency)	f	wave frequency
ω_0	electron plasma frequency	ω_H	electron gyro frequency
ε_0	permittivity of free space	B_0	magnitude of the magnetic field vector $\mathbf{B}_0$
θ	angle between the ambient magnetic field vector and the wave vector	e	electron charge
		m_e	electron mass

Equation 16 is called the Appleton-Hertree formula for the ionospheric refractive index of phase. To evaluate the ionospheric effects more easily, various approximations of Eq. 16 were proposed. According to Tucker and Fanin (1968) and Hartmann and Leitinger (1984) the traditional way of deriving approximate expressions of the refractive index is by assuming that the magnetic field is associated with the propagation direction, with $\sin\theta \approx 0$. Without taking any assumptions about the propagation direction, Brunner and Gu (1991) preferred to use the order of magnitude of the various terms in Eq. 16 in deriving a suitable approximate expression for the ionospheric refractive index and their result is identical to the quasi-longitudinal refractive index expression derived by Budden (1985).

$$n_{ph}^{ion} = 1 - \frac{X}{2} \pm \frac{XY}{2}\cos\theta - \frac{X^2}{8}. \tag{17}$$

Following Brunner and Gu (1991), it is convenient to define the constants C_X and C_Y as

$$C_X \equiv \frac{e^2}{4\pi^2 \varepsilon_o m_e} = 80.62, \tag{18}$$

$$C_Y \equiv \frac{\mu_o e}{2\pi m_e}, \tag{19}$$

so that Eq. 17 can be expressed in orders of $\frac{1}{f^n}$

$$n_{ph}^{ion} = 1 - \frac{C_X}{2} N_e f^{-2} \pm \frac{C_X C_Y}{2} N_e B_0 \cos\theta f^{-3} - \frac{C_X^2}{8} N_e^2 f^{-4}, \tag{20}$$

where N_e is the electron density and μ_o is the permeability in vacuum.

Equation 20 includes the first-order term and higher order terms of the ionospheric propagation effects on microwave frequencies.

First Order Refractive Index

The first two terms in Eq. 20 are denoted as the first order refractive index. Since the third- and fourth-order terms are orders of magnitude smaller than the second-order term, they are in first approximation usually neglected (Alizadeh et al. 2011). Thus, Eq. 20 can be reduced to

$$n^{ion} = 1 - \frac{C_X}{2} N_e f^{-2}. \tag{21}$$

Evaluating the constant factor in Eq. 21, we obtain:

$$C_2 = \frac{C_X}{2} = \frac{e^2}{8\pi^2 \varepsilon_0 m_e} \approx 40.31 \quad [\mathrm{m}^3/\mathrm{s}^2]. \tag{22}$$

By substituting Eq. 22 into Eq. 21 the first-order refractive index is obtained. Equation 21 is used for the phase measurements, so it is denoted as phase refractive index n_{ph}^{ion}:

$$n_{ph}^{ion} = 1 - C_2 \frac{N_e}{f^2} = 1 - 40.31 \frac{N_e}{f^2}. \tag{23}$$

In order to obtain the group refractive index, Eq. 23 is differentiated:

$$\frac{dn_{ph}}{df} = \frac{2C_2}{f^3} N_e, \tag{24}$$

substituting Eqs. 23 and 24 into Eq. 15 yields:

$$n_{gr}^{ion} = 1 - \frac{C_2}{f^2} N_e + f \frac{2C_2}{f^3} N_e df, \tag{25}$$

or

$$n_{gr}^{ion} = 1 + C_2 \frac{N_e}{f^2} = 1 + 40.31 \frac{N_e}{f^2}. \tag{26}$$

It can be seen from Eqs. 23 and 26 that the group and phase refractive indices have the same diversity from one but with an opposite signs. As $n_{gr} > n_{ph}$ it is simply concluded that $v_{gr} < v_{ph}$. As a consequence of the different velocities, when a signal travels through the ionosphere, the carrier phase is advanced and the modulated code is delayed. In the case of GNSS, code measurements which propagate with the group velocity are delayed and the phase measurements that propagate with phase velocity are advanced. Therefore, compared to the geometric distance between a satellite and a receiver, the code pseudo-ranges are measured too long and phase pseudo-ranges are measured too short. The amount of this difference is in both cases the same (Hofmann-Wellenhof et al. 1993).

High Order Refractive Index

The first order refractive index only accounts for the electron density within the ionosphere, while the effect of the Earth's magnetic field and its interactions with the ionosphere are considered in the higher order terms; i.e. the third and fourth terms of Eq. 20. For precise satellite positioning, these terms have to be considered as they will introduce an ionospheric delay error of up to a few centimeters (Brunner and Gu 1991; Bassiri and Hajj 1993).

3 Ionospheric Delay

According to Fermat's principle (Born and Wolf 1964), the measured range s is defined by

$$s = \int n ds, \tag{27}$$

where the integration is performed along the path of the signal. The geometric distance s_0 between the satellite and the receiver may be obtained analogously by setting $n = 1$:

$$s_0 = \int ds_0. \tag{28}$$

The delay (or advance) experienced by signals traveling through the ionosphere is the difference between measured and geometric range. This is called the ionosphere delay or ionospheric refraction:

$$\Delta\rho^{ion} = \int n ds - \int ds_0. \tag{29}$$

By substituting Eq. 20 into Eq. 29, the ionospheric total delay for the phase observations is expressed as

$$\Delta\rho_{ph}^{ion} = -\frac{C_X}{2f^2}\int N_e\, ds \pm \frac{C_X C_Y}{2f^3}\int N_e B_0 \cos\theta\, ds - \frac{C_X^2}{8f^4}\int N_e^2\, ds + \kappa, \quad (30)$$

where $\kappa = \int ds - \int ds_0$ represents the curvature effect. The first three-terms of Eq. 30 denote the first order and higher order ionospheric delays. Assuming that the integrations are evaluated along the geometric path s_0 for simplification, the curvature effect is neglected; thus ds turns to ds_0 and the equation results in

$$\Delta\rho_{ph}^{ion} = -\frac{C_X}{2f^2}\int N_e\, ds_0 \pm \frac{C_X C_Y}{2f^3}\int N_e B_0 \cos\theta\, ds_0 - \frac{C_X^2}{8f^4}\int N_e^2\, ds_0. \quad (31)$$

First Order Delay

In the first-order approximation, the ionospheric delay for phase measurements is derived by neglecting the second and third terms of Eq. 31 and making use of Eq. 22:

$$\Delta\rho_{ph}^{ion1} = -\frac{C_2}{f^2}\int N_e\, ds_0, \quad (32)$$

by substituting C_2 from Eq. 22 we get the phase delay

$$\Delta\rho_{ph}^{ion1} = -\frac{40.31}{f^2}\int N_e\, ds_0. \quad (33)$$

The group delay is similarly obtained using Eq. 26

$$\Delta\rho_{gr}^{ion1} = \frac{40.31}{f^2}\int N_e\, ds_0. \quad (34)$$

Second Order Delay

According to Eq. 31, the second order ionospheric phase delay is

$$\Delta\rho_{ph}^{ion2} = \frac{C_X C_Y}{2f^3}\int N_e B_0 \cos\theta\, ds_0. \quad (35)$$

Examining the constants C_X and C_Y, Eq. 35 can be written as

$$\Delta\rho_{ph}^{ion2} = -\frac{7527\ c}{2f^3}\int N_e B_0 \cos\theta\, ds_0, \quad (36)$$

where c is the speed of light. In order to solve Eq. 36, information of the magnetic field B_0 and the angle θ along the ray path have to be known. Since this is difficult to accomplish, Brunner and Gu (1991) assumed that $B_0 \cos\theta$ does not vary greatly along the ray path, so that one may take the average $\overline{B_0 \cos\theta}$ in front of the integration:

$$\Delta\rho_{ph}^{ion2} = -\frac{7527\ c}{2f^3}\ \overline{B_0 \cos\theta} \int N_e\ ds_0. \tag{37}$$

An alternative way was proposed by Bassiri and Hajj (1993) who assumed the Earth's magnetic field as a co-centric tilted magnetic dipole and approximated the ionospheric layer as a thin shell at the height of 400 km. Thus, the magnetic field vector $\mathbf{B}_0$ can be written as:

$$\mathbf{B}_0 = B_g \left(\frac{R_E}{R_E + H}\right) [\sin\theta_m \cdot \mathbf{Y}_m - 2\cos\theta_m \cdot \mathbf{Z}_m], \tag{38}$$

B_g represents the magnitude of the magnetic field near the equator at surface height ($B_g \approx 3.12 \times 10^{-5}$ T). R_E is the Earth's radius ($R_E \approx 6{,}370$ km). H denotes the height of the ionospheric thin shell above the Earth's surface ($H = 400$ km). $\mathbf{Y}_m$ and $\mathbf{Z}_m$ are the Y and Z unit vectors in the geomagnetic coordinate system, and θ_m is the angle between the ambient magnetic field vector and wave vector in the geomagnetic coordinate system (see Sect. 4.3). The scalar product of the magnitude field vector B_0 and the signal propagation unit vector $\mathbf{k}$ is:

$$\mathbf{B}_0 \cdot \mathbf{k} = B_0\ |\mathbf{k}|\ \cos\theta = B_0\ \cos\theta. \tag{39}$$

Combining Eqs. 36, 38, and 39, an expression similar to Eq. 37 can be derived

$$\Delta\rho_{ph}^{ion2} = -\frac{7527\ c}{2f^3}\ \mathbf{B}_0 \cdot \mathbf{k} \int N_e\ ds_0. \tag{40}$$

Equation 40 is sufficient to approximate the effect of the second order term to better than 90 % on the average (Fritsche et al. 2005).

Third Order Delay

According to Eq. 31 and evaluating the constant C_X, the third order ionospheric phase delay is expressed as

$$\Delta\rho_{ph}^{ion3} = -\frac{812.4}{f^4} \int N_e^2\ ds_0. \tag{41}$$

Brunner and Gu (1991) applied the shape parameter η in such a way that the integral in Eq. 41 can be approximated by

$$\int N_e^2 \, ds_0 = N_{max} \, \eta \int N_e \, ds_0. \tag{42}$$

The shape parameter η may be assumed with 0.66 as an appropriate value to account for different electron density distributions. N_{max} represents the peak electron density along the ray path. Substituting Eq. 42 into Eq. 41, the third order ionospheric phase delay can be written as:

$$\Delta\rho_{ph}^{ion3} = -\frac{812.4}{f^4} \, N_{max} \, \eta \int N_e \, ds_0. \tag{43}$$

Integrated Electron Density

As already shown, the first, second and third order ionospheric delays require the distribution of the electron density N_e along the ray path. If one is interested in signal propagation in the ionosphere, however, the integral of the electron density along the ray path becomes relevant (e.g. Schaer 1999). This quantity is defined as the Total Electron Content (TEC) and represents the total amount of free electrons in a cylinder with a cross section of 1 m^2 and a height equal to the slant signal path. TEC is measured in Total Electron Content Unit (TECU), with 1 TECU equivalent to 10^{16} electrons/m^2. For an arbitrary ray path the slant TEC (STEC) can be obtained from

$$STEC = \int N_e(s) ds, \tag{44}$$

where N_e is the electron density along the line of sight ds.

Using Eq. 44 the relation between the total electron content in TECU and ionospheric delay in meters can be obtained. Taking Eq. 33 into account for the carrier phase measurements we get

$$\Delta\rho_{ph}^{ion} = -\frac{40.31}{f^2} STEC \quad [\text{m}], \tag{45}$$

in the case of group delay measurements, the result is the same, but with opposite sign

$$\Delta\rho_{gr}^{ion} = \frac{40.31}{f^2} STEC \quad [\text{m}]. \tag{46}$$

Finally, using the constant derived from Eq. 22 the factor ϑ can be defined as the ionospheric path delay in meters per one TECU, related to a certain frequency f in Hz

$$\vartheta = \frac{40.31 \cdot 10^{16}}{f^2} \qquad [\text{m/TECU}]. \tag{47}$$

Table 1 Relation between various GPS first-order measured parameters and TEC of Earth's ionosphere extracted from Klobuchar (1996)

$L_2 - L_1$, differential group delay caused by the ionosphere	
1 ns of differential code delay	2.852×10^{16} el/m^2
	1.546 ns of delay at L_1
	0.464 m of range error at L_1
1 ns of delay, measured at L_1	1.8476×10^{16} el/m^2
	0.300 m of range error at L_1
1 m of range error	Measured at $L_1 = 6.15 \times 10^{16}$ el/m^2
	Measured at $L_2 = 3.73 \times 10^{16}$ el/m^2
1 TEC units [1×10^{16} el/m^2]	0.351 ns of differential delay
	0.524 ns of delay at L_1
	0.163 m of range delay at L_1
	0.853 cycles of phase advance at L_1

Table 1 shows some relations between the various GPS parameters and the TEC extracted from Klobuchar (1996).

Single Layer Model and Mapping Function

For absolute TEC mapping using ground-based GNSS data, TEC along the vertical should be taken into account. Since GPS basically provides measurements of STEC, an elevation dependent mapping function is required which describes the ratio between the STEC and the vertical TEC (VTEC):

$$F(z) = \frac{STEC}{VTEC}. \tag{48}$$

To get an approximation, a single-layer model (SLM) is usually adopted for the ionosphere. In SLM it is assumed that all free electrons are concentrated in an infinitesimally thin layer above the Earth's surface (Schaer 1999). The height H of that shell is usually set between 350 and 500 km, which is slightly above the height where the highest electron density is expected (approximately above the height of the F2 layer peak). Figure 1 depicts the basic geometry of the SLM in the sun-fixed coordinate system. The signal transmitted from the satellite to the receiver crosses the ionospheric shell in the so-called ionospheric pierce point (IPP). The zenith angle at the IPP is z' and the signal arrives at the ground station with zenith angle z. From Fig. 1 the relation between z' and z could be derived:

$$\sin z' = \frac{R}{R+H} \sin z. \tag{49}$$

In Eq. 49 $R \approx 6,370$ km is the mean Earth radius and H is the height of the single layer in km.

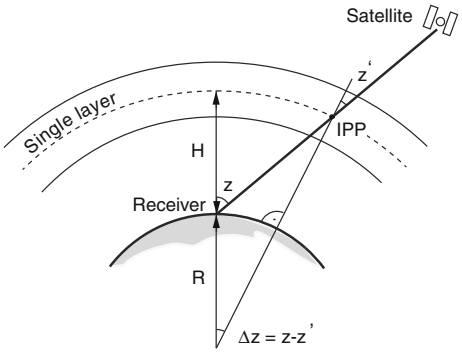

Fig. 1 Single-layer model for the ionosphere (modified from Todorova 2008)

Applying Eq. 49 and the TEC definition Eq. 44 in Eq. 48 leads to the so-called SLM mapping function

$$F(z) = \frac{1}{\cos z'} = \frac{1}{\sqrt{1 - \sin^2 z'}}, \tag{50}$$

where z' is obtained from Eq. 49.

A modified single-layer mapping function (MSLM) is adopted by Dach et al. (2007):

$$F(z) \cong \frac{1}{\sqrt{1 - \left(\frac{R}{R+H} \sin(\alpha z)\right)^2}}, \tag{51}$$

where $\alpha = 0.9782$ and $H = 506.7$ km. It should be clarified that the only difference between MSLM and SLM is the heuristic factor α. The MSLM approximates the Jet Propulsion Laboratory (JPL) extended slab model mapping function. Based on results showing that a single layer height of 550 km tends to be the best choice overall, the extended slab model provides an approximation which closely matches a single layer model with the same shell height of 550 km (Sparks et al. 2000).

4 How to Deal with Ionospheric Delay

The most important parameter of the ionosphere that affects the GNSS signals is the total number of electrons within the ionosphere. As already described in Sect. 3 the integrated number of electrons, commonly called TEC, is expressed as the number of free electrons in a column with 1 m^2 cross section, extending from the receiver to the satellite. This can be seen from Eqs. 45 and 46, where the changes in the range caused by the ionospheric refraction were directly related to the determination of TEC. There are different ways to deal with ionosphere and TEC; some methods are discussed in the following:

4.1 Modeling TEC Using Physical and Empirical Models

4.1.1 Klobuchar Model

In the mid-80s, a simple algorithm was developed for the GPS single-frequency users to correct about 50 % of the ionospheric range error. This correction method was established because the GPS satellite message had space for only eight coefficients to describe the worldwide behavior of the Earth's ionosphere. Furthermore, these coefficients could not be updated more often than once per day, and generally not even that often. Finally, simple equations had to be used to implement the algorithm to avoid causing excessive computational stress on the GPS users. The algorithm was developed by Klobuchar (1986) and led to the model that approximated the entire ionospheric vertical refraction by modeling the vertical time delay for the code pseudo-ranges.

The Klobuchar model does not directly compute the TEC. Instead, it models time delay due to ionospheric effects. Equation 52 shows time delay in nanoseconds. Multiplying this expression by the speed of light will result the vertical ionospheric range delay. The obtained range delay, after applying the SLM function, can be used to correct the ionospheric error in the measurements. Although the model is an approximation, it is nevertheless of importance because it uses the ionospheric coefficients broadcast within the fourth sub frame of the navigation message (Hofmann-Wellenhof et al. 1993). The time delay derived from the Klobuchar model follows from

$$\Delta T_v^{ion} = A_1 + A_2 \cos\left(\frac{2\pi(t - A_3)}{A_4}\right), \tag{52}$$

with

$$\begin{aligned} A_1 &= 5 \cdot 10^{-9}\,\mathrm{s} = 5\,\mathrm{ns}, \\ A_2 &= \alpha_1 + \alpha_2\,\varphi_{IP}^m + \alpha_3\,\varphi_{IP}^{m\,2} + \alpha_4\,\varphi_{IP}^{m\,3}, \\ A_3 &= 14^h\ local\ time, \\ A_4 &= \beta_1 + \beta_2\,\varphi_{IP}^m + \beta_3\,\varphi_{IP}^{m\,2} + \beta_4\,\varphi_{IP}^{m\,3}. \end{aligned}$$

The values A_1 and A_3 are constant values, the coefficients α_i, β_i, i = 1, ..., 4 are uploaded daily from the control segment to the satellites and broadcast to the users through the broadcast ephemeris. t is the local time of the *Ionospheric Pierce Point* (*IPP*), and is derived from:

$$t = \frac{\lambda_{IP}}{15} + t_{UT}, \tag{53}$$

where λ_{IP} is the longitude of *IPP* in degrees (positive to East) and t_{UT} is the observation epoch in Universal Time. Finally φ_{IP}^m in Eq. 52 is the geomagnetic latitude of IPP and is calculated by Lilov 1972:

$$\cos\varphi_{IP}^{m} = \sin\varphi_{IP}\sin\varphi_{P} + \cos\varphi_{IP}\cos\varphi_{P}\cos(\lambda_{IP} - \lambda_{P}). \tag{54}$$

At present (as of 2012) the coordinates of geomagnetic pole are:

$$\varphi_{P} = 80.0°\text{N}, \qquad \lambda_{P} = 72.2°\text{W}. \tag{55}$$

For more details refer to Sect. 4.3 (Bohm et al. 2013).

4.1.2 NeQuick Model

The NeQuick ionospheric model developed by the Aeronomy and Radiopropogation Laboratory (ARPL) of the Abdus Salam International Centre for the Theoretical Physics in Trieste (Italy) and the Institute for Geophysics, Astrophysics and Meteorology of the University of Graz (Austria) allows calculation of TEC and electron density profile for any arbitrary path (Nava 2006). The NeQuick model is based on the so-called DGR model introduced by Di Giovanni and Radicella (1990). The original DGR model uses a sum of Epstein layers to analytically construct the electron density distribution within the ionosphere. The general expression for the electron density in an Epstein layer following (Radicella and Nava 2010) is:

$$N_{Epstein}(h, hm, Nm, B) = \frac{4Nm}{\left(1 + \exp\left(\frac{h-hm}{B}\right)\right)^{2}} \exp\left(\frac{h - hm}{B}\right), \tag{56}$$

where h is the height, hm is the layer peak height, Nm is the electron density and B is the layer's thickness parameter.

Based on the anchor points related to the ionospheric characteristics which are routinely scaled from ionogram data, the analytical functions are constructed.The basic equations that describe the latest NeQuick model (NeQuick 2) are given by Nava et al. (2008):

$$N_{bot}(h) = N_{E}(h) + N_{F1}(h) + N_{F2}(h), \tag{57}$$

where:

$$\begin{aligned}
N_{E}(h) &= \frac{4Nm * E}{\left(1 + \exp\left(\frac{h-hmE}{B_E}\xi(h)\right)\right)^{2}} \exp\left(\frac{h - hmE}{B_E}\xi(h)\right), \\
N_{F1}(h) &= \frac{4Nm * F1}{\left(1 + \exp\left(\frac{h-hmF1}{B_1}\xi(h)\right)\right)^{2}} \exp\left(\frac{h - hmF1}{B_1}\xi(h)\right), \\
N_{F2}(h) &= \frac{4NmF2}{\left(1 + \exp\left(\frac{h-hmF2}{B_2}\right)\right)^{2}} \exp\left(\frac{h - hmF2}{B_2}\right).
\end{aligned} \tag{58}$$

With

$$\begin{aligned} Nm * E &= NmE - N_{F1}(hmE) - N_{F2}(hmE), \\ Nm * F1 &= NmF1 - N_E(hmF1) - N_{F2}(hmF1), \end{aligned} \tag{59}$$

and

$$\xi(h) = \exp\left(\frac{10}{1 + 1|h - hmF2|}\right). \tag{60}$$

$\xi(h)$ is a function assuring a fadeout of the E and F1 layers in the proximity of the F2 layer peak in order to avoid the second maxima around $hmF2$. The Nm values are obtained from the critical frequencies obtained from the ionograms. The peak height of the F2 layer $hmF2$ is computed from $M(3000)F2$ and the ratio $foF2/foE$. The F1 peak height $hmF1$ is modeled in terms of $NmF1$.The geomagnetic dip of the location and the E peak height hmE is fixed at 120 km. The thickness parameter $B2$ of the F2 layer is calculated using the empirical determination of the base point of the F2 layer defined by Mosert de Gonzalez and Radicella (1990) and the thickness parameters corresponding to the Fl and E regions are adjusted numerically (Radicella and Leitinger 2001).

The NeQuick model gives electron density as a function of geographic latitude and longitude, height, solar activity (specified by the sunspot number or by the 10.7 cm solar radio flux), season (month) and time (Universal or local) (Radicella 2009).
The Fortran-77 source code of the NeQuick model is available at Radiocommunication Sector website (ITU 2011). The basic inputs of the code are: position, time and solar flux (or sunspot number) and the output is the electron concentration at any given location in space and time. In addition the NeQuick package includes specific routines to evaluate the electron density along any ray-path and the corresponding TEC by numerical integration (Nava 2006). The first version of the model has been used by the European Space Agency (ESA), European Geostationary Navigation Overlay Service (EGNOS) project for assessment analysis and has been adopted for single-frequency positioning applications in the framework of the European Galileo project. It has also been adopted by the International Telecommunication Union, Radiocommunication Sector (ITU-R) as a suitable method for TEC modeling (ITU 2007).

4.1.3 IRI Model

The International Reference Ionosphere (IRI) is the result of an international cooperation sponsored by the Committee on Space Research (COSPAR) and the International Union of Radio Science (URSI). Since first initiated in 1969, IRI is an internationally recognized standard for the specification of plasma parameters in Earth's ionosphere. It describes monthly averages of electron density, electron temperature, ion temperature, ion composition, and several additional parameters in the altitude range from 60 to 1500 km. IRI has been steadily improved with newer data and better modeling

techniques leading to the release of a number of several key editions of the model. The latest version of the IRI model, IRI-2012 (Bilitza et al. 2011), will include significant improvements not only for the representations of electron density, but also for the description of electron temperature and ion composition. These improvements are the result of modeling efforts, since the last major release, IRI-2007 (Bilitza and Reinisch 2007). IRI is an empirical model based on most of the available data sources for the ionospheric plasma. The data sources of IRI include the worldwide network of ionosondes, which is monitoring the ionospheric electron densities at and below the F-peak since more than fifty years, the powerful incoherent scatter radars which measure plasma temperatures, velocities, and densities throughout the ionosphere, at eight selected locations, the topside sounder satellites which provide a global distribution of electron density from the satellite altitude down to the F-peak, in situ satellite measurements of ionospheric parameters along the satellite orbit, and finally rocket observations of the lower ionosphere. Since IRI is an empirical model it has the advantage of being independent from the advances achieved in the theoretical understanding of the processes that shape the ionospheric plasma. Nevertheless such an empirical model has a disadvantage of being strongly dependent on the underlying data base. Therefore regions and time periods not well covered by the data base will result a lower reliability of the model in that area (Bilitza et al. 2011).

The vertical electron density profile within IRI is divided into six sub-regions: the topside, the F2 bottom-side, the F1 layer, the intermediate region, the E region valley, the bottom-side E and D region. The boundaries are defined by characteristic points such as F2, F1, and E peaks. The strong geomagnetic control of the F region processes is taken into account for the analysis of the global electron density behavior (Feltens et al. 2010).

IRI has a wide range of applications. Among these applications, IRI has played an important role in geodetic techniques as well. In several studies IRI has been used as a background ionosphere in order to validate the reliability and accuracy of an approach for obtaining ionospheric parameters from geodetic measurements (e.g. Hernández-Pajares et al. 2002). Another field which IRI has helped geodetic techniques is with interpolating in areas with no or few available GPS measurements (e.g. Orús et al. 2002).

4.1.4 GAIM Model

In 1999 the Multidisciplinary University Research Initiatives (MURI) sponsored by the U.S. Department of Defense developed the Global Assimilative Ionospheric Model (GAIM). The GAIM model is a time-dependent, three-dimensional global assimilation model of the ionosphere and neutral atmosphere (JPL 2011). GAIM uses a physical model for the ionosphere/plasmasphere and for assimilating real-time measurements, it uses the Kalman filter approach. Within GAIM the ion and electron volume densities are solved numerically using the hydrodynamic equations for individual ions. The model is physical-based or first-principles based and includes state of the art optimization techniques providing the capability of assimilating differ-

ent ionospheric measurements. GAIM reconstructs 3-dimensional electron density distribution from the height of 90 km up to the geosynchronous altitude (35,000 km) in a continuous basis (Scherliess et al. 2004).

The optimization techniques which is incorporated into GAIM include the Kalman Filter and four dimensional variational (4DVAR) approaches. Currently different data types are being examined with GAIM, these data types include line of sight TEC measurements made from ground-based GPS receiver networks and space-borne GPS receivers, ionosondes, and satellite UV limb scans. To validate the model, different independent data sources were used. These sources are namely VTEC measurements from satellite ocean altimeter radar (such as those onboard TOPEX and Jason-1), ionosonde and incoherent scatter radars (JPL 2011). An updated version of the GAIM model became operational at the Air Force Weather Agency (AFWA) on February, 2008. The new version of GAIM assimilates ultraviolet (UV) observations from Defense Meteorological Satellite Program (DMSP) sensors, including the Special Sensor Ultraviolet Limb Imager (SSULI), which has been developed by the U.S. Naval Research Laboratory (NRL) Space Science Division (NRL 2008).

4.1.5 MIDAS Model

The Multi-Instrument Data Analysis System (MIDAS) was designed and developed at the University of Bath in 2001. The analysis algorithm makes use of GPS dual-frequency observations to produce four-dimensional images of electron concentration over large geographical regions or even over the globe (Mitchell and Cannon 2002). Different types of measurements that can be put into the MIDAS are the satellite to ground measurements, satellite to satellite observations, measurements from sea-reflecting radars, electron-concentration profiles from inverted ionograms, and in-situ measurements of ionized concentration from LEO satellites. The MIDAS algorithm reconstructs the free electron density as a piecewise constant 3D distribution, starting from collections of slant TEC data along ray paths crossing the region of interest (Mitchell and Spencer 2003). The essential ingredient of the MIDAS inversion is the use of Empirical Orthogonal Functions (Sirovich and Everson 1992), along which the solution of the inverse problem is assumed to be linearly decomposable (Materassi 2003). MIDAS produces four-dimensional electron density maps which can be used to correct the phase distortions and polarization changes by Faraday rotation in the ionosphere. MIDAS also has a ray tracer which allows accurate determination of the refracting ray paths and hence the apparent sky location of a radio source.

4.2 Eliminating TEC

TEC is a very complicated quantity. It depends on many parameters such as sunspot activity, seasonal and diurnal variations, the line of signal propagation, and the posi-

tion of the observation site. Therefore it's usually hard to find an appropriate model for it. Thus the most efficient method is to eliminate its effect by using signals in different frequencies. This is the main reason why almost all space geodetic techniques transmit signals in at least two different frequencies. Forming linear combinations with different frequencies allows eliminating the effect of the ionosphere to a large extent.

4.2.1 Eliminating First Order Ionospheric Effects in GNSS Measurements

The fundamental observation equation for the GNSS code-pseudorange including the frequency dependent ionospheric refraction, reads

$$\begin{aligned} P_1 &= \rho + c(\delta t_R - \delta t^S) + \Delta\rho^{trop} + \Delta\rho^{ion}_{L_1} + c(b_R + b^S)_{L_1} + \varepsilon, \\ P_2 &= \rho + c(\delta t_R - \delta t^S) + \Delta\rho^{trop} + \Delta\rho^{ion}_{L_2} + c(b_R + b^S)_{L_2} + \varepsilon, \end{aligned} \tag{61}$$

where

ρ	geometric distance between receiver and satellite
$\delta t_R, \delta t^S$	receiver and satellite clock offsets to the GPS time
$\Delta\rho^{trop}$	delay of the signal due to the troposphere
$\Delta\rho^{ion}$	frequency-dependent delay of the signal due to the ionosphere
b_R, b^S	frequency-dependent hardware delays of the satellite and receiver (DCB) (in ns)
ε	random error

Further corrections like relativistic effects, phase-wind up, or antenna phase center corrections are omitted in Eq. 61.

The code ranges are obtained from measurements of the signals $P1$ and $P2$ modulated at the two carriers with the frequencies denoted by L_1 and L_2 and the ionospheric term $\Delta\rho^{ion}$ is equivalent to the group delay in Eq. 46.

A linear combination is now performed by

$$P_{1,2} = n_1 P_1 + n_2 P_2, \tag{62}$$

where n_1 and n_2 are factors to be determined in such a way that the ionospheric refraction cancels out. Substituting Eq. 61 into Eq. 62 leads to the postulate

$$n_1 \Delta\rho^{ion}_{L_1} + n_2 \Delta\rho^{ion}_{L_2} = 0. \tag{63}$$

Assuming n_1 and n_2 as

$$n_1 = +\frac{f^2_{L_1}}{f^2_{L_1} - f^2_{L_2}}, \qquad n_2 = -\frac{f^2_{L_2}}{f^2_{L_1} - f^2_{L_2}}. \tag{64}$$

Substituting these values for n_1 and n_2, Eq. 63 is fulfilled and the linear combination Eq. 62 becomes:

$$P_{1,2} = \frac{f_{L_1}^2}{f_{L_1}^2 - f_{L_2}^2} P_1 - \frac{f_{L_2}^2}{f_{L_1}^2 - f_{L_2}^2} P_2 = P_3. \tag{65}$$

This is the P_3 ionospheric-free linear combination for code ranges. This linear combination can be written in a more convenient expression:

$$P_3 = \frac{1}{1-\gamma} (P_1 - \gamma\ P_2), \tag{66}$$

where

$$\gamma = \frac{f_{L_2}^2}{f_{L_1}^2}. \tag{67}$$

A similar ionospheric-free linear combination for carrier phase may be derived. The carrier phase models can be written as:

$$\begin{aligned} L_1 &= \rho + c(\delta t_R - \delta t^S) + \Delta\rho^{trop} - \Delta\rho_{L_1}^{ion} + \lambda_{L_1} B_{L_1} + \varepsilon, \\ L_2 &= \rho + c(\delta t_R - \delta t^S) + \Delta\rho^{trop} - \Delta\rho_{L_2}^{ion} + \lambda_{L_2} B_{L_2} + \varepsilon, \end{aligned} \tag{68}$$

where λ_{L_1} and λ_{L_2} are the wavelengths at L_1 and L_2 band, and the term λB at each frequency denotes a constant bias expressed in cycles, which contains the integer carrier phase ambiguity N and the phase hardware biases of satellite and receiver. According to Schaer (1999) one cannot separate N from the hardware biases.

Now a linear combination is performed

$$L_{1,2} = n_1 L_1 + n_2 L_2. \tag{69}$$

With similar coefficients as in Eq. 64, the linear combination reads:

$$L_{1,2} = \frac{f_{L_1}^2}{f_{L_1}^2 - f_{L_2}^2} L_1 - \frac{f_{L_2}^2}{f_{L_1}^2 - f_{L_2}^2} L_2 = L_3. \tag{70}$$

The L_3 ionospheric-free linear combination for phase ranges can also be expressed as

$$L_3 = \frac{1}{1-\gamma} (L_1 - \gamma\ L_2). \tag{71}$$

4.2.2 Eliminating Higher-Order Ionospheric Effects in GNSS Measurements

The elimination of the ionospheric refraction is the huge advantage of the two ionospheric-free linear combinations Eqs. 66 and 71. Although the term "ionospheric-free" is not completely correct as in this combination the higher-order terms as well as the curvature effects which are less than 0.1 % of the total value in L-band, are neglected.

Based on the geometrical optic approximation Brunner and Gu (1991) proposed an improved model for the ionospheric-free linear combination that considers the significant higher-order terms, the curvature effect of the ray paths, and the effect of the magnetic field. The improved model is written as:

$$L_3 = \frac{1}{1-\Gamma}\,(L_1 - \Gamma\, L_2) - [\kappa_1 - \kappa_2], \tag{72}$$

where κ_1 is the geometric bending effect,

$$\Gamma = \frac{\Gamma_1}{\Gamma_2}, \tag{73}$$

$$\kappa_2 = \frac{\Gamma}{1-\Gamma}\,\nu, \tag{74}$$

with the electron collision frequency ν and

$$\Gamma_1 = \frac{C_X}{2f_{L_1}^2}\left(1 \pm \frac{C_Y}{f_{L_1}^2}\,\overline{N_e B_0 \cos\theta} - \frac{C_X}{4f_{L_1}^2} N_{max}\eta\right), \tag{75}$$

$$\Gamma_2 = \frac{C_X}{2f_{L_2}^2}\left(1 \pm \frac{C_Y}{f_{L_2}^2}\,\overline{N_e B_0 \cos\theta} - \frac{C_X}{4f_{L_2}^2} N_{max}\eta\right). \tag{76}$$

A comparison of Eq. 71 with Eq. 72 shows that the improved model replaces γ by the more complete Γ and includes two curvature correction terms κ_1 and κ_2.

4.2.3 Using Multi-Frequency Observations

For this topic we refer to the IERS Conventions 2010 (Petit and Luzum 2010) and references therein.

4.2.4 Very Long Baseline Interferometry and the Ionosphere

Like other space geodetic techniques that operate in the microwave frequency band, Very Long Baseline Interferometry (VLBI) is affected by dispersive delays caused by the ionosphere. Two or more radio telescopes are pointed towards a common radio

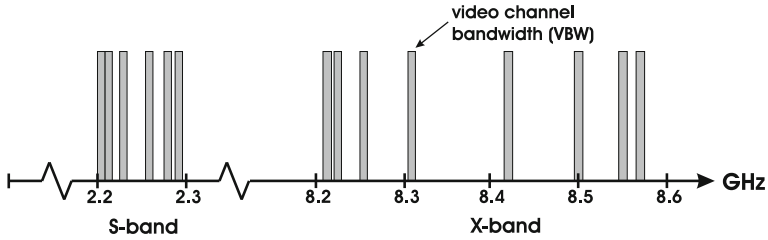

Fig. 2 Typical channel distribution of a geodetic VLBI experiment (the video channel bandwidth is not to scale) (modified from Hobiger (2005))

source which is observed for a certain amount of time in order to cross-correlate the signals. Thereby, so-called fringe phases are the main observables which can be either used for radio astronomical or geodetical purposes. Most of the geodetic experiments are using several video channels per frequency band (see Fig. 2) in order to derive a group delay measurement from the slope of the fringe phases across the covered band.

Thus, other than GNSS which operates with a single carrier, VLBI derived group delays are not assigned to a reference frequency that is actually observed. In a process, called band-width synthesis, phase and group delays are obtained within the so-called fringe fitting procedure by finding the values which maximize the delay resolution function. It can be shown (see e.g. Sekido 2001) that bandwidth synthesis, which takes advantage from Fourier operations, is equivalent to a least squares solution if the correlation amplitude ρ_i of each channel i corresponds to the weight of the phase observable. Thus, one can derive an analytical expression for the so-called effective frequency to which ionosphere group delays can be assigned to. As discussed e.g. in Hobiger (2005) one can express this frequency as

$$f_{gr} = \sqrt{\frac{\sum_{i=1}^{N}\rho_i \cdot \sum_{i=1}^{N}\rho_i (f_i - f_0)^2 - \left(\sum_{i=1}^{N}\rho_i (f_i - f_0)\right)^2}{\sum_{i=1}^{N}\rho_i (f_i - f_0) \cdot \sum_{i=1}^{N}\frac{\rho_i}{f_i} - \sum_{i=1}^{N}\rho_i \cdot \sum_{i=1}^{N}\rho_i \frac{f_i - f_0}{f_i}}}, \tag{77}$$

where f_0 is a reference sky frequency and f_i is the reference frequency of each channel from which fringe phases are obtained. Equation 77 provide the theoretical basis for the treatment of multi-band delays and their ionospheric contributions in the same way as it would be done for single frequency observations. Instead of the observing frequency the effective ionosphere frequency, computed from the frequency distribution has to be taken to express the ionospheric contribution (measured in TECU) to units of time. The equation reads:

$$\tau_{gr} = \tau_{if} + \frac{\alpha}{f_{gr}^2}, \tag{78}$$

where τ_{gr} and τ_{if} are the observed and ionosphere free group delays. The constituent α is given by

$$\alpha = \frac{40.31}{c}\left(\int N_e ds_1 - \int N_e ds_2\right) = \frac{40.31}{c}\left(STEC_1 - STEC_2\right) . \tag{79}$$

The speed of light c is used for conversion to time delay, s_1 and s_2 are the paths of wave propagation from the source to the first and second station of the radio interferometer. This means that VLBI is only sensitive to differences in the ionospheric conditions. By neglecting higher order ionospheric terms as supported by Hawarey et al. (2005) the linearity of Eq. 78 makes it possible to eliminate ionospheric influences when measurements are carried out at two separated frequency bands.

Ionosphere Free Linear Combination

Nowadays any geodetic VLBI experiment is carried out at two distinct frequency bands in order to correct for ionospheric influences. Taking the standard bands (X- and S-band) for such experiments gives two group delay observable, each of them containing the ionospheric free delay τ_{if} (which will be the input for any precise geodetic analysis) and a contribution α from the ionosphere, scaled by the corresponding effective ionosphere frequencies.

$$\begin{aligned} \tau_{gx} &= \tau_{if} + \frac{\alpha}{f_{gx}^2}, \\ \tau_{gs} &= \tau_{if} + \frac{\alpha}{f_{gs}^2}. \end{aligned} \tag{80}$$

Here the first letter in the indices stands for group or phase delay and the second letter represents X- or S-band. Using these equations the unknown parameter α can be eliminated and the ionospheric free delay observable can be obtained. This is carried out by a simple linear combination between two of the expressions, given in Eq. 80. Considering group delay measurements

$$\tau_{if} = \frac{f_{gx}^2}{f_{gx}^2 - f_{gs}^2}\tau_{gx} - \frac{f_{gs}^2}{f_{gx}^2 - f_{gs}^2}\tau_{gs} . \tag{81}$$

The right part of Eq. 81 can be considered as the observable, from which all geodetic target parameter can be determined. Instead of computing the ionosphere-free linear combination Eq. 81, one can also compute the ionospheric contribution in X-band

$$\tau_{igx} = \frac{\alpha}{f_{gx}^2} = -\frac{f_{gs}^2}{f_{gx}^2 - f_{gs}^2}(\tau_{gx} - \tau_{gs}), \tag{82}$$

add it to the theoretical delay and thus "correct" or "calibrate" the group delay at X-band. This approach should not be applied as the observable would be corrected using the measurement itself. For geodetic analysis the ionosphere-free linear combination should be used, although the ionospheric correction Eq. 82 is usually stored in databases together with all the other information.

Ambiguity Resolution and Ionosphere Delays

Due to the finite number and spacing of the video channels, the delay resolution function is repeating after a certain time lag, which introduces an ambiguity term in the obtained delays. Thereby the ambiguity spacing is equal to the inverse of the greatest common measure of the frequency spacing of the video channels. For most geodetic experiments this spacing is between 50 and 200 ns depending on the selection of the video channels in each band. Although the ambiguity correction is an integer multiple of the basic spacing, it is degraded to a real number when the ionosphere linear combination (Eq. 81) is applied. Moreover, as ambiguity shifts can happen independently in either of the bands, the ionosphere free combination cannot be applied for geodetic estimation purposes until all ambiguity terms have been fixed. This is usually done in an iterative procedure, where the initial ionosphere free linear combination is used in a basic geodetic adjustment for which only clock and troposphere are parameterized. Based on the residuals of this estimation, ambiguity shifts are detected and a new ionosphere free linear combination is formed. Depending on the data quality and the geometry of the VLBI session more than two iterations are necessary to fix all ambiguities. Thereby, delays can be shifted to an arbitrary ambiguity reference, since this constant term will later be absorbed in the station clock offset. Nevertheless, closure conditions need to be taken into account during the ambiguity fixing process, in order not to introduce artificial clock breaks.

Instrumental Biases

In fact, real observations do not exactly correspond to Eq. 80, but rather contain an extra delay term caused by instrumental imperfectness. As mentioned by Ray and Corey (1991) an additional delay is caused by instrumental delays in the different bands, which change the delay observable to

$$\begin{aligned}
\tau'_{gx} &= \tau_{if} + \frac{\alpha}{f_{gx}^2} + \tau_{inst,x}, \\
\tau'_{gs} &= \tau_{if} + \frac{\alpha}{f_{gs}^2} + \tau_{inst,s}, \\
\tau'_{px} &= \tau_{if} - \frac{\alpha}{f_{px}^2} + \tau_{inst,x}, \\
\tau'_{ps} &= \tau_{if} - \frac{\alpha}{f_{ps}^2} + \tau_{inst,s}.
\end{aligned} \tag{83}$$

When the ionospheric-free linear combination Eq. 81 is evaluated, a biased delay τ'_{if} is obtained

$$\begin{aligned}\tau'_{if} &= \frac{f_{gx}^2}{f_{gx}^2 - f_{gs}^2}\tau'_{gx} - \frac{f_{gs}^2}{f_{gx}^2 - f_{gs}^2}\tau'_{gs} \\ &= \tau_{if} + \underbrace{\frac{f_{gx}^2}{f_{gx}^2 - f_{gs}^2}\tau_{inst,x} - \frac{f_{gs}^2}{f_{gx}^2 - f_{gs}^2}\tau_{inst,s}}_{\hat{\tau}},\end{aligned} \tag{84}$$

where the notation $\hat{\tau}$ is used to express overall instrumental delay, caused by a weighted difference between X- and S-band receiving system delays. Although one might think that this would cause a problem in further processing steps, geodetic analysis is not affected by these instrumental delays. As long as instrumental delays do not change between the scans, there will be no impact on geodetic results. They can be treated as a constant bias of the delay measurements, independent of azimuth and zenith distance and are absorbed into the clock models (Ray and Corey 1991). Also the computed ionospheric correction for X-band group delay measurements Eq. 82 has to be replaced now by the intrinsic one ($\tau'_{ig,x}$), including the receiving system biases

$$\begin{aligned}\tau'_{igx} &= -\frac{f_{gs}^2}{f_{gx}^2 - f_{gs}^2}(\tau'_{gx} - \tau'_{gs}) \\ &= \frac{\alpha}{f_{gx}^2} + \underbrace{\frac{f_{gs}^2}{f_{gx}^2 - f_{gs}^2}(\tau_{inst,s} - \tau_{inst,x})}_{\tau_{inst}}.\end{aligned} \tag{85}$$

The scaled difference between S- and X-band instrumental delay, denoted by τ_{inst}, is always contained in the X-band ionospheric correction.

VLBI2010

Since 2003 the International VLBI service for Geodesy and Astronomy (IVS) has been developing the next generation VLBI system called VLBI2010 .The VLBI2010 system concept differs from the current geodetic VLBI mode in a variety of ways which also affects the calculations of the ionosphere contribution. With the current data, the geodetic analyst is expected to remove the ionospheric dispersive delay by forming linear combinations and iteratively solving the ambiguity. VLBI2010 will lead to a paradigm change where the dispersive delays are removed during band-width synthesis respectively fringe fitting, taking advantage of the broad-band observables which should permit access to phase delay observables.

4.3 Estimating TEC Using Different Space Geodetic Techniques

Since most of the space geodetic techniques operate in at least two different frequencies, they are capable of eliminating the influence of the ionosphere on the propagation of their signals. This on the other hand provides the ability to gain information about the ionosphere parameters. If the behavior of the ionosphere is known, the ionospheric refraction can be computed and used for development of regional or global models of the ionosphere. Different observation principles result in specific features of the ionosphere parameters derived by each of the techniques. Some of these techniques are:

4.3.1 Determining TEC from GNSS Observations

GNSS including the U.S.A. Global Positioning System (GPS), the Russian Globalnaya Navigatsionnaya Sputnikovaya Sistema (GLONASS), the upcoming European Galileo and the Chinese Beidou system allow for the determination of the station specific ionosphere parameters in terms of STEC values, using carrier phase or code measurements. To extract information about the ionosphere from the GNSS observations, a linear combination is formed, which eliminates the geometric term. This linear combination is called geometry-free linear combination L_4 or the ionospheric observable.

Ionospheric Observable

To form the ionospheric observable, simultaneous observations at two carriers L_1 and L_2 are subtracted. In this way along with the geometric term, all frequency-independent effects such as clock offsets and tropospheric delay are eliminated. This leads to an observable, which contains only the ionospheric refraction and the differential inter-frequency hardware delays. The geometry-free linear combination has the form:

$$L_4 = n_1 L_1 + n_2 L_2 = L_1 - L_2, \tag{86}$$

with $n_1 = 1$ and $n_2 = -1$.

Applying the above combination to the observation equations Eqs. 61 and 68 leads to the geometry-free LC for the code and phase measurements, respectively:

$$P_4 = +\xi_4 I + c\left(\Delta b^S - \Delta b_R\right), \tag{87}$$

$$L_4 = -\xi_4 I + B_4, \tag{88}$$

where:

$\xi_4 = 1 - f_{L1}^2/f_{L2}^2 \approx -0.647$ factor (GPS) for relating the ionospheric refraction on L_4 to L_1,
$B_4 = \lambda_{L_1} B(f_{L_1}) - \lambda_{L_2} B(f_{L_2})$ ambiguity parameter with undefined wavelength, thus defined in length units,
$\Delta b^S = b^{S,1} - b^{S,2}$ differential inter-frequency hardware delay of the satellite S in time units,
$\Delta b_R = b_{R,1} - b_{R,2}$ differential inter-frequency hardware delay of the receiver R in time units.

The ionospheric refraction I in Eqs. 87 and 88 can be related to the VTEC as a function of the geomagnetic latitude and the sun-fixed longitude in the following way:

$$I = \xi_E STEC(\beta, s) = \xi_E F(z) VTEC(\beta, s), \tag{89}$$

with:

$F(z)$ mapping function evaluated at zenith distance z,
β geomagnetic latitude,
s sun-fixed longitude,
$\xi_E = \frac{C_x}{2} f_1^{-2} \approx 0.162$ m/TECU (GPS).

By substituting Eq. 89 in Eqs. 87 and 88 the ionospheric observable for code and phase measurements reads

$$P_4 \approx +\xi_4 \xi_E F(z) VTEC(\beta, s) + c\left(\Delta b^S - \Delta b_R\right), \tag{90}$$

and

$$L_4 \approx -\xi_4 \xi_E F(z) VTEC(\beta, s) + B_4. \tag{91}$$

In Eqs. 90 and 91, the equation sign '=' has been replaced by the approximate equation sign '≈' because of including the simplified single layer assumption. Depending on the study and whether we want to estimate VTEC on a local, regional or global basis, $VTEC(\beta, s)$ is represented with an appropriate base-function. As an example Taylor series expansion can be used for local representation of TEC; B-splines are very suitable for studying TEC in regional applications, and for global representation of TEC, spherical harmonics expansion is most commonly used. Here we briefly discuss the spherical harmonics expansion approach:

Global TEC Representation Using Spherical Harmonics Expansion

In order to develop a global ionosphere model, the vertical TEC has to be represented as a function of longitude, latitude and time, or according to the definition of the adopted coordinate system given in Sect. 4.3—as a function of the geomagnetic latitude β and sun-fixed longitude s (Schaer 1999):

$$VTEC(\beta, s) = \sum_{n=0}^{n_{max}} \sum_{m=0}^{n} \widetilde{P}_{nm}(\sin\beta)\left(a_{nm}\cos(ms) + b_{nm}\sin(ms)\right), \tag{92}$$

where:

$VTEC(\beta, s)$ vertical TEC in TECU,
$\widetilde{P}_{nm} = N_{nm} P_{nm}$ normalized Legendre function from degree n and order m,
N_{nm} normalizing function,
P_{nm} classical Legendre function,
a_{nm} and b_{nm} unknown coefficients of the spherical harmonics expansion,

with the normalizing function written as:

$$N_{nm} = \sqrt{\frac{(n-m)!(2n+1)(2-\delta_{0m})}{(n+m)!}}, \tag{93}$$

where δ_{0m} denotes the Kronecker delta. The number of unknown coefficients of spherical harmonics expansion Eq. 92 is given by:

$$u = (n_{max} + 1)^2, \tag{94}$$

and the spatial resolution of a truncated spherical harmonics expansion is given by:

$$\Delta\beta = \frac{2\pi}{n_{max}}, \qquad \Delta s = \frac{2\pi}{m_{max}}, \tag{95}$$

where

$\Delta\beta$ is the resolution in latitude, and
Δs is the resolution in sun-fixed longitude and local time, respectively.

It is shown that the mean VTEC ($\overline{VTEC}$) of the global TEC distribution expressed by Eq. 92 is generally represented by the zero-degree spherical harmonics coefficient $\widetilde{C}_{00}$ (Schaer 1999):

$$\overline{VTEC} = \frac{1}{4\pi}\int_0^{2\pi}\int_{-\frac{\pi}{2}}^{+\frac{\pi}{2}} E_v(\beta, s)\cos\beta d\beta ds = N_{00}\widetilde{C}_{00} = \widetilde{C}_{00}. \tag{96}$$

Parametrization and Estimation of VTEC

To estimate a global VTEC model, GNSS observations from a set of globally distributed GNSS stations are collected. The computation is carried out on a daily basis, using observations with sampling rate of 30 s and elevation cut-off angle 10°. For all of the observations the ionospheric observable is calculated using Eqs. 90 or 91. This observable forms the observation equation. The observation equations are then

solved for every two hour epoch and the unknowns which are the coefficients of the spherical harmonics expansion (a_{nm} and b_{nm} in Eq. 92) are estimated for every two hours (1 h or 15 min solution is also possible) by a least-square adjustment.
The estimated unknown coefficients are then entered to calculate grid-wise VTEC values over the globe using Eq. 92. This results in thirteen two-hourly global maps for one complete day. These maps are usually called Global Ionosphere Maps (GIM).

The IONospheric EXchange (IONEX) Format

The GIM are usually provided in the IONospheric EXchange (IONEX) format, described in Schaer et al. (1998). The vertical TEC is represented as a function of geocentric longitude and latitude (λ, β), and time (t) in UT in the form of a raster grid. At the time being, the spatial resolution of this grid is $\Delta\lambda = 5°$ in longitude and $\Delta\beta = 2.5°$ in latitude, and the time resolution of the maps are $\Delta t = 2h$; although the International GNSS Service (IGS) is considering going to higher time resolution of 1 h and finally 15 min.

The interpolation of VTEC for a given epoch T_i with $i = 1, 2, ..., n$, was proposed by Schaer et al. (1998), which is interpolating between consecutive rotated TEC maps. This can be formulated as follow:

$$VTEC(\beta, \lambda, t) = \frac{T_{i+1} - t}{T_{i+1} - T_i} VTEC_i(\beta, \lambda'_i) + \frac{t - T_i}{T_{i+1} - T_i} VTEC_{i+1}(\beta, \lambda'_{i+1}), \quad (97)$$

with

$$T_i \leq t < T_{i+1} \quad \text{and} \quad \lambda'_i = \lambda + (t - T_i).$$

The TEC maps are rotated by $t - T_i$ around the Z-axis in order to compensate the strong correlation between the ionosphere and the Sun's position. For the grid interpolation, a bi-variate interpolation method can be applied, which uses a simple four-point interpolation formula:

$$\begin{aligned} VTEC(\lambda_0 + p\Delta\lambda, \beta_0 + q\Delta\beta) &= (1-p)(1-q)VTEC_{0,0} \\ &+ p(1-q)VTEC_{1,0} + (1-p)qVTEC_{0,1} + pqVTEC_{1,1}, \end{aligned} \quad (98)$$

where $0 \leq p < 1$ and $0 \leq q < 1$. $\Delta\lambda$ and $\Delta\beta$ denote the grid widths in longitude and latitude. Figure 3 depicts the interpolation concept.

Ionosphere Working Group of the International GNSS Service

In 1998 a special Ionosphere Working Group (WG) of the IGS was initiated for developing ionospheric products, as described by Schaer et al. (1998) and Hernández-Pajares (2004). The main products provided on a regular basis by the IGS Ionosphere WG are the GIM, representing the VTEC over the entire Earth as a two-dimensional raster in latitude and longitude in two-hourly snapshots, as well as the corresponding

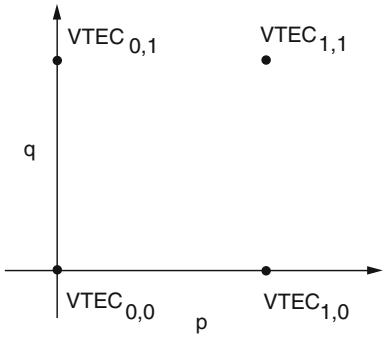

Fig. 3 Bi-variate interpolation using the nearest four TEC values (modified from Schaer et al. 1998)

RMS maps. Additionally, daily and monthly values of the satellite and receiver DCB are provided as well.

The routine generation of ionosphere VTEC maps is currently done at four IGS Associate Analysis Centers (IAAC) for ionosphere products. These IAAC are namely:

- Center for Orbit Determination in Europe (CODE), University of Berne, Switzerland,
- European Space Operations Center of ESA (ESA/ESOC), Darmstadt, Germany,
- Jet Propulsion Laboratory (JPL), Pasadena, U.S.A.,
- Technical University of Catalonia (gAGE/UPC), Barcelona, Spain.

These centers provide results computed with different approaches, which are transmitted to the IGS Ionosphere Product Coordinator, who calculates a weighted combined product. Presently the weights are defined by the IAAC global TEC maps evaluation carried out at the Geodynamics Research Laboratory of the University of the Warmia and Mazury (GRL/UWM) in Olsztyn, Poland (Krankowski et al. 2010). IGS releases a final ionosphere map in IONEX format with resolution of 5° in longitude and 2.5° in latitude with a latency of 10 days and a rapid solution with a latency of 1 day. The IGS GIM and the corresponding RMS maps are available through the IGS server in IONEX format (CDDIS-IONEX 2011).
From long term analysis, it is believed that the IGS VTEC maps have an accuracy of few TECU in areas well covered with GNSS receivers; conversely, in areas with poor coverage, the accuracy can be degraded by a factor of up to five (Feltens et al. 2010).

4.3.2 Obtaining TEC from Satellite Altimetry Measurements

Satellite altimetry is a particular way of ranging in which the vertical distance between a satellite and the surface of the Earth is measured (Seeber 1993). The range between the satellite and the Earth's surface is derived from the traveling time of the radar impulse transmitted by the radar-altimeter and reflected from the ground. Therefore the method is best applicable over the oceans, due to the good reflective properties

of the water. The signals are transmitted permanently in the high frequency domain (about 14 GHz) and the received echo from the sea surface is used for deriving the round-trip time between the satellite and the sea. The satellite-to-ocean range is obtained by multiplication of the traveling time of the electromagnetic waves with the speed of light and averaging the estimates over a second (Todorova 2008).

Satellite Altimetry Missions

The first satellite-borne altimeter missions were the US SKYLAB, consisting of three satellites launched in the period of 1973–1974, GEOS-3 launched in 1975, followed by SEASAT in 1978 and GEOSAT in 1985. As part of several international oceanographic and meteorological programmes a number of satellite altimetry missions were launched in the nineties: ERS-1 (1991–1996), Topex/Poseidon (1992) and ERS-2 (1995). The Jason-1 mission, which was the follow-on to Topex/Poseidon, was launched in 2001 at the same orbit. On the contrary to the ERS-1 and ERS-2 missions, Topex/Poseidon and Jason-1 carried two-frequency altimeters, which gave the opportunity to measure the electron density along the ray path. The latest satellite altimetry mission Jason-2, which is also known as the Ocean Surface Topography Mission (OSTM) was launched in June 2008.

The Topex/Poseidon was a joint project between NASA and the French space agency (CNES) with the objective of observing and understanding the ocean circulation (AVISO 2007). The satellite was equipped with two radar altimeters and precise orbit determination systems, including the DORIS system. The follow-on mission Jason-1 was the first satellite of a series designed to ensure continuous observation of the oceans for several decades. It had received its main features like orbit, instruments, measurement accuracy, and others from its predecessor Topex/Poseidon. The orbit altitude of the two missions was 1,336 km with an inclination of 66°, known as the repeat orbit, causing the satellite pass over the same ground position every 10 days. Jason-1 was followed by Jason-2 as a cooperative mission of CNES, European Organization for the Exploitation of Meteorological Satellites (Eumetsat), NASA, and the National Oceanic and Atmospheric Administration (NOAA). It continued monitoring global ocean circulation, discovering the relation between the oceans and the atmosphere, improving the global climate predictions, and monitoring events such as El Nino conditions and ocean eddies (ILRS 2011). Jason-2 carries nearly the same payload as Jason-1 including the next generation of Poseidon altimeter, the Poseidon-3. The Poseidon-3 altimeter is a two-frequency solid-state sensor, measuring range with accurate ionospheric corrections. Poseidon-3 has the same general characteristics of Poseidon-2, which was onboard Jason-1, but with a lower instrumental noise. The accuracy is expected to be about 1 cm on the altimeter and also on the orbit measurements (Dumont et al. 2009). For more details about the Jason-2 mission refer to CNES (2011).

Ionospheric Parameters from Dual-Frequency Measurements

Although the initial aim of the space-borne altimeters is the accurate measurement of the sea surface height, the two separate operational frequencies give the opportunity to obtain information about TEC along the ray path as well. The primary sensor of both Topex/Poseidon and Jason-1 as well as Jason-2 is the NASA Radar Altimeter, operating at 13.6 GHz (Ku-band) and 5.3 GHz (C-band), simultaneously (Fu et al. 1994). Similar to GNSS, the ionospheric effect on the altimetry measurements is proportional to the TEC along the ray path and inversely proportional to the square of the altimeter frequency. At the Ku-band, the sensitivity of the range delay to the TEC is 2.2 mm/TECU. Thus, the range at this signal can be over-estimated by 2–40 cm due to the ionosphere (Brunini et al. 2005). According to Imel (1994), the precision of the Ku-band range delay correction in one-second data averages is about 5 TECU or 1.1 cm. In fact, the precision of the satellite altimetry derived TEC is a more complex issue, since it is also affected by non-ionospheric systematic effects. A systematic error which might bias the TEC estimates due to its frequency dependence is the so-called Sea State Bias (SSB) (Chelton et al. 2001).

The ionospheric range delay dR derived from the altimeter measurements at the two frequencies is directly provided in mm, and has to be transformed into TECU. It has to be noted, that in the case of satellite altimetry derived TEC no mapping function is needed, since the measurements are carried out normal to the sea surface and thus, the ray path is assumed vertical. Consequently, the transformation formula is:

$$VTEC_{alt} = -dR \cdot 10^{-3} \frac{f_{Ku}^2}{40.31 \cdot 10^{16}} \qquad \text{[TECU]}, \tag{99}$$

with f_{Ku} being the Ku-band carrier frequency in Hz.

Theoretically, the TEC values obtained by satellite altimetry are expected to be lower than the ones coming from GNSS, since unlike GNSS the altimetry satellites do not sample the topside ionosphere due to their lower orbit altitude. However, several studies have demonstrated that Topex/Poseidon and Jason-1 systematically overestimate the VTEC by about 3–4 TECU compared to the values delivered by GNSS; e.g. Brunini et al. (2005), and Todorova (2008).

4.3.3 Estimating TEC from LEO Satellite Data

Low Earth Orbit (LEO) satellites operate at orbital altitudes between 260 and ~3500 km. Among their different scientific objectives, the global sounding of the vertical layers of the neutral atmosphere and the ionosphere is of great importance. Some of these missions carry dual-frequency GPS receivers onboard, which makes them capable of remote sensing the atmosphere using the Radio Occultation (RO) technique. The RO technique is based on detecting the change in a radio signal passing through the neutral atmosphere and the ionosphere. As a radio signal travels through the atmosphere, it bends depending on the gradient of refractivity normal to

the path. Using the RO measurements onboard a LEO satellite the vertical refractivity profile from the LEO satellite orbit height down to the Earth's surface can be computed. Since the index of refractivity depends mainly on the number of free electrons within the ionosphere, the refractivity profile can be inverted to obtain the vertical Electron Density Profile (EDP) (Jakowski et al. 2002b).

Here we will not go into details about the RO technique and the inversion procedure. For more details about the RO technique refer to e.g. Ware et al. (1996), Rocken et al. (1997), and Jakowski et al. (2004). Details about the inversion procedure could be found in e.g. Schreiner et al. (1999), Hernández-Pajares et al. (2000), and Garcia-Fernandez et al. (2005). In the following some of the LEO missions capable of ionosphere monitoring are briefly described:

The German CHAllenging Mini-Satellite Payload (CHAMP) was mainly used for geophysical research and application. The satellite was successfully launched by a Russian COSMOS rocket in July 2000. Although the mission was scheduled for five years, providing a sufficient observation time to resolve long-term temporal variations in the magnetic field, the gravity field and within the atmosphere, the mission lasted more than ten years and the satellite re-entered the Earth's atmosphere on September 2010. The advanced "Black Jack" GPS receiver developed by the JPL could measure GPS carrier phases in the limb sounding mode, starting at CHAMP orbit tangential heights down to the Earth's surface (Jakowski et al. 2002a). The RO measurements performed on board CHAMP were used to retrieve vertical temperature profiles of the global troposphere/stratosphere system (Wickert et al. 2001). The first ionospheric radio occultation (IRO) measurements were carried out in April 2001 yielding reasonable electron density profiles (Jakowski et al. 2002b).

The Gravity Recovery and Climate Experiment (GRACE) is a NASA and German Aerospace Center (DLR) science mission satellite system, established to measure primarily variations in the Earth's gravity field. The system consists of two satellites in a near-polar orbit at about 500 km altitude in the same orbital plane 220 km apart. The twin satellites were launched in March 2002 with an expected life of five years; however the satellites are still operating by the end of 2012. The dual-frequency Blackjack GPS receivers were used for precise orbit determination and atmospheric occultation on each of the satellites, providing capability of global monitoring of the vertical electron density distribution (Wickert et al. 2005).

The Formosat-3/COSMIC-Formosa Satellite Mission-Constellation Observing System for Meteorology, Ionosphere and Climate (F3C) is a joint project between Taiwan and the U.S.A. for weather, climate, space weather, and geodetic research. The F3C mission was successfully launched in April 2006. The mission consists of six micro satellites, each carrying an advanced GPS RO receiver, a Tiny Ionospheric Photometer (TIP) and a Tri Band Beacon (TBB) (Rocken et al. 2000). The satellites were gradually raised from their launched orbit to reach their final orbit altitude of 800 km. F3C mission is currently providing between 1000 and 2500 daily RO profiles in the neutral atmosphere, 1000 and 2500 daily electron density profiles and total electron content arcs, and TIP radiance products (COSMIC 2011).

4.3.4 Determining Ionospheric Parameters from VLBI Data

Although VLBI is a differential space geodetic technique it is possible to derive absolute ionosphere parameters, i.e. VTEC for each station. As shown by Hobiger et al. (2006) VTEC values can be determined similar as troposphere parameters (see section on mapping functions and gradients by Nilsson et al. (2013) in this book) by taking advantage of the fact that the slant ionosphere delays are elevation dependent and can be described by an empirical mapping function (Eq. 50). Thus VTEC values can be estimated for each station and constant instrumental delays can be separated from these parameters within the adjustment process. As one of the drawbacks, the estimation of ionosphere parameters from VLBI needs a mathematical relation between VTEC above the site and the VTEC of each observation as described in Hobiger (2005) or Hobiger et al. (2006). Moreover, as VLBI provides only a single scan per epoch and station, it is important that mapping function errors are reduced to a minimum in order to obtain unbiased VTEC estimates. Dettmering et al. (2011a) carried out a thorough investigation of systematic differences between VTEC obtained by different space-geodetic techniques including VLBI by applying the estimation strategy proposed by Hobiger et al. (2006). Thereby it is concluded that VLBI derived ionosphere parameters are comparable to other space geodetic techniques, like GPS, DORIS, Jason and F3C concerning the accuracy of the estimation. Moreover, the mean biases found in that study are similar to those given in Hobiger et al. (2006) being in the range of a few TECU.

4.3.5 Acquiring Ionospheric Information from DORIS

The Doppler Orbitography and Radio positioning Integrated by Satellite (DORIS) was developed by the French CNES, Institut Géographique National (IGN) and Groupe de Recherche en Géodésie Spatiale (GRGS) to meet scientific and operational user requirements in very precise orbit determination. Although the DORIS system was primarily designed for the precise orbit computation required for observing the oceans by altimetry missions, the unique network of ground stations and its highly accurate positioning capability have also played a great role for geodesy and geophysical applications. This includes measuring continental drift, fitting the local geodetic network, monitoring the geophysical deformations, determining the rotation and the gravity parameters of the Earth, and contributing to the realization of an international terrestrial reference system. Due to the fact that the DORIS system uses two different frequencies for its measurement, it is capable of monitoring the ionosphere as well.

The basic principle of the DORIS system is based on the accurate measurement on board the spacecraft of the Doppler shift of radio frequency signals emitted by ground beacons. Measurements are made on two frequencies: ~2 GHz and 400 MHz. About 56 ground beacon stations transmit dual frequency signals from locations distributed all over the world. The satellites carrying the DORIS receivers include Jason, TOPEX, ENVISAT, SPOT 2, SPOT 4, and SPOT 5. These satellites are at the

range of 800–1,336 km altitude. The ionospheric products deduced from the Doppler measurements are recorded at each count interval of about 10 s, and are used to derive the ionospheric TEC. The ionospheric corrections are available at the CDDIS website (CDDIS 2011). For more details on DORIS mission refer to Fleury et al. (1991) or Yin and Mitchell (2011).

4.3.6 Combination of Different Techniques

Although each of the above mentioned techniques is capable of providing information about the ionosphere, each technique has its pros and cons depending on its characteristics. The classical input data for development of GIM are obtained from dual-frequency observations carried out at GNSS stations. However, GNSS stations are in-homogeneously distributed around the world, with large gaps particularly over the oceans; this fact reduces the precision of the GIM over these areas. On the other hand, dual-frequency satellite altimetry missions such as Jason-1 (see Sect. 4.3.2) provide information about the ionosphere precisely above the oceans; and furthermore LEO satellites, such as F3C (see Sect. 4.3.3) provide well-distributed information of ionosphere on globe. Combining different techniques for developing the ionospheric maps would significantly improve the accuracy and reliability of the developed model, as the combined model uses the advantages of each particular method and provides a more accurate result than from each single techniques alone.

Several studies have investigated the development of combined models of the ionosphere. Todorova et al. (2007) developed combined models of VTEC from GNSS and satellite altimetry data. Alizadeh et al. (2011) developed models using combination of GNSS, satellite altimetry and F3C measurements. Both studies aimed at

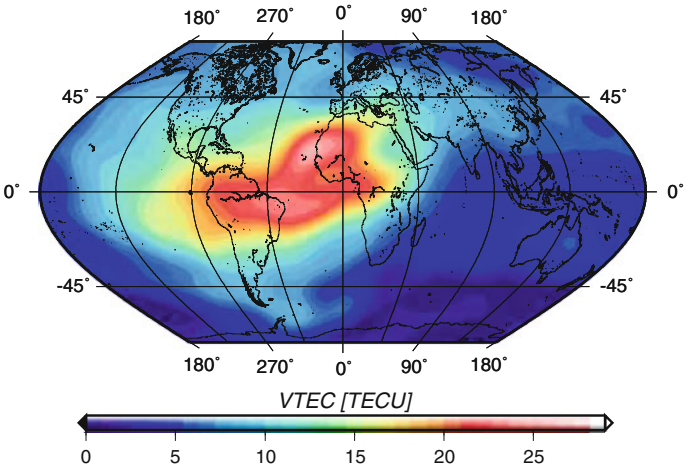

Fig. 4 GNSS, satellite altimetry, and F3C combined GIM, 17UT, day 202, 2007 (Alizadeh et al. 2011)

developing combined maps globally. Dettmering et al. (2011b) performed combination of different techniques for regional modeling of the ionosphere. All these studies prove that the combined maps provide a more homogeneous coverage and higher accuracy and reliability than results of each single method. Figure 4 depicts a snap shot of a GNSS, satellite altimetry, and F3C combined GIM at 9UT of day 202, 2007 (Alizadeh et al. 2011).

Acknowledgments The authors wish to express their heartfelt gratitude to Manuel Hernández-Pajares from the Research group of Astronomy and GEomatics (gAGE) of the Technical University of Catalonia (UPC)—Barcelona, and also to Michael Schmidt from the Deutsches Geodätisches Forschungsinstitut (DGFI)—Munich, for the revision of this part and their valuable advice for improving the script. The Austrian Science Fund (FWF Der Wissenschaftsfonds) is also deeply appreciated for funding projects VlbIonos (project P16136), COMBION (project P19564), MDION (project P22203), and GGOS Atmosphere (project P20902).

References

M.M. Alizadeh, H. Schuh, S. Todorova, and M. Schmidt. Global ionosphere maps of VTEC from gnss, satellite altimetry, and Formosat-3/COSMIC data. *J. Geod.,* 85 (12): 975–987, December 2011.

AVISO. The French active archive data center for multi-satellite altimeter missions, 2007. http://www.aviso.oceanobs.com.

S. Bassiri and G.A. Hajj. Higher-order ionospheric effects on the global positioning system observables and means of modeling them. *Manucsripta Geodaetica,* 18: 280–289, 1993.

M. Bauer. *Vermessung und Ortung mit Satelliten - GPS und andere satellitengestützte Navigationssysteme.* Wichmann, Karlsruhe, 5th Edition, 2003.

D. Bilitza, L.A. McKinnell, B. Reinisch, and T. Fuller-Rowell. The International Reference Ionosphere today and in the future. *J. Geod.,* 85: 909–920, December 2011.

D. Bilitza and B.W. Reinisch. International Reference Ionosphere 2007: Improvements and new parameters. *Adv. Space Res.,* 42: 599–609, 2007.

J. Böhm, D. Salstein, M. Alizadeh, and D. D. Wijaya. Geodetic and atmospheric background. In J. Böhm and H. Schuh, editors, *Atmospheric Effects in Space Geodesy.* Springer-Verlag, 2013.

M. Born and E. Wolf. *Principles of optics: electromagnetic theory of propagation, interference and diffraction of light.* Macmillan, New York, 2nd Edition, 1964.

C. Brunini, A. Meza, and W. Bosch. Temporal and spatial variability of the bias between TOPEX- and GPS-derived total electron content. *J. Geod.,* 79 (4–5):175–188, 2005.

F.K. Brunner and M. Gu. An improved model for the dual frequency ionospheric correction of GPS observations. *Manuscripta geodaetica,* 16(3):205–214, 1991.

K.G. Budden. *The propagation of radio waves.* Cambridge Univ. Press, 1985.

CDDIS. CDDIS ftp site. Website, 2011. ftp://cddis.gsfc.nasa.gov/.

CDDIS-IONEX. IONEX ftp site. Website, 2011. ftp://cddis.gsfc.nasa.gov/pub/gps/products/ionex.

D.B. Chelton, J.C. Ries, B.J. Haines, L.L. Fu, and P. Callahan. *Satellite altimetry and Earth sciences: A handbook of techniques and applications.* Academic Press, London, 2001.

CNES. Jason-2 altimetry mission for ocean observation, 2011. http://smsc.cnes.fr/JASON2/index.htm.

COSMIC. Cosmic program offical. Website, 2011. http://www.cosmic.ucar.edu/about.html.

R. Dach, U. Hugentobler, P. Fridez, and M. Meindl. *Bernese GPS Software,* Version 5.0. Astronomical Institute, University of Bern, 2007.

D. Dettmering, R. Heinkelmann, M. Schmidt. Systematic differences between VTEC obtained by different space-geodetic techniques during CONT08. *J. Geod.,* 85:443–451, 2011a.
D. Dettmering, M. Schmidt, R. Heinkelmann, and M. Seitz. Combination of different space-geodetic observations for regional ionosphere modeling. *J. Geod.,* 85: 989–998, 2011b.
G. Di Giovanni and S.M. Radicella. An analytical model of the electron density profile in the ionosphere. *Adv. Space Res.,* 10 (11): 27–30, 1990.
J.P. Dumont, V. Rosmorduc, N. Picot, S. Desai, H. Bonekamp, J. Figa, J. Lillibridge, and R. Scharroo. *OSTM/Jason-2 Products Handbook.* CNES and EUMETSAT and JPL and NOAA/NESDIS, 4th Edition, August 2009.
J. Feltens, M. Angling, N. Jackson-Booth, N. Jakowski, M. Hoque, C. Mayer, M. Hernández-Pajares, A. García-Rigo, R. Orús-Perez, A. Aragón-Angel, and M.J. Zornoza. GNSS contribution to next generation global ionospheric monitoring. Technical report, ESA/ESOC Final Report, January 2010.
R. Fleury, F. Foucher, and P. Lassudrie-Duchesne. Global TEC measurements capabilities of the DORIS system. *Adv. Space Res.,* 11 (10): 1051–1054, 1991.
M. Fritsche, R. Dietrich, C. Knöfel, A. Rülke, and S. Vey. Impact of higher-order ionospheric terms on GPS estimates. *Geophys. Res. Lett.*, 32, L23311, 2005
L.L. Fu, E.J. Christensen, C.A. Yamarone, M. Lefebvre, Y. Ménard, M. Dorrer, and P. Escudier. Topex/Poseidon mission overview. *J. Geophys. Res.,* 99 (C12):24369–24382, 1994.
M. Garcia-Fernandez, M. Hernández-Pajares, J.M. Juan, and J. Sanz. Performance of the improved Abel transform to estimate electron density profiles from GPS occultation data. *GPS Solut,* 9: 105–110, 2005.
G. K. Hartmann and R. Leitinger. Range errors due to ionospheric and tropospheric effects for signal frequencies above 100 MHz. *Bull. Géod.,* 58: 109–399, 1984.
M. Hawarey, T. Hobiger, and H. Schuh. Effects of the 2nd order ionospheric terms on VLBI measurements. *Geophys. Res. Lett.,* 32, L11304, 2005.
M. Hernández-Pajares. IGS Ionosphere WG Status Report: Performance of IGS Ionosphere TEC map. Technical report, IGS Workshop, Bern, Switzerland, 2004.
M. Hernández-Pajares, J.M. Juan, and J. Sanz. Improving the Abel inversion by adding ground GPS data to LEO radio occultation in ionospheric sounding. *Geophys. Res. Lett.,* 27 (16): 2473–2476, 2000.
M. Hernández-Pajares, J.M. Juan, J. Sanz, and D. Bilitza. Combining GPS measurements and IRI model values for space weather specification. *Adv. Space. Res.,* 29 (6): 949–958, 2002.
T. Hobiger. *VLBI as tool to probe the ionosphere.* PhD thesis, Inst. of Geodesy and Geophysics, Vienna Univ. of Technology, Austria, 2005.
T. Hobiger, T. Kondo, H. Schuh. Very long baseline interferometry as a tool to probe the ionosphere. *Radio Science,* 41 (1): RS1006, 2006.
B. Hofmann-Wellenhof, H. Lichtenegger, and J. Collins. *GPS Theory and Practice.* Springer, Wien New York, 2nd Edition, 1993.
ILRS. Jason2 satellite information. Website, 2011. http://ilrs.gsfc.nasa.gov/satellite_missions/list_of_satellites/jas2_general.html.
D.A. Imel. Evaluation of the TOPEX/POSEIDON dual-frequency ionosphere correction. *J. Geophys. Res.,* 99 (12): 24895–24906, 1994.
ITU. ITU-R Recommendation, 2007. http://www.itu.int/ITU-R.
ITU. Radiocommunication sector. Website, 2011. http://www.itu.int/oth/R0A04000018/en.
N. Jakowski, R. Leitinger, and M. Angling. Radio occultation techniques for probing the ionosphere. *Annals of Geophysics,* Supplement to Vol. 47: 1049–1066, 2004.
N. Jakowski, A. Wehrenpfennig, S. Heise, C. Reigber, and H. Lühr. Status of ionospheric radio occultation CHAMP data analysis and validation of higher level data products. In *1st CHAMP Science Meeting,* Potsdam - Germany, 22–25 January 2002a.
N. Jakowski, A. Wehrenpfennig, S. Heise, CH. Reigber, H. Lühr, L. Grunwaldt, and T. Meehan. GPS radio occultation measurements of the ionosphere from CHAMP early results. *Geophys. Res. Lett.,* 29 (10), 2002b.

JPL. JPL - NASA, Gaim introduction. Website, 2011. http://iono.jpl.nasa.gov/gaim/intro.html.
J. Klobuchar. Design and characteristics of the GPS ionospheric time-delay algorithm for single-frequency users. In *PLANS'86 - Position Location and Navigation Symposium,* pages 280–286, Las Vegas, Nevada, 4–7 November 1986.
J. A. Klobuchar. *Ionospheric effects on GPS, in Global Positioning System: Theory and Application,* Volume I. American Institute of Aeronautics and Astronautics, Washington DC., 1996.
A. Krankowski, M. Hernandez-Pajares, J. Feltens, A. Komjathy, S. Schaer, A. Garcia-Rigo, and P. Wielgosz. Present and future of IGS ionospheric products. Technical report, IGS Workshop, Newcastle, England, 2010.
L.K. Lilov. On stabilization of steady-state motions of mechanical systems with respect to a part of the variables. *Journal of Applied Mathematics and Mechanics,* 36(6):922–930, 1972.
M. Materassi. Ionospheric Tomography, 3d and 4d imaging and data assimilation. In *invited paper,* Matera, Italy, 13–15 October 2003. Atmospheric Remote Sensing using Satellite Navigation Systems Special Symposium of the URSI Joint Working Group FG, ASI Centro di Geodesia Spaziale 'Giuseppe Colombo'.
C.N. Mitchell and P.S. Cannon. Multi-instrumental data analysis system (MIDAS) imaging of the ionosphere. Technical report, University of Bath, United States Air Force European Office of Aerospace Research and Development, February 2002.
C.N. Mitchell and P.S.J. Spencer. A three dimensional time-dependent algorithm for ionospheric imaging using GPS. *Annal. Geophysics,* 46 (4): 687–696, 2003.
M. Mosert de Gonzalez and S.M. Radicella. On a characteristic point at the base of the F2 layer in the ionosphere. *Adv. Space Res.,* 10 (11):17–25, 1990.
B. Nava. A near real-time model-assisted ionosphere electron density retrieval method. *Radio Science,* 41(6), 2006.
B. Nava, P Coïsson, and S.M. Radicella. A new version of the Nequick ionosphere electron density model. *J. Atmos. Solar-Terr. Phys.,* 70: 1856–1862, 2008.
T. Nilsson, J. Böhm, D. D. Wijaya, A. Tresch, V. Nafisi, and H. Schuh. Path delays in the neutral atmosphere. In J. Böhm and H. Schuh, editors, *Atmospheric effects in space geodesy.* Springer-Verlag, 2013. this book.
U.S. Naval Research Laboratory Press Release NRL. Updated version of GAIM model goes operational. Website, 2008. http://www.nrl.navy.mil/pao/pressRelease.php?Y=2008&R=30-08r.
R. Orús, M. Hernández-Pajares, J.M. Juan, J. Sanz, and M. García-Fernández. Performance of different TEC models to provide GPS ionospheric corrections. *J. Atmos. Solar-Terr. Phys.,* 64 (18): 2055–2062, 2002.
G. Petit and B. Luzum, editors. IERS Conventions 2010. Technical Report 36, 2010.
S.M. Radicella. The Nequick model genesis, uses and evolution. *Annals of Geophysics,* 52 (3/4): 417–422, 2009.
S.M. Radicella and R. Leitinger. The evolution of the DGR approach to model electron density profiles. *Adv. Space Res.,* 27 (1): 35–40, 2001.
S.M. Radicella and B. Nava. Nequick model: Origin and evolution. In *Antennas Propagation and EM Theory (ISAPE),* pages 422–425. IEE Xplore, November - December 2010.
J.R. Ray and B.E. Corey. Current precision of VLBI multi-band delay observables. In *Proceedings AGU Chapman Conference on Geodetic VLBI: Monitoring Global Change,* Washington D.C., 22–26 April, 1991.
C. Rocken, R. Anthes, S. Sokolovskiy, M. Exnerand, D. Hunt, R. Ware, M. Gorbunov, W. Schreiner, D. Feng, B. Herman, Y. Kuo, and X. Zou. Analysis and validation of GPS/MET data in the neutral atmosphere. *J. Geophys. Res.,* 102: 29849–29866, 1997.
C. Rocken, Y.H. Kuo, W. Schreiner, D. Hunt, and S. Sokolovskiy. Cosmic system description. *Atmospheric and Oceanic Science,* 11 (1): 21–52, March 2000.
S. Schaer. *Mapping and predicting the Earth's ionosphere using the Global Positioning System.* PhD thesis, Bern University, Switzerland, 1999.

S. Schaer, W. Gunter, and J. Feltens. Ionex: The ionosphere map exchange format version 1. In *In J. M. Dow, J. Kouba, and T. Springer (Eds.),* pages 233–247, Darmstadt, Germany, 1998. Proceeding of the IGS AC Workshop.

L. Scherliess, R.W. Schunk, J.J. Sojka, and D.C. Thompson. Development of a physics-based reduced state Kalman filter for the ionosphere. *Radio Sci.,* 39, 2004.

W. Schreiner, S. Sokolovskiy, C. Rocken, and D. Hunt. Analysis and validation of GPS/MET radio occultation data in the ionosphere. *Radio Sci.,* 34 (4): 949–966, 1999.

G. Seeber. *Satellite Geodesy, Foundations, Methods and Application.* Walter de Gruyter, Berlin, New York, 1993.

M. Sekido. *Pulsar Astrometry by VLBI.* PhD thesis, Department of Astronomical Science, School of Mathematical and Physical Science, The Graduate University for Advanced Studies, Mitaka, Tokyo, Japan, 2001.

L. Sirovich and R. Everson. Management and analysis of large scientific datasets. *Int. J. Supercomputer Appl.,* 6: 50–68, 1992.

L. Sparks, Lijima B.A., Mannucci A.J., Pi X., and Wilson B.D. A new model for retrieving slant TEC corrections for wide area differential GPS. In *2000: Navigating into the New Millennium,* pages 464–473, Anaheim, CA; United States, 26–28 Jan. 2000. Institute of Navigation National Technical Meeting.

S. Todorova. *Combination of space geodetic techniques for global mapping of the ionosphere.* PhD thesis, Vienna University of Technology, Austria, 2008.

S. Todorova, H. Schuh, and T. Hobiger. Using the global navigation satellite systems and satellite altimetry for combined global ionosphere maps. *Adv. Space Res,* 42: 727–736, 2007.

A.J. Tucker and B.M. Fanin. Analysis of ionospheric contributions to the Doppler shift of CW signals from artificial satellites. *J. Geophys. Res.,* 73: 4325–4334, 1968.

R. Ware, D. Exner, M. Feng, K. Gorbunov, K. Hardy, B. Herman, Y. Kuo, T. Meehan, W. Melbourne, C. Roken, W. Schreiner, S. Sokolovskiy, F. Solheim, X. Zou, R. Anthes, S. Businger, and K. Trenberth. GPS sounding of the atmosphere from low earth orbit: preliminary results. *Bull. Am. Meteor. Soc,* 77: 19–40, 1996.

D.E. Wells. Doppler satellite control. Technical Report 29, UNB, Fredricton, 1974.

J. Wickert, G. Beyerle, R. Konig, S. Heise, L. Grunwaldt, G. Michalak, C. Reigber, and T. Schmidt. GPS radio occultation with CHAMP and GRACE: A first look at a new and promising satellite configuration for global atmospheric sounding. *Annales Geophysicae,* 23 (3): 653–658, 2005.

J. Wickert, Ch. Reigber, G. Beyerle, R. König, Ch. Marquardt, T. Schmidt, L. Grunwaldt, R. Galas, T. Meehan, WG. Melbourne, and K. Hocke. Atmosphere sounding by GPS radio occultation: First results from CHAMP. *Geophys. Res. Lett.,* 28: 3263–3266, 2001.

P. Yin and C. N. Mitchell. Demonstration of the use of the doppler orbitography and radio positioning integrated by satellite (DORIS) measurements to validate GPS ionospheric imaging. *Adv. Space Res.,* 48: 500–506, 2011.

Path Delays in the Neutral Atmosphere

Tobias Nilsson, Johannes Böhm, Dudy D. Wijaya, Ana Tresch, Vahab Nafisi and Harald Schuh

Abstract This part describes the effects of the troposphere—strictly speaking the neutral atmosphere—on the propagation delay of space geodetic signals. A theoretical description of this tropospheric propagation delay is given as well as strategies for correcting for it in the data analysis of the space geodetic observations. The differences between the tropospheric effects for microwave techniques, like the

T. Nilsson (✉)
Section 1.1 GPS/Galileo Earth Observations, Helmholtz Centre Potsdam GFZ German Research Centre for Geosciences,
Telegrafenberg A 17, 14473 Potsdam, Germany
e-mail: nilsson@gfz-potsdam.de

J. Böhm
Department of Geodesy and Geoinformation, Vienna University of Technology,
Gußhausstraße 27-29, 1040 Vienna, Austria
e-mail: johannes.boehm@tuwien.ac.at

D. D. Wijaya
Geodesy Research Group, Institute of Technology Bandung,
Ganesha 10, Bandung-West Java, Indonesia
e-mail: dudy@gd.itb.ac.id

A. Tresch
Monitoring Solutions, Leica Geosystems AG,
Heinrich Wild Strasse, CH-9435 Heerbrugg, Switzerland
e-mail: ana.tresch@leica-geosystems.com

V. Nafisi
Department of Surveying Engineering, Faculty of Engineering,
University of Isfahan,
Hezar Jerib street, 81746-73441 Isfahan, Iran
e-mail: nafisi@eng.ui.ac.ir

H. Schuh
Department 1 Geodesy and Remote Sensing,
Helmholtz Centre Potsdam GFZ German Research Centre for Geosciences,
Telegrafenberg A 17, 14473 Potsdam, Germany
e-mail: schuh@gfz-potsdam.de

J. Böhm and H. Schuh (eds.), *Atmospheric Effects in Space Geodesy*,
Springer Atmospheric Sciences, DOI: 10.1007/978-3-642-36932-2_3,

Global Navigation Satellite Systems (GNSS) and Very Long Baseline Interferometry (VLBI), and those for optical techniques, like Satellite Laser Ranging (SLR), are discussed. Usually, residual tropospheric delays are estimated in the data analysis, and the parameterization needed to do so is presented. Other possibilities of correcting for the tropospheric delays are their calculation by ray-tracing through the fields of numerical weather models and by utilizing water vapor radiometer measurements. Finally, we shortly discuss how space geodetic techniques can be used in atmospheric analysis in meteorology and climatology.

1 Introduction

After the signals of the space geodetic techniques have passed through the ionosphere (see Part 2 (Alizadeh et al. 2013) for more information about the ionospheric effects) they also need to pass through the neutral atmosphere (primarly the troposphere) before they are observed at the surface of the Earth. In the troposphere the signals experience propagation delays, just as they do in the ionosphere. However, the frequency dependence of the delays is small. For microwave techniques like Global Navigation Satellite Systems (GNSS) and Very Long Baseline Interferometry (VLBI) there is practically no frequency dependence; thus it is impossible to remove the tropospheric delay with a multi-frequency combination like it is in the ionospheric case. For optical techniques like Satellite Lase Ranging (SLR) there exists a small frequency dependence and thus it is possible in principle to remove the tropospheric delays using two frequencies (see Sect. 4.3.2); however due to the amplification of the noise this is currently not practical. Thus the tropospheric delays need to be corrected for by other means.

For this part of the book it is assumed that the reader is familiar with the basic properties of the atmosphere, i.e. what is described in Part 1 (Böhm et al. 2013). We begin here with the basic description of the refractivity of the air in the neutral atmosphere (Sect. 2). Expressions for calculating the refractivity from basic meteorological measurements are presented, as well as the commonly used division of the refractivity into a hydrostatic and a wet part. In Sect. 3 these results are used for calculating the tropospheric path delay, and the properties of the hydrostatic (Sect. 3.1) and wet (Sect. 3.2) delays are discussed. The modeling of the tropospheric delays in the space geodetic data analysis is described in Sect. 4. Either the tropospheric delays are estimated in the data analysis or tropospheric delays obtained by external measurements are used. Two possible sources of external tropospheric information are considered: from ray-tracing through numerical weather models (Sect. 4.1) and inferred from microwave radiometer measurements (Sect. 4.4). The models that are commonly used when estimating the tropospheric delays in the data analysis are given in Sects. 4.2 (microwaves) and 4.3 (optical). However, since the refractivity of the atmosphere is varying randomly due to atmospheric turbulence these models are not perfect. The effects of turbulence are described in Sect. 5. This part of the book concludes with a discussion of the possible use of space geodetic techniques for studies of the atmosphere (Sect. 6).

2 Basics

The propagation of electromagnetic waves are described by Maxwell's equations (Jackson 1998). For a non-conducting, neutral medium like the troposphere these equations are

$$\nabla \cdot (\varepsilon \mathbf{E}) = 0, \tag{1}$$

$$\nabla \cdot \mathbf{B} = 0, \tag{2}$$

$$\nabla \times \mathbf{E} = -\frac{\partial \mathbf{B}}{\partial t}, \tag{3}$$

$$\nabla \times \mathbf{B} = \mu\varepsilon \frac{\partial \mathbf{E}}{\partial t}. \tag{4}$$

where $\mathbf{E}$ and $\mathbf{B}$ are the electric field and magnetic field vectors, respectively, ε the electric permittivity, μ the magnetic permeability. Assuming that the spatial and temporal variations in μ and ε are small, the equations can be combined into forming a wave equation for the electric field.

$$\nabla^2 \mathbf{E} = \mu\varepsilon \frac{\partial^2 \mathbf{E}}{\partial t^2} = \frac{n^2}{c^2} \frac{\partial^2 \mathbf{E}}{\partial t^2} \tag{5}$$

where $c = 1/\sqrt{\varepsilon_0 \mu_0}$ is the speed of light in vacuum and n is called the refractive index. A similar expression for the magnetic field can also be derived.

It is clear from Eq. (5) that in order to describe the propagation of a radio wave we need to know the refractive index n. In the neutral atmosphere of the Earth n is very close to one, thus it is more convenient to use the so called refractivity instead. The refractivity N (in "N-units", mm/km, or ppm) is related to the refractive index by

$$N = (n - 1) \cdot 10^6 \,. \tag{6}$$

In general the refractivity is a complex number. It can be divided into three parts

$$N = N_0 + N'(\nu) - i\,N''(\nu). \tag{7}$$

In case the spatial and temporal variations of N are small, i.e. the variations over one wavelength or one period are negligible, the effect on the propagation of electromagnetic waves caused by the real and the imaginary parts of the refractivity can be considered separately. For the signals of space geodetic techniques traveling through the atmosphere, this separation is a reasonable assumption since the wavelengths are shorter than a few decimeters. The real part of the refractivity ($N_0 + N'(\nu)$) causes refraction and propagation delay of signals traveling through the atmosphere. It consists of a frequency-independent (non-dispersive) part N_0 and a frequency-dependent (dispersive) part $N'(\nu)$.

The imaginary part of the refractivity, $N''(\nu)$, causes absorption and is related to the absorption coefficient α

$$\alpha(\nu) = 10^{-6} \frac{4\pi\,\nu\,N''(\nu)}{c}. \tag{8}$$

The power W of a signal received after propagating along the path S through the atmosphere will be lower than it would have been (W_0) in vacuum (i.e. no absorption)

$$W = W_0\, e^{-\int_S \alpha(s',\nu)\,\mathrm{d}s'} = W_0\, e^{-\tau(\infty,\nu)}, \tag{9}$$

where $\tau(\infty, \nu)$ is called the opacity.

Since the observables of space geodetic techniques (e.g. GNSS, VLBI, and SLR) typically are measurements of the travel time of the signals, the absorption is typically not important since it does not affect the propagation delay. Of course, absorption will affect the delay measurements by increasing the noise; higher attenuation will cause the signal-to-noise-ratio to be lower, and thus the accuracy of the measured delay will be worse (in the worst case the signal cannot be detected). However, there is typically no need for modeling this effect in the space geodetic data analysis. Thus, in the following we will concentrate on the real part of the refractive index and the effects caused by it. We will come back to the absorption in Sect. 4.4, where measurements of the absorption by microwave radiometry are used to estimate the atmospheric path delay.

The (real part of) refractivity can be expressed as a function of the densities of the different atmospheric gases and the temperature T (Debye 1929)

$$N = \sum_i \left(A_i(\nu)\rho_i + B_i(\nu)\frac{\rho_i}{T} \right), \tag{10}$$

where ρ_i is the density of the ith gas, and A_i and B_i are constants. The $B_i \frac{\rho_i}{T}$ term is caused by the permanent dipole moment of the molecules. Since water vapor is the only major atmospheric gas having a permanent dipole moment, we can ignore this term for all other gases. The relative concentrations of the dry atmospheric gases are approximately constant (except carbon dioxide, see Sect. 2.1). Thus we can assume that $\rho_i = x_i\rho_d$, where x_i is constant and ρ_d is the density of dry air. This makes it possible to express the refractivity as a function of pressure, temperature, and humidity (Essen and Froome 1951)

$$\begin{aligned} N &= \sum_i A_i(\nu) x_i\, \rho_d + A_w(\nu)\rho_w + B_w(\nu)\frac{\rho_w}{T} + A_{lw}(\nu)\rho_{lw} \\ &= k_1(\nu)\frac{p_d}{T}Z_d^{-1} + k_2(\nu)\frac{p_w}{T}Z_w^{-1} + k_3(\nu)\frac{p_w}{T^2}Z_w^{-1} + k_4(\nu)\rho_{lw}, \end{aligned} \tag{11}$$

where ρ_{lw} is the density of liquid water. It is here assumed here that the liquid water droplets are small compared to the wavelength (<1 mm for microwave techniques),

for larger droplets the expression becomes more complicated (Solheim et al. 1999). However, normally the liquid water contribution to the refractivity ($k_4(\nu)\rho_{lw}$) is neglected since it is small, especially outside of clouds. The variables Z_d and Z_w are compressibility factors for dry air and water vapor, respectively. These describe the deviation of the atmospheric constituents from an ideal gas. The compressibility factor for the ith constituent of air is given by

$$Z_i = \frac{p\,M_i}{\rho_i R T}, \tag{12}$$

where M_i is the molar mass and R is the universal gas constant. For an ideal gas we have $Z = 1$. Owens (1967) obtained expressions for Z_d^{-1} and Z_w^{-1} by a least squares fitting to thermodynamic data. These expressions are (for p_d and p_w in hPa and T in K)

$$Z_d^{-1} = 1 + p_d \left[57.97 \cdot 10^{-8} \left(1 + \frac{0.52}{T} \right) - 9.4611 \cdot 10^{-4} \frac{T - 273.15}{T^2} \right], \tag{13}$$

$$Z_w^{-1} = 1 + 1650 \frac{p_w}{T^3} \left[1 - 0.01317\,(T - 273.15) + 1.75 \cdot 10^{-4} (T - 273.15)^2 + 1.44 \cdot 10^{-6} (T - 273.15)^3 \right]. \tag{14}$$

2.1 Microwaves

Figure 1 shows the total refractivity for frequencies between 0 and 100 GHz for the case when the total pressure is 1013 hPa, the temperature is 300 K, and the relative humidity is 100 % (and for three different values for the concentration of liquid water). The refractivity was calculated using the Millimeter-wave Propagation Model (MPM) (Liebe 1985, 1989; Liebe et al. 1993). As can be seen, the variations in the refractivity as function of frequency are relatively small. The biggest variations are in the range 50–70 GHz, a region where several strong absorption lines exist for oxygen. Below 40 GHz the refractivity is more or less constant. There are small variations around the 22.235 GHz water vapor absorption line, however these can typically be neglected. Since all space geodetic techniques that use microwaves operate at frequencies well below 40 GHz, we can consider the refractivity to be frequency independent for microwaves. Thus the phase ($c_p = c_0/n$) and group velocities ($c_g = c_0/(n + f\,\partial n/\partial f)$) in the troposphere will be equal.

In Fig. 1 three different cases are shown corresponding to different concentrations of liquid water: 0 g/m^3, 0.05 g/m^3 (e.g. fog), and 1 g/m^3 (e.g. inside a cloud). The impact of liquid water on the refractivity is typically neglected since it is relatively small, although in order to achieve highest accuracy in the presence of dense clouds the effect should be considered. The difference between the case with 1 g/m^3 liquid water and the case with no liquid water is about 1.44 mm/km for the frequencies below 10 GHz, and then it decreases slightly with frequency to about 1.35 mm/km

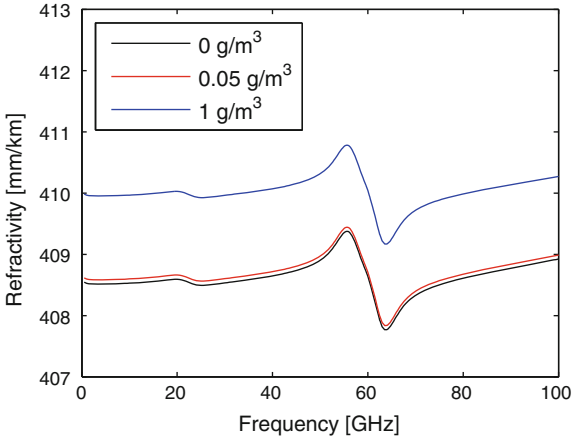

Fig. 1 The total refractivity as function of frequency. The total pressure is 1013 hPa, the temperature 300 K, and the relative humidity is 100 %. Three different cases are shown corresponding to different concentrations of liquid water: 0, 0.05, and 1 g/m^3

at 100 GHz. This agrees with the published values for k_4 in the microwave range, which is generally about 1.45 (Liebe et al. 1993; Solheim et al. 1999).

By ignoring the liquid water term and assuming that the refractivity is frequency independent, Eq. (11) becomes

$$N = k_1 \frac{p_d}{T} Z_d^{-1} + k_2 \frac{p_w}{T} Z_w^{-1} + k_3 \frac{p_w}{T^2} Z_w^{-1}. \tag{15}$$

Several different laboratory measurements have been performed in order to determine the constants k_1, k_2, and k_3 (e.g. Boudouris 1963, Bevis et al. 1994). Thayer (1974) estimated these constants by extrapolating measurements made at optical frequencies to the microwave region. The claimed accuracy was better than what is obtained from other investigations due to more accurate refractivity measurements being available for optical frequencies. However, as pointed out by e.g. Hill et al. (1982) extrapolation of optical measurements is problematic due to several resonance frequencies in the infrared region, thus the values published by Thayer (1974) should not be used. Rüeger (2002a,b) summarized and discussed many of these investigations, and calculated the "best average" values for the constants. These values are given in Table 1. The accuracy of k_1 is 0.015 % and the accuracy of the water vapor part of the refractivity is 0.15 %.

Strictly speaking the constant k_1 is dependent on the relative concentrations of the different dry atmospheric gases, thus if these change k_1 will also change. Most dry atmospheric gases have stable concentrations. Of the major gases only the concentration of carbon dioxide show a significant variation (it is increasing with 1.5–2 ppm/year). Rüeger (2002a) gives a formula for calculating k_1 for different carbon dioxide concentrations. In total the carbon dioxide makes k_1 about 0.03 % larger compared to a carbon dioxide free atmosphere. The k_1 value given by Rüeger

Table 1 The "best average" values of the k_1, k_2, and k_3 coefficients in Eq. (15), as presented by Rüeger (2002a,b)

	k_1 (K/hPa)	k_2 (K/hPa)	k_3 (K^2/hPa)
375 ppm CO_2	77.6890	71.2952	375463
392 ppm CO_2	77.6900	71.2952	375463

For k_1 two values are given corresponding to two different carbon dioxide concentrations: 375 ppm (2004 level, used by Rüeger (2002a,b) and 392 ppm (2012 level)

(2002a,b) assumed a carbon dioxide concentration of 375 ppm (2004 level). Table 1 also shows k_1 for a carbon dioxide concentration of 392 ppm (2012 level). The concentration of carbon dioxide also shows an annual variation of about 5 ppm, meaning that k_1 will have an annual variation of about $2.8 \cdot 10^{-4}$ K/hPa. This variation is negligible for all practical purposes.

Using Eq. (12) it is possible to rewrite Eq. (15) as

$$N = k_1 \frac{R}{M_d}\rho + k_2' \frac{p_w}{T} Z_w^{-1} + k_3 \frac{p_w}{T^2} Z_w^{-1} = N_h + N_w, \tag{16}$$

where $k_2' = k_2 - k_1 \frac{M_w}{M_d}$ and:

$$N_h = k_1 \frac{R}{M_d}\rho, \tag{17}$$

$$N_w = k_2' \frac{p_w}{T} Z_w^{-1} + k_3 \frac{p_w}{T^2} Z_w^{-1}. \tag{18}$$

N_h is called the hydrostatic refractivity and N_w the wet (or non-hydrostatic) refractivity. The hydrostatic refractivity depends only on the total density of air, while the wet part depends only on the partial pressure of water vapor and the temperature. Figure 2 shows examples of vertical profiles of N_h and N_w. While the hydrostatic part

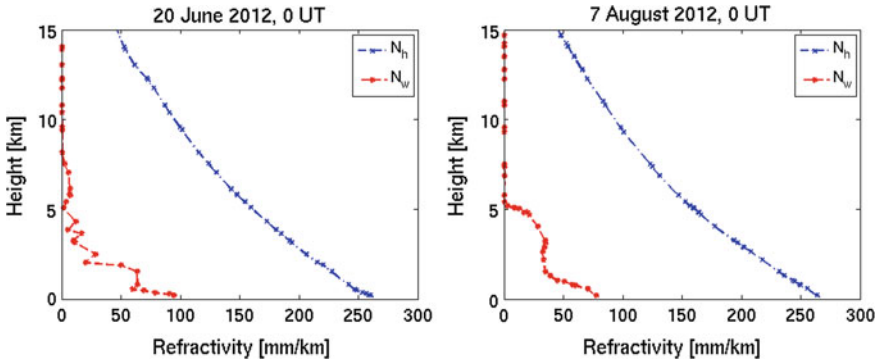

Fig. 2 Examples of vertical profiles of the hydrostatic and wet refractivity. The profiles are calulated using radiosonde data from Vienna, Austria

is larger than the wet part, the wet refractivity is much more variable and difficult to model. We will see in Sect. 3.1 that the effect of the hydrostatic refractivity on the propagation of microwaves can be accurately estimated from just the surface pressure, while the modeling of the wet part is more complicated.

It should be noted that in the literature sometimes a division of the refractivity into a dry and a wet part is used (e.g. Perler et al. 2011). The dry refractivity will be the part caused only by the first term of the righthand side of Eq. (15), while the other two terms are designated as the wet part. It is important to remember that the wet refractivity obtained in this case is not the same as the wet (i.e. non-hydrostatic) refractivity obtained when dividing the refractivity into a hydrostatic and wet part (Eq. 18). The division into dry and wet parts makes sense in that it clearly separates the contributions from the dry gases and water vapor (part of the hydrostatic refractivity is caused by water vapor). However, there are practical advantages of using the division into hydrostatic and wet parts, making it more commonly used. As shown in Sect. 3.1 the propagation delay caused by the hydrostatic refractivity can easily be inferred from surface pressure measurements.

2.2 Optical Refractivity of Moist Air

For optical frequencies, the coefficient k_3 in Eq. (11) is very small and can be ignored. However, the frequency dependence of the k_1 and k_2 coefficients needs to be considered. Normally the refractivity is expressed as a function of the density of dry air and water vapor (see Born and Wolf 1999, pp. 95–103)

$$\begin{aligned} N &= k_1(\nu)\frac{p_d}{T}Z_d^{-1} + k_2(\nu)\frac{p_w}{T}Z_w^{-1} = k_1(\nu)\frac{R}{M_d}\rho_d + k_2(\nu)\frac{R}{M_w}\rho_w \\ &= \tilde{k}_d(\nu)\rho_d + \tilde{k}_w(\nu)\rho_w. \end{aligned} \tag{19}$$

$\tilde{k}_d(\nu)$ and $\tilde{k}_w(\nu)$ are the dispersions of dry air and water vapor components, respectively. ρ_d and ρ_w are the density of dry air and water vapor, respectively.

Similarly for microwaves, N can also be divided into a hydrostatic and a non-hydrostatic (wet) part

$$N = N_h + N_w, \tag{20}$$

where

$$N_h = \tilde{k}_d(\nu)\rho_t, \tag{21}$$

$$N_w = \tilde{k}_w^{\star}(\nu)\rho_w, \tag{22}$$

$$\tilde{k}_w^{\star}(\nu) = \tilde{k}_w(\nu) - \tilde{k}_d(\nu). \tag{23}$$

In the literature, the dispersion formulae for $\tilde{k}_d(\nu)$ and $\tilde{k}_w(\nu)$ proposed by various investigators such as Edlén (1966), Barrell and Sears (Jeske 1988, p. 217),

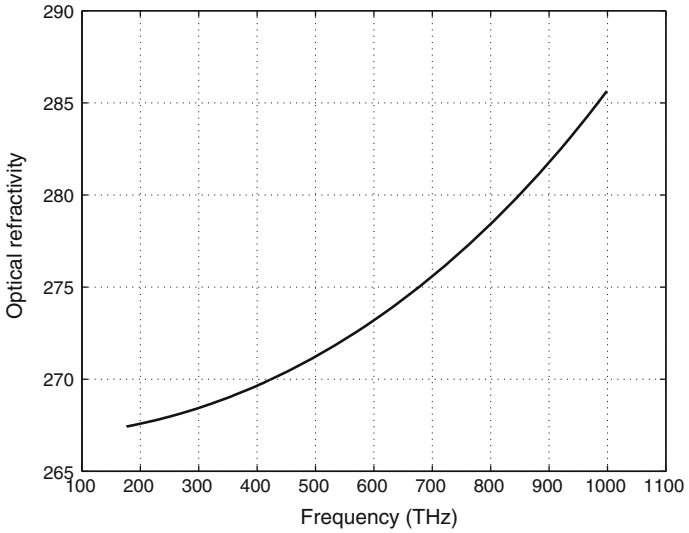

Fig. 3 The total optical refractivity as function of frequency. The total pressure is 1013 hPa, the Temperature 300 K, and the relative humidity is 100 %

Owens (1967), Ciddor (1996), and Ciddor and Hill (1999) can be used. For the accurate calculation of the optical refractivity, IAG has recommended (Rüeger 2002b, Chap. 3) the formulae proposed by Ciddor (1996) and Ciddor and Hill (1999) that are expressed as

$$\tilde{k}_d(\nu) = \frac{1}{\rho_{ds}} \left(\frac{5792105}{238.0185 - \Upsilon^2} + \frac{167917}{57.362 - \Upsilon^2} \right) (1 + 0.534 \times 10^{-6}(x_c - 450)) \times 10^{-2}, \tag{24}$$

$$\tilde{k}_w(\nu) = \frac{1.022}{\rho_{ws}} \left(295.235 + 2.6422\Upsilon^2 - 0.032380\Upsilon^4 + 0.004028\Upsilon^6 \right) \times 10^{-2}, \tag{25}$$

where ρ_{ds} is the density of dry air at 15 °C, 101325 Pa, $x_w = 0$ (where $x_w = p_w/p$ is the molar fraction of water vapor in moist air). ρ_{ws} is the density of pure water vapor at 20 °C, 1333 Pa, $x_w = 1$. Υ is the wave number (reciprocal of the wavelength, $\frac{1}{\lambda} = \frac{\nu}{c_0}$) and x_c is the fractional carbon dioxide content. A plot of the optical refractivity as function of frequency is shown in Fig. 3.

3 Definition of Path Delay in the Neutral Atmosphere

In space geodesy normally the travel time (or difference in travel time) between a source in space (a satellite or a quasar) to a receiver on the surface of the Earth is

measured. This travel time is then converted to a distance measurement by multiplying with the speed of light in vacuum. The atmosphere will introduce an error in this distance since it will affect the propagation path of the signal and since the propagation speed of the signal in the atmosphere is lower than the speed of light in vacuum.

If the variations in the refractivity over the distance of one wavelength is negligible we can use the geometric optics approximation. This means that the propagation of an electromagnetic wave can be described as a ray. When calculating the propagation time of the electromagnetic wave we thus only have to consider the refractivity along the ray path. For the propagation of the signals used in space geodesy the wavelengths are a few decimeters at most, thus in the Earth's atmosphere this approximation will normally be valid. The electric path length L (propagation time divided by the speed of light in vacuum) of a ray propagating along the path S through the atmosphere will be

$$L = \int_S n(s)\,\mathrm{d}s. \tag{26}$$

The electric path will be longer than the geometric length G of a straight line between the endpoints of the path for two reasons (see Fig. 4). Firstly, the propagation velocity is lower in the atmosphere than in vacuum. Secondly, the path S taken by the ray is, according to Fermat's principle, the path which minimizes L. The atmospheric delay, ΔL, is defined as the excess electric path length caused by the atmosphere

$$\Delta L = L - G = \int_S n(s)\mathrm{d}s - G = \int_S [n(s) - 1]\,\mathrm{d}s + \int_S ds - G = 10^{-6}\int_S N(s)\,\mathrm{d}s + S - G, \tag{27}$$

where S is the geometric length of the actual propagation path of the ray. By dividing the refractivity into hydrostatic and wet parts using Eq. (16) we get

$$\Delta L = 10^{-6}\int_S N_h(s)\,\mathrm{d}s + 10^{-6}\int_S N_w(s)\,\mathrm{d}s + S - G = \Delta L_h + \Delta L_w + S - G, \tag{28}$$

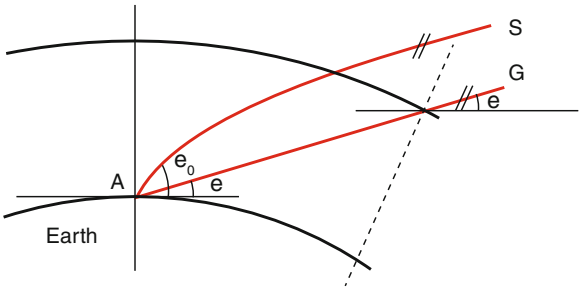

Fig. 4 Path taken by a signal through the atmosphere. The signal will take the path with the shortest propagation time (S). Since the signal propagates slower in the atmosphere than in vacuum, the geometrical length of S will be larger than the straight path G

where ΔL_h and ΔL_w are called the hydrostatic and wet delay, respectively. Commonly, the effect of bending, $S - G$, is by convention considered to be part of the hydrostatic delay, i.e. the hydrostatic mapping function (see Sect. 4.2) includes the bending effect.

In space geodesy it is common to refer the slant delays to the delays in the zenith direction (using mapping functions, see Sect. 4.2). The zenith hydrostatic delay ΔL_h^z and the zenith wet delay ΔL_w^z are given by

$$\Delta L_h^z = 10^{-6} \int_{h_0}^{\infty} N_h(z)\, \mathrm{d}z, \tag{29}$$

$$\Delta L_w^z = 10^{-6} \int_{h_0}^{\infty} N_w(z)\, \mathrm{d}z, \tag{30}$$

where h_0 is the altitude of the site.

3.1 Hydrostatic Delay

From Eqs. (17) and (29) we see that the hydrostatic delay only depends on the total density and not on the mixing ratio of wet and dry parts. Following Davis et al. (1985), the hydrostatic delay can be determined by using the hydrostatic equation

$$\frac{\mathrm{d}p}{\mathrm{d}z} = -\rho\,(z)\, g\,(z), \tag{31}$$

where $g(z)$ is the gravity along the vertical coordinate z, and integration of Eq. (31) yields the pressure p_0 at the height h_0

$$p_0 = \int_{h_0}^{\infty} \rho\,(z)\, g\,(z)\, \mathrm{d}z = g_{eff} \int_{h_0}^{\infty} \rho\,(z)\, \mathrm{d}z. \tag{32}$$

Instead of the height-dependent gravity $g(z)$, we introduce the mean effective gravity g_{eff}

$$g_{eff} = \frac{\int_{h_0}^{\infty} \rho\,(z)\, g\,(z)\, \mathrm{d}z}{\int_{h_0}^{\infty} \rho\,(z)\, \mathrm{d}z}, \tag{33}$$

and the inversion yields the height h_{eff} which is the height of the center of mass of the atmosphere above the site and can be determined with

$$h_{eff} = \frac{\int_{h_0}^{\infty} \rho\,(z)\, z \mathrm{d}z}{\int_{h_0}^{\infty} \rho\,(z)\, \mathrm{d}z}. \tag{34}$$

Saastamoinen (1972b) used the approximation for the effective height

$$h_{eff} = (0.9h_0 + 7300\,\mathrm{m}) \pm 400\,\mathrm{m}, \tag{35}$$

which holds for all latitudes and all seasons.

3.1.1 Microwaves

With the pressure p_0 at the site, it is now possible to determine the zenith hydrostatic delay

$$\Delta L_h^z = 10^{-6} k_1 \frac{R\,p_0}{M_d\,g_{eff}}. \tag{36}$$

We follow Saastamoinen (1972b) and Davis et al. (1985) to find the appropriate coefficients in Eq. (36). At first, the gravity g_{eff} at the effective height h_{eff} is determined with

$$g_{eff} = 9.8062\left(1 - 0.00265\cos(2\theta) - 0.31 \cdot 10^{-6} h_{eff}\right), \tag{37}$$

which combined with Eq. (35) can be written as

$$g_{eff} = g_m \cdot f(\theta, h_0), \tag{38}$$

with $g_m = 9.7840$ and

$$f = \left(1 - 0.00266\cos(2\theta) - 0.28 \cdot 10^{-6} h_0\right), \tag{39}$$

where θ and h_0 are latitude and orthometric (or ellipsoidal) height of the station. Thus, the zenith hydrostatic delay is

$$\Delta L_h^z = 10^{-6} k_1 \frac{R\,p_0}{M_d\,g_m f(\theta, h_0)}, \tag{40}$$

and after substitution of all values we get for the zenith hydrostatic delay in meters

$$\Delta L_h^z = 0.0022768 \frac{p_0}{f(\theta, h_0)}, \tag{41}$$

where p_0 is in hPa. The molar masses M_d and M_w stay constant up to heights of about 100 km (Davis 1986), which is essential for all troposphere delay models. The errors in the zenith hydrostatic delays are mainly caused by errors in k_1 and in the surface pressure measurements. At typical meteorological conditions the zenith hydrostatic delays are about 2.3 m at sea level. An error in the surface pressure of 1 hPa causes an error of about 2.3 mm. In order to reach an accuracy of 0.1 mm, the pressure has to be measured with an accuracy of 0.05 hPa. The error due to the assumption of hydrostatic equilibrium depends on the wind and is about 0.01 % (0.2 mm path delay). Under severe weather conditions vertical accelerations can reach 1% of the

gravity acceleration, which can cause errors in the zenith hydrostatic delays of about 20 mm (Davis et al. 1985).

3.1.2 Optical Zenith Hydrostatic Delays

The optical zenith hydrostatic delay can, just as for microwaves, be expressed as a function of the surface pressure. The derivation is in principle the same and will not be repeated here. The final expression is

$$\Delta L_h^z = 0.1022\ \tilde{k}_d(\nu) \times 10^{-6} \frac{p_0}{f(\theta, h_0)}. \tag{42}$$

The above equation is slightly different from the one developed by Mendes and Pavlis (2004), which is expressed as

$$\Delta L_h^z = 24.16579 f_h(\nu) \times 10^{-6} \frac{p_0}{f(\theta, h_0)}. \tag{43}$$

Mendes and Pavlis (2004) derived their own dispersion factor $f_h(\nu)$ based on the modified dispersion formula in Eq. (24) for the wavelength of 0.532 μm. Equations (42) and (43) produce similar accuracy results if they are applied to real SLR observations.

3.1.3 Pressure Values

For the analysis of space geodetic techniques, there are three possibilities to obtain pressure values at the stations: local pressure recordings at the sites, pressure values from numerical weather models, or empirical models for the pressure (Böhm et al. 2009a). For instance, simple empirical models are the ones by Berg (1948)

$$p = 1013.25 \cdot (1 - 0.0000226h)^{5.225}, \tag{44}$$

with the pressure p in hPa and orthometric station height h in m, or the model by Hopfield (1969)

$$p = 1013.25 \cdot \left(\frac{T_k - \alpha h}{T_k}\right)^{\frac{g}{R_d \alpha}}, \tag{45}$$

with the atmospheric temperature at sea level $T_k = 293.16$ K, the normal lapse rate of temperature with elevation $\alpha = 4.5$ K/km, gravity g at the surface of the Earth (9.7867 m/s^2) and the gas constant $R_d = 0.287$ kJ/K/kg for dry air. More sophisticated empirical models are UNB3m (Leandro et al. 2006) or Global Pressure and Temperature (GPT; Böhm et al. (2007)). UNB3m is based on meteorological parameters (pressure, temperature, humidity, temperature lapse rate, and water vapor pressure

Table 2 Availability of pressure values from local recordings at the sites, from numerical weather models (e.g. the hydrostatic zenith delays from ECMWF data as provided by the Vienna University of Technology), and from the empirical model GPT

Pressure	Local recordings	Grid values	GPT
Availability	At sites	All (by interpolation)	All
Time span	Per observation	Since 1994	Unlimited
Spatial resolution	Per site	2.0 x 2.5°	Spherical harmonics (9/9)
Time resolution	Per observation	6 h	Annual

height factor) at five latitude bands which are symmetric w.r.t. the equator (similar to the Niell Mapping Functions (Niell 1996)). Input parameters for GPT are station latitude, longitude, height and the day of the year, which is similar to the Global Mapping Functions (GMF; Böhm et al. 2006a) as both, GPT and GMF, are based on spherical harmonics up to degree and order 9.

Table 2 summarizes some properties of the pressure values (or zenith hydrostatic delays) from different sources. Unfortunately, local pressure measurements are usually not available, in particular at GNSS stations. Thus, to get consistent values of a priori zenith hydrostatic delays for global GNSS networks it is preferable to take these values from numerical weather models. For example, the Department of Geodesy and Geoinformation (GEO) at the Vienna University of Technology provides zenith hydrostatic delays calculated from ECMWF data. These are provided on global grids (2.5° times 2.0°) and with a temporal resolution of 6 h starting in 1994 (Böhm et al. 2009a). For scientific purposes also forecast values are made available so that they can be used for real-time applications without significant loss of accuracy (Böhm et al. 2009b). Empirical models like GPT are always available for all time epochs, but the spatial resolution is limited as it is represented by spherical harmonics up to degree and order 9 (≈20° in latitude/longitude), respectively. The model only includes an annual variation with the zero phase set to 28 January, so it cannot capture short-term and sub-annual weather phenomena. As an example, Fig. 5 shows pressure values at station O'Higgins in Antarctica. It is evident that empirical models like the model by Berg (1948) or GPT cannot describe the short term pressure variations and that the model by Berg (1948) is offset by about 20 hPa.

We have also compared and validated the empirical models Berg and GPT with pressure values from the ECMWF on global grids (10° in latitude times 12.5° in longitude) (Böhm et al. 2009a). The comparison was performed for the year 2005 and the temporal resolution was 10 days (i.e. one global grid was taken every 10 days and consequently 36 grids were used for the statistics). An error in the pressure of 1 hPa corresponds (at sea level) to approximately a 2.3 mm error in the L_h^z. This error will result in an error in the position—especially the vertical component – estimated with a space geodetic technique. In Sect. 4.2 a rule of thumb relating the error in the delay to the error in the vertical coordinate is presented, from this we find that 3 hPa (7 mm zenith delay error) correspond to 1 mm station height difference. It was found that the Berg model has large deficiencies especially around Antarctica, resulting in

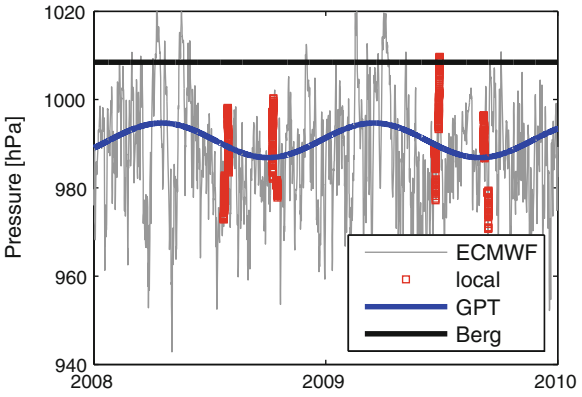

Fig. 5 Pressure values for station O'Higgins in Antarctica from the ECMWF (*grey line*), local pressure recordings at the radio telescope (*red squares*), GPT (*blue line*), and pressure determined with the model by Berg (1948) (*black bold line*)

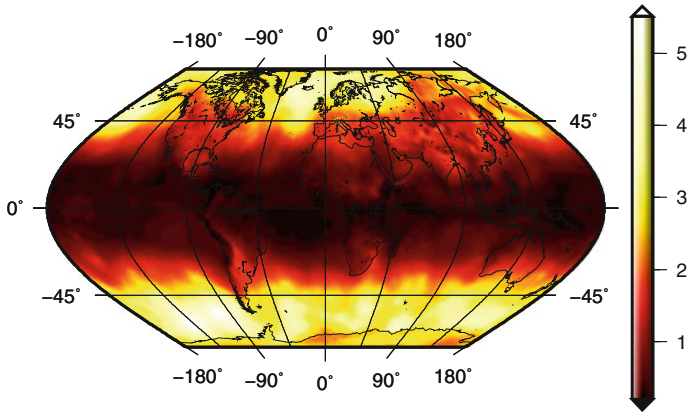

Fig. 6 Simulated station height standard deviations in mm for GPT with respect to the pressure values provided by the ECMWF (based on 36 epochs in 2005 for a 2° latitude times 2.5° longitude grid) (modified from Böhm et al. (2009b))

station height errors of more than 10 mm. The errors for GPT for this region are smaller, and these might completely disappear with an increased degree and order of the spherical harmonic expansion. There are almost no biases for the rest of the Earth (see Böhm et al. (2009b)).

GPT only accounts for an annual variation of the pressure with rather small amplitudes compared to the other (e.g. weekly) variations of the pressure. Thus, the standard deviations of the differences to the grid values from the ECMWF are almost the same for the Berg model (constant pressure per site) and GPT. In Fig. 6 the simulated station height standard deviations are plotted for the case of using GPT compared pressure values from the ECMWF. There is an increase of the standard deviations

towards higher latitudes (with maximum values at around ±60° latitude), which is due to the larger pressure variations in these regions compared to equatorial regions (Böhm et al. 2009a).

3.2 Wet Delay

3.2.1 Microwave Zenith Wet Delays

From Eq. (30) the zenith wet delay is

$$\Delta L_w^z = 10^{-6}\left[\int_{h_0}^{\infty}\left(k_2'\frac{p_w}{T}Z_w^{-1}\right)\mathrm{d}z + \int_{h_0}^{\infty}\left(k_3\frac{p_w}{T^2}Z_w^{-1}\right)\mathrm{d}z\right]. \tag{46}$$

The first term in Eq. (46) is about 1.6 % of the second term.

The derivation of a model to account for the zenith wet delay (ΔL_w^z) is by far more challenging than the one for the hydrostatic delay. This is due to high spatial and temporal variability and unpredictability of the amount of water vapor. Thus, the temperature and the water vapor content at the Earth surface are not representative for the air masses above. This is the reason why numerous models have been developed over the past few decades for the wet delay, while preserving Saastamoinen's model (with slight modifications) for determining the hydrostatic delay. The zenith wet delay varies between a few mm at the poles and about 40 cm above the equatorial regions. In order to keep millimeter accuracy in space geodetic techniques, the ΔL_w^z is nowadays estimated as an additional parameter within the data analysis. Nevertheless, some models are listed below and can be used as an initial value in the data analysis or for applications not requiring high accuracy.

Saastamoinen (1972b) proposes the calculation of the zenith wet delay ΔL_w^z based on ideal gas laws using a simple relation

$$\Delta L_w^z = 0.0022768(1255 + 0.05T_0)\frac{p_{w0}}{T_0}, \tag{47}$$

where p_{w0} is the water vapor pressure and T_0 is the temperature at the surface. Similar to the hydrostatic delay, Hopfield (1969) proposes an expression for ΔL_w^z as follows

$$\Delta L_w^z = \frac{10^{-6}}{5}N_w(h_0)h_w, \tag{48}$$

with $N_w(h_0)$ the refractivity of wet air at the surface (located at height h_0) and a mean value $h_w = 11000$ m for the height of the troposphere up to which water vapor exists. Ifadis (1986) proposes to model the zenith wet delay as a function of surface pressure, partial water vapor pressure and temperature. Mendes and Langley (1998) derived a linear relation between ΔL_w^z and partial water vapor pressure. Some other

models are being described by Mendes (1999). An approximate relation between water vapor pressure and delay reads

$$\Delta L_w^z \approx \frac{0.217 p_w}{T}. \tag{49}$$

Assuming an isothermal atmosphere with exponential decrease of water vapor pressure p_w, and assuming that water vapor exists until a height of 2 km, we get an approximation for the wet delay as a function of water vapor pressure at the Earth's surface p_{w0}

$$\Delta L_w^z \approx 748 \frac{p_{w0}}{T_0^2}. \tag{50}$$

An even simpler way is a rule of thumb that suggests that the wet zenith delay in cm equals the water vapor pressure in hPa at the Earth's surface

$$\Delta L_w^z \,[\text{cm}] \approx p_{w0}\,[\text{hPa}]. \tag{51}$$

In any case, information of water vapor pressure and/or temperature at the surface has to be known. If no surface meteorological observation is available, we can use the simple model of the standard atmosphere where p_w can be calculated as a function of the relative humidity f, i.e.

$$p_w = \frac{f}{100} \exp(-37.2465 + 0.213166T - 0.000256908T^2). \tag{52}$$

3.2.2 Conversion of Zenith Wet Delays to Precipitable Water

The zenith wet delay can be related to the amount of integrated water vapor above the station. Following Eq. (46) and using the expression for integrated mean temperature T_m (Bevis et al. 1992)

$$T_m = \frac{\int_s (\frac{e}{T} Z_w^{-1}) \mathrm{d}s}{\int_s (\frac{e}{T^2} Z_w^{-1}) \mathrm{d}s} \approx \frac{\int_{h_0}^{\infty} (\frac{e}{T} Z_w^{-1}) \mathrm{d}z}{\int_{h_0}^{\infty} (\frac{e}{T^2} Z_w^{-1}) \mathrm{d}z}, \tag{53}$$

we can write

$$\Delta L_w = 10^{-6} \left[k_2' + \frac{k_3}{T_m} \right] \int_s \left(\frac{e}{T} Z_w^{-1} \right) \mathrm{d}s. \tag{54}$$

Applying the ideal gas laws, Eq. (54) can be reformulated as

$$\Delta L_w = 10^{-6} \left[k_2' + \frac{k_3}{T_m} \right] \frac{R}{M_w} \int_s \rho_w \mathrm{d}s. \tag{55}$$

To be able to calculate the mean temperature T_m the vertical profiles of the water vapor and temperature have to be known. Such data can be obtained from radiosonde measurements or calculated (and predicted) from operational meteorological models (Wang et al. 2005). In absence of this data, the empirically derived model by e.g. Bevis et al. (1992) and Emardson and Derks (2000) can be used. The determination of the mean temperature T_m from Eq. (53) is based on the weighting with water vapor pressure in the atmosphere. Since water vapor is mainly located near the Earth surface the mean temperature T_m will be highly correlated with the temperature at the Earth surface T_0. Using 8718 profiles of radiosonde launches at 13 stations in the United States between 27 and 65° northern latitude, between 0 and 1600 m height, and over a time span of 2 years Bevis et al. (1992) found

$$T_m \approx 70.2 + 0.72 T_0, \tag{56}$$

with a standard deviation of ± 4.74 K. If ΔL_w^z and surface temperature are known without error, the integrated water vapor can be computed with an average error of less than 4 %.

It is clear from Eq. (55) that the wet delay is proportional to the integrated water vapor content IWV ($IWV = \int_0^\infty \rho_w \, dz$). Since IWV is a variable that can be easily obtained from numerical weather prediction models or measured by other techniques, it is of great interest to have a simple expression for calculating the wet delay from IWV, and vice versa. Thus we define the proportionality constant Π such that

$$IWV = \Pi \, \Delta L_w^z, \tag{57}$$

where ΔL_w^z is the wet tropospheric delay in the zenith direction. By comparing Eqs. (55) and (57), we find that Π can be related to T_m by

$$\Pi = \frac{10^6 M_w}{\left[k_2' + \frac{k_3}{T_m}\right] R}, \tag{58}$$

The integrated water vapor in zenith direction can also be provided as precipitable water (PW) which corresponds to the height of the equivalent water column above the station

$$PW = \frac{IWV}{\rho_{w,fl}}, \tag{59}$$

where $\rho_{w,fl}$ is the density of liquid water in kg/m^3. With a dimensionless quantity κ we can relate the ΔL_w^z and PW

$$PW = \kappa \Delta L_w^z, \tag{60}$$

with κ defined as

$$\kappa = \frac{\Pi}{\rho_{w,fl}}. \tag{61}$$

The precipitable water is roughly 0.16 of ΔL_w^z. This value can vary by more than 15 %, mainly as a function of latitude and season (Fölsche 1999).

Errors in the factor Π are mainly caused by errors in T_m and the constants in Eq. (58). According to Fölsche (1999) the influence of errors in the mean temperature is at least one order of magnitude larger than errors in the constants. It is shown in the following how accurate T_m has to be determined to get the amount of water vapor with a certain accuracy.

The partial derivative of Π with respect to the mean temperature yields

$$\frac{\partial \Pi}{\partial T_m} = \frac{10^6 M_w k_3}{R\left[k_2' + \frac{k_3}{T_m}\right]^2 T_m^2}. \tag{62}$$

This means that Π is changed by about 20 kg/m^3 if $T_m (= 270$ K) is changed by 4 K. Assuming a zenith wet delay of 200 mm this corresponds to an error in the precipitable water of about 4 mm. Requirements for better accuracies of PW (1 mm or better) indicate that the real weather data should be used to derive the mean temperature instead of approximations such as provided in Eq. (56).

3.2.3 Optical Zenith Wet Delays

Substituting Eq. (22) into Eq. (30) yields

$$\Delta L_w^z = 10^{-6} \tilde{k}_w^\star(\nu) \int_{h_0}^{\infty} \rho_w(z)\, \mathrm{d}z. \tag{63}$$

Following Saastamoinen (1972a), the integral $\int_{h_0}^{\infty} \rho_w(h)\, \mathrm{d}h$ can be approximated by

$$\int_{h_0}^{\infty} \rho_w(z)\, \mathrm{d}z \approx \frac{R_d}{4 g_m} p_{w0}, \tag{64}$$

where p_{w0} is the surface pressure of water vapor. Substituting Eq. (64) into Eq. (30), the zenith wet delay of optical measurements can be modeled as

$$\Delta L_{w0}^z = 10^{-6} \tilde{k}_w^\star(\nu) \frac{R_d}{4 g_m} p_{w0}. \tag{65}$$

Equation (65) is slightly different from the one developed by Mendes and Pavlis (2004), which is expressed as

$$\Delta L^z_{w0} = 10^{-6}(5.316 f_{nh}(\nu) - 3.759 f_h(\nu)) \frac{R_d}{4 g_m} p_{w0}. \quad (66)$$

Mendes and Pavlis (2004) derived their own dispersion factors $f_h(\lambda)$ and $f_{nh}(\lambda)$ based on the modified dispersion formula in Eq. (24) for the 0.532 μm wavelength. Equations (65) and (66) produce similar accuracy results if they are applied to real SLR observations.

4 Modeling Delays in the Neutral Atmosphere

There are basically two ways to handle the atmospheric delays when analyzing space geodetic data; either external measurements of the atmospheric delays are used to correct the measurements, or the atmospheric delays are parameterized and estimated in the data analysis. As seen in Sect. 3.1 the hydrostatic delay can be accurately determined from surface pressure measurements. However, the wet delay cannot be estimated that accurately from meteorological measurements at the surface. Thus it is common when analyzing space geodetic data to use surface pressure measurements to model the hydrostatic delay, while the wet delay is estimated in the data analysis. In the data analysis the tropospheric delays are modeled using mapping functions and gradients (see Sect. 4.2). An alternative strategy is to also use external estimates of the hydrostatic and wet delays. Such estimates could for example be obtained from ray-tracing though numerical weather models (Sect. 4.1), a technique also commonly applied for deriving expression for the tropospheric mapping functions. Another possibility is to infer the tropospheric delay from measurements by external instruments such as Water Vapor Radiometers (WVR) (Sect. 4.4). The numerical values etc. given in these sections are for microwaves, although the general principles could of course also be applied in the case of optical techniques. Tropospheric modeling for optical frequencies (e.g. SLR) is discussed in Sect. 4.3.

4.1 Ray-Tracing

From e.g. radiosonde data or numerical weather prediction models we can calculate the refractivity field of the atmosphere. This could be used to estimate the atmospheric delay simply by integrating the refractivity along the propagation path of the signal. However, the problem is that we normally do not exactly know the propagation path. To discover it we can apply the so-called ray-tracing technique. The ray-tracing technique has been used in many fields of science where the propagation of an electro-magnetic wave through a stratified medium has to be quantified. The ray-tracing is based on the so-called Eikonal equation, which represents the solution of

the Helmholtz equation for an electro-magnetic wave propagating through a slowly varying medium (Iizuka 2008; Wheelon 2001). Using the Eikonal equation, we can determine the ray path and the optical path length. In the following sub-sections, we present a ray-tracing system that can be applied for tropospheric modeling and discuss some basic elements in tropospheric ray-tracing calculations through Numerical Weather Prediction Models.

4.1.1 Eikonal Equation and Ray Path

To derive the Eikonal equation we start from Maxwell's equations (Eqs. 1–4). It is convenient to use the H-field $\mathbf{H}$ instead of the magnetic field $\mathbf{B}$, where $\mathbf{H}$ is defined by

$$\mathbf{B} = \mu \mathbf{H}. \tag{67}$$

We can consider a general time-harmonic field

$$\mathbf{E}(r,t) = \mathbf{e}(\mathbf{r}) e^{i(k_0 L(\mathbf{r}) - 2\pi\nu t)}, \tag{68}$$

$$\mathbf{H}(r,t) = \mathbf{h}(\mathbf{r}) e^{i(k_0 L(\mathbf{r}) - 2\pi\nu t)}, \tag{69}$$

where $L(\mathbf{r})$ is the optical path, and $\mathbf{e}(\mathbf{r})$ and $\mathbf{h}(\mathbf{r})$ are (complex) vector functions. The wave number for vacuum (k_0) is defined as

$$k_0 = \frac{2\pi\nu}{c} = \frac{2\pi}{\lambda_0}, \tag{70}$$

where λ_0 is the vacuum wavelength. By inserting these equations into Maxwell's equations (Eqs. 1–4) and assume that there are no free charges and zero conductivity, we get after some calculations (Born and Wolf 1999)

$$\nabla L \times \mathbf{h} + c\,\varepsilon \mathbf{e} = -\frac{1}{ik_0} \nabla \times \mathbf{h}, \tag{71}$$

$$\nabla L \times \mathbf{e} - c\,\mu \mathbf{h} = -\frac{1}{ik_0} \nabla \times \mathbf{e}, \tag{72}$$

$$\mathbf{e} \cdot \nabla L = -\frac{1}{ik_0} \left(\mathbf{e} \cdot \frac{\nabla \varepsilon}{\varepsilon} + \nabla \cdot \mathbf{e} \right), \tag{73}$$

$$\mathbf{h} \cdot \nabla L = -\frac{1}{ik_0} \left(\mathbf{h} \cdot \frac{\nabla \mu}{\mu} + \nabla \cdot \mathbf{h} \right). \tag{74}$$

For small vacuum wavelength, and therefore large wave number for vacuum (k_0)

$$\nabla L \times \mathbf{h} + c\,\varepsilon \mathbf{e} = \mathbf{0}, \tag{75}$$

$$\nabla L \times \mathbf{e} - c\,\mu \mathbf{h} = \mathbf{0}, \tag{76}$$

$$\mathbf{e} \cdot \nabla L = 0, \tag{77}$$

$$\mathbf{h} \cdot \nabla L = 0. \tag{78}$$

By eliminating **h** between Eqs. (75) and (76), and considering Eq. (77), the following differential equation is obtained which is independent of the amplitude vectors **e** and **h**

$$\|\nabla L\|^2 = n\,(\mathbf{r})^2\,, \tag{79}$$

where ∇L comprises the components of the ray directions, L is the optical path length, $n = c\sqrt{\varepsilon\mu}$ is the refractivity index of a medium, and **r** is the position vector. This equation is the well-known Eikonal equation. The surfaces $L(\mathbf{r}) = constant$ are called geometrical wave surfaces or the geometrical wave-fronts.

4.1.2 Hamiltonian Formalism of Eikonal Equation

The above mentioned Eikonal equation is a partial differential equation of the first order for $n\,(\mathbf{r})$ and it is possible to express it in many alternative forms. In general, the Eikonal equation can be written in the Hamiltonian canonical formalism as follows (Born and Wolf 1999; Cerveny 2005; Nafisi et al. 2012a)

$$\mathscr{H}\,(\mathbf{r}, \nabla L) = \frac{1}{\alpha}\left((\nabla L \cdot \nabla L)^{\frac{\alpha}{2}} - n(\mathbf{r})^{\alpha}\right) = 0, \tag{80}$$

$$\frac{\mathrm{d}\mathbf{r}}{\mathrm{d}u} = \frac{\partial \mathscr{H}}{\partial \nabla L}, \tag{81}$$

$$\frac{\mathrm{d}\nabla L}{\mathrm{d}u} = -\frac{\partial \mathscr{H}}{\partial \mathbf{r}}, \tag{82}$$

$$\frac{\mathrm{d}L}{\mathrm{d}u} = \nabla L \cdot \frac{\partial \mathscr{H}}{\partial \nabla L}. \tag{83}$$

Here α is a scalar value related to the parameter of interest u (see Table 3). In general it is a real number but in our applications we can consider it to be an integer. $\mathscr{H}\,(\mathbf{r}, \nabla L)$ is called Hamiltonian function or just the Hamiltonian. In a 3D space this system consists of seven equations. Six equations are obtained from Eqs. (81) and (82) must be solved together. The result of these six equations is $\mathbf{r} = \mathbf{r}(u)$ which is the trajectory of the signal in space. The seventh equation, i.e. Eq. (83), can be solved independently and yields the optical path length.

4.1.3 Ray-Tracing System for Tropospheric Modeling

Equations (80)–(82) can be used for constructing a ray-tracing system for any specific application by simply selecting a correct value for the scalar α (Nafisi et al. 2012a).

Table 3 Different cases for Hamiltonian formalism

α		Parameter of interest
0	$du = dT$	Travel time T along the ray
1	$du = ds$	Arc-length s along the ray
2	$du = d\sigma = \frac{dT}{n^2}$	Natural variables along the ray

For $\alpha = 0$, the parameter u represents travel time t along the ray. If $\alpha = 1$, the parameter u represents the arc-length s along the ray. In case of $\alpha = 2$, the parameter u is equal to dt/dn, which represents the natural variables along the ray (Cerveny 2005).

When applying ray-tracing for the determination of total delays along the ray path the natural choice is $\alpha = 1$. However, it is also possible to use $\alpha = 2$ to construct a tropospheric ray-tracing system (see Gegout et al. (2011)). Ray-tracing systems can be expressed and solved in any curvilinear coordinate system, including spherical coordinates. Selecting $\alpha = 1$ and representing the function $\mathscr{H}$ in a spherical polar coordinate system (r, θ, λ), Eq. (80) can be rewritten as

$$\mathscr{H}(r, \theta, \lambda, L_r, L_\lambda, L_\theta) \equiv \left(L_r^2 + \frac{1}{r^2} L_\theta^2 + \frac{1}{r^2 \sin^2 \theta} L_\lambda^2 \right)^{\frac{1}{2}} - n(r, \theta, \lambda) = 0, \quad (84)$$

where r is the radial distance, θ is the co-latitude, and λ is the longitude ($0 \leq \theta \leq \pi$, $0 \leq \lambda \leq 2\pi$). $L_r = \frac{\partial L}{\partial r}$, $L_\theta = \frac{\partial L}{\partial \theta}$ and $L_\lambda = \frac{\partial L}{\partial \lambda}$ are the elements of ray directions. Now, by substituting Eq. (84) into Eqs. (81) and (82), we obtain

$$\frac{dr}{ds} = \frac{1}{\beta} L_r, \quad (85)$$

$$\frac{d\theta}{ds} = \frac{1}{\beta} \frac{L_\theta}{r^2}, \quad (86)$$

$$\frac{d\lambda}{ds} = \frac{1}{\beta} \frac{L_\lambda}{r^2 \sin^2 \theta}, \quad (87)$$

$$\frac{dL_r}{ds} = \frac{\partial n(r, \theta, \lambda)}{\partial r} + \frac{1}{\beta r} \left(\frac{L_\theta^2}{r^2} + \frac{L_\lambda^2}{r^2 \sin^2 \theta} \right), \quad (88)$$

$$\frac{dL_\theta}{ds} = \frac{\partial n(r, \theta, \lambda)}{\partial \theta} + \frac{1}{\beta} \frac{L_\lambda^2}{r^2 \sin^3 \theta}, \quad (89)$$

$$\frac{dL_\lambda}{ds} = \frac{\partial n(r, \theta, \lambda)}{\partial \lambda}, \quad (90)$$

where

$$\beta = \left(L_r^2 + \frac{1}{r^2} L_\theta^2 + \frac{L_\lambda^2}{r^2 \sin^2 \theta} \right)^{\frac{1}{2}} = n(r, \theta, \lambda). \quad (91)$$

This system of equations is a direct result of Eqs. (81) and (82) in a 3D medium, and we need to solve all six differential equations simultaneously. The final output is the positions of the points along the trajectory of the ray. For solving the above ray-tracing system, the following initial conditions at the starting point (station) can be used (Nafisi et al. 2012a)

$$r = r_0, \tag{92}$$
$$\lambda = \lambda_0, \tag{93}$$
$$\theta = \theta_0, \tag{94}$$
$$L_{r0} = n_0 \cos z_0, \tag{95}$$
$$L_{\theta 0} = n_0 r_0 \sin z_0 \cos a_0, \tag{96}$$
$$L_{\lambda 0} = n_0 r_0 \sin z_0 \sin a_0 \sin \theta_0, \tag{97}$$

where a_0 and z_0 are the initial geodetic azimuth and zenith angle, respectively. In the 3D case, gradients are important factors which can affect the bending of the ray path and therefore of the total ray-traced delay. The gradient can be rewritten as

$$\nabla n(r, \lambda, \theta) = \left[\frac{\partial n(r, \theta, \lambda)}{\partial r}, \frac{1}{r} \frac{\partial n(r, \theta, \lambda)}{\partial \theta}, \frac{1}{r \sin \theta} \frac{\partial n(r, \theta, \lambda)}{\partial \lambda} \right]^T. \tag{98}$$

From a practical point of view, we must find a sophisticated technique for computing the gradients of the refractive index in Eqs. (88), (89) and (90), which are

$$\nabla n_r = \frac{\partial n(r, \theta, \lambda)}{\partial r}, \tag{99}$$
$$\nabla n_\theta = \frac{\partial n(r, \theta, \lambda)}{\partial \theta}, \tag{100}$$
$$\nabla n_\lambda = \frac{\partial n(r, \theta, \lambda)}{\partial \lambda}. \tag{101}$$

Taking the effects of the gradients on the ray-traced delay into account is important for a ray-tracing algorithm. In particular in the case of symmetries, ray-tracing in curvilinear coordinates system would be easier. However, in general the ray-tracing systems in a curvilinear coordinates are more complex and sometimes fail. A typical example in atmospheric ray-tracing is the solution for ray-tracing in spherical polar coordinates when $\theta \approx 0°$ or $\theta \approx 180°$. According to Cerveny (2005) a general solution for removing such singularities is the use of transformations between ray-tracing systems in various forms. Using standard transformation relations, a ray-tracing system represented in curvilinear coordinates can be transformed into the universal Cartesian coordinates, and after ray-tracing computations in this coordinate system the results can be again transformed back to the curvilinear coordinates. In another method suggested by Alkhalifah and Fomel (2001) a small constant parameter (δ) is added in the denominator of fractions in the ray-tracing equations to

provide numerical stability. The value of this constant must be chosen carefully; otherwise we may get unreasonable results. Other stability solutions have been suggested by Schneider (1993) and Fowler (1994). In addition, the variation of the size of the grid cells in polar coordinates can causes a stability problems, especially in presence of small-scale inhomogeneities (Fowler 1994).

By substituting Eq. (84) into Eq. (83) and solving the equation, we can obtain this well-known equation to calculate the optical path length L

$$L = \int_S n(r, \theta, \lambda) \mathrm{d}s. \tag{102}$$

Once the position of a point along the ray path has been determined by Eqs. (85)–(90), the refractivity index n and the optical path length L can be calculated using Eq. (102). As mentioned before, the total delay is defined as the difference between the optical path length L and the straight line distance G

$$\Delta L = L - G. \tag{103}$$

3D ray-tracing can be easily reduced to 2D ray-tracing by substituting $\frac{\partial n}{\partial \theta} = 0$ and $\frac{\partial n}{\partial \lambda} = 0$ into Eqs. (85)–(90). In this case, we assume that the ray does not leave a plane of constant azimuth angle. For the 2D system, the coupled partial derivatives in Eqs. (85)–(90) reduce to four equations

$$\frac{\mathrm{d}r}{\mathrm{d}s} = \frac{1}{\beta} L_r, \tag{104}$$

$$\frac{\mathrm{d}\theta}{\mathrm{d}s} = \frac{1}{\beta} \frac{L_\theta}{r^2}, \tag{105}$$

$$\frac{\mathrm{d}L_r}{\mathrm{d}s} = \frac{\partial n(r, \theta, \lambda)}{\partial r} + \frac{1}{\beta r} \left(\frac{L_\theta^2}{r^2} + \frac{L_\lambda^2}{r^2 \sin^2 \theta} \right), \tag{106}$$

$$\frac{\mathrm{d}L_\theta}{\mathrm{d}s} = \frac{1}{\beta} \frac{L_\lambda^2}{r^2 \sin^3 \theta}. \tag{107}$$

Equation (91) remains valid also for 2D ray-tracing systems. For a horizontally stratified atmosphere, further simplifications can be applied to improve the calculation speed (Thayer 1967). According to Böhm (2004), we can develop a 1D ray-tracing. Figure 7 shows the geometry of this method for a troposphere with k different refractivity layers. The geocentric distances can be estimated by adding the radius of the Earth (R_e) to the heights of each layer

$$r_i = R_e + h_i. \tag{108}$$

In this method, the elevation angles (e_i) are with respect to a horizontal plane of the station, whereas θ_i show the angles between the ray path and the tangents to the

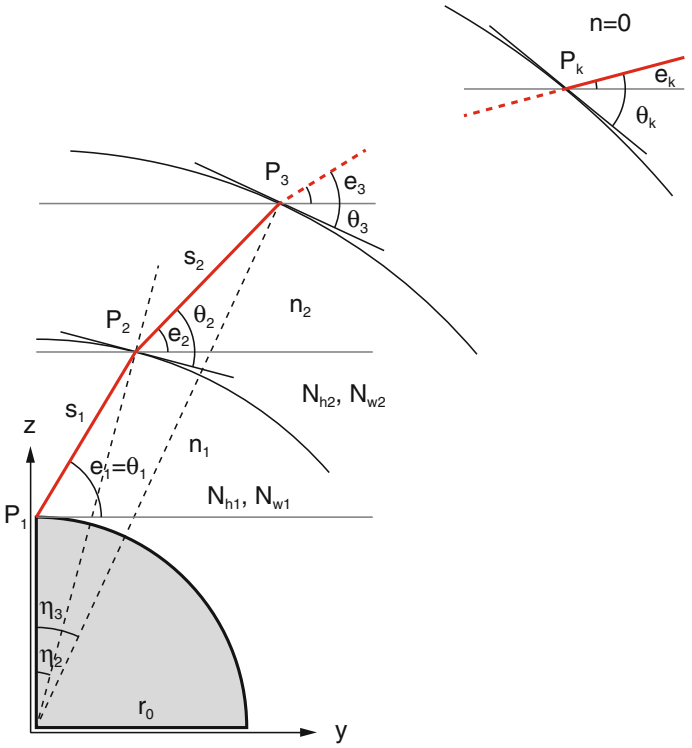

Fig. 7 Geometry of a 1D ray-tracing method, for a receiver located at P_1 and the upper limit of the troposphere at P_k. Points P_2 and P_3 show two sample points of the ray path. The y- and z-axis of the Cartesian coordinate system are parallel to horizon and zenith direction at the site, respectively. $S_2 = \|\mathbf{P}_3 - \mathbf{P}_2\|$ is the distance between two successive points along the path

layers in each intersection point of the trajectory. At the first point (receiver) these two are same, i.e. $e_1 = \theta_1$.

In this coordinate system, the z and y components are equal to r_1 and zero, respectively. Following the geometrical relation in Fig. 7 we find

$$S_i = \sqrt{r_{i+1}^2 - r_i^2 \cos\theta_i} - r_i \sin\theta_i, \tag{109}$$

$$z_{i+1} = z_i + S_i \sin e_i, \tag{110}$$

$$y_{i+1} = y_i + S_i \cos e_i, \tag{111}$$

$$\eta_{i+1} = \arctan\frac{y_{i+1}}{z_{i+1}}, \tag{112}$$

$$\delta_{i+1} = \eta_{i+1} - \eta_i, \tag{113}$$

$$\theta_{i+1} = \arccos\left(\frac{1+\eta_i \times 10^{-6}}{1+\eta_{i+1} \times 10^{-6}} \cos(\theta_i + \delta_{i+1})\right), \tag{114}$$

$$e_{i+1} = \theta_{i+1} - \eta_{i+1}. \tag{115}$$

These parameters must be calculated for all layers, and then it is possible to find the total slant delay (ΔL_d) as follow

$$\Delta L_d = \sum_{i=1}^{n-1} S_i N_i. \tag{116}$$

This equation can be divided into two terms for finding hydrostatic and non-hydrostatic components of the delay separately. By inserting h_i (along the zenith direction) instead of S_i (along the slant path) an equation for total zenith delay will be derived. As mentioned before, the bending effect is a part of the total delay and must be estimated separately. This parameter is zero for the zenith direction and

$$\Delta L_b = \sum_{i=1}^{n-1} (S_i - \cos(e_i - e_k) S_i). \tag{117}$$

for a slant direction. Implementation of the above ray-tracing system can vary substantially, with different degrees of complexity and accuracy. Examples of ray-tracing algorithms in atmospheric studies are given by Bean and Thayer (1959), Thayer (1967), Budden (1985), Davis (1986), Mendes (1999), Pany (2002), Böhm and Schuh (2003), Thessin (2005), Hulley (2007), Hobiger et al. (2008), Nievinski (2009), Wijaya (2010), Gegout et al. (2011) and Nafisi et al. (2012a). Several ray-tracing algorithms were compared by Nafisi et al. (2012b). Also it is possible to express the Eikonal equation and the ray-tracing system in curvilinear non-orthogonal coordinates systems. For details see Cerveny et al. (1988).

4.2 Mapping Functions and Gradients

In the analysis of space geodetic data the troposphere path delay $\Delta L(e)$ at the elevation angle e is usually represented as the product of the zenith delay ΔL^z and an elevation-dependent mapping function $mf(e)$ with

$$\Delta L(e) = \Delta L^z \cdot mf(e). \tag{118}$$

This concept is not only used to determine a priori slant delays for the observations, but the mapping function is also the partial derivative to estimate residual zenith delays. Typically, the zenith delay is estimated with a temporal resolution of 20–60 min in VLBI and GPS analysis. In VLBI analysis—when there is only one observation at a time at a station—this allows the zenith delays to be estimated in a least-squares adjustment. In the analysis of space geodetic observations not only the zenith delays are estimated, but also other parameters like the station clocks and the stations heights (Fig. 8). The partial derivatives of the observed delays w.r.t. the

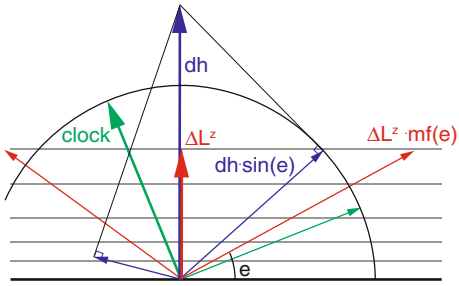

Fig. 8 Different elevation-dependence of the tropospheric delays (*red*), clock values (*green*), and height components (*blue*). Whereas the partial derivatives for the estimation of clocks and height components are strictly 1 and $\sin(e)$, respectively, the partial derivative for the estimation of the zenith delay is the mapping function which is approximately $1/\sin(e)$, but is not perfectly known (modified from Rothacher et al. (1998))

station heights are dependent on the elevation angle only, but whereas the partial derivatives w.r.t. the clocks (= 1) and the station heights (=$\sin(e)$) are exactly known, the partial derivatives for the zenith delays (i.e. the mapping functions) are only known with a limited accuracy. Consequently—via the correlations between zenith delays, station heights, and clocks—any imperfection of the mapping function will also result in errors in the station height estimates (and clock errors).

Considering Eq. (118) we find the following relationship: If the mapping function is in error (too large), then the estimated zenith delay ΔL^z is too small, because the observed tropospheric delay $\Delta L(e)$ does not change. Consequently, the estimated station height goes up. Niell et al. (2001) set up a rule of thumb specifying that the error in the station height is approximately one third of the delay error at a cutoff elevation angle of 7°. Böhm (2004) revisited this rule of thumb for VLBI analysis (and a cutoff elevation angle of 5°) specifying that the station height error is about one fifth of the delay error at the lowest elevation angle. This is close to the value 0.22 found by MacMillan and Ma (1994). The corresponding decrease of the zenith delay is about one half of the station height increase.

4.2.1 Azimuthal Symmetry: Mapping Functions

Assuming azimuthal symmetry of the neutral atmosphere around the station (i.e. at a constant elevation angle the delay is not dependent on the azimuth angle of the observation), the approach as described in Eq. (119) is used (e.g. Davis et al. 1985)

$$\Delta L(e) = \Delta L_h^z \cdot mf_h(e) + \Delta L_w^z \cdot mf_w(e). \tag{119}$$

$\Delta L(e)$ is the total path delay of the microwaves in the neutral atmosphere and e is the elevation angle of the observation to the satellite or the quasar (vacuum or geometric elevation angle). ΔL_h^z and ΔL_w^z are the a priori zenith hydrostatic and the

estimated wet delays, and $mf_h(e)$ and $mf_w(e)$ are the so-called mapping functions which provide the ratio of the delay to the delay in zenith direction. The input to both mapping functions is the vacuum elevation angle e, because the bending effect is accounted for by the hydrostatic mapping function.

Errors in the zenith hydrostatic delays or the mapping functions have an influence on station height errors as described with the rules of thumb by Niell et al. (2001) or Böhm (2004) mentioned above. The following two examples illustrate this rule of thumb, which—holding for both GPS and VLBI—depends on the actual distribution of elevation angels and on whether elevation angle-dependent weighting is used: The zenith hydrostatic and wet delays shall be 2000 and 200 mm, respectively, the minimum elevation angle is 5°, and the corresponding values for the true hydrostatic and wet mapping functions are 10.15 ($mf_h(5°)$) and 10.75 ($mf_w(5°)$) (Böhm et al. 2006b).

- We assume an error in the total pressure at the station of +10 hPa, e.g. when using the "mean" pressure from GPT during a time of low pressure. +10 hPa correspond to ≈+20 mm zenith hydrostatic delay (Saastamoinen 1972b), which is then mapped down to 5° elevation angle using the wrong mapping function (wet instead of hydrostatic, factor −0.6 = 10.15–10.75). At 5° elevation angle the mapping function error is −12 mm, and one fifth of it, i.e. −2.4 mm, would be the resulting station height error. This results in a kind of atmosphere loading correction (see Part 4, Wijaya et al. (2013)), because during a pressure low the station heights go up (Tregoning and Herring 2006; Steigenberger et al. 2009).
- We consider an error in the wet mapping function of 0.1 ($mf_w(5°) = 10.85$ instead of 10.75) or in the hydrostatic mapping function of 0.01 ($mf_h(5°) = 10.16$ instead of 10.15). The error at 5° elevation angle is in both cases 20 mm, i.e. the resulting error in the station height would be approximately +4 mm.

The scale height of the wet part in the troposphere is about 2 km, whereas the scale height of the hydrostatic part is about 8 km (cf. Fig. 9). The mapping functions describe the ratio $(AB)/(B_0B)$ (wet) and $(AC)/(C_0C)$ (hydrostatic). Due to the curvature of the Earth and the smaller scale height of the wet part, the hydrostatic

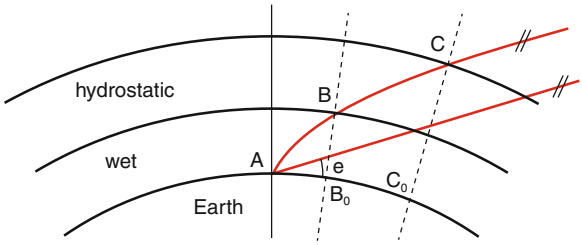

Fig. 9 The scale height of the wet part of the troposphere is about 2 km, the scale height of the hydrostatic part is about 8 km. The mapping functions describe the ratio of the paths $(AB)/(B_0B)$ (wet) and $(AC)/(C_0C)$ (hydrostatic). The wet mapping function is larger than the hydrostatic mapping function

mapping function is smaller than the wet mapping function. Exceptions are mapping functions for observations at very low elevation angles where the geometric bending effect, which is attributed to the hydrostatic mapping function, is increasing considerably. Thus, the mapping functions are a measure for the thickness of the atmosphere compared to the Earth radius (Niell et al. 2001). If the thickness of the atmosphere gets smaller, it appears to be flatter, and the mapping function approaches $1/\sin(e)$. Assuming a flat and evenly stratified atmosphere the mapping function is $1/\sin(e)$. For higher elevation angles (>20° elevation) these mapping functions are sufficiently accurate. Marini (1972) showed that the dependence on the elevation angle of the mapping functions for any horizontally stratified atmosphere can be described with continued fractions, when a, b, c, etc. are constants (Eq. 120). For verification Marini (1972) used standard atmosphere data but no real weather data.

$$mf(e) = \cfrac{1}{\sin(e) + \cfrac{a}{\sin(e) + \cfrac{b}{\sin(e) + \cfrac{c}{\sin(e) + \ldots}}}}. \tag{120}$$

This concept was first used in a model for the refraction of the hydrostatic atmosphere (Marini and Murray 1973) which has since then been applied in the analysis of geodetic and astrometric VLBI observations for a long time. The zenith delay corresponds to that by Saastamoinen (1972b), and the mapping functions are represented by a continued fraction form with two coefficients a and b. The first mapping functions for space geodetic applications with different coefficients for the hydrostatic and wet parts were published by Chao (1974) who replaced the second $\sin(e)$ by $\tan(e)$ to get unity in zenith direction.

Davis et al. (1985) developed the mapping function CfA2.2 for the hydrostatic delays down to 5° elevation; it is based on the approach by Chao (1974) but extended by an additional constant c. Based on ray-tracing through various standard atmospheres with elevation angles between 5 and 90°, the coefficients a, b, and c were determined as functions of pressure, water vapor pressure, and temperature at the Earth surface, and from vertical temperature gradients and the height of the troposphere. Herring (1992) developed coefficients for the mapping function MTT (MIT Temperature) as functions of latitude, height, and the temperature at the site. Unlike Davis et al. (1985) he did not use standard atmospheres but radiosonde data. The MTT mapping functions are based on a slightly changed continued fraction form which is widely accepted nowadays

$$mf(e) = \cfrac{1 + \cfrac{a}{1 + \cfrac{b}{1 + c}}}{\sin(e) + \cfrac{a}{\sin(e) + \cfrac{b}{\sin(e) + c}}}. \tag{121}$$

The factor in the denominator ensures that the mapping function is equal to one in the zenith direction. The strong dependence of the MTT mapping function (Herring 1992) on surface temperature induced Niell (1996) to develop the New Mapping Functions (NMF, now often called Niell Mapping Functions). The NMF do not use meteorological parameters at the sites, but only the day of the year (doy), station latitude, and station height as input parameters. Thus, they can be easily applied at stations without meteorological sensors, which often is the case for GNSS stations. Niell (1996) used standard atmosphere data at various latitudes to determine hydrostatic and wet mapping functions down to 3° elevation. Similar to Davis et al. (1985) and Herring (1992), he used ray-tracing methods to determine the coefficients a, b, and c of the continued fraction form in Eq. (121). NMF is based on sine functions to describe the temporal variation of the coefficients. The period is 365.25 days and the maximum/minimum is set to January 28 (doy 28). There is also a height correction for the hydrostatic NMF (NMFh) which describes that mapping functions increase with increasing height, i.e. the atmosphere above the site becomes flatter.

Niell (2000) was the first to determine mapping functions from numerical weather models which are often available with a time resolution of 6 h. For the Isobaric Mapping Functions (IMF), he used empirical functions for b and c, and he determined the coefficients a of the continued fraction in Eq. (121) from re-analysis data of the Goddard Space Flight Center Data Assimilation Office (DAO) (Schubert et al. 1993). For the hydrostatic IMF he used the height of the 200 hPa pressure level which is readily available with most numerical weather models and which is describing the thickness of the atmosphere well. For the wet IMF Niell suggested to use a coarse ray-trace at 3.3° initial elevation angle through numerical weather models. However, some practical and conceptual limitations in the computation of the wet IMF induced Böhm and Schuh (2004) to develop the Vienna Mapping Functions (VMF).

Thus, the VMF are characterized by the removal of some weaknesses of the IMFw, e.g. the coarse vertical resolution of weather model data is improved by vertical interpolation and the bending effect is taken into account rigorously. The same approach is applied for the wet and the hydrostatic mapping function, i.e. a ray-tracing is performed at an initial elevation angle of 3.3° for the hydrostatic and wet components yielding the hydrostatic delay, the wet delay, as well as the bending effect and the outgoing (vacuum) elevation angle which is ≈3°. (Please notice that always the refractivity profile above the site vertical is used, which makes the 1D ray-tracing simple and causes the delays to be symmetric with azimuth.) Together with the zenith hydrostatic and wet delays which are also determined by ray-tracing, the hydrostatic and wet mapping functions (Eq. (121)) at the outgoing elevation angle are calculated. The geometric bending effect is added to the hydrostatic mapping function. Similar to IMF, empirical functions are used for the b and c coefficients, which allows the determination of a in Eq. (121) by simple inversion. Since the coefficients a, b, and c are highly correlated, small errors in b and c can easily be compensated with the a coefficients. However, Böhm et al. (2006b) improved the b and c coefficients, and consequently the a coefficients had to be re-calculated. The coefficients of the so-called VMF1 are $b_h = 0.0029$, $b_w = 0.00146$, $c_w = 0.04391$, and the coefficient c_h is provided with Eq. (122) and Table 4

Table 4 Parameters c_0, c_{10}, c_{11}, and ψ needed for computing the coefficient c of the hydrostatic mapping function

Hemisphere	c_0	c_{10}	c_{11}	ψ
Northern	0.062	0.001	0.005	0
Southern	0.062	0.002	0.007	π

Mind that the c_{xx} coefficient is incorrect in the paper by Böhm et al. (2006b)

Table 5 Parameters c_0, c_{10}, c_{11}, and ψ needed for computing the coefficient c of the total mapping function

Hemisphere	c_0	c_{10}	c_{11}	ψ
Northern	0.063	0.000	0.004	0
Southern	0.063	0.001	0.006	π

$$c_h = c_0 + \left(\left(\cos\left(\frac{\text{doy} - 28}{365.25} \cdot 2\pi + \psi\right) + 1\right) \cdot \frac{c_{11}}{2} + c_{10}\right) \cdot (1 - \cos\theta). \quad (122)$$

The VMF1 are valid (tuned) for elevation angles above 3°, and the largest deviations from ray-traces at other elevations show up at about 5° elevation angle. The Vienna Mapping Function 1 is realized as discrete time series (resolution 6 h) of coefficients a, either on a global grid or at certain geodetic sites (see http://ggosatm.hg.tuwien.ac.at/). Mind that with the gridded version of the VMF1, the height correction of Niell (1996) has to be applied.

Instead of separating the delays into a hydrostatic and a wet part, an alternative concept of total mapping functions has also been investigated for troposphere delay modeling (Böhm et al. 2006b), i.e. the use of a single total mapping function mf_t (Eq. 123) both for mapping down the a priori zenith total delays $\Delta L^z_{t,0}$ and as partial derivative for the estimation of the residual total delays $\Delta L^z_{t,res}$ (Eqs. 124 and 125). Table 5 summarizes the parameters for the c_t coefficient which have been determined with the same approach as the c_h coefficients of the hydrotstatic VMF1. The b coefficient of the total VMF1 is also $b_t = 0.0029$.

$$mf_t(e) = \frac{\Delta L_h(e) + \Delta L_w(e) + \Delta L_{bend}}{\Delta L^z_h + \Delta L^z_w}, \quad (123)$$

$$\Delta L^z_t = \Delta L^z_h + \Delta L^z_w = \Delta L^z_{t,0} + \Delta L^z_{t,res}, \quad (124)$$

$$\Delta L(e) = \Delta L^z_{t,0} \cdot mf_t(e) + \Delta L^z_{t,res} \cdot mf_t(e). \quad (125)$$

Although a priori zenith total delays are required in the data analysis, a priori zenith hydrostatic delays can also be applied because the mapping function for the a priori zenith delays is the same as for the residual zenith delays (this only holds if there are no constraints on the estimated zenith delays). With the classical separation into a hydrostatic and a wet part, errors of the a priori zenith hydrostatic delays cannot be fully compensated by the estimation of the remaining wet part since the hydrostatic and wet mapping functions are not identical, especially at low elevation angles. The advantage of the concept of total mapping functions is that the results are not affected

by poor a priori zenith hydrostatic delays (Böhm et al. 2006b). On the other hand, the value of total mapping function is close to that of the hydrostatic mapping function, so it cannot account for the rapid variation of the wet zenith delays which occurs even between the 6 hourly epochs of the total VMF1. Thus, it is preferable to keep the separation into a hydrostatic and a wet mapping function, at least as long as the time resolution is not 3 h or better.

The goal of the Global Mapping Functions (GMF; Böhm et al. 2006a) is to make available mapping functions which can be used globally and implemented easily in existing geodetic data analysis softwares and which are consistent with NWM-based mapping functions, in particular with the VMF1 (Böhm et al. 2006b). Compared to the NMF (Niell 1996), the parameterization of the coefficients in the three-term continued fraction (Eq. 121) has been refined to include also a longitude dependence. Using global grids of monthly mean profiles for pressure, temperature, and humidity from the ECMWF 40 years reanalysis data (ERA40), the coefficients a_h and a_w were determined using data from the period September 1999 to August 2002 applying the same strategy and the same b and c coefficients used for VMF1. Thus, at each of the 312 grid points, 36 monthly a values were obtained for the hydrostatic and wet mapping functions, respectively. The hydrostatic coefficients were reduced to mean sea level by applying the height correction given by Niell (1996). The mean values, a_0, and the annual amplitudes, A, of the sinusoidal function (Eq. 126) were fitted to the a parameter time series of each grid point, with the phases referred to January 28, corresponding to the NMF. The standard deviations of the monthly values at the single grid points with respect to the values obtained from Eq. (126) increase from the equator towards larger latitudes, with a maximum value of 8 mm (expressed as equivalent station height error) in Siberia. For the wet component, the standard deviations are generally smaller, with the maximum values being about 3 mm at the equator Böhm et al. (2006a).

$$a = a_0 + A \cdot \cos\left(\frac{\text{doy} - 28}{365.25} \cdot 2\pi\right), \tag{126}$$

$$a_0 = \sum_{n=0}^{9} \sum_{m=0}^{n} P_{nm}(\sin\theta)(A_{nm}\cos(m\lambda) + B_{nm}\sin(m\lambda)). \tag{127}$$

Then, the global grid of the mean values a_0 and that of the amplitudes A for both the hydrostatic and wet coefficients of the continued fraction form were expanded into spatial spherical harmonic coefficients up to degree and order 9 (according to Eq. (127) for a_0) in a least-squares adjustment. The residuals of the global grid of a_0 and A values to the spherical harmonics are in the sub-millimeter range (in terms of station height). The hydrostatic and wet coefficients a for any site coordinates and day of year can then be determined using Eq. (126).

In Fig. 10 VMF1 and GMF hydrostatic mapping functions at 5° elevation angle are plotted for Fortaleza, Brazil. The GMF reflects a seasonal variability and, in this respect, agrees well with the VMF1. However, a deficiency is evident in the empirical mapping function compared to the VMF1 because GMF does not reveal

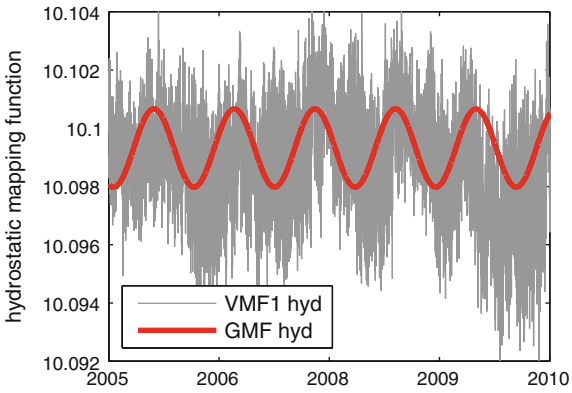

Fig. 10 Hydrostatic mapping functions VMF1 and GMF at 5° elevation at Fortaleza, Brazil. Phenomena such as the El Niño event in 2009 cannot be captured with empirical mapping functions like GMF that contain only average seasonal terms

the special meteorological conditions described by the VMF1 during the El Niño event in 2009/10.

Niell (2006) compared the mapping functions VMF1, IMF, GMF, and NMF with mapping functions derived from ray-tracing of radiosonde data in 1992, which were assumed to be the most accurate reference possible. The standard deviation was converted to station height scatter with the rule of thumb by Niell et al. (2001) (one third of the delay at 7° elevation angle). The best agreement was found for the VMF1, both for the hydrostatic and the wet mapping function. All hydrostatic mapping functions show the lowest scatter at the equator, because there are only small pressure and temperature variations. The scatter increases with station latitude, in particular for the empirical GMF and NMF, which of course cannot account for the variations at synoptic time scales (∼10 days). The situation is different for the wet mapping functions where the scatter is largest at the equator. This is due to the fact that the zenith wet delays are largest over the equator (up to 40 cm). At the poles, there is hardly any humidity; thus, errors in the wet mapping functions are not critical for the estimation of station heights (and zenith wet delays). Again, the performance of the wet VMF1 is best. However, it has to be mentioned here that the radiosonde data might have been assimilated in the NWM which are used to determine the VMF1 and IMF. Consequently the station height scatter for these two mapping functions may be too optimistic.

There have been many investigations comparing the application of different mapping functions in VLBI or GPS analysis. For example, Böhm et al. (2007) and Steigenberger et al. (2009) compared various mapping functions in GPS analysis, and Tesmer et al. (2007) compared them in VLBI analysis. Moreover, Kouba (2008) compared the gridded VMF1 against the VMF1 determined for specific sites, or Böhm et al. (2009b) assessed the accuracy of forecast VMF1 for the application in real time analysis.

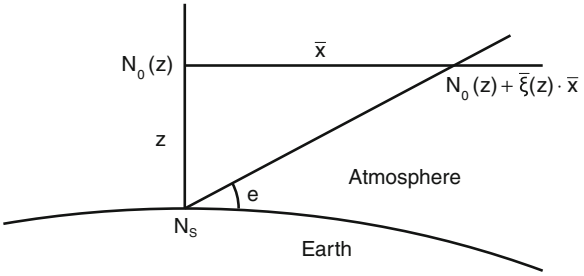

Fig. 11 The refractivity in the vicinity of the vertical profile above the site can be determined with the linear horizontal gradients of refractivity ξ

4.2.2 Azimuthal Asymmetry: Gradients

Mapping functions as described above allow for the modeling of path delays under the assumption of azimuthal symmetry of the neutral atmosphere around the station. Consequently, vertical refractivity profiles above the sites are sufficient to determine the path delays at arbitrary elevation angles or the mapping functions, respectively, because the refractivity is always taken from the vertical profile as it is the case for the VMF1. However, due to certain climatic and weather phenomena path delays will not be constant at varying azimuths. For example, at sites at northern latitudes the path delay towards south will be systematically larger than towards north, because the height of the troposphere above the equator is larger than above the poles.

In the following the derivation of linear horizontal gradients is shown following Davis et al. (1993). The Taylor series up to degree one for the refractivity at a station is (Fig. 11)

$$N(\mathbf{x}, z) = N_0(z) + \boldsymbol{\xi}(z) \cdot \mathbf{x}, \tag{128}$$

$$\xi_i(z) = \left. \frac{\partial N(\mathbf{x}, z)}{\partial x_i} \right|_{\mathbf{x}=0}. \tag{129}$$

$N_0(z)$ is the refractivity above the site, $\mathbf{x}$ is the horizontal position vector (origin is placed at the site), and $\boldsymbol{\xi}(z)$ is the linear horizontal gradient vector of refractivity at height z. The index i refers to the i-th component of $\mathbf{x}$: 1 towards north and 2 towards east. The path delay (hydrostatic or wet) at an arbitrary direction can be found by integration of Eq. (128) along the path s. If expressed with elevation angle e and azimuth angle a, we get

$$\Delta L(a, e) = 10^{-6} \int_0^\infty N(s)\, \mathrm{d}s = 10^{-6} \int_0^\infty N_0(z)\, \mathrm{d}s + 10^{-6} \int_0^\infty \boldsymbol{\xi}(z) \cdot \mathbf{x}\, \mathrm{d}s, \tag{130}$$

$$\Delta L(a, e) = \Delta L_0(e) + 10^{-6} \int_0^\infty \boldsymbol{\xi}(z) \cdot \mathbf{x}\, \mathrm{d}s, \tag{131}$$

where ΔL_0 is the delay without gradients. In Eq. (131) the difference between the paths with and without gradients has been neglected. Davis et al. (1993) state that this difference is as large as 1 mm for $N = 300$, $\partial N/\partial x_i = 1\ \mathrm{km}^{-1}$, and $e = 20°$. If the concept of an azimuth-dependent mapping function is used, Eq. (131) can be written as

$$\Delta L(a, e) = \Delta L^z \cdot mf(a, e), \tag{132}$$

with

$$mf(a, e) = mf_0(e) + \delta mf(a, e) = mf_0(e) + 10^{-6} \int_0^\infty \boldsymbol{\zeta}(z) \cdot \mathbf{x}\, \mathrm{d}s, \tag{133}$$

where

$$\boldsymbol{\zeta}(z) = \frac{\boldsymbol{\xi}(z)}{\Delta L^z}, \tag{134}$$

and mf_0 and ΔL^z are the mapping function and the path delay in zenith direction for the symmetric case. Thus, the gradients cause a change in the mapping function which can be described by an additional term δmf. With

$$\mathbf{x}(a, e) \approx z \cdot \cot(e')(\cos(a)\hat{\mathbf{n}} + \sin(a)\hat{\mathbf{e}}), \tag{135}$$

$$ds \approx \mathrm{d}z \cdot mf_0(e), \tag{136}$$

and normalized gradients of refractivity

$$\boldsymbol{\zeta}(z) = \zeta_n \cdot \hat{\mathbf{n}} + \zeta_e \cdot \hat{\mathbf{e}}, \tag{137}$$

and when $\hat{\mathbf{n}}$ and $\hat{\mathbf{e}}$ refer to the unit vectors in north and east direction and e' is the refracted elevation angle (which only differs from the geometric elevation angle at low elevations), we get

$$\delta mf(a, e) \approx 10^{-6} mf_0(e)\ \cot(e') \left(\cos(a) \int_0^\infty z \cdot \zeta_n(z) \cdot \mathrm{d}z + \sin(a) \int_0^\infty z \cdot \zeta_e(z) \cdot \mathrm{d}z \right), \tag{138}$$

and

$$\delta mf(a, e) = mf_0(e) \cot(e')(Z_n \cos(a) + Z_e \sin(a)), \tag{139}$$

when

$$\mathbf{Z} = 10^{-6} \int_0^\infty z \cdot \boldsymbol{\zeta}(z)\, \mathrm{d}z. \tag{140}$$

Equation (138) shows that the elevation-dependence of the azimuth-dependent mapping function $\delta mf(a, e)$ consists of two parts: the dependence on mf_0 and on the factor $\cot(e')$. As already mentioned the mapping functions are dependent on the geometric elevation angle e, whereas the cotangent depends on the refracted eleva-

tion angle e', because close to the site this angle determines the refraction. It holds that

$$e' = e + \delta e(e), \tag{141}$$

where δe can be described with (Davis et al. 1993)

$$\delta e \approx 10^{-6} N_S \cot(e). \tag{142}$$

N_S is the refractivity at the Earth surface, and for $N_S = 300$, $e = 5°$ we get $\delta e \approx 0.2°$. Since δe is small, $\cot(e')$ can be expanded into a series, and we get for the deviation from the symmetric mapping function

$$\delta mf(a, e) = mf_0(e) \cot(e)(1 - 10^{-6} N_S \csc^2(e))(Z_n \cos(a) + Z_e \sin(a)). \tag{143}$$

With the delay gradients (or just gradients) $\mathbf{G}$

$$\mathbf{G} = \mathbf{Z} \cdot \Delta L^z, \tag{144}$$

we get for the path delay

$$\Delta L(a, e) = \Delta L_0(e) + mf_0(e) \cot(e)(1 - 10^{-6} N_S \csc^2(e))(G_n \cos(a) + G_e \sin(a)). \tag{145}$$

The equations above can be used to determine gradients by integrating over the horizontal gradients of refractivity along the site vertical (see e.g. MacMillan and Ma (1997), Böhm and Schuh (2007))

$$G_a = 10^{-6} \int_0^\infty \xi_a \, z \, \mathrm{d}z, \tag{146}$$

where a denotes the azimuth direction (e.g. e or n). Figure 12 shows refractivity gradients at the site vertical for the station Fortaleza.

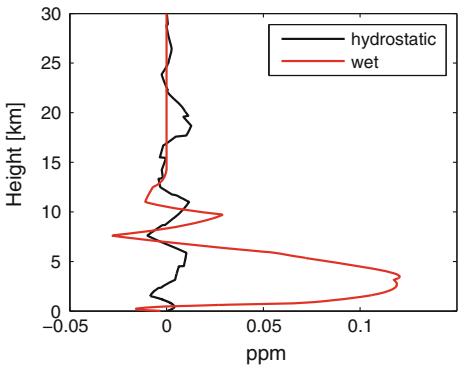

Fig. 12 Weighted (with height) refractivity gradients ($dN(z) \cdot z$) towards east at Fortaleza (Brazil) on 21 November 2011 at 0:00 UT. The *black line* shows the hydrostatic, the *red line* the wet gradients

In the following it is shown how gradients can be interpreted. Equation (128) can be written in the form

$$N(\mathbf{x}, z) = N_0(z)(1 + \boldsymbol{\alpha} \cdot \mathbf{x}), \tag{147}$$

$$\boldsymbol{\alpha} = \boldsymbol{\xi}(z)/N_0(z), \tag{148}$$

with the constant vector $\boldsymbol{\alpha}$. This means that the relative gradient of refractivity is constant, and we get for the gradient of the delay

$$\mathbf{G} = 10^{-6}\,\boldsymbol{\alpha} \int_0^\infty z\, N_0(z)\, \mathrm{d}z. \tag{149}$$

Supposing that refractivity decreases exponentially with height, i.e.

$$N_0(z) = N_S\, e^{-z/H}, \tag{150}$$

and H is the scale height, we get for the integral in Eq. (149) the expression

$$\mathbf{G} = 10^{-6}\boldsymbol{\alpha} \cdot N_S \cdot H^2, \tag{151}$$

and for the gradient of refractivity

$$\boldsymbol{\xi}(z) = 10^6 \frac{\mathbf{G}}{H^2} e^{-z/H}. \tag{152}$$

The scale height H is the height of the neutral atmosphere (or of a part of it) if the density is constant with height and the total mass is conserved. For the gradients of refractivity at the Earth surface we get

$$\boldsymbol{\xi}(z) = 10^6 \frac{\mathbf{G}}{H^2}. \tag{153}$$

This shows that for a given value of $\mathbf{G}$ the gradients of refractivity $\boldsymbol{\xi}$ are inversely proportional to the squared scale heights H. A typical value for the gradients $\mathbf{G}$ is 1 mm. This corresponds to a path delay of ≈65 mm at 7° elevation. Assuming a scale height H of 1 km the gradient of refractivity $\boldsymbol{\xi}$ is $1\,\mathrm{km}^{-1}$. With a scale height of 8 km $|\boldsymbol{\xi}| = 0.015\ \mathrm{km}^{-1}$. Hydrostatic atmospheric gradients which are caused by pressure and temperature gradients, have a large spatial resolution of about 100 km (Gardner 1976) and a temporal resolution of hours to days. Wet gradients have a small spatial resolution (<10 km) and they can vary at hourly time scales or faster, although longer time scales are also possible (e.g. at coastal regions). Wet gradients are functions of water vapor pressure and temperature.

Presently, two models for the gradients are used in the analysis of space geodetic techniques. These are the model by MacMillan (1995) that follows Davis et al. (1993) and the model by Chen and Herring (1997). Both concepts will be described below.

Furthermore, it is shown that the concept of horizontal gradients corresponds to a tilting of the mapping functions. This is used by Niell (2001) who uses the tilting of the 200 hPa pressure level to get hydrostatic gradients. MacMillan (1995) proposes to use the simple model

$$\Delta L(a, e) = \Delta L_0(e) + mf_h(e)\cot(e)(G_n \cos(a) + G_e \sin(a)), \tag{154}$$

i.e. the difference between e and e' is neglected. Chen and Herring (1997) use the gradient model

$$\Delta L(a, e) = \Delta L_0(e) + mf_g(e)(G_n \cos(a) + G_e \sin(a)), \tag{155}$$

$$mf_g(e) = \frac{1}{\sin(e)\tan(e) + C}, \tag{156}$$

and

$$C = \frac{3\int \xi \cdot z^2 \cdot \mathrm{d}z}{2\int \xi \cdot z \cdot (z + R_e) \cdot \mathrm{d}z}. \tag{157}$$

After integration they get for the coefficient C

$$C = 3H/R_e. \tag{158}$$

For scale heights of 6.5 km for the hydrostatic part and 1.5 km for the wet part of the neutral atmosphere, they find the values 0.0031 and 0.0007 for the hydrostatic and wet coefficients C, respectively. For the estimation of total gradients, Herring (1992) suggests using 0.0032.

Gradients can also be interpreted by a tilting of the mapping function (Rothacher et al. 1998) see Fig. 13. The basic relations are shown below assuming that the atmosphere is flat (mapping function $1/\sin(e)$) and that the path delay in zenith direction is not changed by the tilting. If the gradient G is the deflection of the path

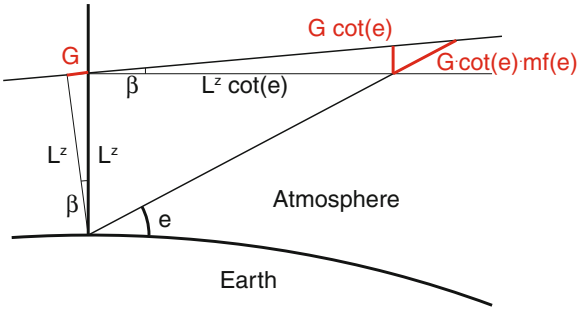

Fig. 13 Tilting of the mapping function by the angle β assuming a horizontally stratified atmosphere

delay in zenith direction due to the tilting angle β, it is shown that the path delay at the elevation angle e due to the gradients is $\cot(e)mf(e)G$, which is exactly what is proposed by MacMillan (1995). Starting with

$$\Delta L(e-\beta) = \Delta L^z \cdot mf(e-\beta) \approx \Delta L^z \left(mf(e) + \frac{\partial mf}{\partial e}(-\beta) \right), \tag{159}$$

and using $1/\sin(e)$ as mapping function and with

$$\beta = G/L^z, \tag{160}$$

we get

$$\Delta L(e-\beta) = \Delta L^z \cdot mf(e) + \cot(e)mf(e)G. \tag{161}$$

A gradient G of 1 mm corresponds to tilting angles of 1.5' (hydrostatic) and 17' (wet). The effects on the zenith delays are $2 \cdot 10^{-4}$ and $2 \cdot 10^{-5}$ mm, respectively, and can be neglected.

It is important to estimate gradients in the analysis of space geodetic observations, in particular when observing at low elevation angles. On the other hand, there is no need to apply a priori gradients if no constraints are applied on the estimation of gradients.

4.3 Atmospheric Delays for SLR

4.3.1 Single-Color SLR Observations

The accuracy of the results obtained from Satellite Laser Ranging (SLR) measurements is ultimately limited by the atmospheric propagation effects (as well as by by the hardware system). In the 1970s, Marini and Murray (1973) developed a model to correct the atmospheric delays in SLR measurements and their model became a standard correction model at that time. In the early 2000s, Mendes et al. (2002) pointed out some limitation in that model, namely as regards the modeling of the elevation dependency of the zenith atmospheric delays (the mapping function component of the model). Thus, Mendes et al. (2002) developed their mapping functions (FCULa and FCULb) that represents significant improvement over the mapping functions of the Marini-Murray model. Of particular interest is the ability of the new mapping functions to be used in combination with any zenith delay model, i.e. Mendes and Pavlis (2004) model, used to predict the atmosphere delay in the zenith direction.

Similar to the microwave frequencies, the mapping functions are normally modeled using Eq. (121). New mapping functions have been developed based on ray-tracing through one full year (1999) of radiosonde data from 180 stations, globally distributed, with a variable number of balloon launches per day. Two different parameterizations were proposed by Mendes et al. (2002) with the coefficients in Eq. (121)

written as functions of the selected parameters. One parameterization of the mapping function (FCULa) requires both site location and meteorological (surface temperature) data. The coefficients of the mapping function have the following mathematical formulation

$$a = a_0 + a_1\ T_0 + a_2\ \cos\theta + a_3\ h_0, \tag{162}$$

where T_0 is the temperature at the station in degrees centigrade, θ is the station latitude, and h_0 is the orthometric height of the station, in meters. The coefficients b and c are modeled similarly.

The second parameterization (FCULb) does not depend on any meteorological data, i.e. similar to the model developed by Niell (1996) for radio wavelengths. For this function, the coefficients have the following form

$$a = a_0 + (a_1 + a_2\ \theta_d^2)\cos\left(\frac{2\pi}{365.25}\ (\text{doy} - 28)\right) + a_3\ h_0 + a_4\ \cos\theta, \tag{163}$$

where θ_d is the latitude of the station, in degrees, and doy is the decimal day of year (UTC day since the beginning of the year). The coefficients in Eq. (163) are different with those in Eq. (122) as the later one is derived based on microwave refractivity index, which is independent on frequency.

These mapping functions along with the zenith delay model of Mendes and Pavlis (2004) have become the standard model for correcting SLR measurements. Comparing to the previously used mapping functions, the advantages of the new mapping functions are obvious. They represent simpler expressions than those proposed by the Marini and Murray (1973) model and allow the use of better zenith delay models. The coefficients of the mapping functions are presented in Table 6.

The latest progress in atmospheric corrections for single-color SLR is provided by Hulley and Pavlis (2007) who applied a ray-tracing technique to calculate propagation effects, including the effects of horizontal refractivity gradients. The use of ray-tracing trough numerical weather models has been shown to improve the accuracy of the SLR results.

4.3.2 Two-Color SLR Observations

The alternative to modeling is the application of two-color (i.e. two-frequency) SLR measurements for the direct computation of the propagation delay by utilizing the fact that the neutral atmosphere is dispersive for optical frequencies. The dispersion causes the optical path lengths at two different frequencies to differ. This difference depends on the two frequencies and is proportional to the path integrated atmospheric density. Thus, the difference between the two optical paths can be used for calculating the propagation delays (Wijaya and Brunner 2011). This method has the potential to improve the accuracy of SLR results (Abshire and Gardner 1985).

Based on the previous works of Prilepin (1957) and Bender and Owens (1965), Abshire and Gardner (1985) developed an atmospheric correction formula for the

Table 6 Coefficients (a_i, b_i, and c_i) for FCULa and FCULb mapping functions (Mendes et al. 2002)

	FCULa	FCULb
a_0	$(12100.8 \pm 1.9) \times 10^{-7}$	$(11613.1 \pm 1.6) \times 10^{-7}$
a_1	$(1729.5.8 \pm 4.3) \times 10^{-9}$	$(-933.8 \pm 9.7) \times 10^{-8}$
a_2	$(319.1 \pm 3.1) \times 10^{-7}$	$(-595.8 \pm 4.1) \times 10^{-11}$
a_3	$(-1847.8 \pm 6.5) \times 10^{-11}$	$(-2462.7 \pm 6.8) \times 10^{-11}$
a_4	–	$(1286.4 \pm 2.2) \times 10^{-7}$
b_0	$(30496.5 \pm 6.6) \times 10^{-7}$	$(29814.1 \pm 4.5) \times 10^{-7}$
b_1	$(234.6 \pm 1.5) \times 10^{-8}$	$(-56.9 \pm 2.7) \times 10^{-7}$
b_2	$(-103.5 \pm 1.1) \times 10^{-6}$	$(-165.5 \pm 1.1) \times 10^{-10}$
b_3	$(-185.6 \pm 2.2) \times 10^{-10}$	$(-272.5 \pm 1.9) \times 10^{-10}$
b_4	–	$(302.0 \pm 5.9) \times 10^{-7}$
c_0	$(6877.7 \pm 1.2) \times 10^{-5}$	$(68183.9 \pm 9.1) \times 10^{-6}$
c_1	$(197.2 \pm 2.8) \times 10^{-7}$	$(93.5 \pm 5.4) \times 10^{-6}$
c_2	$(-345.8 \pm 2.0) \times 10^{-5}$	$(-239.4 \pm 2.3) \times 10^{-9}$
c_3	$(106.0 \pm 4.2) \times 10^{-9}$	$(30.4 \pm 3.8) \times 10^{-9}$
c_4	–	$(-230.8 \pm 1.2) \times 10^{-5}$

two-color SLR measurements (the 2C-SLR formula). This formula was later studied by several investigators (Greene and Herring 1986).

From the two-color SLR measurements theoretical path lengths $\mathscr{R}_1$ and $\mathscr{R}_2$ are obtained (assume that the system measures simultaneously individual optical paths). With the 2C-SLR formula (Abshire and Gardner 1985), the chord (straight line) distance σ can be calculated by adding the term $\mu(\mathscr{R}_2 - \mathscr{R}_1)$ to $\mathscr{R}_1$

$$\sigma = \mathscr{R}_1 + \mu(\mathscr{R}_1 - \mathscr{R}_2), \tag{164}$$

where

$$\mu = \frac{k(\nu_1)}{k(\nu_2) - k(\nu_1)}, \tag{165}$$

with $k(\nu_i)$ being the dispersion factor. This factor depends on frequency and can be calculated using (Edlén 1966; Abshire and Gardner 1985)

$$k(\nu_i) = 0.9650 + \frac{0.0164}{\lambda_i^2} + \frac{0.000228}{\lambda_i^2}, \tag{166}$$

where λ_i is the i:th wavelength in meters.

The 2C-SLR formula presented in Eq. (164) remove the largest part of the total propagation delay, namely that associated with the dry atmospheric density. However, the water vapor density and curvature effects still remain (Abshire and Gardner 1985;

Greene and Herring 1986). At optical frequencies, water vapor contributes only about 1 % of the refractivity, however, since it is highly variable and it can introduce substantial errors. By using ray-tracing through atmospheric profiles, Wijaya and Brunner (2011) showed that the zenith wet delay can be several millimeters for SLR measurements. Furthermore, the magnitude of the bending effects could reach a few centimeters for measurements taken at an elevation angle of 10°.

The precision required for the range difference $(\mathscr{R}_1 - \mathscr{R}_2)$ measurements is very stringent (few micrometers), which is mainly due to amplification of the measurement noise by the scaling factor μ (Abshire and Gardner 1985; Greene and Herring 1986). This requirement cannot currently be achieved. However, if in the future the range difference measurements could be improved to reach the required precision, the two-color SLR system would be an interesting way of reduce atmospheric propagation effects.

In order to anticipate possible future development of the two-color SLR systems, Wijaya and Brunner (2011) have developed a new correction formula that can be seen as an extension of the 2C-SLR formula

$$\sigma = \mathscr{R}_1 + \mu(\mathscr{R}_1 - \mathscr{R}_2) + (\nu P_{21} - \kappa_1) + H_{21} \cdot \text{SIWV}. \tag{167}$$

The power of dispersion μ is given by

$$\mu = \frac{\tilde{k}_d(\nu_1)}{\tilde{k}_d(\nu_2) - \tilde{k}_d(\nu_1)}, \tag{168}$$

and the water vapor factor is

$$H_{21} = 10^{-6}\tilde{k}^{\star}_w(\nu_1)\nu\, K, \tag{169}$$

where $K = \left(\frac{\tilde{k}^{\star}_w(\nu_2)}{\tilde{k}^{\star}_w(\nu_1)} - \frac{\tilde{k}_d(\nu_2)}{\tilde{k}_d(\nu_1)}\right)$. The slant integrated water vapor (SIWV) is

$$\text{SIWV} = \int_{S_1} \rho_v(\mathbf{r}_1)\, \mathrm{d}s_1. \tag{170}$$

The formula in Eq. (167) eliminates the total atmospheric density effect including its gradient and provides two terms to calculate the water vapor and the curvature effects. The dispersion effect (contained in the second term in Eq. (167)) can be obtained from the observed optical path length difference $(\mathscr{R}_1 - \mathscr{R}_2)$. The third term represents the curvature effect of the ray path S_1 and the propagation corrections from S_2 to S_1. The last term represents the effects of the water vapor density. The constant μ represent the power of the dispersion effects and the constant H_{21} is the scaling factor for the wet delays. Both of these coefficients only dependent on the frequencies of the optical signals and can be calculated using Eqs. (168) and (169). The new formula, Eq. (167), is a general expression for the atmospheric correction

of two-color SLR measurements. When the water vapor and the curvature effects are neglected, the new formula reduces to the 2C-SLR formula, Eq. (164). Further detail of this new formula can be found in Wijaya and Brunner (2011).

4.4 Water Vapor Radiometry

A Water Vapor Radiometer (WVR) is an instrument that can be used to estimate the atmospheric wet delay. It does this by measuring the thermal radiation from the sky at microwave frequencies where the atmospheric attenuation due to water vapor is relatively high. These measurements can then be related to the wet delay.

Equation (9) describes the attenuation of radio signals caused by the atmosphere. The attenuation will depend upon frequency, as well as on temperature, pressure, humidity, and liquid water content. For details about how α can be modeled as function of these quantities, see e.g. Liebe et al. (1993) and Rosenkranz (1998).

Normally the radiation power from the sky is expressed using the brightness temperature T_B, which is defined as the physical temperature a black body would have if it radiates the same amount of power as the sky. For low frequencies T_B is related to W_{sky} by

$$W_{sky}(\nu) = k_b\, T_B(\nu)\, B, \tag{171}$$

where k_b is Bolzmann's constant and B the observed bandwidth. This relation is valid for frequencies $\nu \ll k_b T/h$, where h is Planck's constant. This requirement is fulfilled at microwave frequencies for normal atmospheric conditions.

The brightness temperature can be calculated from the equation of radiative transfer

$$T_B(\nu) = T_{bg}\, e^{-\tau(\infty,\nu)} + \int_S T(s)\, \alpha(s,\nu)\, e^{-\tau(s,\nu)}\, \mathrm{d}s, \tag{172}$$

where T_{bg} is the brightness temperature of the cosmic microwave background ($\approx$2.7 K). The opacity $\tau(s,\nu)$ is given by

$$\tau(s,\nu) = \int_0^s \alpha(s',\nu)\, \mathrm{d}s'. \tag{173}$$

T_B depends upon the pressure, temperature, humidity, and liquid water density profiles. The dependencies on these quantities will vary with frequency; for some frequencies (e.g. close to the center of a water vapor absorption line like 22.235 or 183 GHz) there will be a high sensitivity to water vapor while other frequencies (e.g. close to the center of the oxygen absorption lines around 60 and 120 GHz) are more sensitive to the pressure and temperature. For good sensitivity to these parameters, the attenuation needs to be high but not too high. If the attenuation is too high the brightness temperature will approach the physical temperature of the atmosphere, thus the sensitivity to the atmospheric properties will be lost. For retrieval of the

water vapor content the frequencies close to the 22.235 GHz line are normally the most suitable ones since this line is not too strong. For very dry conditions (e.g. high altitudes) higher frequencies (e.g. 183 GHz) will give higher sensitivity, however for normal conditions the attenuation is too high.

The sensitivity to the different atmospheric quantities also varies with height, e.g. some frequencies have a higher sensitivity to humidity close to the ground (frequencies on the edge of a water vapor absorption line) while others are more sensitive to the humidity at high altitudes (frequencies close to a water vapor absorption line). Thus it is in principle possible to estimate the humidity profile using radiometer measurements at several different frequencies having different sensitivity to humidity with height, a so-called radiometric profiler (Askne and Westwater 1986; Scheve and Swift 1999). This humidity profile could then be taken to calculate the tropospheric delay. However, the need for using many channels makes the radiometric profilers expensive, and it is difficult to find a set of frequencies from which the humidity profile can be estimated without running into any singularity problems. Furthermore, if only the integrated amount of water vapor—or the wet delay—is of interest we do not necessarily need to know the profile. If a frequency can be found where the sensitivity to the refractivity is constant with height, this is sufficient.

Normally the brightness temperature is not used directly to estimate the wet delay. Instead the opacity $\tau(\infty, \nu)$ is calculated from the brightness temperature, which is then used for the wet delay estimation. By introducing the effective temperature of the atmosphere T_{eff}

$$T_{eff}(\nu) = \frac{\int_S T(s)\,\alpha(s,\nu)\,e^{-\tau(s,\nu)}\,\mathrm{d}s}{\int_S \alpha(s,\nu)\,e^{-\tau(s,\nu)}\,\mathrm{d}s}, \tag{174}$$

we can write T_B as

$$T_B(\nu) = T_{bg}\,e^{-\tau(\infty,\nu)} + T_{eff}(\nu)\left(1 - e^{-\tau(\infty,\nu)}\right). \tag{175}$$

Thus the opacity can be estimated by

$$\tau(\infty,\nu) = -\ln\left[\frac{T_{eff} - T_B}{T_{eff} - T_{bg}}\right]. \tag{176}$$

Some WVR retrieval algorithms to estimate the wet delay from τ directly (Westwater et al. 1989; Bosisio and Mallet 1998). However, this requires that the effective temperature T_{eff} is accurately estimated. An alternative way is to use the linearized brightness temperature T_B' (Wu 1979)

$$T_B'(\nu) = T_{bg}\,[1 - \tau(\infty,\nu)] + \int_S T(s)\,\alpha(s,\nu)\,\mathrm{d}s. \tag{177}$$

The linearized brightness temperature can be calculated from the opacity by

$$T'_B(\nu) = T_{bg} + \left(T'_{eff}(\nu) - T_{bg}\right)\tau(\infty, \nu), \tag{178}$$

where the linearized effective temperature T'_{eff} is given by

$$T'_{eff}(\nu) = \frac{\int_S T(s)\,\alpha(s, \nu)\,\mathrm{d}s}{\tau(\infty, \nu)}. \tag{179}$$

If T_{eff} and T'_{eff} are consistently modeled, the error in T'_B caused by an error in T_{eff} will be approximately canceled by the error in T'_{eff}. Thus the linearized brightness temperature can normally be estimated with higher accuracy than the opacity.

The linearized brightness temperature can be divided into four parts

$$T'_B(\nu) = T_{bg} + T'_{wv} + T'_{lw} + T'_{ox}, \tag{180}$$

where T'_{wv}, T'_{lw}, and T'_{ox} are the contributions from water vapor, liquid water, and oxygen, respectively. T_{bg} is constant and well known. The oxygen part can be accurately modeled using measurements of the surface pressure and temperature (Jarlemark 1997), while the liquid water contribution is approximately proportional to the frequency squared (if the water droplets are much smaller than the wavelength). If the frequencies are properly chosen, T'_{wv} is proportional to the wet delay. Thus the wet delay can be estimated by a combination of measurements at two different frequencies ν_1 and ν_2

$$\Delta L_w = c_b \left[\left(\frac{\nu_2}{\nu_1}\right)^2 T'_B(\nu_1) - T'_B(\nu_2) - T_{bg,ox} \right], \tag{181}$$

where $T_{bg,ox}$ is the contribution from oxygen and the cosmic microwave background.

For the estimation of the wet delay we need to know the retrieval coefficient c_b, as well as $T_{bg,ox}$, T_{eff}, and T'_{eff}. Normally these parameters are modeled as functions of the surface pressure, temperature, and humidity. To model c_b, one can use WVR measurements and simultaneous observations of the wet delay made by another instruments. Then the model coefficients can be obtained by fitting the radiometer observations to the wet delay observations. The disadvantage of this method is that it requires a long time series of measurements, ideally longer than one year in order to be able to take seasonal variations into account. Furthermore, any systematic error in the wet delay measurements will cause systematic errors in the retrieval coefficient. A more commonly used method is to use profiles of pressure, temperature and humidity obtained from e.g. radiosondes to calculate the theoretical values of T'_B, $T_{bg,ox}$, T_{eff}, T'_{eff}, and ΔL_w. These can then be used to estimate appropriate models for the parameters. For details, see e.g. Elgered (1993) and Jarlemark (1997).

Several studies have been performed where WVRs have been used to correct for the wet tropospheric delays in space geodetic (mostly VLBI) data analysis. Examples of such studies are Elgered et al. (1991), Kuehn et al. (1991), Ware et al. (1993),

Emardson et al. (1999) and Nothnagel et al. (2007). The results indicate that the accuracy of the VLBI estimates can be improved if WVRs are used to calibrate the tropospheric delay compared to the normal method of estimating the tropospheric delay as function in the data analysis (see Sect. 4.2), although the results are inconclusive. It should be noted that the WVR calibration was only applied at a few sites since most VLBI stations are not equipped with radiometers. One problem with radiometers is that they cannot be used during rain for several reasons (liquid water on radiometer antenna, saturation problems, water droplets may not be "small", …). Furthermore, most radiometer antennas have relatively large beam-widths (several degrees), and thus the observations are limited to high elevation angles (>15–20°) in order to avoid picking up radiation from the ground. Hence, either VLBI observations made at low elevation angles have to be excluded, or the WVR measurements need to be extrapolated to low elevation angles, which is a process that can introduce errors.

5 Atmospheric Turbulence

The normal modeling of atmospheric delays in space geodesy, i.e. using mapping functions and horizontal gradients assumes that the spatial variations in the refractivity are linear, and that the temporal variations can be described by e.g. piece-wise linear functions. For the large-scale variations this is an adequate approximation, however at small scales there are non-linear variations caused by atmospheric turbulence. Although it is normally impossible to correct for these random fluctuations, it can be important to model them in order to minimize their effect on the results.

Atmospheric turbulence occurs when energy from e.g. wind shears and temperature gradients creates turbulent eddies. These eddies then break down into smaller eddies until at very small scales the energy of the eddies are dissipated into heat. Inside each eddy the air is mixed, and thus large-scale variations in any atmospheric quantity, e.g. refractivity, will be mixed to create random small-scale variations.

A turbulent eddy with a size R will have a characteristic wind velocity v. Kolmogorov (1941a, b) assumed that the rate of which kinetic energy (per unit mass) of an eddy is transferred to smaller eddies is only dependent on R and v. By dimensional analysis it is clear that this rate must be proportional to v^3/R. For stationary turbulence the kinetic energy for the eddies of a specific size will be constant, i.e. the kinetic energy received from larger eddies must be equal to the energy lost to smaller scale eddies (assuming no dissipation into heat at larger scale). At small scales the kinetic energy is dissipated into heat with a dissipation rate ε, which thus must be equal to the kinetic energy rate of all larger eddies. Thus $v \propto \varepsilon^{1/3} R^{1/3}$, or equivalently that the structure function for the velocity fluctuations between $\mathbf{r}$ and $\mathbf{r} + \mathbf{R}$ is given by

$$D_v(\mathbf{R}) = \left\langle [\mathbf{v}(\mathbf{r}) - \mathbf{v}(\mathbf{r} + \mathbf{R})]^2 \right\rangle = C_v^2 \varepsilon^{2/3} \, \|\mathbf{R}\|^{2/3} \,, \tag{182}$$

where C_v is the velocity structure constant.

It can be shown that the structure functions for other atmospheric variables, like the temperature and the refractive index, are similar (i.e. also proportional to $\|\mathbf{R}\|^{2/3}$). Thus the fluctuations in refractive index between two locations, $\mathbf{r}$ and $\mathbf{r}+\mathbf{R}$, can be described by the structure function $D_n(\mathbf{R})$

$$D_n(\mathbf{R}) = \left\langle [n(\mathbf{r}) - n(\mathbf{r}+\mathbf{R})]^2 \right\rangle = C_n^2 \, \|\mathbf{R}\|^{2/3} . \tag{183}$$

The constant C_n^2 is called the refractive index structure constant. This equation is however not valid for large scales since it becomes infinite when the distance approaches infinity, which is unrealistic. In order to fix this problem, Treuhaft and Lanyi (1987) modified the expression by introducing a saturation length scale L

$$D_n(\mathbf{R}) = \left\langle [n(\mathbf{r}) - n(\mathbf{r}+\mathbf{R})]^2 \right\rangle = C_n^2 \frac{\|\mathbf{R}\|^{2/3}}{1 + \left[\dfrac{\|\mathbf{R}\|}{L} \right]^{2/3}} . \tag{184}$$

With this expression $D_n(\mathbf{R})$ will converge to $C_n^2 L^{2/3}$ as $\|\mathbf{R}\|$ goes to infinity.

Turbulence does not only cause spatial variations in the refractive index, but also temporal variations. One way to describe the temporal variations is to assume Taylor's frozen flow hypothesis (Taylor 1938). In this hypothesis the turbulent variations in the refractive index in the atmosphere are frozen and move with the wind velocity $\mathbf{v}$, i.e. it is assumed that $n(\mathbf{r}, t) = n(\mathbf{r} - \mathbf{v}(t - t_0), t_0)$. This is an approximation which works well over shorter time periods but may not be valid over longer time periods (hours, days). By using Taylor's frozen flow hypothesis the temporal variations in the refractive index over a time period T can be d escribed by the structure function $D_n(T)$

$$D_n(T) = \left\langle [n(t) - n(t+T)]^2 \right\rangle = C_n^2 \frac{[\|\mathbf{v}\| \, T]^{2/3}}{1 + \left[\dfrac{\|\mathbf{v}\| \, T}{L} \right]^{2/3}} . \tag{185}$$

By combining Eqs. (184) and (185) we get a general expression for the structure function for the fluctuations in the refractive index between $\mathbf{r}_1$ at time t_1 and $\mathbf{r}_2$ at time t_2

$$D_n(\mathbf{r}_1, t_1; \mathbf{r}_2, t_2) = \left\langle [n(\mathbf{r}_1, t_1) - n(\mathbf{r}_2, t_2)]^2 \right\rangle = C_n^2 \frac{[\|\mathbf{r}_1 - \mathbf{r}_2 - \mathbf{v}(t_1 - t_2)\|]^{2/3}}{1 + \left[\dfrac{\|\mathbf{r}_1 - \mathbf{r}_2 - \mathbf{v}(t_1 - t_2)\|}{L} \right]^{2/3}} . \tag{186}$$

5.1 Turbulence Effects on Tropospheric Delays

For the modeling of the effects of turbulence on tropospheric delays we make two assumptions. First that the geometric optics approximation is still valid, i.e. that the turbulent variation within one wavelength can be ignored. Furthermore, we assume that there is no effect on the propagation path of the signal. Both these assumption can be considered approximately valid for weak turbulence. For the case of very strong turbulence more advanced considerations need to be made, see e.g. Tatarskii (1971) and Ishimaru (1978).

The fluctuations in the refractive index will cause variations in the atmospheric delays of radio signals; both in time and as function of direction and location. When describing these fluctuations it is convenient to work with the *Equivalent Zenith Tropospheric Delay* (EZTD) instead of the slant delays. The EZTD ΔL^z is the slant tropospheric delay divided by a symmetric mapping function *mf*

$$\Delta L^z(e,a,t) = \frac{\Delta L(e,a,t)}{mf(e)} = \int_0^\infty [n(\mathbf{r}(z),t) - 1]\, \mathrm{d}z, \tag{187}$$

where e is the elevation angle, a is the azimuth angle, and $\mathbf{r}(z)$ denotes the position of the ray at height z.

The structure function between two EZTD, observed at two different times in two different directions and possibly from two different locations, can be calculated by:

$$\begin{aligned} D_L &= \left\langle \left[\Delta L_1^z - \Delta L_2^z\right]^2 \right\rangle \qquad (188)\\ &= \left\langle \left(\int_0^\infty [n(\mathbf{r}_1(z),t_1) - 1]\, \mathrm{d}z - \int_0^\infty [n(\mathbf{r}_2(z),t_2) - 1]\, \mathrm{d}z \right)^2 \right\rangle \\ &= \int_0^\infty \int_0^\infty \Big[\left\langle n(\mathbf{r}_1(z),t_1)\, n(\mathbf{r}_1(z'),t_1) \right\rangle + \left\langle n(\mathbf{r}_2(z),t_2)\, n(\mathbf{r}_2(z'),t_2) \right\rangle \\ &\qquad \left\langle n(\mathbf{r}_1(z),t_1)\, n(\mathbf{r}_2(z'),t_2) \right\rangle + \left\langle n(\mathbf{r}_2(z),t_2)\, n(\mathbf{r}_1(z'),t_1) \right\rangle \Big]\, \mathrm{d}z\, \mathrm{d}z' \,. \end{aligned}$$

Using the relation $A \cdot B = 0.5(A^2 + B^2 - (A-B)^2$, this simplifies to

$$\begin{aligned} D_L = \int_0^\infty \int_0^\infty \Big[& D_n(\mathbf{r}_1(z),t_1;\mathbf{r}_2(z'),t_2) - \frac{1}{2} D_n(\mathbf{r}_1(z),t_1;\mathbf{r}_1(z'),t_1) \qquad (189)\\ & - \frac{1}{2} D_n(\mathbf{r}_2(z),t_2;\mathbf{r}_2(z'),t_2) \Big]\, \mathrm{d}z\, \mathrm{d}z'. \end{aligned}$$

With the expression for D_n given by Eq. (186), the structure function D_L can be calculated.

Figure 14 shows the structure function $D_L(\rho)$ for spatial variations in the zenith wet delay as function of the distance ρ. In the calculations it was assumed that $C_n^2 = 1 \cdot 10^{-14}\ \mathrm{m}^{-2/3}$ up to a height of $H = 2$ km and zero above, and $L = 3000$ km.

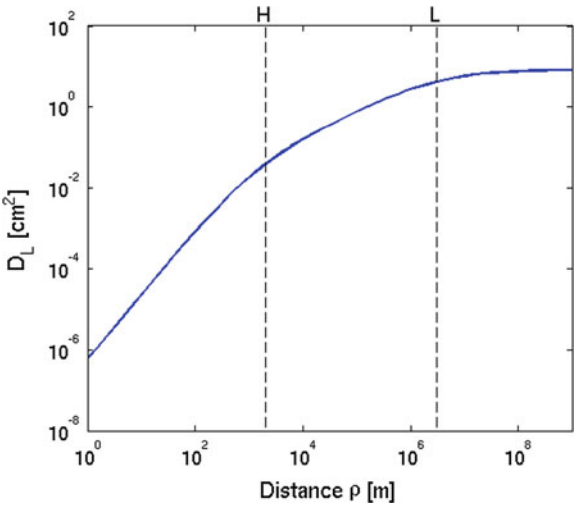

Fig. 14 The spatial structure function D_L (Eq. 186) for the zenith wet delay

We can here note three regions: for $\rho \ll H$ we have $D_L(\rho) \propto \rho^{5/3}$, for $H \ll \rho \ll L$ we have $D_L(\rho) \propto \rho^{2/3}$, and for $\rho \gg L$ we $D_L(\rho) \approx C_n^2 H^2 L^{2/3}$ (i.e. constant).

From he structure function D_L the covariance matrix for the turbulent fluctuations in the tropospheric delay can be calculated. This can then be applied to weight the observations in the estimation procedure. For more details, see e.g. Treuhaft and Lanyi (1987). It is also possible to use D_L for simulating tropospheric delays, see e.g. Nilsson and Haas (2010).

5.2 Estimating C_n^2

In order to calculate the structure function D_L the profile of the structure constant C_n^2 needs to be known. This parameter is highly variable, both in time and between different locations. Several methods to determine C_n^2 exist, see Nilsson and Haas (2010) for a review of some of them.

One way to determine C_n^2 is to use observations of variations in the tropospheric delay. For example, C_n^2 can be estimated from the observed variations of the tropospheric delay between different directions (Nilsson et al. 2005) or between different locations (Treuhaft and Lanyi 1987). Here we describe how to estimate C_n^2 from observations of the zenith delay variance over a time period T

$$\sigma_L^2(T) = \left\langle \frac{1}{T} \int_0^T \left[\Delta L^z(t + t_0) - \frac{1}{T} \int_0^T L^z(t' + t_0)\, \mathrm{d}t' \right]^2 \mathrm{d}t \right\rangle. \tag{190}$$

After some calculations, it can be shown that (Treuhaft and Lanyi 1987)

$$\sigma_L^2(T) = \frac{1}{T^2} \int_0^T (T - t)\, D_L(t)\, \mathrm{d}t. \tag{191}$$

In order to estimate C_n^2 using observations of σ_L^2 we need to know the shape of the C_n^2 profile. When we want to estimate a C_n^2 that can be used for calculating D_L it is however not critical to know the exact shape of the profile, most important is then that the integrated value of C_n^2 is correct. Thus we can for example make the approximation that C_n^2 has an exponential profile or, even more simple, assume that C_n^2 is constant up to a height H and zero above as done by Treuhaft and Lanyi (1987). Using the latter approximation, C_n^2 at heights lower than H can be calculated from

$$C_n^2 = \frac{\sigma_L^2(T)}{\int_0^T (T - t) \int_0^H \int_0^H \left\{ \left[(z - z')^2 + (v\, t)^2 \right]^{1/3} - |z - z'|^{2/3} \right\} \mathrm{d}z\, \mathrm{d}z'\, \mathrm{d}t}. \tag{192}$$

The height H should be chosen such that the largest fluctuations in the refractive index occur below H. For microwaves where the fluctuations in the wet delay is dominating an appropriate choice is the scale height of water vapor (approximately 2 km).

Another possible way to obtain C_n^2 is to use vertical profiles of pressure, temperature, and humidity obtained from e.g. radiosonde measurements. As discussed above, when turbulence is present, large-scale variations (gradients) in the atmosphere are mixed and create small-scale fluctuations. Thus there will be variations caused by both the large-scale gradients as well as turbulence. At large scales the variations due to gradients will dominate, and at small scales turbulence. At some scale in between the magnitudes of the large-scale gradients and by turbulence will be equal. This scale is proportional to the so-called *outer scale of turbulence* L_0. Typically values of L_0 range between a few meters to several hundreds of meters. The value can vary with time, but for the calculations of C_n^2 typically a mean value is used (d'Auria et al. 1993). Hence

$$C_n^2\, L_0^{2/3} \propto \|\nabla n\|^2\, L_0^2. \tag{193}$$

Thus C_n^2 could be calculated from the gradient in n. Since the gradient of the refractive index is typically more than one order of magnitude larger in the vertical direction than in the horizontal direction, we can approximate the refractive index gradient by its vertical component. However, one problem that needs to be considered is that the refractive index is not conserved in adiabatic motion in the atmosphere. When an air parcel is moved up or down in the atmosphere (e.g. due to turbulence) its size will change due to the change of atmospheric pressure with height. This in turn will cause the temperature and partial pressure of water vapor—and thus also the refractivity—to change. This needs to be corrected for when calculating C_n^2. The way to do this is to consider the vertical gradient in the refractive index caused by vertical gradients in quantities conserved under adiabatic motion in the atmosphere, e.g. the potential

temperature θ and the specific humidity q

$$\theta = T\left(\frac{p_0}{p}\right)^{0.286}, \tag{194}$$

$$q = \frac{p_w}{1.62p}, \tag{195}$$

where p_0 =1000 hPa. Thus C_n^2 can be calculated as

$$C_n^2 = a^2 L_0^{4/3}\left[\frac{\partial n}{\partial \theta}\frac{\partial \theta}{\partial z} + \frac{\partial n}{\partial q}\frac{\partial q}{\partial z}\right]^2, \tag{196}$$

where a^2 is a constant ($a^2 \approx 2.8$ (d'Auria et al. 1993)). The vertical gradients should not contain any variations due to turbulence, thus they should be evaluated over height intervals larger than L_0.

Equation (196) is however only valid if there is turbulence present. When no turbulence is present C_n^2 should be (close to) zero. One way to determine if the air is turbulent or not is to use the Richardson number Ri (Richardson 1920)

$$Ri = \frac{g}{\theta}\frac{\partial \theta}{\partial z}\left\|\frac{\partial \mathbf{v}}{\partial z}\right\|^{-2}. \tag{197}$$

The atmosphere is turbulent when Ri is larger than a critical Richardson number Ri_c, typically $Ri_c \approx 0.25$. Thus Eq. (196) modifies to

$$C_n^2 = a^2 L_0^{4/3} F\left[\frac{\partial n}{\partial \theta}\frac{\partial \theta}{\partial z} + \frac{\partial n}{\partial q}\frac{\partial q}{\partial z}\right]^2, \tag{198}$$

where $F = 1$ if $Ri < Ri_c$ and zero otherwise. This is however still a bit too simplistic since this assumes a very sharp transition between a turbulent and a non-turbulent state. d'Auria et al. (1993) presented a model for F giving a more smooth transition between 0 and 1 around Ri_c.

6 Applications of Space Geodetic Techniques for Atmospheric Studies

As discussed earlier, it is important to have a good model of the delay in the neutral atmosphere in order to obtain the highest accuracy in the space geodetic results (e.g. station positions). Since external estimates of the wet delay with high enough accuracy are typically not available (at least for microwave techniques), the common way of handling the wet delay in the data analysis is to estimate it, i.e. by modeling it using mapping functions and gradients as described in Sect. 4.2. Thus the results of

the data analysis will also contain information about the tropospheric delay, which is closely related to the IWV (see Sect. 3.2.2). Several studies investigated the accuracy of the zenith wet delays and IWV estimated from VLBI and GNSS (e.g. Herring et al. 1990, Tralli and Lichten 1990, Bevis et al. 1992, Snajdrova et al. 2006, Teke et al. 2011), and these show that it is on the same level or better then that of other techniques. Thus there exists a large interest in applying space geodetic techniques, especially GNSS, for atmospheric studies. For example, zenith wet delays can be used to study climate trends (Sect. 6.1), or assimilated into numerical weather prediction models to improve weather forecasts (Sect. 6.2). With wet delays estimated from a local GNSS network one can even attempt to estimate the 3D structure of the atmospheric water vapor by applying tomographic methods (Sect. 6.3).

6.1 Long-Term Water Vapor Trends

Since the zenith wet delay is closely related to the integrated water vapor content (see Sect. 3.2.2), we can analyze ΔL_w^z estimated from space geodetic techniques to study the variations of the atmospheric water vapor content in time. For example, it is possible to study diurnal and seasonal variations as well as long term trends in the water vapor content. Such information is of great interest in climatology since the water vapor content is closely related to the temperature. Climate models typically predict that the average relative humidity remains constant as the temperature changes (Trenberth et al. 2003). Since the saturation water vapor pressure depends approximately exponentially on the temperature, this means that a a change in the temperature will cause a corresponding change in the water vapor content. It is predicted that an increase in temperature of 1 K will increase the water vapor content by 6–7 % (Trenberth et al. 2003; Bengtsson et al. 2004). It is important to monitor the water vapor content since water vapor is a greenhouse gas, in fact the most important one. Additionally, higher water vapor content can also indicate an intensified hydrological cycle, including increased precipitation.

Several studies have calculated long-term trends in ΔL_w^z (or IWV) estimated from GNSS and VLBI, e.g. Gradinarsky et al. (2002); Jin et al. (2007); Steigenberger et al. (2007); Heinkelmann et al. (2007); Ning and Elgered (2012). An example of ΔL_w^z trends calculated from ten years of GPS data in Sweden and Finland is shown in Fig. 15. For more details, see Nilsson and Elgered (2008).

6.2 GNSS Meteorology

Water vapor is a very important parameter in meteorology and in order to get accurate weather forecasts it is very important to have accurate measurements of the water vapor content. A problem is that the water vapor content is highly variable in both space and time, and traditional instruments (e.g. radiosondes) do not pro-

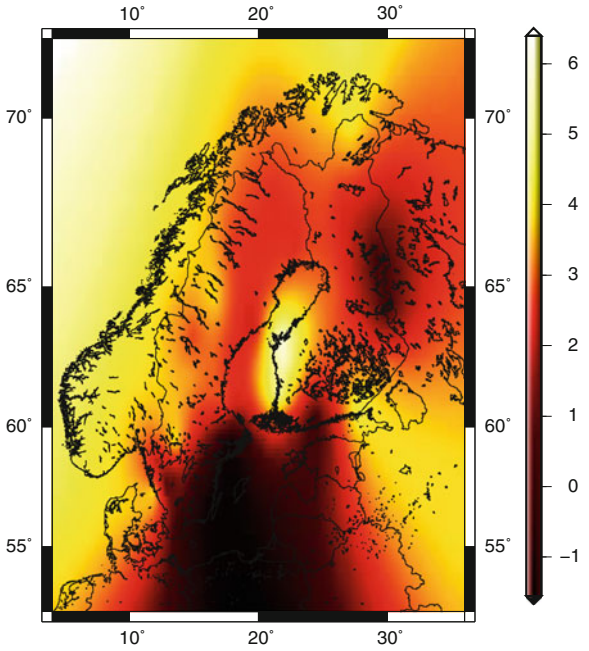

Fig. 15 Zenith wet delay trends in mm/decade estimated from GPS data in Sweden and Finland, 1997–2006. Modified from Nilsson and Elgered (2008)

vide the water vapor content with high enough spatial and temporal resolution. With the establishment of relative dense GNSS networks the meteorological community has started to be interested in assimilating zenith total delays or zenith wet delays estimated from these GNSS networks in the numerical weather prediction models (Gutman and Benjamin 2001; Poli et al. 2007).

Several investigations of assimilating GNSS tropospheric delays in numerical weather prediction models have been performed. For example, in Europe this has been investigated in the projects COST-716 (Elgered et al. 2005), TOUGH (Vedel 2006), and E-GVAP (http://egvap.dmi.dk/). It has been shown that the quality of the forecasts improve if GNSS data are assimilated, especially in cases of high precipitation (Vedel and Huang 2004; Karabatić et al. 2011).

6.3 GNSS Tropospheric Tomography

Tomography is a method which can be used to estimate the 2D or 3D structure of a quantity from measurements of the integral of the quantity along different paths. It is a method commonly used in medicine, seismology, material science, and a number of other fields. Tomography can also be applied to atmospheric delay measurements

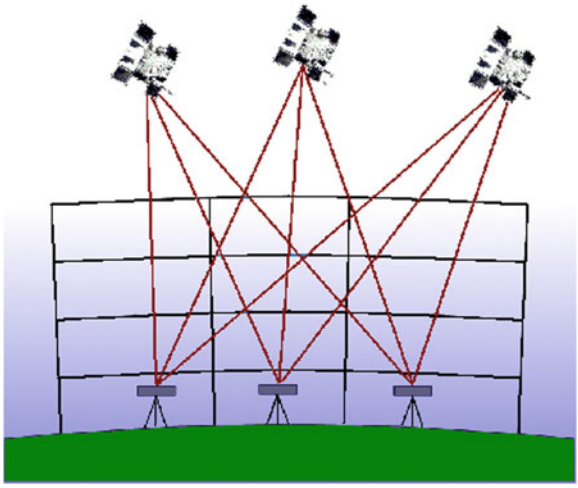

Fig. 16 Example of a GNSS tomography scenario. Note that for better visibility the relative size of the troposphere have been enlarged; in reality the troposphere (= top of highest voxel) is about 10 km heigh, the inter-station distances a few km, while the satellites are are at about 20000 km altitude

in order to reconstruct the 3D structure of the wet (or total) refractivity. This requires that the slant wet delays are measured by several stations in a local (inter-station distance maximum a few km) network. The only space geodetic technique for which such dense networks are available is GNSS.

A picture of a GNSS tomography scenario is shown in Fig. 16. In order to estimate the wet refractivity field from the observed wet delays, the atmosphere above the GNSS network is parameterized. The most commonly used parameterization is voxels, although other parameterizations are also possible (Perler et al. 2011). Voxel parameterization means that the atmosphere is divided into a number of boxes (called voxels, volume pixels) in which the refractivity is assumed constant. Thus the wet tropospheric delays along the rays of the observed GNSS signals can be described by a linear combination of the voxel refractivities

$$\Delta L_i = \sum_{j=1}^{n_{vox}} N_j \, D_{ij}. \tag{199}$$

ΔL_i is the wet tropospheric delay along the ith ray, n_{vox} is the number of voxels, N_j is the refractivity of the jth voxel, and D_{ij} is the distance traveled by ray i in voxel j. Since the station and satellite coordinates are normally known, D_{ij} can be calculated. Having observations of the tropospheric delays along several different rays, a linear system of equations is obtained

$$\Delta \mathbf{L} = \mathbf{DN}. \tag{200}$$

$\Delta\mathbf{L}$ and $\mathbf{N}$ are vectors containing the wet delays and the refractivities, respectively, and $\mathbf{D}$ is a matrix containing the D_{ij} values. By inverting the system, the voxel refractivities are estimated.

There are however a few problems with this method. One is how to estimate the slant wet delays along the GNSS signal rays. One way is to estimate the zenith wet delay and gradients in a normal GNSS analysis, then use these to calculate the slant wet delays. This is for example done by Champollion et al. (2005). However, this method will limit the accuracy since it assumes that all horizontal variations in the refractivity above a station are linear, something which is not always realistic. In order to improve the slant wet delays, it is often assumed that the post-fit residuals of the GNSS analysis will contain the unmodeled parts of the slant wet delays, and thus adding these to the calculated slant wet delays will give the true delays (Alber et al. 2000; Troller et al. 2006). This is not true, the residuals will contain also other errors of the GNSS measurements (e.g. multi-path). Another approach is to model the slant delays by using Eq. (199) in the GNSS data analysis instead of zenith delays and gradients. First results using this approach are presented by Nilsson and Gradinarsky (2006) and Nilsson et al. (2007).

Another problem is the normally weak geometry since tomography ideally requires that there are rays crossing the investigated volume in all possible directions. In GNSS tomography, however, all rays are going between the top of the troposphere to the stations on the surface of the Earth, while there are no rays entering and/or leaving the voxel grid at the sides. This makes the sensitivity to the vertical refractivity profile very low and as a result the equation system (200) will be ill-conditioned. This problem can be solved by either constraining the refractivity field to some a priori field obtained either by models or external measurements like radiosondes. The problem is not as big if the GNSS stations are placed at very different altitudes (e.g. if there are differences of several kilometers between highest and lowest stations) (Nilsson and Gradinarsky 2006).

Furthermore, since the satellite geometry will change during the day, some voxels may at times have no or only a few rays passing through it. Thus, in order to avoid singularity problems, constraints need to be applied. Simple constraints are for example inter-voxel constraints which constrain the refractivity of a voxel to the mean refractivity of the neighboring voxels (Flores et al. 2000). A more advanced approach is to use a Kalman filter with a covariance matrix for the voxel refractivity calculated from turbulence theory using Eq. (186) (Gradinarsky and Jarlemark 2004; Nilsson and Gradinarsky 2006).

Figure 17 shows the results of two simulations demonstrating the strengths and weaknesses of GNSS tomography. In the upper plot the case where the refractivity is 20 mm/km in the layer between 3 and 4 km altitude and zero elsewhere is simulated. As seen the tomographic reconstruction is not working well. This is because of the weak geometry in the vertical direction, resulting in a very low sensitivity to the height of the layer with non-zero refractivity. Thus the refractivity is spread out over all layers in the tomographic reconstruction. Most refractivity is put in the lower layers simply because the tomographic software is set up to allow for a higher variability in the refractivity at lower altitudes than at higher altitudes. The estimated refractivity

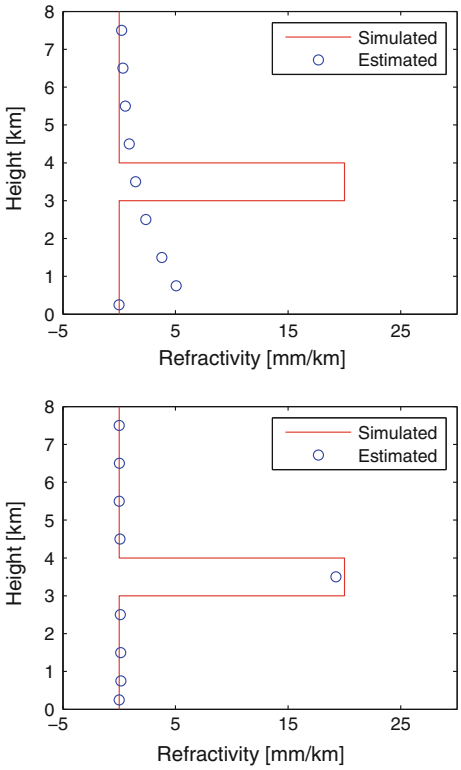

Fig. 17 Simulation results of tomographic reconstruction of the refractivity field. The *upper plot* shows the result obtained when the simulated refractivity field was 20 mm/km in the fifth layer and zero elsewhere. In the *lower plot* the simulated refractivity field is 20 mm/km only in the middle voxel of the fifth layer, and zero elsewhere. These results are from Nilsson (2007)

in the lowest layer is however correctly estimated to zero. Here the sensitivity is higher since the stations are at slightly different altitudes. In the lower plot of Fig. 17 the simulated refractivity field is non-zero just in one voxel: the middle voxel (of 25) of the layer between 3 and 4 km. In this case the tomographic reconstruction is working better. This demonstrates that GNSS tomography can have a good sensitivity to horizontal fluctuations in the refractivity field, and is even able to determine at which height these fluctuations are occurring. For more details about the simulation setup and other results from similar simulations, see Nilsson (2007).

Acknowledgments First of all we would like to thank the reviewer, Gunnar Elgered, for providing very valuable suggestions to improve the quality of this part of the book. We are grateful for the financial support from the German Science Foundation (DFG, SCHU 1103/3-2), and from the Austrian Science Fund (FWF, P20902-N10).

References

J. B. Abshire and C. S. Gardner. Atmospheric refractivity corrections in Satellite Laser Ranging. *IEEE Trans. Geosc. Rem. Sens.*, GE-23(4):414–425, 1985. doi:10.1109/TGRS.1985.289431.

C. Alber, R. Ware, C. Rocken, and J. Braun. Obtaining single path delays from GPS double differences. *Geoph. Res. Lett.*, 27:2661–2664, 2000. doi:10.1029/2000GL011525.

M. Alizadeh, D. D. Wijaya, T. Hobiger, R. Weber, and H. Schuh. Ionospheric effects on microwave signals. In *Atmospheric Effects in Space Geodesy*. Springer-Verlag, 2013. this book.

T. Alkhalifah and S. Fomel. Implementing the fast marching Eikonal solver: Spherical versus cartesian coordinates. *Geophys. Prospect.*, 49:165 178, 2001. doi:10.1046/j.1365-2478.2001.00245.x.

J. I. H. Askne and E. R. Westwater. A review of ground-based remote sensing of temperature and moisture by passive microwave radiometers. *IEEE Trans. Geosci. Remote Sensing*, GE-24 (3):340–352, 1986. doi:10.1109/TGRS.1986.289591.

B. R. Bean and G. D. Thayer. CRPL exponential reference atmosphere. Technical report, U.S. Government Printing Office, 1959. URL http://digicoll.manoa.hawaii.edu/techreports/PDF/NBS4.pdf.

P. L. Bender and J. C. Owens. Correction of optical distance measurements for the fluctuating atmospheric index of refraction. *J. Geophys. Res.*, 70:2461, 1965. doi:10.1029/JZ070i010p02461.

L. Bengtsson, S. Hagemann, and K. I. Hodges. Can climate trends be calculated from reanalysis data? *J. Geophys. Res.*, 109:D11111, 2004. doi:10.1029/2004JD004536.

H. Berg. *Allgemeine Meteorologie.* Dümmlers Verlag, Bonn, 1948.

M. Bevis, S. Businger, S. Chiswell, T. A. Herring, R. A. Anthes, C. Rocken, and R. H. Ware. GPS meteorology: Mapping zenith wet delays onto precipitable water. *J. Appl. Meteorology*, 33(3):379–386, 1994. doi:10.1175/1520-0450(1994)033<0379:GMMZWD>2.0.CO;2.

M. Bevis, S. Businger, T.A. Herring, C. Rocken, R.A. Anthes, and R.H. Ware. GPS meteorology: remote sensing of atmospheric water vapor using the global positioning system. *J. Geophys. Res.*, 97(D14):15787–801, 1992. ISSN 0148–0227. doi:10.1029/92JD01517.

J. Böhm. *Troposphärische Laufzeitverzögerungen in der VLBI.* PhD thesis, Technische Universität Wien, 2004.

J. Böhm, R. Heinkelmann, and H. Schuh. Short Note: A global model of pressure and temperature for geodetic applications.*J. Geodesy*, 81(10):679–683, OCT 2007. doi:10.1007/s00190-007-0135-3.

J. Böhm, R. Heinkelmann, and H. Schuh. Neutral atmosphere delays: Empirical models versus discrete time series from numerical weather models. In H. Drewes, editor, *Geodetic Reference Frames - IAG Symposium*, volume 134 of IAG Symposia, pages 317–321, Munich, Germany, 2009a. doi:10.1007/978-3-642-00860-3_49.

J. Böhm, J. Kouba, and H. Schuh. Forecast Vienna mapping functions 1 for real-time analysis of space geodetic observations. *J. Geodesy*, 83(5), 2009b. doi:10.1007/s00190-008-0216-y.

J. Böhm, P.J. Mendes Cerveira, H. Schuh, and P. Tregoning. The impact of mapping functions for the neutral atmosphere based on numerical weather models in GPS data analysis. In P. Tregoning and C. Rizos, editors, *Dynamic Planet, volume 130 of IAG Symposia Series*, pages 837–843. Springer-Verlag, 2007. doi:10.1007/978-3-540-49350-1_118.

J. Böhm, A. Niell, P. Tregoning, and H. Schuh. Global mapping function (GMF): a new empirical mapping function based on numerical weather model data. *Geophys. Res. Lett.*, 33:L07304, 2006a. doi:10.1029/2005GL025546.

J. Böhm, D. Salstein, M. Alizadeh, and D. D. Wijaya. Geodetic and atmospheric background. In *Atmospheric effects in space geodesy*. Springer-Verlag, Berlin, Germany, 2013. this book.

J. Böhm and H. Schuh. Vienna mapping functions. In *Proc. 16th Working Meeting on European VLBI for Geodesy and Astrometry*, page 131 143, Leipzig, Germany, 2003. Verlag des Bundesamtes für Kartographie und Geodäsie.

J. Böhm and H. Schuh. Vienna mapping functions in VLBI analyses. *Geophys. Res. Lett.*, 31:L01603, 2004. doi:10.1029/2003GL018984.

J. Böhm and H. Schuh. Tropospheric gradients from the ECMWF in VLBI analysis. *J. Geodesy,* 81(6–8):409–421, 2007. doi:10.1007/s00190-006-0126-9.

J. Böhm, B. Werl, and H. Schuh. Troposphere mapping functions for GPS and very long baseline interferometry from european centre for medium-range weather forecasts operational analysis data. *J. Geophys. Res.*, 111:B02406, 2006b. doi:10.1029/2005JB003629.

M. Born and E. Wolf. *Principles of optics*. Cambridge Univ. Press, New York, 7th edition, 1999.

A. V. Bosisio and C. Mallet. Infuence of cloud temperature on brightness temperature and consequences for water retrieval. *Radio Sci.*, 33(4):929–939, 1998. doi:10.1029/98RS00949.

G. Boudouris. On the index of refraction of air, the absorption and dispersion of centimeter waves in gases. *J. Res. Natl. Bur. Stand.*, 67D:631–684, 1963.

K. G. Budden. *The propagation of radio waves*. Cambridge University Press, New York, 1 edition, 1985.

V. Cerveny. *Seismic ray theory*. Cambridge University Press, New York, 2005.

V. Cerveny, L. Klimes, and I. Psencik. Complete seismic-ray tracing in three-dimensional structures. In D. J. Doornbos, editor, *Seismological algorithms*, page 89–168. Academic Press, New York, 1988.

C. Champollion, F. Mason, M.-N. Bouin, A. Walpersdorf, E. Doerflinger, O. Bock, and J. van Baelen. GPS water vapour tomography: preliminary results from the ESCOMPTE field experiment. *Atmospheric Research*, 74:253–274, 2005. doi:10.1016/j.atmosres.2004.04.003.

C.C. Chao. The troposphere calibration model for mariner mars 1971. Technical Report 32–1587, NASA JPL, Pasadena, CA, 1974.

G. Chen and T. A. Herring. Effects of atmospheric azimuthal asymmetry on the analysis of space geodetic data. *J. Geophys. Res.*, 102(B9):20489–20502, 1997. doi:10.1029/97JB01739.

P. E. Ciddor. Refractive index of air: new equations for the visible and near infrared. *Appl. Opt.*, 35(9):1566–1573, 1996. doi:10.1364/AO.35.001566.

P. E. Ciddor and R. J. Hill. The refractive index of air 2. Group index. *Appl. Opt.*, 38:1663–1667, 1999. doi:10.1364/AO.38.001663.

G. d'Auria, F. S. Marzano, and U. Merlo. Model for estimating the refractive-index stucture constant in clear-air intermittent turbulence. *Applied Optics*, 32:2674–2680, 1993. doi:10.1364/AO.32.002674.

J. L. Davis, G. Elgered, A. E. Niell, and C. E. Kuehn. Ground-based measurement of gradients in the "wet" radio refractivity of air. *Radio Sci.*, 28(6):1003–1018, 1993. doi:10.1029/93RS01917.

J. L. Davis, T. A. Herring, I. I. Shapiro, A. E. E. Rogers, and G. Elgered. Geodesy by radio interferometry: Effects of atmospheric modeling errors on estimates of baseline length. *Radio Sci.*, 20(6):1593–1607, 1985. doi:10.1029/RS020i006p01593.

J.L. Davis. Atmospheric propagation effects on radio interferometry. Technical Report AFGL-TR-86-0243, Scientific Report No. 1, Air Force Geophysics Laboratory, 1986.

P. Debye. *Polar Molecules.* Dover, New York, 1929.

B. Edlén. The refractive index of air. *Metrologia*, 2(2):71–80, 1966. doi:10.1088/0026-1394/2/2/002.

G. Elgered. Tropospheric radio-path delay from ground based microwave radiometry. In M. Janssen, editor, *Atmospheric Remote Sensing by Microwave Radiometry*, chapter 5. Wiley & Sons, Inc., N.Y., 1993.

G. Elgered, J. L. Davis, T. A. Herring, and I. I. Shapiro. Geodesy by radio interferometry: Water vapor radiometry for estimation of the wet delay. *J. Geophys. Res.*, 95(B4):6541–6555, 1991. doi:10.1029/90JB00834.

G. Elgered, H.-P. Plag, H. van der Marel, S. Barlag, and J. Nash, editors. *Exploitation of ground-based GPS for operational numerical weather prediction and climate applications*. COST action 716: Final Report. European Union, Brussels, Belgium, 2005.

T. R. Emardson and H. J. P. Derks. On the relation between the wet delay and the integrated precipitable water vapour in the European atmosphere. *Meteorol. Appl.*, 7(1):61–68, 2000. doi:10.1017/S1350482700001377.

T. R. Emardson, G. Elgered, and J. M. Johansson. External atmospheric corrections in geodetic very-long-baseline interferometry. *J. Geodesy*, 73:375–383, 1999. doi:10.1007/s001900050256.

L. Essen and K. D. Froome. The refractive indices and dielectric constants of air and its principal constituents at 24,000 Mc/s. *Proc. Phys Soc.* B, 64(10):862–875, 1951. doi:10.1088/0370-1301/64/10/303.

A. Flores, G. Ruffini, and A. Rius. 4D tropospheric tomography using GPS slant delays. *Ann. Geophysicae*, pages 223–234, 2000. doi:10.1007/s00585-000-0223-7.

U. Fölsche. *Tropospheric water vapor imaging by combination of spaceborne and ground-based GNSS sounding data*. PhD thesis, Univ. Graz, Graz, Austria, 1999.

P. J. Fowler. Finite-difference solutions of the 3d eikonal equation in spherical coordinates. In *Proc. 64th SEG meeting*, pages 1394–1397, Los Angeles, USA, 1994.

C. S. Gardner. Effects of horizontal refractivity gradients on the accuracy of laser ranging to satellites. *Radio Sci.*, 11(12):1037–1044, 1976. doi:10.1029/RS011i012p01037.

P. Gegout, R. Biancale, and L. Soudarin. Adaptive mapping functions to the azimuthal anisotropy of the neutral-atmosphere. *J. Geodesy*, 85(10):661–677, 2011. doi:10.1007/s00190-011-0474-y.

L. Gradinarsky and P. Jarlemark. Ground-based GPS tomography of water vapor: Analysis of simulated and real data. *J. Meteorol. Soc. Japan*, 82:551–560, 2004. doi:10.2151/jmsj.2004.551.

L. P. Gradinarsky, J. M. Johansson, H. R. Bouma, H.-G. Scherneck, and G. Elgered. Climate monitoring using GPS. *Physics and Chemistry of the Earth*, 27:335–340, 2002. doi:10.1016/S1474-7065(02)00009-8.

B. A. Greene and T. A. Herring. Multiple wavelength laser ranging. In *The 6th International Workshop on Laser Ranging Instrumentation*, 1986.

S. I. Gutman and S. G. Benjamin. The role of ground-based GPS meteorological observations in numerical weather prediction. *GPS Solutions*, 4(4):16–24, 2001. doi:10.1007/PL00012860.

R. Heinkelmann, J. Böhm, H. Schuh, S. Bolotin, G. Engelhardt, D. S. MacMillan, M. Negusini, E. Skurikhina, V. Tesmer, and O. Titov. Combination of long time-series of troposphere zenith delays observed by VLBI. *J. Geodesy,* 81(6–8):483–501, 2007. doi:10.1007/s00190-007-0147-z.

T. A. Herring. Modeling atmospheric delays in the analysis of space geodetic data. In J.C. De Munk and T. A. Spoelstra, editors, *Symposium on Refraction of Transatmospheric Signals in Geodesy*, pages 157–164. Netherlands Geod. Comm., Delft, 1992.

T. A. Herring, J. L. Davis, and I. I. Shapiro. Geodesy by radio interferometry: The application of Kalman filtering to the analysis of Very Long Baseline Interferometry data. *J. Geophys. Res.*, 95(B8):12,561–12,581, 1990. 90JB00683.

R. J. Hill, R. S. Lawrence, and J. T. Priestley. Theoretical and calculational aspects of the radio refractive index of water vapor. *Radio Sci.*, 17(5):1251–1257, 1982. doi:10.1029/RS017i005p01251.

T. Hobiger, R. Ichikawa, Y. Koyama, and T. Kondo. Fast and accurate ray-tracing algorithms for real-time space geodetic applications using numerical weather models. *J. Geophys. Res.*, 113:D20302, 2008. doi:10.1029/2008JD010503.

H.S. Hopfield. Two-quartic tropospheric refractivity profile for correcting satellite data. *J. Geophys. Res.*, 74:4487–4499, 1969. doi:10.1029/JC074i018p04487.

C. G. Hulley. *Improved Refraction Corrections for Satellite Laser Ranging (SLR) by Ray Tracing through Meteorological Data*. PhD thesis, University of Maryland, 2007.

G. C. Hulley and E. C. Pavlis. A ray-tracing technique for improving Satellite Laser Ranging atmospheric delay corrections, including the effects of horizontal refractivity gradients. *J. Geophys. Res.*, 112(B06417):1–19, 2007. doi:10.1029/2006JB004834.

I. Ifadis. The atmospheric delay of radio waves: Modeling the elevation dependence on a global scale. Technical Report 38L, School Electrical Computer Engineering, Chalmers University of Technology, Göteborg, Sweden, 1986. ISBN:99-0605353-4.

K. Iizuka. Engineering optics, volume 35 of *Springer Series in Optical Sciences*. Springer-Verlag, New York, 3rd edition, 2008.

A. Ishimaru. *Wave Propagation and Scattering in Random Media*. Academic Press, New York, 1978.

J. D. Jackson. *Classical electrodynamics*. Wiley & Sons, Inc., N.Y., 3rd edition, 1998.

P. O. J. Jarlemark. Analysis of temporal and spatial variations in atmospheric water vapor using microwave radiometry. PhD Thesis, Tech. Rep. 308, School Electrical Computer Engineering, Chalmers Univ. Tech., 1997. Göteborg, Sweden.

H. Jeske. Meteorological optics and radiometeorology. In Landolt-Börnstein, editor, *Numerical data and functional relationships in science and technology*, volume 4b of Group V. Springer, 1988.

S. Jin, J.-U. Park, J.-H. Cho, and P.-H. Park. Seasonal variability of GPS-derived zenith tropospheric delay (1994–2006) and climate implications. *J. Geophys. Res.*, 112:D09110, 2007. doi:10.1029/2006JD007772.

A. Karabatić, R. Weber, and T. Haiden. Near real-time estimation of tropospheric water vapour content from ground based GNSS data and its potential contribution to weather now-casting in Austria. *Adv. Space Res.*, 47(10):1691–1703, 2011. doi:10.1016/j.asr.2010.10.028.

A. N. Kolmogorov. Dissipation of energy in the locally isotropic turbulence. *Dokl. Akad. Nauk SSSR*, 32(1):16–18, 1941a. English translation in: *Proc R. Soc. Lond. A*, 434:15–17.

A. N. Kolmogorov. The local structure of turbulence in incompressible viscous fluid for very large Reynolds numbers. *Dokl. Akad. Nauk SSSR*, 30(4):299–303, 1941b. English translation in: *Proc R. Soc. Lond. A*, 434:9–13.

J. Kouba. Implementation and testing of the gridded vienna mapping function 1 (VMF1). *J. Geodesy*, 82(4–5):193–205, 2008. doi:10.1007/s00190-007-0170-0.

C. E. Kuehn, W. E. Himwich, T. A. Clark, and C. Ma. An evaluation of water vapor radiometer data for calibration of the wet path delay in very long baseline interferometry experiments. *Radio Sci.*, 26(6):1381–1391, 1991. doi:10.1029/91RS02020.

R.F. Leandro, M.C. Santos, and R.B. Langley. UNB neutral atmosphere models: Development and performance. In *National Technical Meeting of The Institute of Navigation, Monterey, California, 18–20 January 2006*, pages 564–573, 2006.

H. J. Liebe. An updated model for millimeter wave propagation in moist air. *Radio Sci.*, 20(5): 1069–1089, 1985. doi:10.1029/RS020i005p0106.

H. J. Liebe. MPMan atmospheric millimeter-wave propagation model. *Int. J. Infrared Millimeter Waves*, 10(6): 631–650, 1989. doi:10.1007/BF01009565.

H. J. Liebe, G. A. Hufford, and M. G. Cotton. Propagation modeling of moist air and suspended water/ice particles at frequencies below 1000 GHz. In *Proc. AGARD 52d Specialists Meeting of the Electromagnetic Wave Propagation Panel, pages 3.1–3.10, Palam de Mallorca*, Spain, 1993. AGARD.

D. S. MacMillan. Atmospheric gradients from very long baseline interferometry observations. *Geophys. Res. Lett.*, 22(9):1041–1044, 1995. doi:10.1029/95GL00887.

D. S. MacMillan and C. Ma. Evaluation of very long baseline interferometry atmospheric modeling improvements. *J. Geophys. Res.*, 99(B1):637–651, 1994. doi:10.1029/93JB02162.

D. S. MacMillan and C. Ma. Atmospheric gradients and the VLBI terrestrial and celestial reference frames. *Geophys. Res. Lett.*, 24(4):453–456, 1997. doi:10.1029/97GL00143.

J.W. Marini. Correction of satellite tracking data for an arbitrary tropospheric profile. *Radio Science*, 7(2):223–231, 1972. doi:10.1029/RS007i002p00223.

J.W. Marini and C.W. Murray. Correction of laser range tracking data for atmospheric refraction at elevation angles above 10 degrees. Technical Report X-591-73-351, NASA, 1973.

V. B. Mendes. Modeling of the neutral-atmosphere propagation delay in radiometric space techniques. PhD dissertation, Department of Geodesy and Geomatics Engineering Tech. Report No. 199, University of New Brunswick, Fredericton, New Brunswick, Canada, 1999. General definitions of IWV, relative humidity etc.

V. B. Mendes and R. Langley. Tropospheric zenith delay prediction accuracy for airborne GPS high-precision positioning. In *Proc. of* ION GPS-98, pages 337–347, Nashville, TN, USA, 1998.

V. B. Mendes and E. C. Pavlis. High-accuracy zenith delay prediction at optical wavelengths. *Geophys. Res. Lett.*, 31, 2004. doi:10.1029/2004GL020308.L14602.

V. B. Mendes, G. Prates, E. C. Pavlis, D. E. Pavlis, and R. B. Langley. Improved mapping functions for atmospheric refraction correction in SLR. *Geophys. Res. Lett.*, 29(10):10.1029-10.1032, 2002. doi:10.1029/2001GL014394.

V. Nafisi, M. Madzak, J. Böhm, A. A. Ardalan, and H. Schuh. Ray-traced tropospheric delays in VLBI analysis. *Radio Sci.*, 47:RS2020, 2012a. doi:10.1029/2011RS004918.

V. Nafisi, L. Urquhart, M. C. Santos, F. G. Nievinski, J. Böhm, D. D. Wijaya, H. Schuh, A. A. Ardalan, T. Hobiger, R. Ichikawa, F. Zus, J. Wickert, and P. Gegout. Comparison of ray-tracing packages for troposphere delays. *IEEE Trans. Geosci. Remote Sensing*, 50(2):469–481, 2012b. doi:10.1109/TGRS.2011.2160952.

A. Niell. Global mapping functions for the atmosphere delay at radio wavelengths. *J. Geophys. Res.*, 101(B2):3227–3246, 1996. doi:10.1029/95JB03048.

A. E. Niell. Improved atmospheric mapping functions for VLBI and GPS. *Earth Planets Space*, 52:699–702, 2000.

A. E. Niell. Preliminary evaluation of atmospheric mapping functions based on numerical weather models. *Phys. Chem. Earth (A)*, 26:475–480, 2001. doi:10.1016/S1464-1895(01)00087-4.

A. E. Niell, A. J. Coster, F. S. Solheim, V. B. Mendes, P. C. Toor, R. B. Langley, and C. A. Upham. Comparison of measurements of atmospheric wet delay by Radiosonde, Water Vapor Radiometer, GPS, and VLBI. *J. Atmos. Oceanic Technol.*, 18(6):830–850, 2001. doi:10.1175/1520-0426(2001)018<0830:COMOAW>2.0.CO;2.

A. E. Niell. Interaction of atmosphere modeling and vlbi analysis strategy. In D. Behrend and K. Baver, editors, *International VLBI Service for Geodesy and Astrometry 2006 General Meeting Proceedings*, number NASA/CP-2006-214140, 2006.

F. G. Nievinski. Ray-tracing options to mitigate the neutral atmosphere delay in GPS. Master's thesis, University of New Brunswick, Department of Geodesy and Geomatics Engineering, 2009. URL http://hdl.handle.net/1882/1050. Technical Report No. 262.

T. Nilsson. Improving GNSS tropospheric tomography by better knowledge of atmospheric turbulence. In *Proc. 1:st Colloquium Scientific and Fundamental Aspects of the Galileo Programme*, Toulouse, France, 2007. European Space Agency.

T. Nilsson and G. Elgered. Long-term trends in the atmospheric water vapor content estimated from ground-based GPS data. *J. Geophys. Res.*, 113:D19101, 2008. doi:10.1029/2008JD010110.

T. Nilsson and L. Gradinarsky. Water vapor tomography using GPS phase observations: Simulaton results. *IEEE Trans. Geosci. Remote Sensing*, 44(10):2927–2941, 2006. doi:10.1109/TGRS.2006.877755.

T. Nilsson, L. Gradinarsky, and G. Elgered. Correlations between slant wet delays measured by microwave radiometry. *IEEE Trans. Geosci. Remote Sensing*, 43(5):1028–1035, 2005. doi:10.1109/TGRS.2004.840659.

T. Nilsson, L. Gradinarsky, and G. Elgered. Water vapour tomography using GPS phase observations: Results from the ESCOMPTE experiment. *Tellus A*, 59:574–682, 2007. doi:10.1111/j.1600-0870.2007.00247.x.

T. Nilsson and R. Haas. Impact of atmospheric turbulence on geodetic very long baseline interferometry. *J. Geophys. Res.*, 115:B03407, 2010. doi:10.1029/2009JB006579.

T. Ning and G. Elgered. Trends in the atmospheric water vapor content from ground-based GPS: The impact of the elevation cutoff angle. *IEEE Journal of Selected Topics in Applied Earth Observations and Remote Sensing*, 5:744–751, 2012. doi:10.1109/JSTARS.2012.2191392.

A. Nothnagel, J. Cho, A. Roy, and R. Haas. WVR calibration applied to European VLBI observing sessions. In P. Tregoning and C. Rizos, editors, *Dynamic Planet*, volume 130 of *IAG Symposia*, pages 152–157. Springer, Berlin, Germany, 2007. doi:10.1007/978-3-540-49350-1_24.

J. C. Owens. Optical refractive index of air: Dependence on pressure, temperature and composition. *Appl. Opt.*, 6(1):51–59, 1967. doi:10.1364/AO.6.000051.

T. K. Pany. *Development and application of tropospheric GPS slant delay models based on numerical weather prediction models and turbulence theory*. PhD thesis, Institute of Engineering Geodesy and Measurements Systems, Graz University of Technology, 2002.

D. Perler, A. Geiger, and F. Hurter. 4D GPS water vapor tomography: new parameterized approaches. *J. Geodesy*, 85(8):539–550, 2011. doi:10.1007/s00190-011-0454-2.

P. Poli, P. Moll, F. Rabier, G. Desroziers, B. Chapnik, L. Berre, S. B. Healy, E. Andersson, and F.-Z. El Guelai. Forecast impact studies of zenith total delay data from European near real-time GPS stations in météo france 4DVAR. *J. Geophys. Res.*, 112:D06114, 2007. doi:10.1029/2006JD007430.

M. T. Prilepin. Light modulating method for determining average index of refraction of air along a line. *Tr. Tsentr. Nauchno-Issled. Inst. Geod. Aero. Kartog.*, 114:127, 1957.

L. F. Richardson. The supply of energy from and to atmospheric eddies. *Proc. Roy. Soc. Lond. A*, 97(686):354–373, 1920.

P. W. Rosenkranz. Water vapor microwave continuum absorption: a comparison of measurements and models. *Radio Sci.*, 33(4):919–928, 1998. doi:10.1029/98RS01182.

M. Rothacher, T.A. Springer, S. Schaer, and G. Beutler. Processing strategies for regional GPS networks. In F.K. Brunner, editor, *Advances in Positioning and Reference Frames, volume 118 of IAG Symposia Series*, pages 93–100. Springer-Verlag, 1998.

J. M. Rüeger. Refractive index formulae for radio waves. In *Proc. XXII FIG International Congress*, Washington DC, USA, 2002a. FIG. URL http://www.fig.net/pub/fig_2002/procmain.htm

J. M. Rüeger. Refractive indices of light, infrared and radio waves in the atmosphere. Technical report, UNISURV S-68, School of Surveying and Spatial Information Systems, The University of New South Wales, Australia, 2002b.

J. Saastamoinen. Atmospheric correction for the troposphere and stratosphere in radio ranging of satellites. In S. W. Henriksen et al., editors, *The Use of Artificial Satellites for Geodesy*, volume 15, pages 247–251, AGU, Washington, D.C., 1972b.

J. Saastamoinen. Introduction to practical computation of astronomical refraction. *Bull. Géod.*, 106:383–397, 1972a. doi:10.1007/BF02522047.

T. M. Scheve and C. T. Swift. Profiling atmospheric water vapor with a K-band spectral radiometer. *IEEE Trans. Geosci.* Remote Sensing, 37(3):1719–1729, 1999. doi:10.1109/36.763294.

W. A. Schneider, Jr. Robust, efficient upwind finite-difference traveltime calculations in 3d. In *Proc. 63rd SEG meeting*, pages 1036–1039, Washington, DC, USA, 1993.

S. D. Schubert, J. Pjaendtner, and R. Rood. An assimilated data set for earth science applications. *Bull. American. Meteo. Soc.*, 74:2331–2342, 1993. doi:10.1175/1520-0477(1993)074<2331:AADFES>2.0.CO;2.

K. Snajdrova, J. Böhm, P. Willis, R. Haas, and H. Schuh. Multi-technique comparison of tropospheric zenith delays derived during the CONT02 campaign. *J. Geodesy,* 79(10–11):613–623, 2006. doi:10.1007/s00190-005-0010-z.

F. S. Solheim, J. Vivekanandan, R. H. Ware, and C. Rocken. Propagation delays induced in GPS signals by dry air, water vapor, hydrometeors, and other particulates. *J. Geophys. Res.*, 104(D8):9663–9670, 1999. doi:10.1029/1999JD900095.

P. Steigenberger, J. Böhm, and V. Tesmer. Comparison of GMF/GPT with VMF1/ECMWF and implications for atmospheric loading. *J. Geodesy*, 83:943–951, 2009. doi:10.1007/s00190-009-0311-8.

P. Steigenberger, V. Tesmer, M. Krügel, D. Thaller, R. Schmid, S. Vey, and M. Rothacher. Comparisons of homogeneously reprocessed GPS and VLBI long time-series of troposphere zenith delays and gradients. *J. Geodesy*, 81(6–8):503–514, 2007. doi:10.1007/s00190-006-0124-y.

V. I. Tatarskii. *The Effects of the Turbulent Atmosphere on Wave Propagation*. Israel Program for Scientific Translations, Jerusalem, 1971.

G. I. Taylor. The spectrum of turbulence. *Proc. Roy. Soc. Lond. A*, 164(919):476–490, 1938. URL http://www.jstor.org/stable/97077.

K. Teke, J. Böhm, T. Nilsson, H. Schuh, P. Steigenberger, R. Dach, R. Heinkelmann, P. Willis, R. Haas, S. Garcia-Espada, T. Hobiger, R. Ichikawa, and S. Shimizu. Multi-technique comparison of troposphere zenith delays and gradients during CONT08. *J. Geodesy*, 85(7):395–413, 2011. doi:10.1007/s00190-010-0434-y.

V. Tesmer, J. Böhm, R. Heinkelmann, and H. Schuh. Effect of different tropospheric mapping functions on the TRF, CRF and position time-series estimated from VLBI. *J. Geodesy*, 81(6–8): 409–421, 2007. doi:10.1007/s00190-006-0126-9.

G. D. Thayer. A rapid and accurate ray tracing algorithm for a horizontally stratified atmosphere. *Radio Sci.*, 1(2):249–252, 1967.

G. D. Thayer. An improved equation for the radio refractive index of air. *Radio Sci.*, 9(10):803–807, 1974. doi:10.1029/RS009i010p00803.

R. N. Thessin. Atmospheric signal delay affecting GPS measurements made by space vehicles during launch, orbit and reentry. Master's thesis, Massachusetts Institute of Technology, Dept. of Aeronautics and Astronautics, Cambridge, Mass., 2005. URL http://hdl.handle.net/1721.1/33211.

D. M. Tralli and S. M. Lichten. Stochastic estimation of tropospheric path delays in global positioning system geodetic measurements. *Bull. Geod.*, 64:127–159, 1990. doi:10.1007/BF02520642.

P. Tregoning and T.A. Herring. Impact of a priori zenith hydrostatic delay errors on GPS estimates of station heights and zenith total delays. *Geophys. Res. Lett.*, 33(L23303), 2006. doi:10.1029/2006GL027706.

K. E. Trenberth, A. Dai, R.M. Rasmussen, and D.B. Parsons. The changing character of precipitation. *Bull. Amer. Meteor. Soc.*, 84(9):12051217, 2003. doi:10.1175/BAMS-84-9-1205.

R. N. Treuhaft and G. E. Lanyi. The effect of the dynamic wet troposphere on radio interferometric measurements. *Radio Sci*., 22(2):251–265, 1987. doi:10.1029/RS022i002p00251.

M. Troller, A. Geiger, E. Brockmann, J.-M. Bettems, B. Bürki, and H.-G. Kahle. Tomographic determination of the spatial distribution of water vapor using GPS observations. *Adv. Space Res.*, 37(12):2211–2217, 2006. doi:10.1016/j.asr.2005.07.002.

H. Vedel. Targeting optimal use of GPS humidity measurements in meteorology: Final report of the TOUGH project, 2006. URL http://web.dmi.dk/pub/tough/.

H. Vedel and X.-Y. Huang. Impact of ground based GPS data on numerical weather prediction. *J. Met. Soc. Japan*, 82(1B):459–472, 2004. doi:10.2151/jmsj.2004.459.

J. Wang, L. Zhang, and A. Dai. Global estimates of water-vapor-weighted mean temperature of the atmosphere for GPS applications. *J. Geophys. Res.*, 110(D21101), 2005. doi:10.1029/2005JD006215.

R. Ware, C. Rocken, F. Solheim, T. van Hove, C. Alber, and J. Johnson. Pointed water vapor radiometer corrections for accurate global positioning system surveying. *Geophys. Res. Lett.*, 20(23): 2635–2638, 1993. doi:10.1029/93GL02936.

E. R. Westwater, M. J. Falls, and I. A. Popa-Fotin. Ground-based microwave radiometric observations of precipitable water vapor: A comparison with ground truth from two radiosonde observing systems. *J. Atmos. Oceanic Technol.*, 6(4):724–730, 1989. doi:10.1175/1520-0426(1989)006.

A. D. Wheelon. *Electromagnetic scintillation: Geometrical optics*. Cambridge University Press, 2001.

D. D. Wijaya. *Atmospheric correction formulae for space geodetic techniques*. PhD thesis, Graz University of Technology, Institute of Engineering Geodesy and Measurements Systems, Graz, Austria, 2010.

D. D. Wijaya, J. Böhm, M. Karbon, and H. Schuh. Atmospheric pressure loading. In *Atmospheric Effects in Space Geodesy*. Springer-Verlag, 2013. this book.

D.D. Wijaya and F.K. Brunner. Atmospheric range correction for two-frequency SLR measurements. *J. Geodesy*, 85(9):623–635, 2011. doi:10.1007/s00190-011-0469-8.

S.-C. Wu. Optimum frequencies of a passive microwave radiometer for tropospheric path-length correction. *IEEE Trans. Antennas Propagat.*, 27:233–239, 1979. doi:10.1109/TAP.1979.1142066.

Atmospheric Pressure Loading

Dudy D. Wijaya, Johannes Böhm, Maria Karbon, Hana Kràsnà and Harald Schuh

Abstract Loading of the Earth's crust due to variations of global atmosphere pressure can displace the positions of geodetic sites by more than 1 cm both vertically and horizontally on annual to sub-diurnal time scales, and thus has to be taken into account in the analysis of space geodetic observations. This part of the book discusses methods for the calculation of the displacements. In particular, it summarizes the simple approach with regression coefficients between surface pressure and the vertical displacement and the more rigorous geophysical approach with load Love numbers and Green's functions. Furthermore, we describe the special treatment of the thermal tides (S1 and S2), the importance of the reference pressure, as well as the inverted barometer hypothesis for the oceans. Finally, we present space geodetic results with the application of those correction models for the analysis of Very Long Baseline Interferometry observations.

D. D. Wijaya (✉)
Geodesy Research Group, Institute of Technology Bandung,
Ganesha 10, Bandung-West Java, Indonesia
e-mail: dudy@gd.itb.ac.id

J. Böhm · H. Kràsnà
Department of Geodesy and Geoinformation,Vienna University of Technology,
Gußhausstraße 27-29,1040 Vienna, Austria
e-mail: johannes.boehm@tuwien.ac.at

H. Kràsnà
e-mail: hana.krasna@tuwien.ac.at

M. Karbon
Section 1.1 GPS/Galileo Earth Observations, Helmholtz Centre Potsdam GFZ German Research Centre for Geosciences, Telegrafenberg A 17, 14473 Potsdam, Germany
e-mail: karbon@gfz-potsdam.de

H. Schuh
Department 1 Geodesy and Remote Sensing, Helmholtz Centre Potsdam GFZ German Research Centre for Geosciences, Telegrafenberg A 17, 14473 Potsdam, Germany
e-mail: schuh@gfz-potsdam.de

J. Böhm and H. Schuh (eds.), *Atmospheric Effects in Space Geodesy*,
Springer Atmospheric Sciences, DOI: 10.1007/978-3-642-36932-2_4,

1 Surface Pressure Variations and Deformation of the Solid Earth

Differential heating between low and high latitudes gives rise to atmospheric motions on a wide range of scales. Prominent features of the so-called atmospheric general circulation include westerly (west-to-east) mid-latitude tropospheric jet streams and lower mesospheric jet streams. Superimposed on the jet streams are eastward propagating baroclinic waves that are one of a number of types of weather systems. Examples of baroclinic waves are cyclones and anticyclones, which are representing variations of low and high air pressure from mean pressure (Wallace and Hobbs 2006). Figure 1 shows spatial variations of surface pressure anomaly (the pressure minus a mean of the pressure field) over the Northern hemisphere (10–90°N) at 00 UTC on January 1, 2010. The highest pressure anomaly (≈25 hPa) is over the far northern portions of Siberia and North America extending into the Arctic Ocean. The lowest pressure anomaly (≈ − 35 hPa) is over the middle Atlantic Ocean, south of Iceland. Both cyclones and anti-cyclones typically have spatial extent between some hundreds (tropical cyclones) and some thousands (continental anti-cyclones) of kilometers. Their duration is generally of the order of a few days and sometimes they can remain stable for weeks (Rabbel and Zschau 1985).

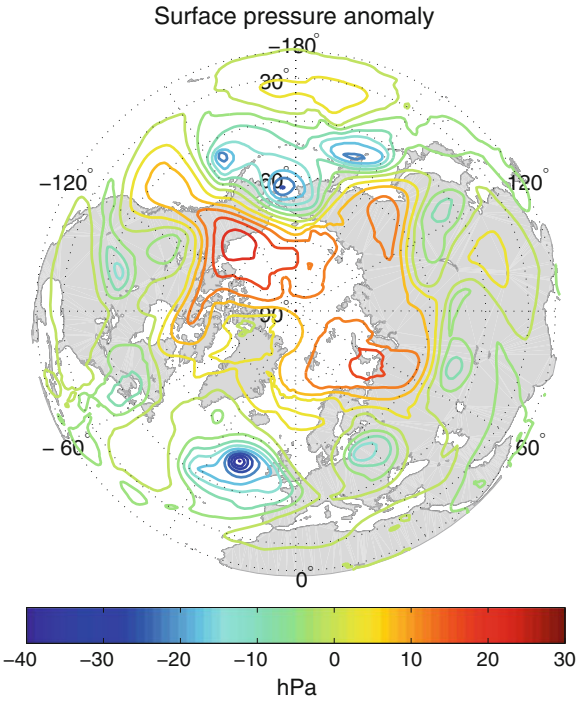

Fig. 1 Surface pressure anomaly (the pressure minus a mean of the pressure field) over Northern hemisphere (10–90°N) from data of the European Centre for Medium-range Weather Forecast (ECMWF) at 00 UTC on January 1, 2010

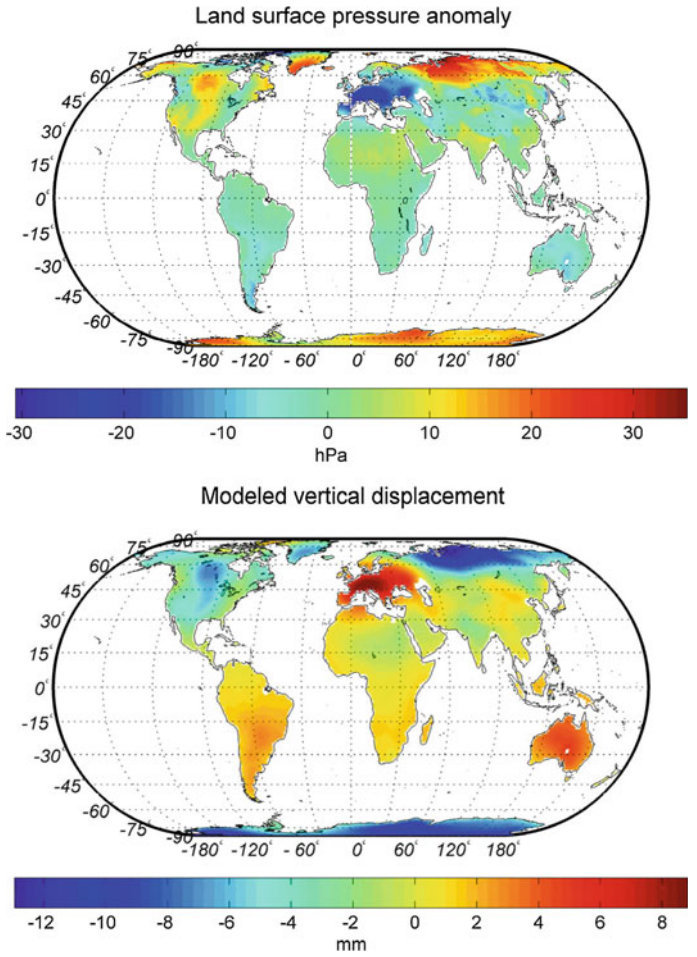

Fig. 2 Spatial variations of surface pressure anomaly and modeled vertical displacements at 00 UTC on January 1, 2010

Complex interactions between the Earth and the atmosphere lead these global atmospheric pressure variations to produce several geodynamic effects as e.g. surface load deformations (Farrell 1972; Rabbel and Zschau 1985; van Dam and Wahr 1987), changes of the gravity potential (Farrell 1972; Boy and Chao 2009), and variations in the Earth's rotational motion (Wahr 1983). In the context of surface load deformations, global variations in surface pressure can displace the Earth's surface by more than 1 cm both vertically and horizontally on annual to sub-diurnal timescales. Figure 2 shows spatial variations of land surface pressure and modeled vertical displacements over the globe with an obvious negative correlation. A large (positive) pressure anomaly of about 30 hPa over Siberia deforms the Earth's surface by about 10 mm. On the other side, a negative pressure anomaly (≈ -20 hPa) over Europe uplifts the region. The magnitude of atmospheric pressure loading (APL) effects for

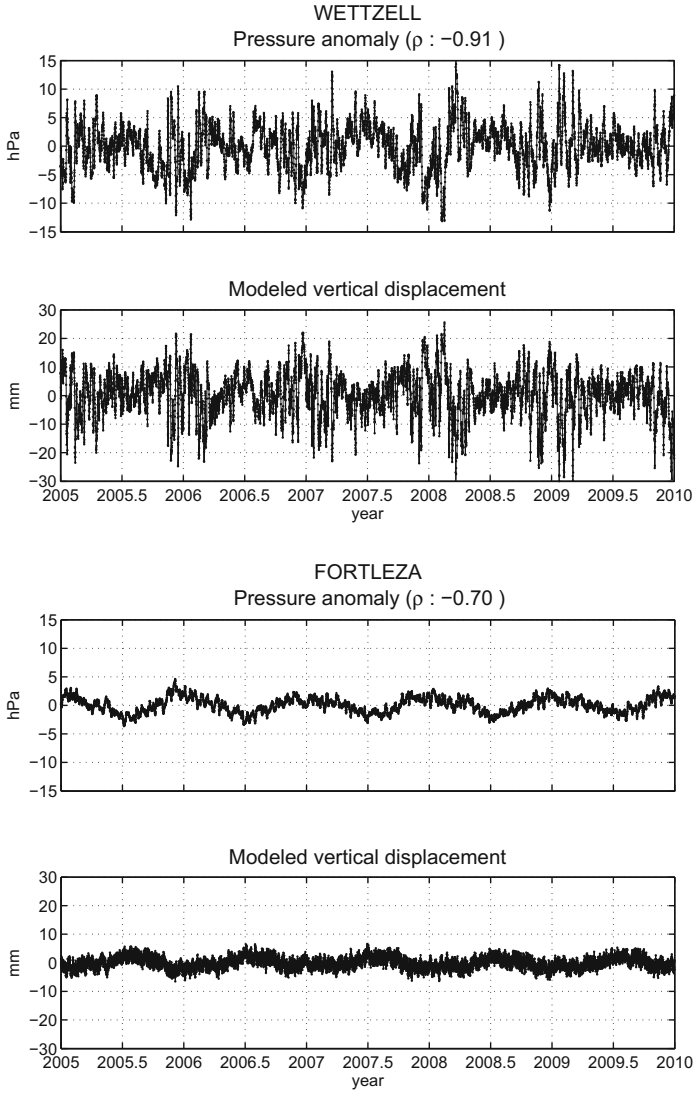

Fig. 3 Temporal variation of pressure anomalies and modeled vertical displacements at stations Wettzell (Germany) and Fortaleza (Brazil) from 2005.0 to 2010.0

a particular area depends primarily on geographical latitude and proximity to the oceans where the inverted barometer (IB) effects are significant. It can be seen that variations of pressure anomaly at mid-latitudes are large and, therefore, the effects of APL in this region are more dominant than those in other regions.

Figure 3 shows temporal variations of pressure anomalies and the corresponding vertical displacements for the two geodetic stations Wettzell, Germany (49.15°N) and Fortaleza, Brazil (3.88°S) with correlation coefficients between −0.9 and −0.7.

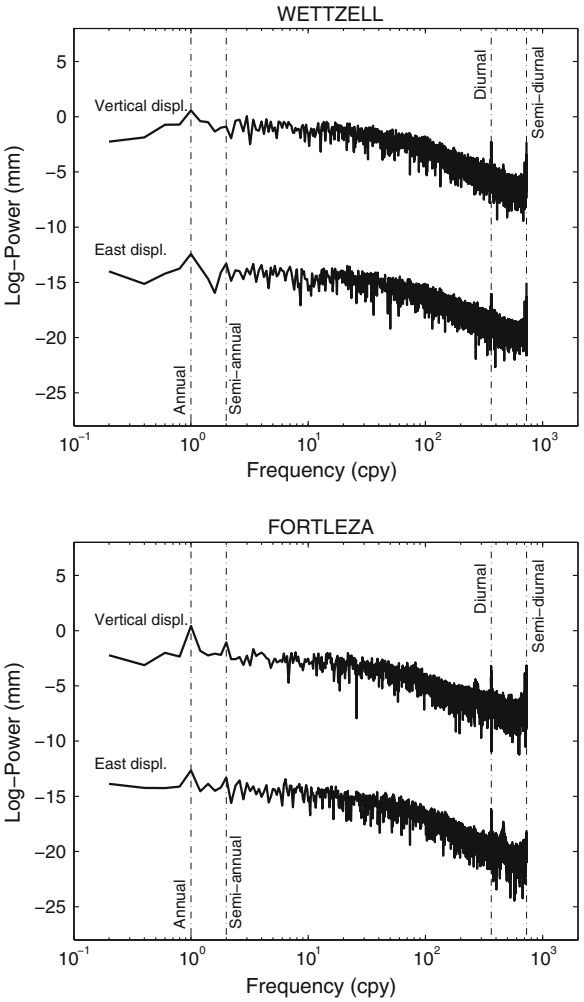

Fig. 4 Amplitude spectra of the displacements in vertical and east directions at stations Wettzell (Germany) and Fortaleza (Brazil). The amplitude of the east direction is translated by log (10^5)

The displacements at Fortaleza are typical for coastal and lower latitude sites. The magnitude of the variations is fairly low due to smaller pressure fluctuation near the equator. Because of the IB effects, the magnitude of APL effects is also further reduced by the site's proximity to the Atlantic Ocean. The displacements at a mid-latitude and non-coastal site (Wettzell) indicate large vertical variations with amplitudes in the order of 5–15 mm. The horizontal displacements are subjected to similar temporal variations with magnitudes of approximately three times smaller than those of the vertical displacements (not shown here).

The amplitude spectra of the displacements in vertical and east directions (Fig. 4) shows significant narrow-band diurnal and semi-diurnal signals. Petrov and Boy (2004) mentioned that strong wide-band annual and semi-annual signals and relatively weak signal for period below 10 days, except strong peaks at the diurnal and semi-diurnal bands, are typical for the displacements at low-latitude stations. In the mid-latitude regions, peak-to-peak variations in the vertical direction occur with a period of about 5–12 days that correspond to the circulations of high and low pressure structures in this regions, partly due to baroclinic variability (Dell'Aquila et al. 2005). These timescales represent the limit of validity of the IB assumption for describing the oceanic response to atmospheric pressure forcing.

The effects of APL have been observed in high-precision space geodetic data, i.e., Very Long Baseline Interferometry (VLBI) (van Dam and Wahr 1987; MacMillan and Gipson 1994; Petrov and Boy 2004; Böhm et al. 2007), Global Navigation Satellite Systems (GNSS) (van Dam and Herring 1994; van Dam et al. 1994; Tregoning and van Dam 2005; Dach et al. 2011), and Satellite Laser Ranging (SLR) (Bock et al. 2005). These observational data are often used for geodynamic studies and can be important to remove the displacement signals due to APL, which otherwise propagate into other parameters and effects like hydrological loading and tropospheric delay estimation. For the purpose of correcting APL signals in space geodetic observations, it is necessary to provide the model and corrections for routine data reduction. In the following sections, different approaches to model APL corrections will be discussed.

2 Modeling Atmosphere Pressure Loading

The IERS (International Earth Rotation and Reference Systems Service) Conventions 2010 (Petit and Luzum 2010) describe two possibilities to model the APL effects: (i) a geophysical approach using convolution of the actual loading distribution over the entire surface of the solid Earth, (ii) an empirical model which is based on the actual deformations derived from geodetic observations taken at individual sites. Both approaches will be described in this section.

2.1 Geophysical Approach

Farrell (1972) considered the elastic yield of the solid Earth to changing surface loads and solved the point loading problem for a spherically symmetric, non-rotating, elastic, and self-gravitating Earth with a liquid core, by devising the Green's functions, which encompass the Earth's response, over spherical harmonic degrees. The essential step in the calculation of surface displacements due to loading comprises the global convolution of the load influence, which is represented by the corresponding Load Love Numbers (LLN) inside the Green's functions, see Eqs. (4) and (5).

As for the mathematical formulation, let $\mathbf{r}$ be the position of an arbitrary station where the surface deformation shall be determined. The station displacements (vertical, east and north directions) evoked by surface pressure loads $P(\mathbf{r}', t)$ over the entire surface of the Earth S are written as:

$$U_r(\mathbf{r}, t) = \iint_S [P(\mathbf{r}', t) - P_{ref}(\mathbf{r}')]\, G_r(\psi)\, \cos\vartheta'\, d\vartheta'\, d\lambda', \tag{1}$$

$$U_e(\mathbf{r}, t) = \iint_S [P(\mathbf{r}', t) - P_{ref}(\mathbf{r}')]\, G_h(\psi)\, \sin\alpha_{\mathbf{rr}'}\, \cos\vartheta'\, d\vartheta'\, d\lambda', \tag{2}$$

$$U_n(\mathbf{r}, t) = \iint_S [P(\mathbf{r}', t) - P_{ref}(\mathbf{r}')]\, G_h(\psi)\, \cos\alpha_{\mathbf{rr}'}\, \cos\vartheta'\, d\vartheta'\, d\lambda'. \tag{3}$$

$P_{ref}(\mathbf{r}')$ denotes the reference pressure, which represents the pressure of an unperturbed atmosphere. Various methods for determination of the reference pressure are summarized by Schuh et al. (2009). ϑ' is the geocentric latitude and λ' is the longitude. The Green's functions are computed from Load Love Numbers (LLNs) h'_n and l'_n according to

$$G_r(\psi) = \frac{GR}{g^2} \sum_{n=0}^{\infty} h'_n P_n(\cos\psi), \tag{4}$$

$$G_h(\psi) = \frac{GR}{g^2} \sum_{n=0}^{\infty} l'_n \frac{\partial P_n(\cos\psi)}{\partial\psi}, \tag{5}$$

where G is the universal gravitational constant, ψ is the angular distance between the station with the position $\mathbf{r}$ and the pressure source with the position $\mathbf{r}'$ g is the mean gravitational acceleration at the surface of the Earth, R is the mean Earth radius and P_n is the Legendre polynomial of degree n.

Cosine and sine of the azimuth angle $\alpha_{\mathbf{rr}'}$ between the station and the pressure load can be calculated using the formalism described by Hofmann-Wellenhof and Moritz (2005):

$$\cos\alpha_{\mathbf{rr}'} = \frac{\cos\vartheta\ \sin\vartheta' - \sin\vartheta\ \cos\vartheta'\ \cos(\lambda' - \lambda)}{\sin\psi} \tag{6}$$

$$\sin\alpha_{\mathbf{rr}'} = \frac{\cos\vartheta'\ \sin(\lambda' - \lambda)}{\sin\psi} \tag{7}$$

In the calculation, a complex IB model describing the oceanic response to atmospheric pressure and wind forcing should be introduced (Geng et al. 2012). Instead of using such a complex model, van Dam and Wahr (1987) proposed a

slightly modified IB hypothesis. If there is a net increase or decrease in the mass of air above the oceans, the seafloor experiences a uniform pressure $\Delta\bar{P}_o$ acting everywhere on the ocean bottom surface:

$$\Delta\bar{P}_o = \frac{\iint_{ocean} [P(\mathbf{r}', t) - P_{ref}(\mathbf{r}')] \cos\vartheta' \, d\vartheta' \, d\lambda'}{\iint_{ocean} \cos\vartheta' \, d\vartheta' \, d\lambda'}. \tag{8}$$

The IB model above is adequate to describe the sea height variations with periods longer than 5–20 days but is not accurate enough for shorter periods. Wunsch and Stammer (2010) showed that the (non-equilibrium) diurnal and sub-diurnal ocean tides imply that the global oceanic response is certainly not an IB at shorter periods.

Following Petrov and Boy (2004), the integrals in Eqs. (1), (2) and (3), can be split up into land and ocean contributions, thus an IB correction for the oceanic portion can be applied:

$$U_r(\mathbf{r}, t) = \iint_{land} [P(\mathbf{r}', t) - P_{ref}(\mathbf{r}')] \, G_r(\psi) \, ds + \Delta\bar{P}_o \iint_{ocean} G_r(\psi) \, ds, \tag{9}$$

$$U_e(\mathbf{r}, t) = \iint_{land} [P(\mathbf{r}', t) - P_{ref}(\mathbf{r}')] \, G_h(\psi) \, \sin\alpha_{\mathbf{rr}'} \, ds + \Delta\bar{P}_o \iint_{ocean} G_h(\psi) \, \sin\alpha_{\mathbf{rr}'} \, ds, \tag{10}$$

$$U_n(\mathbf{r}, t) = \iint_{land} [P(\mathbf{r}', t) - P_{ref}(\mathbf{r}')] \, G_h(\psi) \, \cos\alpha_{\mathbf{rr}'} \, ds + \Delta\bar{P}_o \iint_{ocean} G_h(\psi) \, \cos\alpha_{\mathbf{rr}'} \, ds, \tag{11}$$

where $ds = \cos\vartheta' \, d\vartheta' \, d\lambda'$.

In order to calculate the displacements using Eqs. (9)–(11), the following physical information is required:

- **Global surface pressure**. The parameter $P(\mathbf{r}', t)$ can be derived from data from a Numerical Weather Model (NWM), e.g. from those of the European Centre for Medium-range Weather Forecasts (ECMWF) and the National Centers for Environmental Prediction (NCEP). Both centers provide the data every 3 or 6 h with various spatial resolutions.
- **Reference pressure**. $P_{ref}(\mathbf{r}')$ can be determined by long-term averaging of surface pressure data. Schuh et al. (2009) thoroughly review various methods for the definition of reference pressure for geodetic applications and they propose a new method that is called the Global Reference Pressure (GRP) which is based on the application of pressure level data instead.
- **Green's functions and Load Love Numbers**. The vertical and horizontal Green's functions ($G_r(\psi)$ and $G_h(\psi)$) are used as weighting factors for surface pressure anomaly data $[P(\mathbf{r}', t) - P_{ref}(\mathbf{r}')]$. In the definition of the Green's functions, high

degree LLN are required. Farrell (1972) suggest to compute the LLN values up to degree $n = 10000$.

- **Land-sea mask**. For separation of the integration over land and the oceans, appropriate land-sea masks should be provided. Topography models can be used to generate land-sea masks with various spatial resolutions.

Surface pressure data of the ECMWF or NCEP are known to contain signals associated with the diurnal $S_1(p)$ and semi-diurnal $S_2(p)$ atmospheric tides. Unfortunately, the representation of these tides is significantly distorted owing to the sampling interval of 6 hours of most numerical weather models. This particularly holds for the $S_2(p)$ tide (van den Dool et al. 1997; Petrov and Boy 2004), which is located exactly at the Nyquist frequency of 2 cycles/day and, thus, cannot be modeled correctly. Ponte and Ray (2002) suggested to remove the diurnal and semi-diurnal tidal power from the six-hourly atmospheric pressure fields and re-calculate them using a harmonic model. This leads to the calculation of the displacement corrections in three steps:

1. Calculate non-tidal loading displacements using pressure fields in which the tidal signals have been removed (Sect. 2.1.1).
2. Calculate tidal loading displacements using a gridded global model of pressure tides (Sect. 2.1.2).
3. Calculate total loading displacements by summing both non-tidal and tidal loading displacements.

2.1.1 Non-Tidal Loading Displacements

Petrov and Boy (2004) removed the diurnal and semi-diurnal tidal power from the six-hourly atmospheric pressure fields by subtracting gridpoint-wise sinusoids with the frequencies 1 and 2 cycles/day, that were estimated from several years of six-hourly surface pressure data. As amplitude and phase of sub-daily tidal variations are only quasi-harmonic quantities and might change considerably over time, this approach cannot account for the full $S_1(p)$ and $S_2(p)$ pressure variations. Moreover, it also neglects the seasonal modulation of atmospheric tides, which is manifested in spectral domain as small side lobes around the main frequencies of 1 and 2 cycles/day. However, it has been shown that such an approach is appropriate for correcting APL effects at globally distributed VLBI sites (Petrov and Boy 2004). Most importantly, it is well suited for the operational calculations because it can also be used for real-time applications. An alternative method has been applied by Tregoning and van Dam (2005), who convolved the plain pressure data and then employed a low-pass filter on the time series of the displacements. Note that both approaches only aim at removing the $S_1(p)$ and $S_2(p)$ tidal signals as they are contained in the six-hourly data, regardless of whether their representation in the undersampled meteorological data is accurate or not. Another possibility is the determination of a sinusoidal model from three-hourly numerical weather model data which is then removed from the surface pressure data.

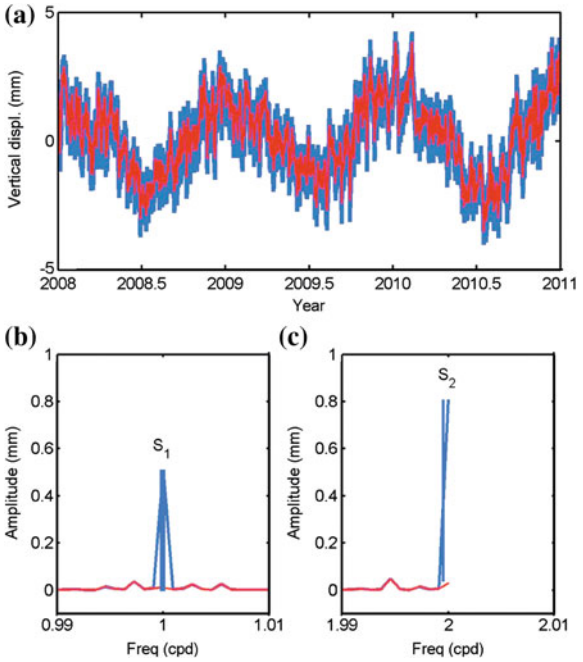

Fig. 5 **a** Time series with (*blue*) and without (*red*) tidal loading of vertical displacements at Fortaleza, Brazil and (**b**,**c**) the corresponding amplitude spectra of atmospheric loading signals

Following Petrov and Boy (2004), we derived the pressure tide model for each node of a 1° global grid of the ECMWF by estimating mean pressure, sine and cosine amplitudes of the $S_1(p)$ signal, and sine and cosine amplitudes of the $S_2(p)$ signal in the six-hourly pressure level data over the period from 1980.0 to 2011.0. After subtracting the modeled sinusoids from six-hourly pressure fields, Eqs. (9)–(11) were applied in order to obtain non-tidal loading displacements. Figure 5 shows the non-tidal loading vertical displacements at Fortaleza station (low-latitude, 3.88°S) in the time domain and the amplitude spectra of the corresponding atmospheric loading signals. Strong peaks containing tides at the frequencies of $S_1(p)$ and $S_2(p)$ are reduced to negligible magnitudes when the tidal signals in surface pressure are removed. The total loading displacement is the sum of non-tidal displacement and the harmonic model of tidal loading displacements (see Sect. 2.1.2).

Examples for signals of non-tidal loading displacements at Fortaleza and Wettzell (mid-latitude, 49.15°N) in vertical and horizontal directions are shown in Fig. 6. The horizontal displacements are derived by taking the square-root of the sum of the squares of the East and North components. The displacements at Fortaleza are typical for coastal and lower latitude sites as the variations are fairly low due to smaller pressure fluctuations near the equator and because of the IB effect, due to the proximity to the Atlantic Ocean. The displacements at a mid-latitude and non-coastal site (Wettzell) indicate large vertical variations in the order of 5–15 mm.

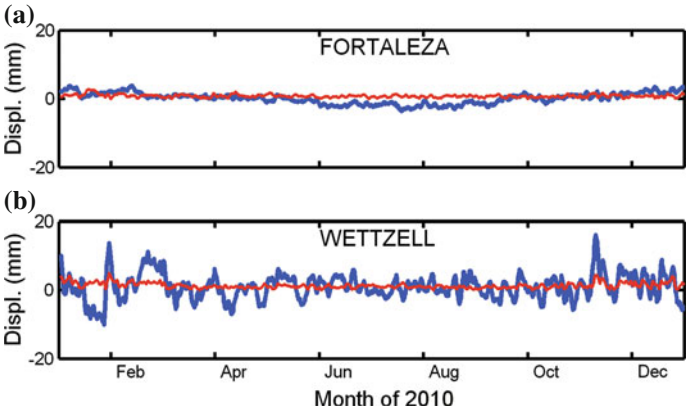

Fig. 6 Non-tidal loading displacements at Fortaleza, Brazil and Wettzell, Germany in *vertical* (*blue*) and *horizontal* (*red*) directions. The horizontal displacements are derived by taking the square-root of the sum of the squares of the East and North components

Examining Fig. 6b, we find that peak-to-peak variations in the vertical direction occur with a period of about 5–12 days which corresponds to the circulations of high and low pressure structures in mid-latitude regions, partly due to baroclinic variability (Dell'Aquila et al. 2005). These timescales also represent the limit of validity of the IB assumption for describing the oceanic response to atmospheric pressure forcing. It is obvious that the displacements contain annual (Fig. 5a) as well as sub-seasonal signals (Fig. 6b), with increasing magnitude during the winter months.

2.1.2 Tidal Loading Displacements

To account for tidal loading displacements, Ponte and Ray (2002) developed a gridded global model of $S_1(p)$ and $S_2(p)$ pressure tides using the six-hourly field of the ECMWF operational analysis. The $S_2(p)$ standing wave was propagated by applying the interpolation procedure proposed by van den Dool et al. (1997). Comparisons with "ground station" tidal estimates at meteorological stations suggest that their model is reasonably realistic and, thus, it has been recommended in the IERS Conventions 2010 (Petit and Luzum 2010). However, a large drawback remains, as the resulting spatial variations of amplitude and phase of atmospheric tides are somewhat too smooth, especially for the $S_2(p)$ tide (Petrov and Boy 2004). This disadvantage is due to the interpolation procedure that requires filtering out non-migrating tidal components.

At Vienna University of Technology, we used the three-hourly pressure level data from the so-called 'Delayed Cut-off Data Analysis' (DCDA) stream of the ECMWF over the time period from 2005.0 to 2011.0 with a spatial resolution of 1°. The 'cut-off time' is the latest possible arrival time for meteorological observations to

be incorporated in an analysis cycle. Six-hourly and twelve-hourly analysis cycles are combined with short-term forecasts, so that the cut-off time can be delayed and operational products can be made available earlier, as well. A further characteristic is the higher temporal resolution of 3 h that makes use of short-term forecasts.

The use of these data provides some potential for improvements since the known westward propagating waves can be well captured avoiding the need to propagate the $S_2(p)$ standing wave by interpolation. Instead we are able to consider both migrating and non-migrating tidal components. Furthermore, the sampling data permit the proper determination of the $S_1(p)$, $S_2(p)$, and $S_3(p)$ atmospheric tides.

We developed a global gridded model of the $S_1(p)$, $S_2(p)$, and $S_3(p)$ pressure tides using the annual mean model described in Ray and Ponte (2003). Then, sine and cosine amplitudes of each model were convolved with the Green's functions to determine sine and cosine amplitudes of the $S_1(l)$, $S_2(l)$, and $S_3(l)$ tidal loading displacements in vertical and horizontal directions. In the convolution step, we did not invoke the IB assumption but instead considered that the oceanic response at subdaily timescales to the tidal variation in pressure is negligible (Tregoning and Watson 2009).

Since the amplitude of the vertical tidal loading displacement is about three times larger than that in the horizontal displacement, we only show the displacements in the vertical direction in Fig. 7. The displacement magnitude for $S_1(l)$ and $S_2(l)$ reaches 1–2 mm in low latitude regions, but decreases to negligible displacements at the poles. The $S_3(l)$ tidal displacement shows weak latitude dependency and its amplitude is about ten times smaller than those of the $S_1(l)$ and $S_2(l)$ vertical tidal displacements.

It is well known that the $S_1(p)$ atmospheric tide is dominated by large non-migrating components with complicated spatial distributions (Haurwitz and Cowley 1973; Dai and Wang 1999; Ray and Ponte 2003). This signal is susceptible to significant diurnal boundary-layer effects over land masses and land-ocean boundaries. Dai and Wang (1999) mentioned that the upward sensible heat flux from the ground due to solar heating contributes significantly to the non-migrating component of $S_1(p)$. The main migrating component is most apparent over the tropical oceans where the progression of phases shows an approximately constant westward motion. These $S_1(p)$ pressure tide characteristics are well captured in the $S_1(l)$ tidal displacements, where topographic and land-ocean boundary features are clearly seen.

The latent heating associated with convective precipitation, which has a strong diurnal cycle and supplements the direct solar radiational heating, was found to be important mostly for the $S_2(p)$ tide. Therefore, oscillation of the $S_2(p)$ tide is dominated by its migrating component, which is moving westward with the speed of the mean Sun, and is regularly distributed over the globe (Dai and Wang 1999). These $S_2(p)$ pressure tide characteristics can be seen clearly in the $S_2(l)$ tidal displacements.

According to Aso (2003), the ter-diurnal $S_3(p)$ tide has also been detected in the temperature and wind fields in various radar and optical observations. The origin of this tide is still uncertain. If it is a global and migrating tidal wave with zonal wave number three, it is excited either by the third harmonic of heating due to solar insolation absorption by water vapor and ozone or by non-linear interaction of the migrating components of $S_1(p)$ and $S_2(p)$. Interactions between the $S_2(p)$ tide and

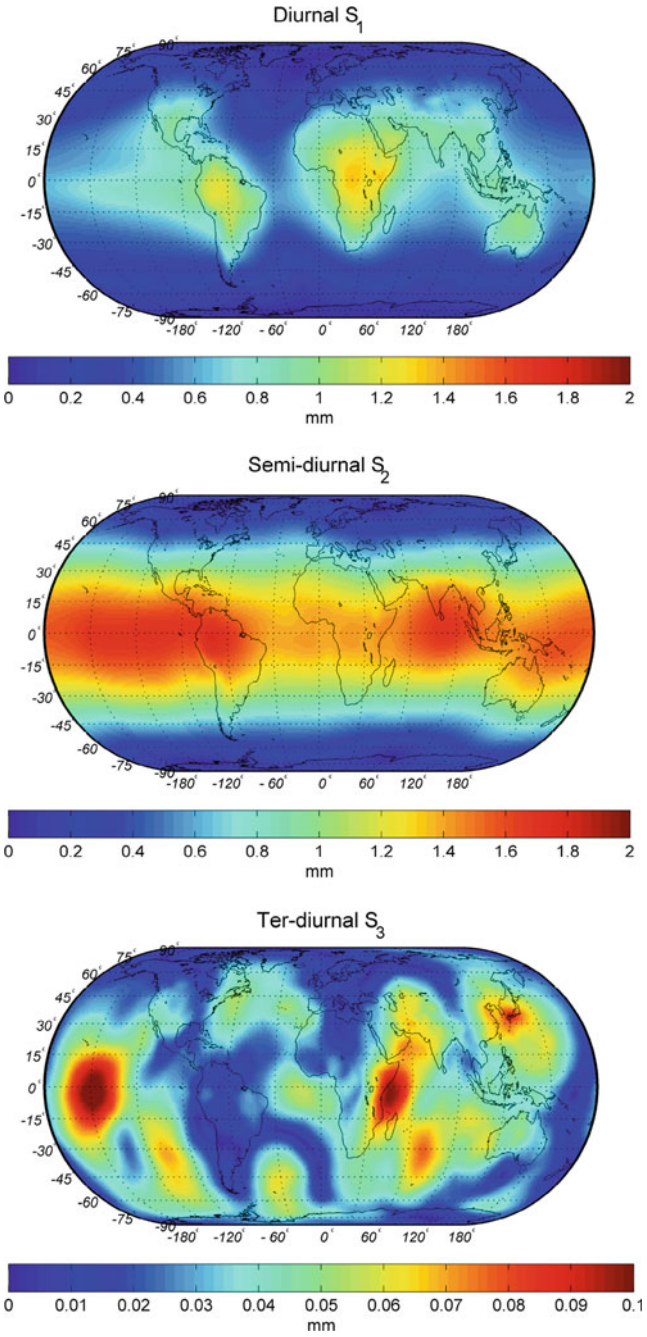

Fig. 7 The amplitude of the $S_1(l)$ (*upper panel*), $S_2(l)$ (*middle panel*), and $S_3(l)$ (*lower panel*) tidal loading displacements in *vertical* direction

gravity waves can also produce ter-diurnal oscillations. Due to interactions of tidal and gravity waves, the $S_3(p)$ tide is irregularly distributed over the globe (Aso 2003).

2.1.3 APL Services

APL services that provide 6-hourly vertical and horizontal corrections for VLBI, GNSS, SLR sites as well as for the nodes on global grids have been established by several institutions. Each service applies different methods and data to calculate the displacements. Here, we briefly describe three services that provide global models of the displacements from 1980 onward.

- **University of Luxembourg**. The displacements have been derived using the method originally outlined in van Dam and Wahr (1987) with slight modifications in determination of the ocean mask, reference pressure and removing the erroneous atmospheric tides. In van Dam and Wahr (1987), a 2.5° × 2.5° land-sea mask was used. Presently, they use a 0.25° × 0.25° land-sea mask. Units that contain only land are assigned the surface pressure defined by the original NCEP gridded file. Those with only water are assigned the modified IB pressure, defined in van Dam and Wahr (1987). 2.5° × 2.5° grid units containing water and land are subdivided into 0.25° × 0.25° units, each assigned either the land value or the IB value as appropriate. They use a reference pressure determined as a 20 years mean. The pressure data are low pass filtered to remove the erroneous atmospheric tides in the surface pressure data. The filtering means that the online data are always 3–4 days behind the actual date.
- **Goddord Space Flight Center**. The method to calculate the displacements is thoroughly described by Petrov and Boy (2004). Non-tidal loading displacements are determined based on surface pressure data from NCEP with a horizontal resolution of 2.5°. The reference pressure is calculated by averaging 20 years of surface pressure data. To determine tidal loading displacements, the pressure tide model of Ponte and Ray (2002) is used. Petrov and Boy (2004) adopt the method of van Dam and Wahr (1987) to determine the land-sea mask.
- **Vienna University of Technology**. We use surface pressure as derived from pressure level data from operational analysis as well as re-analysis data sets from the ECMWF with a horizontal resolution of 1°. Tidal and non-tidal loading displacements are calculated using the methods described in Sects. 2.1.1 and 2.1.2. The Global Reference Pressure (GRP) model (Schuh et al. 2009) is used to calculate reference pressure. The 6-hourly vertical and horizontal corrections are provided for all VLBI sites as well as for the nodes on a global 1° grid.

Figure 8 shows the displacements at Algonquin Park (ALGOPARK), Canada in vertical and horizontal directions (unit mm) determined by the three APL services. It is obvious that the displacements provided by the Luxembourg and the Petrov and Boy services are very similar with very small differences. The Vienna service produces slightly different results from those of the other two. The difference could

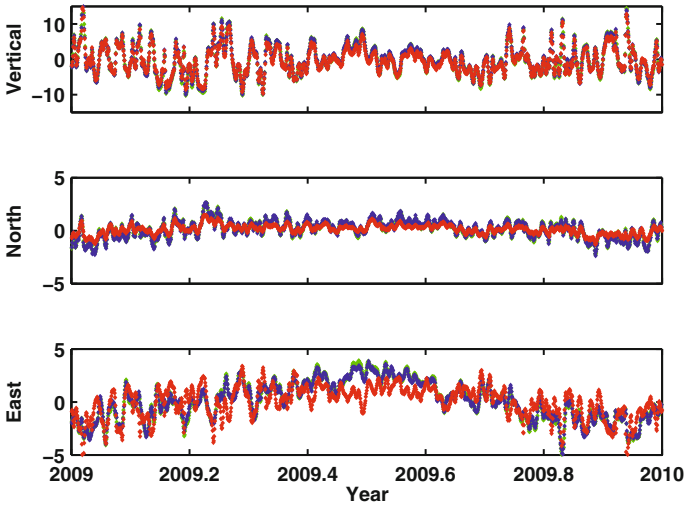

Fig. 8 APL displacements at Algonquin Park (ALGOPARK), Canada in *radial* and *horizontal* directions (unit mm) determined by the three services: Luxembourg (*green*), Petrov and Boy (*blue*) and Vienna (*red*)

be due to different data input (surface versus pressure level, NCEP versus ECMWF) and the land-sea masks used.

2.2 Empirical Model

From Sect. 2.1, it can be seen that APL effects primarily cause vertical displacements of the Earth's crust and therefore it is possible to determine linear regression coefficients between the size of the vertical displacement and surface pressure variation. To estimate the regression coefficients, Rabbel and Zschau (1985) utilized a geophysical approach (Sect. 2.1) with idealized Gaussian pressure distributions $P(\mathbf{r}) = P_m \; exp\left(\frac{-r^2}{r_o^2}\right)$ where P_m is the maximum pressure anomaly at the center of the geometric distribution of cyclones or anticyclones, r is the distance from the center of the distribution, and r_o is the scale length. They found that in general the line of regression between surface pressure and the vertical displacement has the form

$$U_r(\mathbf{r}) = C_1 \; [P(\mathbf{r}') - P_{ref}(\mathbf{r}')] + C_2 \; P_m \tag{12}$$

where C_1 and C_2 are the coefficients which are dependent on r_o and $\frac{P(\mathbf{r})}{P_m}$, respectively. They concluded that there is no unique single regression coefficient between local displacements and local surface pressure and that it is therefore also necessary to

Table 1 C_1 coefficients at some space geodetic stations in mm/hPa

Station	GPS (van Dam et al. 1994)	VLBI (MacMillan and Gipson 1994)	Model (van Dam et al. 1994)
Fairbank	-0.59 ± 0.14	-0.35 ± 0.07	-0.44 ± 0.006
Onsala	-0.00 ± 0.11	-0.16 ± 0.13	-0.29 ± 0.005
Wettzell	-0.30 ± 0.17	-0.53 ± 0.80	-0.43 ± 0.008
Goldstone	-0.80 ± 0.47	-0.30 ± 0.13	-0.40 ± 0.019
Kokee	0.35 ± 0.77	-0.49 ± 0.35	-0.11 ± 0.024

specify the scale length r_o. Their regression coefficient C_1 (mm/hPa) changes from approximately -0.1 mm/hPa at $r_o = 160$ km to -0.9 mm/hPa at $r_o = 5500$ km.

The work of Rabbel and Zschau (1985) had been extended by determining the C_1 coefficient from the vertical displacements as deduced by VLBI (van Dam and Wahr 1987; MacMillan and Gipson 1994; Petrov and Boy 2004) and GNSS (van Dam and Herring 1994; van Dam et al. 1994; Kaniuth and Vetter 2006; Dach et al. 2011) observations. The C_1 coefficient determined by van Dam and Herring (1994) and MacMillan and Gipson (1994) are in the range of -0.4 to -0.6 mm/hPa for inland sites, which corresponds to scale lengths r_o of 1000–2000 km (synoptic scale) in the simple Gaussian pressure model of Rabbel and Zschau (1985). Therefore, most of the variance of APL displacements is determined by synoptic scale pressure variations. This is reasonable since the largest surface pressure variations are synoptic. In most regions of the Earth it should be a good approximation to model the loading effects at a site using only the site pressure.

Table 1 shows the C_1 coefficients at some fundamental stations derived by linear regression between GPS or VLBI vertical positions and local pressure as well as regression between modeled vertical displacement (derived using the method in Sect. 2.1) and local pressure. The coefficients determined by VLBI observations more closely match the coefficients predicted by the model than the GPS results. This may indicate that the loading signal is correlated with another signal in the GPS data processing. GPS or VLBI vertical position estimates and modeled vertical displacements produce different coefficients for Kokee Park, which may be due to inverted barometer effects as this station is located on Kauai, a rather small island in the Pacific Ocean. As Rabbel and Zschau (1985) noted the simple loading functions as given by Eq. (12) can only be applied to anomalous pressure on the continental surface far from any coastlines. On the ocean floor, passing cyclones cause a more complicated effective pressure distribution due to reaction of the water masses. In general, this reaction is dynamical and is affected by water depth, geometry of the coastlines, velocity of the cyclone in a highly complex way. Without any dynamical effects the ocean would react to air pressure changes like an inverse barometer and would compensate an air pressure low by raising the water level so that there is no pressure change on the ocean floor.

3 Study of APL Effects on Space Geodetic Measurements

Studies of APL effects on space geodetic measurements include the detection of the loading signal in the measurements (van Dam and Herring 1994; van Dam et al. 1994; Petrov and Boy 2004), the application of APL corrections at the observation level versus the post-processing level (Tregoning and van Dam 2005; Böhm et al. 2007; Dach et al. 2011), the impact of APL modeling on the precision of the measurements and other parameters (van Dam and Herring 1994; van Dam et al. 1994; Petrov and Boy 2004; Dach et al. 2011). A recent study was carried out by van Dam et al. (2010) who investigated the effects of unmodeled topographic variability on surface pressure estimates and subsequent estimates of vertical surface displacements.

van Dam and Herring (1994) used 1085 VLBI baseline length measurements (1984–1992) from 74 stations to detect the presence of APL signals in the measurements and to investigate the impact of applying APL corrections on the measurement precision. Their analysis indicates that 62 % of APL signal is found in the VLBI baseline residuals. For very accurate measurements, this signal has to be removed in order to avoid misinterpretation of the results. Applying APL effects on the observation level significantly reduces the weighted root-mean-square (WRMS) scatter of the baseline length residuals on 11 of the 22 baselines investigated.

Petrov and Boy (2004) carried out further studies on the presence of APL signals in the VLBI baseline measurements and coordinates. They stated that their approach can estimate the APL displacements with errors less than 15 % of the effect itself. Their analysis of VLBI measurements of 40 stations for the time period from 1980 to 2002 demonstrates that approximately 95 % of the power of modeled vertical pressure loading signal and 97 % of the signal in the baseline lengths is found in VLBI data. They found also that approximately 84 % of the horizontal signal is contained in the VLBI measurements. Neglecting this signal adds noise to the horizontal position with an RMS of 0.6 mm and to the estimates of the EOP with an RMS of 20μas.

van Dam et al. (1994) assessed the influence of APL effects on GNSS station heights by analyzing daily positions of 20–40 GNSS sites for the time period of approximately 300 days. The application of APL corrections reduces the variance of the station heights by up to 24 % and the WRMS scatter of the baseline length residuals. Approximately 62 % of the investigated GNSS baselines show a reduction in their WRMS scatter. Fifty seven percent of APL signal is evident in the GNSS baseline length measurements. Furthermore, the use of regression coefficients of local pressure measurements appears to be valid at many GNSS sites. However, there are sites where the coefficients are unreliable.

Similar studies were done by Dach et al. (2011) who evaluated the impact of different methods of APL corrections in GNSS data analysis. They applied the corrections from a geophysical model at observation level, on weekly mean estimates of station coordinates at the post processing level, and they also solved for regression coefficients between the station displacements and the local pressure. Analysis of GNSS measurements from IGS stations in the period from 1994 to 2008 showed that the repeatability of station coordinates improves by 20 % when applying the cor-

rections at the observation level and by 10 % when applying them as weekly mean values at the post processing level to the resulting weekly coordinates, both compared with a solution without applying APL corrections. Furthermore, Dach et al. (2011) stated that APL corrections via regression coefficients are less beneficial than APL corrections at the observation level. This is due to the fact that the distribution of the pressure in the vicinity of the station has a significant impact on APL displacements and the effects in the horizontal components are completely ignored.

Bock et al. (2005) showed that an improvement of SLR measurements has been obtained when APL effects are modeled, but the magnitude of the improvement is rather small. Furthermore, there appears to be no noticeable effect in the SLR station time bias after accounting for APL effects.

We have studied the performance of the Vienna APL corrections and the Petrov and Boy (2004) models by analyzing 3183 24 h VLBI sessions from January 1990 to December 2009. The number of participating stations in each individual session was varying from 3 to 8. Figure 9 shows the difference between the variance of time series of site vertical components with and without applying APL corrections. In general, the application of APL models obviously improves the accuracy of the estimated coordinates, especially for the vertical components and to a lesser degree for the horizontal components (not shown here). We found that the variance of vertical components is deteriorated for only four sites, all of them are located near the coast, after applying either the Vienna-APL model or the Petrov and Boy (2004) model. SC-VLBA and MK-VLBA are placed on Bahamas and Hawaii islands, respectively, while SESHAN25 is near the coast. NL-VLBA is an inland site but it is close to the Great Lakes. Those sites are probably affected by the oceanic response

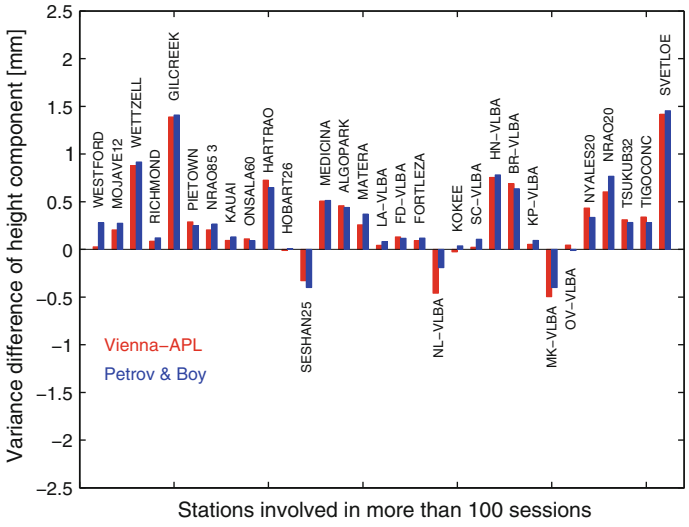

Fig. 9 Variance difference of time series of vertical component. Station name and latitude are plotted above the bar

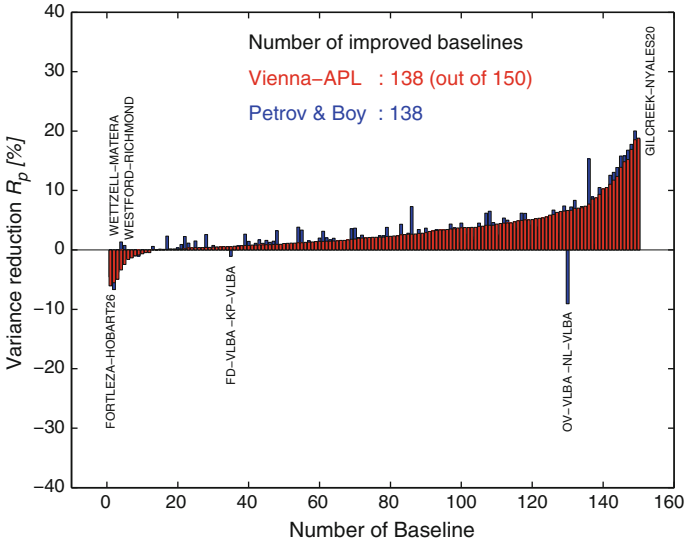

Fig. 10 Variance reduction power R_p of the baseline length residuals after applying the Vienna-APL (*red*) and the Petrov and Boy (*blue*) model

that is not adequately modeled in the IB corrections. This holds also for stations on a small island (Kokee Park on Hawaii) and near the coast (RICHMOND, ONSALA60) where the variance of vertical components is either only slightly improved or deteriorated marginally. It can clearly be seen that the biggest improvement is obtained for mid-latitude, inland sites (WETTZELL, GILCREEK, ALGOPARK, SVETLOE, HARTRAO), which are subject to the largest atmospheric loading effects.

To assess the improvement in power of the baseline repeatability after applying the APL corrections, we analyzed the variance reduction power R_p (in percent) as:

$$R_p = \frac{\Delta\sigma^2}{\sigma^2_{no-apl}} \times 100\,\%, \tag{13}$$

where positive R_p will give an indication of baseline improvement when applying an APL model. We plot the variance reduction power R_p in Fig. 10. The use of the Vienna-APL model reduces the variance of the baseline length residuals by as much as 20 % (with the mean variance reduction about 3 %) and improves the repeatability for 85 % (127 out of 150) of the baseline lengths. These improvements are similar those reported by Petrov and Boy (2004) (77 %, 116 out of 150).

Acknowledgments We would like to thank the reviewer, Jean-Paul Boy, for checking this part of the book and providing very valuable suggestions. We are grateful for the financial support from the Austrian Science Fund (FWF, P20902-N10).

References

T. Aso. An overview of the terdiurnal tide observed by polar radars and optic. *Adv. Polar Upper Atmos. Res.*, 17: 167–176, 2003.

D. Bock, R. Noomen, and H.G. Scherneck. Atmospheric pressure loading displacement of SLR stations. *J. Geodyn.*, 39: 247–266, 2005.

J. Böhm, R. Heinkelmann, P.J. Mendes, and H. Schuh. Short note: a global model of pressure and temperature for geodetic applications. *J. of Geod.*, 81 (10):679–683, doi:10.1007/s00190-007-0135-3, 2007.

J.P. Boy and B.F. Chao. Precise evaluation of atmospheric loading effects on earth's time-variability gravity field. *J. Geophys. Res.*, 110: B08412, doi:10.1029/2002JB002333, 2009.

R. Dach, J. Böhm, S. Lutz, P. Steigenberger, and G. Beutler. Evaluation of the impact of atmospheric pressure loading modeling on GNSS data analysis. *J. Geod.*, 85: 75–91, doi:10.1007/s00190-010-0417-z, 2011.

A. Dai and J. Wang. Diurnal and semidiurnal tides in global surface pressure fields. *J. of Atm. Science*, 56: 3874–3891, 1999.

A. Dell'Aquila, V. Lucarni, and P.M. Ruti. Hayashi spectra of the northern hemisphere mid-latitude atmospheric variability in the NCEP-NCAR and ECMWF reanalysis. *Climate Dynamics*, 25: 639–652, 2005.

W.E. Farrell. Deformation of the earth by surface loads. *Rev. Geophys.*, 10: 751–797, 1972.

J. Geng, S.D.P. Williams, F.N. Teferle, and A.H. Dodson. Detecting storm surge loading deformations around the southern North Sea using subdailly GPS. *Geophys. J. Int.*, 191: 569–578 doi:10.1111/j.1365-246X.2012.05656.x, 2012.

B. Haurwitz and A.D. Cowley. The diurnal and semidiurnal barometric oscillations, global distribution and annual variation. *Pure Appl. Geophys.*, 102: 193–222, 1973.

B. Hofmann-Wellenhof and H. Moritz. *Physical Geodesy.* pringer, Wien - New York, 2005.

K. Kaniuth and S. Vetter. Estimating atmospheric pressure loading regression coefficients from gps observations.*GPS Solut.,* 10: 126–134, doi:10.1007/s10291-005-0014-4, 2006.

D.S. MacMillan and J.M. Gipson. Atmospheric pressure loading parameters from very long baseline interferometry observations. *J. Geophys. Res.,* 99 (B9): 18,081–18,087, doi:10.1029/94JB01190, 1994.

G. Petit and B. Luzum. IERS Conventions 2010. Technical Report 36, IERS Technical Note, 2010.

L. Petrov and J.P. Boy. Study of the atmospheric pressure loading signal in very long baseline interferometry observations. *J. Geophys. Res.,* 109 (B03405): 1–14, doi:10.1029/2003JB002500, 2004.

R.M. Ponte and R.D. Ray. Atmospheric pressure corrections in geodesy and oceanography: A strategy for handling air tides. *Geophys. Res. Lett.,* 29 (24): 2153–2156, doi:10.1029/2002GL016340, 2002.

W. Rabbel and J. Zschau. Static deformation and gravity changes at the earth's surface due to atmospheric loading. *J. Geophys.,* 56:81–99, 1985.

R.D. Ray and R.M. Ponte. Barometric tides from ECMWF operational analyses. *Ann. Geophys.,* 21:1897–1910, 2003.

H. Schuh, M. Schindelegger, D.D. Wijaya, J. Böhm, and D.A. Salstein. Memo: A method for the definition of global reference pressure. http://www.ggosatm.hg.tuwien.ac.at/LOADING/REFPRES/global_reference_pressure_memo.pdf, 2009

P. Tregoning and T.M. van Dam. Atmospheric pressure loading corrections applied to GPS data at the observation level. *Geophys. Res. Lett.,* 32:L22310, doi:10.1029/2005GL024104, 2005.

P. Tregoning and C. Watson. Atmospheric effects and spurious signals in GPS analysis. *J. Geophys. Res.,* 114 (B09403, 15 PP.): doi:10.1029/2009JB006344, 2009.

T.M. van Dam, G. Blewitt, and M.B. Heflin. Atmospheric pressure loading effects on global positioning system coordinate determinations. *J. Geophys. Res.,* 99 (B12): 23,939–23,950, doi:10.1029/94JB02122, 1994.

T.M. van Dam and J. Wahr. Displacements of the earth's surface due to atmospheric loading: Effects on gravity and baseline measurements. *J. Geophys. Res.,* 92 (B2): 1281–1286, doi:10.1029/JB092iB02p01281, 1987.

T.M. van Dam and T.A. Herring. Detection of atmospheric pressure loading using very long baseline interferometry measurements. *J. Geophys. Res.,* 99 (B3): 4505–4517, doi:10.1029/93JB02758, 1994.

T.M. van Dam, Z. Altamimi, X. Collilieux, and J. Ray. Topographycally induced height errors in predicted atmospheric loading effects. *J. Geophys. Res.,* 115 (B07415, 10 PP.): doi:10.1029/2009JB006810, 2010.

H. van den Dool, S. Saha, J. Schemm, and J. Huang. A temporal interpolation method to obtain hourly atmospheric surface pressure tides in reanalysis 1979–1995. *J. Geophys. Res.,* 102 (D18): 22,013–22,024, doi:10.1029/97JD01571, 1997.

J.M. Wahr. The effects of the atmosphere and oceans on the Earth's wobble and on the seasonal variations in the length of day - II. Results. *Geophysical Journal of the Royal Astronomical Society,* 74: 451–487, 1983.

J.M. Wallace and P.V. Hobbs. *Atmospheric science: an introductory survey*. Academic Press, 2nd edition, 2006.

D. Wunsch and D. Stammer. Atmospheric loading and the oceanic "inverted barometer" effects. *Rev. Geophys.,* 35: 79–107, 2010.

Atmospheric Effects on Gravity Space Missions

Maria Karbon, Johannes Böhm, Dudy D. Wijaya and Harald Schuh

Abstract The varying atmosphere exerts two disturbing forces on the gravity signal: first the so-called direct effect or Newtonian attraction, where the object in questions is attracted by the atmospheric mass itself; and second the indirect effect or atmospheric loading, where the overlying atmospheric mass has a deforming effect on the Earth's surface, also changing the measured gravity signal. In satellite gravity missions, these short-period signals cause aliasing effects in the gravity field determination and their elimination is indispensable. For the determination of the required atmospheric gravity field coefficients, it is state of the art to use high-resolution numerical weather models, which take into account the three-dimensional distribution of the atmospheric mass. In this part of the book, we address many relevant issues, including the theoretical fundamentals of the Earth's gravity field and its description using spherical harmonics, as well as the basics of the atmospheric pressure distribution. A short overview of the gravity satellite missions of the last decade like GRACE (Gravity Recovery and Climate Experiment) is given and the

M. Karbon (✉)
Section 1.1 GPS/Galileo Earth Observations, Helmholtz Centre Potsdam GFZ German Research Centre for Geosciences, Telegrafenberg A 17, 14473 Potsdam, Germany
e-mail: karbon@gfz-potsdam.de

J. Böhm
Department of Geodesy and Geoinformation, Vienna University of Technology, Gußhausstraße 27-29, 1040 Vienna, Austria
e-mail: johannes.boehm@tuwien.ac.at

D. D. Wijaya
Geodesy Research Group, Institute of Technology Bandung, Ganesha 10, Bandung-West Java, Indonesia
e-mail: dudy@gd.itb.ac.id

H. Schuh
Department 1 Geodesy and Remote Sensing, Helmholtz Centre Potsdam GFZ German Research Centre for Geosciences, Telegrafenberg A 17, 14473 Potsdam, Germany
e-mail: schuh@gfz-potsdam.de

J. Böhm and H. Schuh (eds.), *Atmospheric Effects in Space Geodesy*, Springer Atmospheric Sciences, DOI: 10.1007/978-3-642-36932-2_5,

impact of the atmosphere on the satellite measurements is examined. We present a descriptions of the oceanic mass response to overlying atmospheric pressure and of the models used for de-aliasing of atmospheric effects.

1 Theory of the Gravity Field

The purpose of this section is to introduce the fundamentals of the potential theory, i.e. gravity acceleration and gravity potential with their most important relationships. Also an introduction to spherical harmonics is given. The following information can be found in more detail in Hofmann-Wellenhof and Moritz (2005) and Torge (1989).

1.1 Gravity Potential and Gravity Acceleration

According to Newton's law of gravitation, two point masses m_1 and m_2 separated by a distance r attract each other with a force

$$\mathbf{F} = G\frac{m_1 m_2}{r^2}\mathbf{r}_0, \tag{1}$$

where $G = 6.6742 \times 10^{-11}\,\mathrm{m^3\,kg^{-1}\,s^{-2}}$ is the gravitational constant (Hofmann-Wellenhof and Moritz 2005). By setting one mass to unity and denoting the attracting mass with m, we express the force $\mathbf{F}$ exerted by the mass m on a unit mass at location P and distance r as

$$\mathbf{F} = G\frac{m}{r^2}\mathbf{r}_0. \tag{2}$$

This representation of the *gravitational attraction* can be simplified if instead of the vector quantity acceleration $\mathbf{F}$ the scalar quantity of the *potential* V is used. Especially when looking at the attraction of point systems and solid bodies as it is done in geodesy, calculations can be simplified greatly.
Following Torge (1989)

$$rot\ \mathbf{F} = 0, \tag{3}$$

and therefore a corresponding potential V for the gravitational field $\mathbf{F}$ exists so that

$$\mathbf{F} = grad\ V, \tag{4}$$

where

$$V = \frac{Gm}{r}. \tag{5}$$

If more point masses are present, it is possible to sum up the individual forces. If the number of point masses becomes infinite the sum can be replaced by the integral, leading for a body v to

$$V = G \iiint_v \frac{\mathrm{d}m}{r} = G \iiint_v \frac{\rho}{r} \mathrm{d}v, \tag{6}$$

where $\mathrm{d}m$ is a mass element, $\mathrm{d}v$ a volume element, r the distance between the mass element and the attracted point P and ρ describes the density

$$\rho = \frac{\mathrm{d}m}{\mathrm{d}v}. \tag{7}$$

The potential V with the unit $\mathrm{m}^2\ \mathrm{s}^{-2}$ is continuous and finite and vanishes following $1/r$ for $r \to \infty$ which allows to approximate a body at large distances as a point mass. Also the first derivatives are continuous and finite in interior and exterior space. But at points where the density changes discontinuously, i.e. at the bounding surface or at density jumps in the interior, the second derivatives show discontinuities. This becomes evident when looking at *Poisson's equation*, which has to be satisfied by the potential V

$$\Delta V = -4\pi G\rho, \tag{8}$$

with

$$\Delta V = \frac{\delta^2 V}{\delta x^2} + \frac{\delta^2 V}{\delta y^2} + \frac{\delta^2 V}{\delta z^2}, \tag{9}$$

where Δ is the so called Laplace operator. In exterior space, where $\rho = 0$, this equation becomes the *Laplace equation*:

$$\Delta V = 0. \tag{10}$$

1.2 Gravity field of the Earth

In a rotating system, such as the Earth, the total force acting on a resting mass on the Earth's surface is the sum of the *gravitational force* and the *centrifugal force* due to the rotation. This quantity is called gravity vector:

$$\mathbf{g} = \mathbf{F} + \mathbf{F}_z. \tag{11}$$

In a rectangular coordinate system with its origin in the Earth center, its z-axis coinciding with the rotation axis and assuming that the x-axis points to the Greenwich meridian, the components of the centrifugal force acting on P are given by the vector of Earth rotation ω and the distance $p = \sqrt{x^2 + y^2}$ to the rotation axis (see Fig. 1).

Fig. 1 Centrifugal force

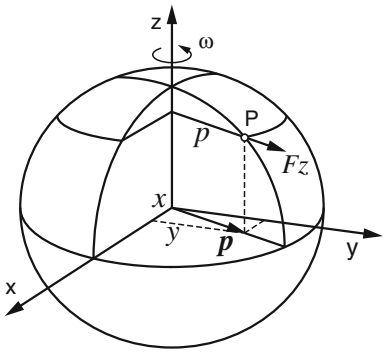

The vector $\mathbf{F}_z$ is given by

$$\mathbf{F}_z = \omega^2 \mathbf{p} = \begin{pmatrix} \omega^2 x \\ \omega^2 y \\ 0 \end{pmatrix} = grad\ \Phi = \begin{pmatrix} \frac{\delta \Phi}{\delta x} \\ \frac{\delta \Phi}{\delta y} \\ \frac{\delta \Phi}{\delta x} \end{pmatrix}. \tag{12}$$

The corresponding centrifugal potential function is

$$\Phi = \frac{1}{2}\omega^2(x^2 + y^2). \tag{13}$$

As mentioned above the gravity vector **g** is the resultant of the gravitational force **F** and the centrifugal force $\mathbf{F}_z$. Accordingly, the potential of gravity W is the sum of the potentials of the gravitational potential V and the centrifugal potential Φ:

$$W = W(x, y, z) = V + \Phi = G \iiint_v \frac{\rho}{r} \mathrm{d}v + \frac{1}{2}\omega^2(x^2 + y^2). \tag{14}$$

Combining the Laplace expression of Φ with Poisson's equation for V (Eq. 8), leads to the generalized Poisson equation for the gravity potential W:

$$\Delta W = -4\pi G\rho + 2\omega^2. \tag{15}$$

The gradient of W is called gravity vector and describes the total force acting on a unit mass.

$$\mathbf{g} = grad\ W = \left[\frac{\delta W}{\delta x} \frac{\delta W}{\delta y} \frac{\delta W}{\delta z} \right]. \tag{16}$$

The vector magnitude is called *gravity* and has the unit of an acceleration, and the direction of the vector is the direction of the plumb line.

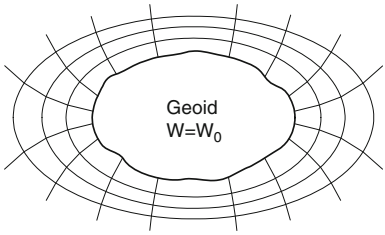

Fig. 2 Equipotential surfaces and plumb lines

Additionally to the centrifugal force $\mathbf{F}_z$ another fictitious force is acting on a moving body, the *Coriolis force*. It is proportional to the velocity of a moving mass within a rotating reference system. In case of the Earth it can be observed at clouds. As air moves from high to low pressure in the northern hemisphere, it is deflected to the right by the Coriolis force, in the southern hemisphere to the left (Hofmann-Wellenhof and Moritz 2005).

1.2.1 The Geometry of the Gravity Field

The gravity field can be described by surfaces of constant gravitational potential (see Fig. 2), i.e. equipotential surfaces or level surfaces, where

$$W(x, y, z) = const. \tag{17}$$

The surface of the oceans in a first approximation is part of such an equipotential surface. This particular surface was proposed by Carl Friedrich Gauss as the "mathematical figure of the Earth" and was later named *geoid* by the mathematician Johann Benedict Listing (Torge, 1989). Lines that intersect all equipotential surfaces orthogonally are called lines of force or plumb lines. The tangent to such a plumb line at any point equals the direction of the gravity vector at that point.

The differentiation of Eq. (16) leads to the *gravity gradient tensor*, also called *Eötvös tensor*:

$$grad\ \mathbf{g} = \Delta W = \begin{bmatrix} W_{xx} & W_{xy} & W_{xz} \\ W_{yx} & W_{yy} & W_{yz} \\ W_{zx} & W_{zy} & W_{zz} \end{bmatrix}. \tag{18}$$

The unit of the components is 1 Eötvös corresponding to 10^{-9} s^{-2} in SI-units. Due to the irrotational nature of the gravity field,

$$rot\ \mathbf{g} = rot\ grad\ W = 0, \tag{19}$$

and considering Poisson's differential in Eq. (8) and the centrifugal potential Φ in Eq. (13),

$$\Delta W = W_{xx} + W_{yy} + W_{zz} = -4\pi G\rho + 2\omega^2, \tag{20}$$

the gravity gradient tensor Eq. (18) contains only five independent elements, meaning the tensor is symmetric: $W_{xy} = W_{yx}$,$W_{xz} = W_{zx}$ and $W_{yz} = W_{zy}$. The third line of

the tensor represents the gravity gradient

$$(grad\ \mathbf{g}) = \left[W_{zx} W_{zy} W_{zz} \right], \tag{21}$$

which describes the changes of gravity with respect to the coordinate axes. W_{zx} and W_{zy} are the two components of the horizontal gradient lying in a local horizontal plane and W_{zz} describes the vertical gradient respectively. The vertical component is fundamental for the interpretation of the gravity data, with Eq. (20) we get

$$W_{zz} = \frac{\delta^2 W}{\delta z^2} = \frac{\delta g}{\delta z} = -(W_{xx} + W_{yy}) - 4\pi G\rho + 2\omega^2. \tag{22}$$

$(W_{yy} - W_{xx})$ and 2 W_{xy} characterize the curvature of potential surfaces, i.e. how the shape of potential surfaces differs from the shape of a sphere, W_{xy} and W_{zy} characterize how potential surfaces are not parallel to each other (Völgyesi 2001). The elements of the Eötvös tensor can be measured directly in space (see Sect. 3.1.3) or derived from gravity measurements. The torsion balance, also called torsion pendulum used for geodetic application, is usually credited to Loránd Eötvös (1848–1919) and can measure the components of the horizontal gradient W_{zx}, W_{zy} as well as the curvature $(W_{yy} - W_{xx})$ and W_{xy}, but not the vertical gradient W_{zz}.

1.3 Spherical Harmonics

Given that outside the attracting masses the gravitational potential V is a harmonic function, it is easier to handle if expanded into a series of *spherical harmonics*. Spherical harmonics are a special solution of the Laplace's equation; for the full derivation see Hofmann-Wellenhof and Moritz (2005).
In the exterior space V can be represented as

$$V(r, \theta, \lambda) = \frac{GM}{r} \sum_{n=0}^{\infty} \sum_{m=0}^{n} \left(\frac{a}{r}\right)^n P_{nm}(\cos\theta)(C_{nm} \cos m\lambda + S_{nm} \sin m\lambda), \tag{23}$$

where G is the gravitational constant and M the total mass of the Earth (solid, liquid and gaseous portions) and a is the mean radius of the Earth. The *associated Legendre functions* P_{nm} of degree n and order m are given for the argument $t = \cos\theta$ by:

$$P_{nm}(t) = (1 - t^2)^{\frac{m}{2}} \frac{\mathrm{d}^m}{\mathrm{d}t^n} P_n(t), \tag{24}$$

with the Legendre polynomials P_n

$$P_n(t) = P_{n0}(t) = \frac{1}{2^n n!} \frac{\mathrm{d}^n}{\mathrm{d}t^n} (t^2 - 1)^n. \tag{25}$$

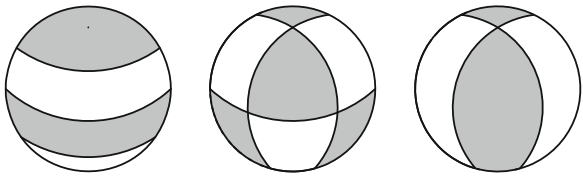

Fig. 3 Spherical harmonics: **a** zonal, **b** tesseral, **c** sectoral

For the gravity field determination, *fully normalized spherical harmonics* are usually used, with the condition that the average square of any fully normalized harmonic is unity:

$$\overline{P}_{nm}(t) = \sqrt{\frac{k(2n+1)(n-m)!}{(n+m)!}} P_{nm}(t), \tag{26}$$

with $k = 1$ for $m = 0$ and $k = 2$ for $m \neq 0$. Legendre functions multiplied by $\cos m\lambda$ or $\sin m\lambda$ are called surface spherical harmonics and are used as in Eq. (23) to describe the spatial characteristics of V on a spherical surface.
The associated Legendre functions change their sign $(n-m)$ times within the interval $0 \leq \theta \leq \pi$ and the functions $\cos m\lambda$ and $\sin m\lambda$ do change the sign $2m$ times in the interval $0 \leq \lambda \leq 2\pi$, dividing the surface at geodetic parallels and meridians into cells which are alternatingly positive and negative. For $m \neq 0$ they divide the sphere into a chequered pattern and are called tesseral harmonics (Fig. 3b). For special cases when $m = 0$ the spherical harmonics do not depend on the longitude and divide the sphere into zones parallel to the equator and are called zonal (Fig. 3a), or if $n = m$ then the spherical harmonics degenerate into functions that divide the sphere into sectors following the meridians and are therefore named sectoral (Fig. 3c).

Comparing Eq. (23) with Eq. (6) it becomes clear that the spherical harmonic coefficients C_{nm} and S_{nm} are describing mass integrals of the Earth gravity field with

$$\left\{ \begin{matrix} C_{nm} \\ S_{nm} \end{matrix} \right\} = \frac{1}{(2n+1)Ma^n} \iiint\limits_{Earth} r^n \overline{P}_{nm}(\cos\theta) \left\{ \begin{matrix} \cos m\lambda \\ \sin m\lambda \end{matrix} \right\} \mathrm{d}M. \tag{27}$$

The first degree coefficients are related to the rectangular coordinates of the center of gravity, i.e. the geocenter. Following Hofmann-Wellenhof and Moritz (2005) and Torge (1989) we get:

$$C_{10} = \frac{1}{a^2 M} \iiint\limits_{Earth} z' \mathrm{d}M\,, \qquad C_{11} = \frac{1}{a^2 M} \iiint\limits_{Earth} x' \mathrm{d}M,$$

$$S_{10} = \frac{1}{a^2 M} \iiint\limits_{Earth} y' \mathrm{d}M. \tag{28}$$

If the origin of the coordinate system coincides with the center of gravity, then these coordinates and thus the degree 1 coefficients are zero. The second degree coefficients are functions of the momentum of inertia and can be related directly to the figure of the Earth. Thus C_{20} describes the flattening of the Earth and corresponds to the dynamic form factor $J_2 \widehat{=} -C_{20}$. $C_{21} = S_{21} = 0$ given that the z-axis approximately coincides with the principal axis of inertia. C_{22} and S_{22} describe the asymmetry of the equatorial mass in relation to the rotation axis and the torsion of the corresponding principal axes of inertia (Hofmann-Wellenhof and Moritz 2005; Torge 1989).

2 Atmospheric Surface Pressure

2.1 Total Mass of the Atmosphere

The mass changes within the atmosphere, i.e. the gaseous part of the system Earth, contribute to the total mass exchange inside the entire system. However, there is no possibility to separate the individual components through gravity field observations. Various authors have tried to estimate the total mass of the atmosphere evaluating different global pressure fields as pressure reflects directly the mass of the atmosphere (Ekholm 1902; Trenberth and Guillemot 1994; Trenberth and Smith 2005).

The estimates of the authors vary significantly, starting from 5.16×10^{18} to 5.32×10^{18} kg. One reason for this are the different approaches within the atmospheric sciences and for geodesy. A second reason are the different models used, and the differences within the models themselves. Most recent studies however, show a slight increase in the atmospheric mass over the last decades that can be associated with an increase of water vapor. Figure 4 shows a time series of the global mean surface

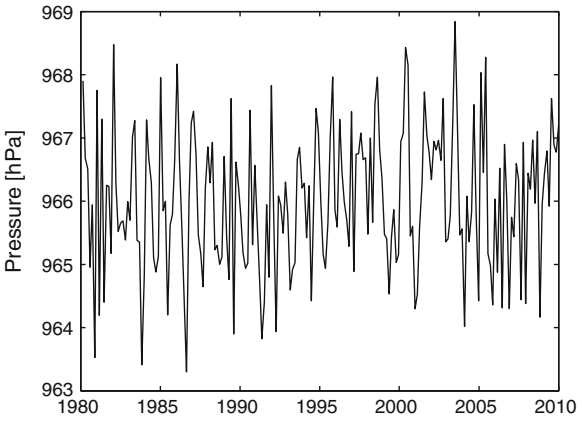

Fig. 4 Global mean surface pressure in hPa from ECMWF analysis (1980–2009) pressure level data reduced to surface topography

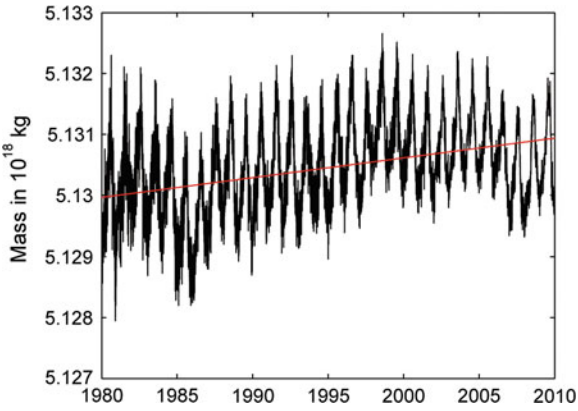

Fig. 5 Global mass change of the atmosphere derived from C_{00} based on ECMWF operational analysis (1980–2009) pressure level data reduced to surface topography

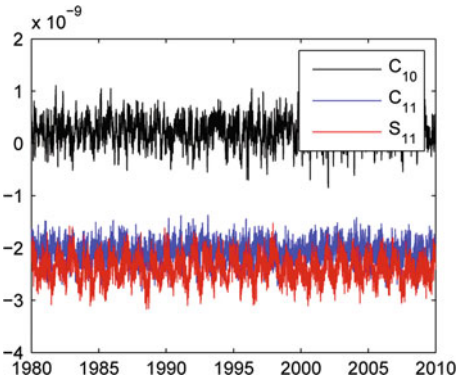

Fig. 6 Degree 1 TL-coefficients derived from ECMWF operational analysis (1980–2009) pressure level data reduced to surface topography, in black C_{10}, in blue C_{11} and in red S_{11}

pressure from the ECMWF operational analysis and re-analysis data over 30 years, where the most prominent signal is the yearly variation, which is primarily due to changes in the hydrological cycle adding water vapor to the air, particularily in the Northern Hemisphere summer.

The degree 0 coefficient of the atmospheric potential field is directly linked to the total mass of the atmosphere. Figure 5 shows the time series of the mass change derived from the C_{00} atmospheric gravity coefficient of the years 1980 until 2009. The yearly signal is clearly visible. Also a notable trend becomes evident which suggests an increase of the atmospheric mass of 3.26×10^{13} kg/year. Considering that atmospheric mass changes are caused mainly through variation of its wet part, it is an indication that the atmosphere has become warmer and thus more humid within this period.

Figure 6 shows a time series of the degree 1 coefficients C_{10}, C_{11} and S_{11} which are closely tied to the center of mass (see Eq. (28)). In contrast to the mass, in this

time series no significant trend becomes evident, although other studies (Gruber et al. 2009) show changes of the geocenter up to 2.6 mm per year in x-, 0.8 in y- and 6.7 in z-direction.

2.2 Variation of the Atmospheric Pressure

Although the change in the global mean of the atmospheric mass is small (the range for the 30 years in Fig. 4 is 5.5 hPa), the changes within smaller temporal and spacial scales can be of several tens of hPa. Such changes in the atmosphere are responsible for one of the biggest signals in the time variable gravity field (Warburton and Goodkind 1977). Typically, the surface pressure variations are larger in mid and high latitudes, whereas in tropical regions they are rather small. Figure 7 shows the RMS pressure variability using ECMWF surface pressure data for 2008.

Generally atmospheric phenomena can be categorized based on their time variability. One class consists of long term variations, such as seasonal, annual and inter-annual variations. The global atmospheric pressure cycle (Fig. 4), the seasonal variation between northern and southern hemisphere or mass transport between land and ocean such as the monsoon fall into this category. The El Niño southern oscillation (ENSO) classifies for inter-annual variations (McPhaden 2002), just as the North-Atlantic Oscillation (NAO) (Hurrell and van Loon 1997).

The second class contains short term variations, containing signals like the diurnal and semi-diurnal solar tides (see Fig. 8a, b). But the most prominent variations are introduced by (anti-) cyclones, which can reach 50–60 hPa in central Europe (Rabbel and Zschau 1985) within a few days, in Scandinavia even 80 hPa. But also extreme events such as hurricanes fall into this class. At the center of a hurricane the pressure can drop by 100 hPa within hours.

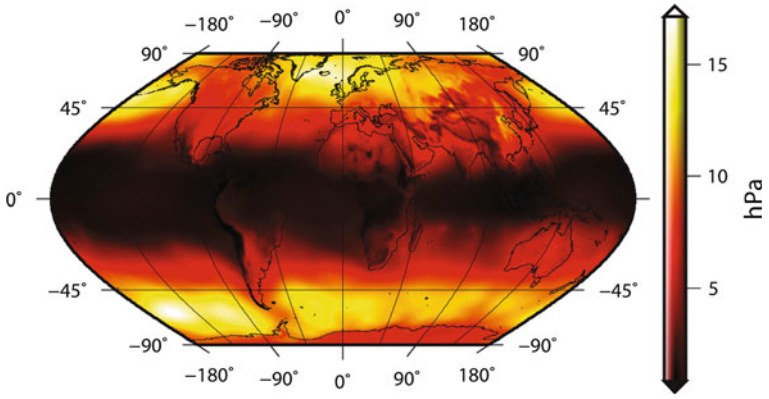

Fig. 7 RMS of ECMWF surface pressure over the year 2008

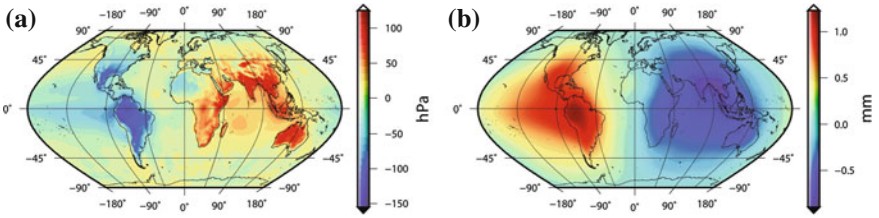

Fig. 8 **a** Diurnal S1 tide at 00 UTC in hPa. **b** Corresponding effect on the geoid in millimeter

3 Atmospheric Modeling for Space Missions

This section gives an introduction to the various satellite borne systems developed in the recent decade to determine the Earth gravity field from space as well as some ideas and proposals for future missions. Furthermore the interaction between the satellites and the atmosphere plus the resulting effects will be addressed as well as methods to correct for them.

3.1 Satellite Gravity Missions

Prior to the satellite era, when the gravity measurements were terrestrial and airborne, the Earth gravity field was known with a high accuracy only for a few regions of the world, whereas in large parts of the globe were virtually no gravity data. The aim of satellite based gravity field exploration was to close these gaps. For this purpose three different concepts were developed and realized. A short introduction is given in the following chapters.

3.1.1 CHAMP: Satellite-to-Satellite-Tracking in High-Low Mode

The orbit of a Low Earth Orbit (LEO) satellite is continuously monitored by GNSS satellites and an on board three-dimensional accelerometer measures the perturbing accelerations caused by the Earth gravity field. These observables correspond to the first derivative of the gravitational potential. This principle was realized within CHAMP (CHAllenging Minisatellite Payload, (Reigber et al. 2002)) (Fig. 9).

CHAMP was a satellite mission led by the GFZ (German Research Centre for Geosciences) for geoscientific and atmospheric research and applications, launched on 15 July 2000 and ended 19 September 2010. It was equipped with magnetometer, accelerometer, star sensor, GPS receiver, laser retro reflector, and an ion drift meter, operated in a near polar orbit in 454 km initial altitude. CHAMP was the first satellite to be able to simultaneously generate highly precise gravity and magnetic field measurements. For further information see: http://www-app2.gfz-potsdam.de/pb1/op/champ/.

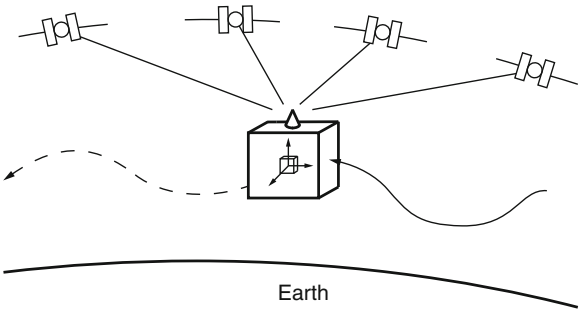

Fig. 9 Scheme of CHAMP: one on-board 3-axis accelerometer, tracked by GNSS satellites

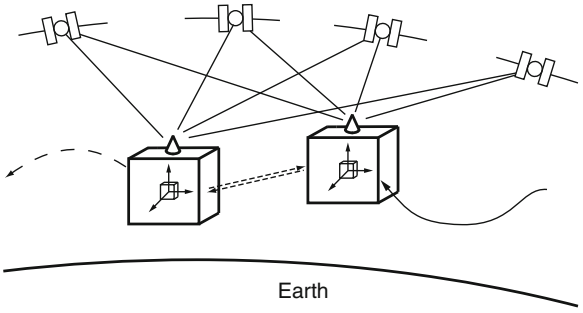

Fig. 10 Scheme of GRACE: twin-satellites with one on-board 3-axis accelerometer and microwave ranging system, both tracked by GNSS satellites

3.1.2 GRACE: Satellite-to-Satellite-Tracking in Low-Low Mode

Two LEO satellites equipped with three-dimensional accelerometers are placed in the same orbit but separated by several hundred kilometers. Both satellite orbits are monitored by GNSS and additionally the range rate between them is measured, corresponding to differences in gravity acceleration (Fig. 10).

The GRACE (Gravity Recovery and Climate Experiment, (Tapley et al. 2004)) mission was launched in March 2002 under the NASA Earth System Science Pathfinder (ESSP) Program, to accurately map variations in the Earth's gravity field over its lifetime. The GRACE mission has two identical spacecrafts flying about 220 km apart in a polar orbit initially 500 km above the Earth making accurate measurements of the distance between the two satellites, using GPS and a microwave ranging system. The ranging system is sensitive enough to detect separation changes as small as some μm over the distance of 220 km between the satellites (Wahr et al. 1998).

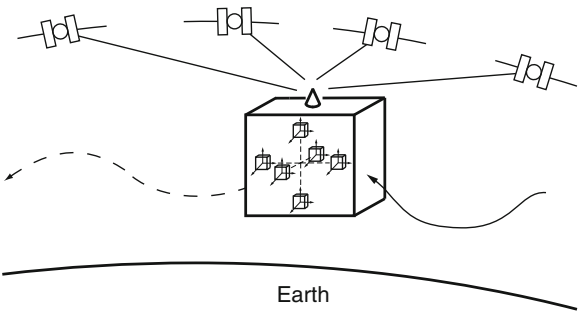

Fig. 11 Scheme of GOCE: Six on-board 3-axis accelerometers, tracked by GNSS satellites

Gravity variations that GRACE is sensitive to include: changes due to surface and deep currents in the ocean, runoff and ground water storage on land masses, exchanges between polar ice sheets or glaciers and the oceans. For further information see: http://www.csr.utexas.edu/grace/.

3.1.3 GOCE: Satellite Gravity Gradiometry

Satellite gradiometry consists basically of the measurement of the acceleration differences in three spatial orthogonal directions between the six test masses situated on each end of the axes. This measurement quantity corresponds to the gradients of the gravity acceleration, i.e. the second derivative of the gravitational potential (Fig. 11).

GOCE (Gravity field and steady-state Ocean Circulation Explorer, (Rummel et al. 2000)) was launched on 17 March 2009 and was the first mission of ESA's Living Planet Program. It is the first satellite equipped with a gradiometer and thus helps to better understand the static gravitational field of the Earth. The missions objectives are to obtain gravity gradients from which new global and regional models can be deduced at length scales down to 100 km and the geoid with an accuracy of 1–2 cm. To achieve this it is necessary to determine gravity field anomalies with an accuracy of 1 mGal. For further information see: http://www.esa.int/goce.

3.1.4 Future Missions

The *GRACE Follow-On* mission, a cooperation between GFZ and NASA, is focused on maintaining data continuity from GRACE and is planned for launch in 2017 (Watkins et al. 2010). To minimize the project schedule as well as the technical and cost risk a high inheritance "replica" of GRACE is conceptualized, taking into account the lessons learned from GRACE. Additionally to the microwave ranging system a laser interferometer will be installed to demonstrate an improved ranging at the nm/sec level, which also serves as a technical demonstration of this technology for future missions with more satellites and different orbit constellations in the time frame beyond 2020 (Gruber et al. 2011).

As a possible successor of the GOCE mission several projects using *atom interferometry* are under consideration (Yu et al. 2006). Such atom interferometers make it possible to measure the absolute acceleration value plus the complete gravity gradient tensor at very high sensitivity, i.e. 10^{-15} m s^{-2} or well below 1 mE in space. Implementing such a device would allow to observe a broader frequency range at a higher temporal resolution leading to a higher accuracy of the measurement.

3.2 Impact of the Atmosphere on Satellite Gravity Observations

Exploring the Earth gravity field through satellites requires the removal of short term (sub-daily) mass variations in the system Earth, including all solid, liquid and atmospheric particles. Due to the fluctuation of those masses at various temporal and spatial scales, like high and low atmospheric pressure systems, as well as due to a strong dependency on the sampling rate of the ground track of the satellite, a long observation time does not guarantee that the introduced variations in the gravity field are canceled out by the mean operator. De-aliasing then denotes incorporating such instantaneous variations of atmospheric masses with respect to a static mean state of the atmosphere, either during the preprocessing of observations or during the estimation procedure of the gravity field solution. The same holds for all other mass variation effects inside the system Earth; only that within the atmosphere also the center of mass of the atmospheric column is varying, which interferes again with the satellite observations (Flechtner 2007; Gruber et al. 2009).

In order to minimize the aliasing signals the determination of accurate *Atmospheric Gravity field Coefficients* (AGC) is indispensable. For the determination of AGC it has become state of the art to use high resolution Numerical Weather Models (NWM), which take into account the three-dimensional distribution of the atmospheric mass. By subtracting the gravity spherical harmonics of the instantaneous atmosphere from the ones of the mean atmospheric field, the residual gravity spherical harmonic series are obtained. These describe the deviation of the actual gravity field from the mean gravity field due to atmospheric mass variations.

3.3 From Atmosphere to Gravity

The atmosphere is nearly in hydrostatic equilibrium, which means that the change in atmospheric pressure on the surface is proportional to the change of mass in the corresponding atmospheric column, including variations in water vapor mass as well as in the dry air mass. ρ describes the density along the column which can be expressed in terms of surface load $\Delta\sigma$ (Boy et al. 2001; Flechtner 2007) and which is linked directly to the surface pressure variation Δp.

$$\Delta p = g_0 \int_0^{\infty} \Delta\rho \mathrm{dr} = \mathrm{g}_0\sigma, \tag{29}$$

$$\Delta\sigma = \frac{\Delta p}{g_0}, \tag{30}$$

where g_0 is the mean gravity acceleration at the Earth surface and $\Delta\rho$ the pressure variation.

The atmosphere affects the Earth gravity field in two different ways: a *direct attraction* of the atmospheric masses acting on the orbiting satellite and a much smaller *indirect effect* introduced by the deformation of the Earths surface due to elastic loading. Both effects are always evaluated with respect to a mean atmosphere model. This approach is described in detail by Torge (1989). The following sections deal exclusively with the direct effect, the indirect effect will be addressed in Sect. 3.3.3.

Due to mass redistribution in the atmosphere the potential V changes with time. This time-dependency of atmospheric density $\Delta\rho$ can be represented in terms of time-dependent ΔC_{nm} and ΔS_{nm} coefficients, taking into account Eqs. (29) and (30), as follows

$$\left\{ \begin{array}{c} \Delta C_{nm} \\ \Delta S_{nm} \end{array} \right\} = \frac{1}{(2n+1)Ma^n} \iint\limits_{Earth} \left[\int_{r_s}^{\infty} \Delta\rho r^{n+2} \mathrm{d}r \right] \overline{P}_{nm}(\cos\theta) \left\{ \begin{array}{c} \cos m\lambda \\ \sin m\lambda \end{array} \right\} \sin\theta \mathrm{d}\theta \mathrm{d}\lambda, \tag{31}$$

where r_s is the Earth surface radius.

3.3.1 Thin Layer Approximation

In the simplest approach for calculating AGC the vertical extent of the atmosphere is neglected and all the atmospheric masses are concentrated in a *thin layer* (TL) at the Earth surface. This can be done under the assumption that most of the mass changes occur in the lower 10 km of the atmosphere and act as variable loading effects on the solid Earth's surface (Boy and Chao 2005).

Surface loads are defined as mass per surface element; therefore the density change in the atmosphere can be expressed in terms of surface load,

$$\left\{ \begin{array}{c} \Delta C_{nm} \\ \Delta S_{nm} \end{array} \right\} = \frac{a^2}{(2n+1)M} \iint\limits_{Earth} \Delta\sigma \overline{P}_{nm}(\cos\theta) \left\{ \begin{array}{c} \cos m\lambda \\ \sin m\lambda \end{array} \right\} \mathrm{dS}, \tag{32}$$

considering that the mass element $\mathrm{dM} = \rho r^2 \mathrm{d}r \sin\theta \mathrm{d}\theta \mathrm{d}\lambda = r^2\sigma \sin\theta \mathrm{d}\theta \mathrm{d}\lambda = r^2\sigma \mathrm{dS}$.

Following the definition of the surface load $\Delta\sigma$ in Eq. (30), the surface pressure p_s can be introduced, whereas a mean pressure field $\overline{p}_s$, representing a static mean

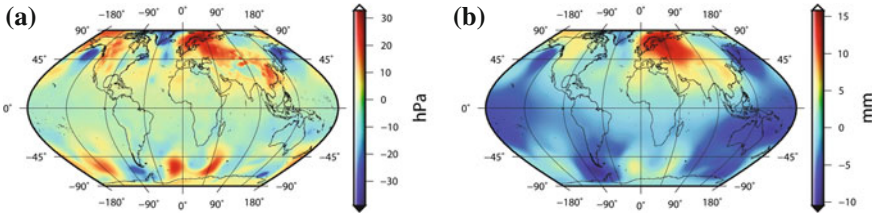

Fig. 12 **a** Pressure variation (actual-mean) in hPa at 1 January 2008, 00 UTC **b** Resulting geoid height variation following the TL approach in millimeter

state of the atmosphere, has to be subtracted to obtain the mass variation:

$$\left\{ \begin{array}{c} \Delta C_{nm} \\ \Delta S_{nm} \end{array} \right\} = \frac{a^2}{(2n+1)Mg_0} \iint\limits_{Earth} (p_s - \overline{p}_s) P_{nm}(\cos\theta) \left\{ \begin{array}{c} \cos m\lambda \\ \sin m\lambda \end{array} \right\} \mathrm{d}S\,. \tag{33}$$

As an example the first epoch (00 UTC) of 1 January 2008 is selected. Figure 12a on the left depicts the pressure variation at the surface and on the right (Fig. 12b) the corresponding change in geoid height following the thin layer approach is shown.

3.3.2 3D Atmosphere

As mentioned in the introduction, also the change of the center of mass of the atmospheric column has an impact on the orbiting satellite, not only the mass change itself. This variation of the center of mass is not addressed in the thin layer approximation but has to be taken into account for satellite gravity missions such as GRACE (Flechtner 2007; Swenson and Wahr 2002; Velicogna et al. 2001). This deficiency can be overcome by considering the whole vertical structure of the atmosphere by performing a *vertical integration* (VI) of the atmospheric masses. To do so, Numerical Weather Models which describe the vertical structure by introducing various numbers of pressure or model levels are needed.

In order to formulate the vertical integration we start from the basic Eqs. (23) and (27), introducing the volume element used in Eq. (32); for details see (Flechtner 2007; Zenner et al. 2010, 2011).

$$\left\{ \begin{array}{c} C_{nm} \\ S_{nm} \end{array} \right\} = -\frac{1}{(2n+1)Ma^n} \iint\limits_{Earth} \left[\int\limits_{r}^{\infty} r^{n+2} \rho \mathrm{d}r \right] \overline{P}_{nm}(\cos\theta) \left\{ \begin{array}{c} \cos m\lambda \\ \sin m\lambda \end{array} \right\} \sin\theta \mathrm{d}\theta \mathrm{d}\lambda\,, \tag{34}$$

Adopting the hydrostatic equation, where g_r is the gravity acceleration at each level, we get:

$$\left\{\begin{array}{c} C_{nm} \\ S_{nm} \end{array}\right\} = -\frac{1}{(2n+1)Ma^n} \iint\limits_{Earth} \left[\int\limits_{p_s}^{0} \frac{r^{n+2}}{g_r} \mathrm{d}p\right] \overline{P}_{nm}(\cos\theta) \left\{\begin{array}{c} \cos m\lambda \\ \sin m\lambda \end{array}\right\} \sin\theta \mathrm{d}\theta \mathrm{d}\lambda . \tag{35}$$

Again, to analyze gravity field variations caused by atmospheric effects, a quantity $\overline{p}_{VI}$ representing the mean state of the atmosphere, has to be subtracted from the inner integral, leading to:

$$\left\{\begin{array}{c} \Delta C_{nm} \\ \Delta S_{nm} \end{array}\right\} = -\frac{1}{(2n+1)Ma^{n+2}g_0} \iint\limits_{Earth} \left(\left[\int\limits_{p_s}^{0} r^{n+4} \mathrm{d}p\right] - \overline{p}_{\mathrm{VI}}\right) \overline{P}_{\mathrm{nm}}(\cos\theta) \left\{\begin{array}{c} \cos m\lambda \\ \sin m\lambda \end{array}\right\} \sin\theta \mathrm{d}\theta \mathrm{d}\lambda . \tag{36}$$

To evaluate the significance of the vertical structure of the atmospheric column, the spherical harmonic series resulting from the TL approach and the ones of the VI are compared. In Fig. 13 the degree standard deviation of the coefficients of the year 2008 up to degree 100 are plotted, in blue the vertical integration approach, in red the corresponding difference to the thin layer approach. The results indicate that at the 2010 error level of RL04 (solid line in Fig. 13) the differences between the two approaches are negligible. But if GRACE reaches the targeted error level (dashed line in Fig. 13), then the VI approach has to be chosen. Figure 14 shows exemplarily the geoid height variability for the C_{20} coefficient, in black for the vertical integration in blue for the thin layer approach, in red the difference.

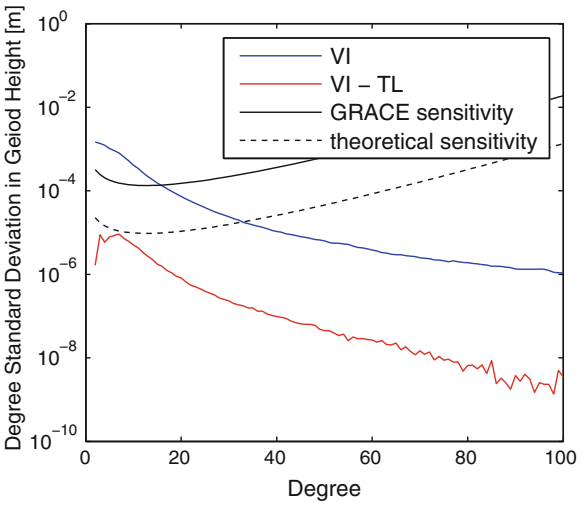

Fig. 13 Degree standard deviation in terms of geoid height for the year 2008 in meter, in *blue* for the VI approach, in *red* the corresponding difference between VI and TL. The *black line* marks the GRACE RL04 error level, the *dashed* one the theoretical error as obtained by pre-launch simulations

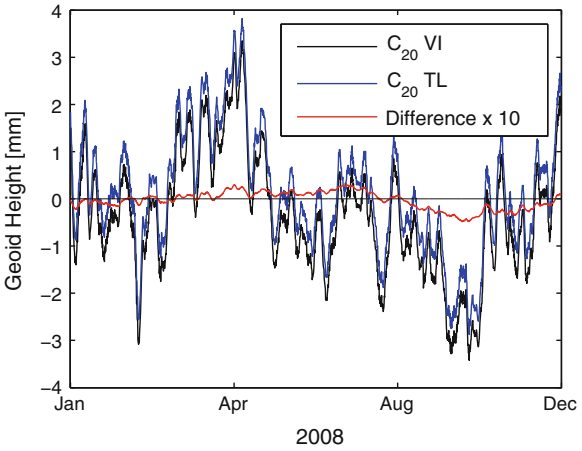

Fig. 14 Time variation of the C_{20} coefficient in geoid height for the year 2008 in millimeter, in *black* following the VI approach in *blue* the TL approach, in *red* the difference multiplied by 10, bias removed

3.3.3 Indirect Effect

The indirect effect of the atmosphere on the gravity field, i.e. the elastic deformation of the solid Earth due to atmospheric loading, is counteracting the direct effect due to the deformation towards the geocenter. In general, for small deformations the additional change in the potential ΔV depends linearly on the potential, following Farrell (1972):

$$\Delta V_n^{ind} = k_n \Delta V, \tag{37}$$

$$\Delta V_n^{tot} = \Delta V + k_n \Delta V = (1 + k_n)\Delta V, \tag{38}$$

where k_n denote the degree dependent *load Love numbers* and represent the deformational behavior based on the rheology of the Earth.

Figure 15 shows the difference between a solution without considering loading and one which includes loading, both for the thin layer approximation. As expected only differences at a large spatial scale appear since the Earth's elastic surface deformation due to mass redistribution is mainly sensitive to large scale pressure variations with wavelengths greater than 2000 km, corresponding to $n < 10$ (Boy et al. 2001). This result is confirmed by the degree standard deviation expressed in geoid height calculated for the year 2008 in Fig. 16.

Given the fact that the differences up to degree 4 lie above the GRACE RL04 error level and up to degree 15 above the predicted error level, the indirect effect has to be accounted for, as it was already shown by Flechtner (2007). The same conclusion is drawn looking at the difference between introducing and neglecting loading in terms of geoid height variability for low degrees (Fig. 17), considering the aimed precision of GRACE to be a few micrometers for degree 3–5 (Tapley et al. 2004).

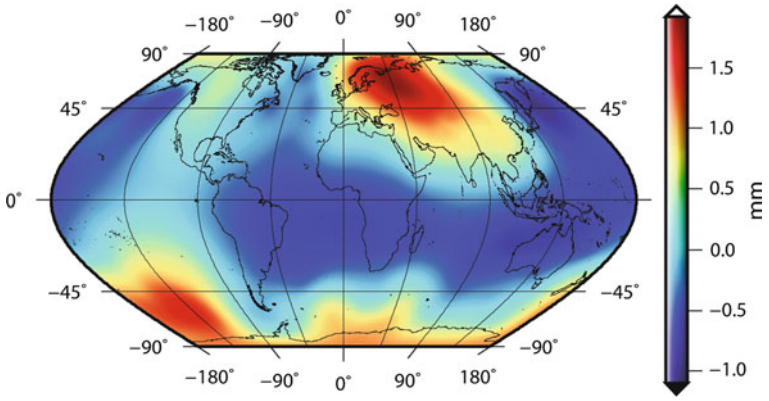

Fig. 15 Difference of the geoid height variation in millimeter for the thin layer approach between the variant with and without loading for January 1, 2008, 00 UTC

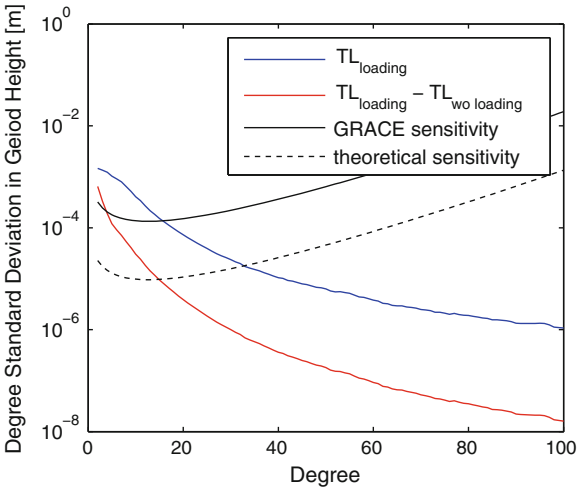

Fig. 16 Degree standard deviation in terms of geoid height in meter for the year 2008, in *blue* for the TL approach with loading, in red the corresponding difference of VI without loading. The *black line* marks the GRACE RL04 error level, the *dashed* one the theoretical error as obtained by pre-launch simulations

4 The Atmosphere and the Ocean

Generally, the ocean responds to atmospheric forcing like wind, pressure, evaporation, precipitation, and radiation from the Sun. The responses are classically divided into barotropic and baroclinic ones (Higdon 2008). Barotropic is the depth-independent part of the flow. In classic wind-driven ocean circulation theory, it is

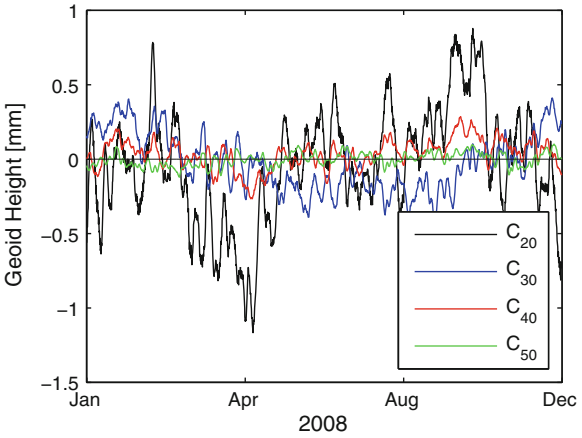

Fig. 17 Time variations of low degree coefficients expressed in geoid height in millimeter, difference between neglecting and including loading, in *black* C_{20}, in *blue* C_{30}, in *red* C_{40} and in *green* C_{50}

the flow that results from, or is in balance with, a sea surface slope. Baroclinic is the depth-dependent part of the flow and results from the density distribution within the ocean and tries to cancel the sea surface flow. Commonly the barotropic motions are fast (hours to days) such as tides, although they include a small baroclinic contribution. The El Niño (Hurrell and van Loon 1997) for example is a mainly baroclinic phenomenon with its slow motions.

Compared to the atmosphere, the time-variable mass signal of the ocean is rather small, the RMS surface mass variability is typically only 2–3 cm (Wahr et al. 1998). Still, ocean signals are evident in GRACE data and have to be considered and corrected. There are various ways to model the oceanic response due to atmospheric forcing, here only a short overview shall be given:

- *Non-inverted barometer* (NIB): Atmospheric pressure variations are fully transmitted to the sea floor and the oceanic response is the same as for the solid Earth.
- *Inverted barometer* (IB): Pressure variations in the atmosphere Δp are compensated by static variations of the sea depth and the pressure on the sea floor, i.e., the ocean bottom pressure, does only change to a minor extent corresponding to a mean surface pressure over all the entire world ocean (Dickman, 1988). In the simplest case IB assumes 1 cm change in sea depth due to 1 hPa change in the atmospheric pressure:

$$\delta h_w = -\frac{\Delta p}{\rho_w g_0} \tag{39}$$

where ρ_w is the sea water density, g_0 the Earth mean gravity acceleration, and respectively δh_w the change in sea depth, respectively.
However the ocean does not respond perfectly like the IB simulates, especially in the tropics and in the southern ocean (Ponte and Gaspar 1999), but also shallow

seas or the changing ice coverage in the Arctic pose problems. Those deficiencies are linked to the inability of the model to consider various interactions occurring between the atmosphere, solid Earth and the oceans (Wunsch and Stammer 1997).

- *Ocean models*: They can be divided in the same classes as the oceanic responses, i.e. barotropic and baroclinic. Barotropic ocean models assume one density for the whole water column and are forced only by wind and pressure. Although this approach simplifies the ocean to a rather plain model, it has advantages in easier parameterizations and lesser needs in computational power. The PPHA model developed by Pacanowski, Ponte, Hirose and Ali (Hirose et al. 2001) is such a model.

  Baroclinic models on the other hand include vertical changes and also effects introduced by radiation, evaporation, and precipitation. The OMCT (Ocean Models for Circulation and Tides), developed for studying non-linear interactions among tides and the general circulation, is an example for such a model (Thomas 2002; Dobslaw and Thomas 2007).

Acknowledgments We greatly acknowledge Frank Flechtner for reviewing this part of the book. Furthermore, we would like to thank the Austrian Science Fund (FWF) for supporting project GGOS Atmosphere (P20902) and the ECMWF for providing the meteorological data.

References

J. P. Boy and B. F. Chao. Precise evaluation of atmospheric loading effects on earth's time-variable gravity field.*Journal of Geophysical Research, 110, B08412,* doi:10.1029/2002JB002333, 2005.

J. P. Boy, P. Gegout, and J. Hinderer. Reduction of surface gravity data from global atmospheric pressure loading. *Geophysics Journal International, 149, pp 534–545,* 2001.

S. R. Dickman. Theoretical investigation of the oceanic inverted barometer hypothesis. *Geophysical Research, 93, pp 14.941-14.946,* 1988.

H. Dobslaw and M. Thomas. Simulation and observation of global ocean mass anomalies. *Journal of Geophysical Research, 112, C05040,* 2007.

N. Ekholm. Über die Höhe der homogenen Atmosphäre und die Masse der Atmosphäre. *Meteorologische Zeitschrift, 19, pp 249–260*, 1902.

W. E. Farrell. Deformation of the Earth by Surface Loads. *Reviews of Geophysics and Space Physics, 10, 3, pp. 761–797*, 1972.

F. Flechtner. AOD1B Product Description Document for Product Releases 01 to 04 (rev. 3.1, April 13, 2007). Technical report, GFZ, 2007.

Th. Gruber, e.motion Team, and NGGM Team. Recent Studies on Future Gravity Field Missions in Europe: e.motion vs. NGGM. *GRACE Science Team Meeting: GRACE Follow-On and Data, Continuity,* 2011.

Th. Gruber, Th. Peters, and L. Zenner. The Role of the Atmosphere for Satellite Gravity Field Missions. *Observing our Changing Earth, International Association of Geodesy Symposia 133, ed. by M. Sideris, Springer-Verlag Berlin Heidelberg,* 2009.

Robert L. Higdon. A comparison of two formulations of barotropic - baroclinic splitting for layered models of ocean circulation. *Ocean Modelling, 24, 1–2, pp 29–45,* 2008.

N. Hirose, I. Fukumori, V. Zlotnicki, and R. M. Ponte. High-frequency barotropic response to atmospheric disturbances: Sensitivity to forcing, topography, and friction. *Journal of Geophysical Research,* 2001.

B. Hofmann-Wellenhof and H. Moritz. *Physical Geodesy.* Springer Wien New York, 2005.
J. W. Hurrell and H. van Loon. Decadal variations in climate associated with the north atlantic oscillation. *Climatic Change, 36, pp 301–326,* 1997.
M.J. McPhaden. El Niño and La Niña: Causes and Global Consequences. *Encyclopedia of Global Environmental Change, Vol 1, John Wiley and Sons, LTD., Chichester, UK, pp 353–370,* 2002.
R. Ponte and P. Gaspar. Regional Analysis of the Inverted Barometer Effect over the Global Ocean Using TOPEX/POSEIDON Data and Model results.*Journal of Geophysical Research, 104, C7, 15587–15601,* 1999.
W. Rabbel and J. Zschau. Static deformation and gravity changes at the earth's surface due to atmospheric loading.*Journal of Geophysics, 56, 81–99,* 1985.
C. Reigber, H. Luehr, and P. Schwintzer. CHAMP mission status. *Advanced Space Research, 30(2), 129–134,* 2002.
R. Rummel, J. Müller, H. Oberndorfer, N. Sneeuw. Satellite Gravity Gradiometry with GOCE. *Towards an Integrated Global Geodetic Observing System (IGGOS), IAG, Symposium 120, 66–72,* 2000.
S. Swenson and J. Wahr. Estimated Effects of the Vertical Structure of Atmospheric Mass on the Time- Variable Geoid.*Journal of Geophysical Research, 107, 2194,* doi:10.1029/2000JB000024, 2002.
B. Tapley, S. Bettadput, M. Watkins, and C. Reigber. The Gravity recovery and Climate Experiment: Mission overview and early results. *Geophysical research Letters, 31, L09607,* doi:10.1029/2004GL019920, 2004.
M. Thomas. *Ocean induced variations of Earth's rotation - Results from a simultaneous model of global circulation and tides.* PhD thesis, Univ. of Hamburg, Germany, 2002.
W. Torge.*Gravimetry*. Walter de Gruyter-Berlin-New York, ISBN: 3-11-010702-3, 1989.
K.E. Trenberth and C.J. Guillemot. The total Mass of the Atmosphere. *Journal of Geophysical Research, 99, D11, 23079–23088,* 1994.
K.E. Trenberth and L. Smith. The Mass of the Atmosphere: A Constraint on Global Analyses.*Journal of Climate, 18, 6, 864–875*, 2005.
I. Velicogna, J. Wahr, and H. Van den Dool. Can Surface Pressure be used to remove atmospheric contributions from GRACE data with sufficient accuracy to recover hydrological signals? *Journal of Geophysical Research, 106, B8, 16415–16434*, 2001.
L. Völgyesi. Geodetic applications of torsion balance measurements in Hungary. *Reports on Geodesy, Warsaw University of Technology, 57, 2, 203–212*, 2001.
J. Wahr, M. Molenaar, and F. Bryan. Time variability of the Earth's gravity Field: hydrological and oceanic effects and their possible detection using GRACE. *Journal of Geophysical Research, 103, 30, 205–230*, 1998.
R. J. Warburton and J. M. Goodkind. The influence of barometric pressure fluctuations on gravity. *Geophys. J. Roy. Astron. Soc., 48, 281–292,* 1977.
M. M. Watkins, F. Flechtner, and B. D. Tapley. Status of the GRACE Follow-On Mission. *American Geophysical Union, Fall Meeting 2010, abstract G44A–01,* 2010.
C. Wunsch and D. Stammer. Atmospheric loading and the oceanic 'inverted barometer' effect. *Reviews of Geophysics, 35, 1, pp 79–107*, 1997.
N. Yu, J.M. Kohel, J.R. Kellogg, and L. Maleki. Development of an atom-interferometer gravity gradiometer for gravity measurements from Space. *Appl. Phys. B 84, 647–652 (2006),* doi:10.1007/s00340-006-2376-x, 2006.
L. Zenner, T. Gruber, A. Jäggi, and G. Beutler. Propagation of atmospheric model errors to gravity potential harmonics - Impact on GRACE De-Aliasing. *Geophysical Journal International, 182(2), 797–807,* 2010.
L. Zenner, T. Gruber, G. Beutler, A. Jäggi, F. Flechtner, T. Schmidt, J. Wickert, E. Fagiolini, G. Schwarz, and T. Trautmann. Using Atmospheric Uncertainties for GRACE De-Aliasing - First Results. *Geodesy for Planet Earth, International Association of Geodesy Symposia, Springer, 147–152, ISBN 987-3-642-20337-4,* 2011.

Atmospheric Effects on Earth Rotation

Michael Schindelegger, Sigrid Böhm, Johannes Böhm and Harald Schuh

Abstract One of the pivotal sources for fluctuations in all three components of the Earth's rotation vector is the set of dynamical processes in the atmosphere, perceptible as motion and mass redistribution effects on a multitude of temporal and spatial scales. This review outlines the underlying theoretical framework for studying the impact of such geophysical excitation mechanisms on nutation, polar motion, and changes in length of day. It primarily addresses the so-called *angular momentum approach* with regard to its physical meaning and the application of data from numerical weather models. Emphasis is placed on the different transfer functions that are required for the frequency-dependent intercomparison of Earth rotation values from space geodetic techniques and the excitations from the output of atmospheric circulation models. The geophysical discussion of the review assesses the deficiencies of present excitation formalisms and acknowledges the oceans as other important driving agents for observed Earth rotation variations. A comparison of the angular momentum approach for the atmosphere to an alternative but equivalent modeling method involving Earth-atmosphere interaction torques is provided as well.

M. Schindelegger (✉) · S. Böhm · J. Böhm
Department of Geodesy and Geoinformation, Vienna University of Technology,
Gußhausstraße 27-29, 1040 Vienna, Austria
e-mail: michael.schindelegger@tuwien.ac.at

S. Böhm
e-mail: sigrid.boehm@tuwien.ac.at

J. Böhm
e-mail: johannes.boehm@tuwien.ac.at

H. Schuh
Department 1 Geodesy and Remote Sensing, Helmholtz Centre Potsdam
GFZ German Research Centre for Geosciences,
Telegrafenberg A 17, 14473 Potsdam, Germany
e-mail: schuh@gfz-potsdam.de

J. Böhm and H. Schuh (eds.), *Atmospheric Effects in Space Geodesy*,
Springer Atmospheric Sciences, DOI: 10.1007/978-3-642-36932-2_6,

1 The Earth's Variable Rotation

The rotation of the Earth is not uniform but subject to manifold spatio-temporal variations. Both the direction of the spin axis as well as its absolute value, the rotation rate, undergo significant perturbations as the Earth system responds to the action of external and internal torques. External torques are generated by the gravitational attraction of the Sun, the Moon and the planets, while internal torques can be assigned to large-scale geodynamical processes prompting exchange of angular momentum between the solid parts of the Earth and the surrounding fluid layers like the atmosphere, the oceans and the liquid core. Highly precise monitoring of the induced rotational fluctuations, carried out by space geodetic techniques, is an indispensable scientific task since the interpretation of the observed variations shed light on interactions in Earth's dynamical system and can constrain particular structural parameters of our planet. Enhanced understanding of Earth's rheology and dynamics will in turn be reflected in improved rotational models, which are essential to accurate positioning and navigation on Earth and in space.

1.1 Parametrization of Earth Rotation

The full orientation of our planet in space is a complicated time-dependent function, whose knowledge is required for the direct and precise transformation of station coordinates from the rotating terrestrial frame to the quasi-inertial celestial frame. While the rotational behavior of a body would be unambiguously determined by three time-dependent Euler angles, astronomy traditionally uses an intermediate reference frame for the complete transformation of terrestrial and celestial station positions. As a result, Earth rotation is parameterized by five *Earth orientation parameters* (EOP), which can be summarized in three categories (Schuh and Böhm 2011): *precession* and *nutation* comprise long-periodic motions of the Earth's rotation axis in a celestial reference system. *Polar motion* denotes direction changes of the spin axis with respect to a body-fixed reference system. Magnitude fluctuations of the rotation vector are reckoned in changes in *length of day* (LOD) or, equivalently, in $\mathrm{dUT1} = \mathrm{UT1} - \mathrm{UTC}$, i.e. the deviation of UT1 (*Universal time 1*) from the uniform atomic time UTC (*Universal Time Coordinated*). The subset of polar motion and dUT1 or LOD is known as *Earth rotation parameters* (ERP). A more detailed description of these quantities is presented in the next paragraphs and largely follows Schuh and Böhm (2011).

The actual definition of the EOP depends on the kind of the underlying transformation method, on which the IERS (*International Earth Rotation and Reference Systems Service*) issues regular recommendations (McCarthy and Luzum 2010). The current transformation procedure according to the IAU (*International Astronomical Union*) resolutions 2000 and 2006 is defined from the body-fixed, geocentric TRS (*Terrestrial Reference System*) to the quasi-inertial GCRS (*Geocentric Celestial Reference System*) or vice versa. Both systems are of similar orientation along the mean

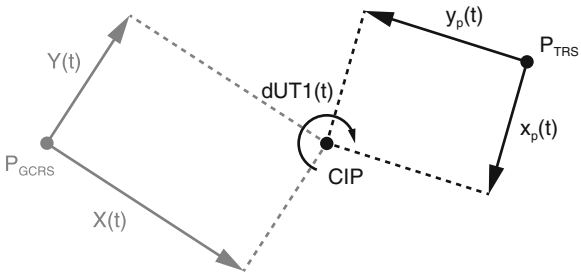

Fig. 1 Poles of reference and time-dependent Earth orientation parameters with regard to the coordinate systems TRS and GCRS. Figure modified from Mendes Cerveira et al. (2009)

equator of the reference epoch. Assuming that all effects associated with the transition between barycentric and geocentric system are taken into account, the transformation from the TRS to the GCRS can be expressed as a series of time-dependent rotation matrices (McCarthy and Luzum 2010)

$$[\mathbf{GCRS}] = \mathbf{Q}(t) \cdot \mathbf{R}(t) \cdot \mathbf{W}(t) \cdot [\mathbf{TRS}]\,. \tag{1}$$

Herein, $\mathbf{W}(t)$ describes polar motion as calculated from x_p and y_p, which are the coordinates of the intermediate system's reference pole, the CIP (*Celestial Intermediate Pole*), in the Earth-fixed reference system. The argument of the spin component matrix $\mathbf{R}(t)$ is named *Earth Rotation Angle* (ERA) and directly relates to UT1. Precession and nutation are accounted for by the matrix $\mathbf{Q}(t)$ based on the angles X and Y, which represent the coordinates of the CIP in the celestial reference system. Within the framework of the transformation according to the IAU 2000 resolutions, the set of $\{x_p, y_p, \text{dUT1}, X, Y\}$ constitutes the EOP, see the schematic description displayed in Fig. 1. If we deploy the old transformation concept based on ecliptic and equator, X and Y need to be replaced by nutation in obliquity and longitude, usually denoted as $\Delta\varepsilon$ and $\Delta\psi$. For an extended discussion on the EOP and the transition as defined in Eq. (1), refer to Seitz and Schuh (2010).

The aforementioned Celestial Intermediate Pole represents the reference pole to which measurements of space geodetic techniques are related, and thus defines the observed axis. This is a pure convention, which is realized by an accordingly adapted precession-nutation theory. The direction towards the CIP does not correspond to any physically defined axis, like the rotation axis, the figure axis or the angular momentum axis (Schuh and Böhm 2011). Nevertheless, it is possible to connect it to each of those axes.

As already indicated, the CIP can be viewed as intermediate pole that separates the motion of the TRS-pole in the GCRS into a celestial part and a terrestrial part. According to McCarthy and Luzum (2010), precession and nutation $\{X, Y\}$ are considered as long-periodic motion of the CIP in the celestial reference frame within the frequency range $\sigma_c \in (-0.5, 0.5)$ cpsd (cycles per sidereal day). With the minus sign labeling retrograde motion (opposite to the sense of Earth rotation) and the plus sign denoting prograde motion (in the sense of Earth rotation), all motions of the CIP in the terrestrial frame outside the retrograde diurnal band $\sigma_t \in (-1.5, -0.5)$ cpsd are allocated to polar motion $\{x_p, y_p\}$ (Schuh and Böhm 2011). The given frequency

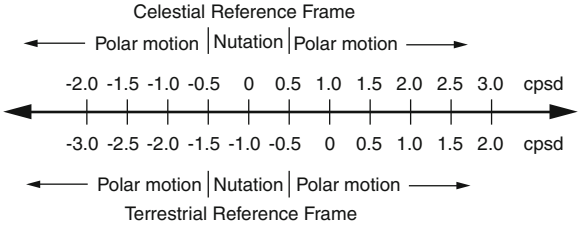

Fig. 2 Relationship between the frequency of some motion as viewed from the celestial reference frame (*top* half of figure) and the corresponding frequency of the same motion as observed from the terrestrial reference frame (*bottom* half of figure) (Gross 2007)

bands are thus connected by

$$\sigma_c = \sigma_t + \Omega, \tag{2}$$

where Ω signifies the angular velocity of the Earth. Equation (2), illustrated in Fig. 2, is the basic frequency relation for some motion as observed simultaneously in the celestial frame c and in the terrestrial frame t. The separation of polar motion and precession-nutation based on frequencies represents the current conventional approach, replacing the traditional distinction between astronomical and geophysical Earth rotation, for which it is decisive whether external or internal torques are acting upon the planet.

1.2 Precession and Nutation

The Earth can be characterized approximately as an oblate spheroid, its rotation axis inclined by $\varepsilon \approx 23.5°$ with respect to the ecliptic normal (Schuh and Böhm 2011). Subject to the gravitational torques of Moon and Sun, which try to force the equatorial plane into the ecliptic, the rotating Earth acts like a gyroscope and swerves by moving in space. The resulting motion is a retrograde revolution around the ecliptic pole, the rotation axis describing a cone with aperture 2ε. This steady or secular motion (period: 25800 yr corresponding to 1 Platonic year) with respect to the space-fixed reference system is called precession.

Smaller periodic changes of the spin axis with respect to the space-fixed system are superimposed on precession. Such motions with periods from a few days to 18.6 yr are summarized as nutation and originate from the gravitational interaction of the Earth with other celestial bodies. Those forced parts of precession and nutation can be modeled and predicted precisely using time-dependent harmonic series expansions (Schuh and Böhm 2011). The currently most accurate precession-nutation model adopted by the latest IAU resolutions (IAU Resolutions 2000, 2006) considers both lunisolar and planetary effects, mantle anelasticity, electromagnetic coupling mechanisms between core and mantle as well as between inner and outer core, but also geophysical effects, like ocean tides, which are characterized as nutation following

the frequency definition of Sect. 1.1, see Mathews et al. (2002). Remaining nutational motions of the axis that are not accounted for by the model can be measured by means of VLBI (Very Long Baseline Interferometry) and are published by the IERS as *Celestial Pole Offsets*. These residuals arise from existing model deficiencies and from unpredictable effects such as the *Free Core Nutation* (FCN). The FCN is a free rotational mode of the Earth, caused by a misalignment of the rotation axes of mantle and core and probably excited by diurnal retrograde atmosphere and ocean loading of the Earth's surface (Sasao and Wahr 1981). Studies from VLBI observations show that the FCN period is likely to be around 430 d (Herring et al. 1986), while its amplitude is at the level of 0.1–0.3 mas (McCarthy and Luzum 2010).

1.3 Polar Motion

The terrestrial part of CIP variations has an order of magnitude of several meters and is routinely reported by the IERS as pole coordinates $\{x_p, y_p\}$ in a two-dimensional coordinate system, of which the x-axis is oriented in the direction of the Greenwich meridian and the y-axis points positively towards 90° E longitude (Fig. 1). If the Earth were a rigid oblate spheroid, the resulting misalignment of the rotation axis with the axis of figure would engender a circular motion of the pole with a period of around 304 d, recognized already in 1765 by Euler. The real Earth departs from this simplified model. Astronomical observations at the end of the nineteenth century revealed that polar motion is mainly composed of an annual variation of about 90 mas (or 2.7 m on the Earth's surface) and the 14-month *Chandler oscillation* or *Chandler wobble* (CW) with a mean amplitude of about 160 mas (or 4.8 m). The CW is another pivotal eigenmode of the Earth, a nearly circular, damped oscillation, which would have subsided due to friction in Earth's interior, if it were not for a constantly renewed excitation (Schuh and Böhm 2011). The exact excitation mechanism is still under investigation, even though nowadays there is broad consensus that the necessary energy to maintain the CW emerges from irregular processes in the atmosphere-ocean-system, such as ocean-bottom pressure fluctuations and air pressure variability over the continents (Gross 2000; Brzeziński et al. 2012). The interference of the Chandler mode with the annual motion leads to a distinct beat-like pole behavior with a maximum amplitude up to 9 m every 6.3 yr.

The polar motion spectrum below the annual cycle is characterized by semi- and terannual wobbles as well as retrograde oscillations associated with atmospheric normal modes at periods of about 1.2 and 10 d (Brzeziński et al. 2002, and references therein). Dominant short-periodic variations are due to ocean tides with essentially diurnal and semidiurnal periods, albeit the total effect is only about 1/100 of the CW. Processes in Earth's interior, such as dynamic coupling between core and mantle, are associated with long-term and decadal polar motion signals. The linear trend in the position of the pole towards 76–78° W is labeled *secular polar motion* and amounts to about 3.3 mas yr^{-1} according to Schuh et al. (2001). This effect is supposed to be predominantly caused by postglacial rebound and melting of polar ice masses.

1.4 Length of Day

The parameter which is usually quoted to represent changes in Earth's rotation rate is LOD, the so-called excess length of day or the deviation of the effective length of day from the nominal value of 86400 s (Schuh and Böhm 2011), cf. also Sect. 3.3. By integration, LOD can be alternatively related to dUT1, which is directly connected to the Earth rotation angle.

Variations of Earth's angular velocity can be assigned to different frequency bands and different physical processes. For daily and subdaily periods, the strongest influence emerges from the ocean tides as a response to the gravitational attraction of the Sun and the Moon. On time scales of a few weeks to months, solid Earth tides provide distinct peaks near 14 and 28 d. Additional fluctuations of the axial rotational component can be attributed to the atmosphere, which are highlighted in the next section. A pronounced annual spectral component in LOD, predominantly associated with the annual seesawing of wind patterns, is amplified every 4–6 yr by large-scale climate anomalies (El Niño-Southern Oscillation phenomenon). Angular momentum changes in the fluid core generate decadal LOD fluctuations and are transfered to the mantle via mechanic or electromagnetic coupling. Tidal dissipation (angular momentum losing to the Earth-moon system) and long-term mass variations steadily decrease the Earth's angular velocity. This secular prolongation of the day amounts to 1.8 ms in 100 yr (Morrison and Stephenson 2001).

1.5 Influence of the Atmosphere on Earth Rotation

The substantial influence of the atmosphere on all three components of the Earth's rotation vector has been recognized for a long time, see e.g. the pioneering study of Jeffreys (1916). While the sum of all air masses amounts only to about 1/300 of the oceanic mass, the atmosphere's mobility, chiefly driven by the diurnal and seasonal thermodynamic cycles, is unprecedented compared to that of the oceans or the core. By interaction with the underlying mantle (attached to the crust), the resulting atmospheric angular momentum (AAM) is transfered to the solid parts of the Earth and can be recognized as substantial geophysical variation of Earth rotation.

Large-scale atmospheric mass redistributions as well as changes in the pattern of winds are the dominating driving agents for observed changes in LOD and polar motion at periods from a few days up to several years, see the works of Lambeck (1980) or Eubanks (1993). The distinct seasonal excitation signals in ERP, which are generated by atmospheric pressure and wind variations at annual, semiannual and terannual frequencies, have been treated thoroughly by Gross et al. (2003) and Gross et al. (2004). Earlier studies on this subject are Wahr (1983) or Barnes et al. (1983). Intraseasonal fluctuations, i.e. non-seasonal excitation signals at periods ranging from 4 d up to 1 yr, are present in both polar motion and LOD. On those time scales, the most prominent feature in the atmosphere coupling with variations in Earth's rotation

rate is called *Madden-Julian Oscillation* (Madden and Julian 1971). While mass redistributions and changing winds are equally important for the equatorial part of intraseasonal Earth rotation variations, the axial component is almost solely affected by zonal winds, especially those below an isobaric level of 10 hPa (Gross et al. 2004). On short time scales such as daily and subdaily periods, the contribution of ocean tides to Earth rotation is about 30 times larger than that of the atmosphere (Brzeziński et al. 2002), both for variations in Earth's rotation rate (Ray et al. 1994) and for polar motion (Chao et al. 1996). Nonetheless, by using data from numerical weather models (NWM), the high-frequency contribution of the atmosphere to EOP can be estimated. The discernable effects are predominantly tidal waves of thermal origin that cause sharp peaks at $T = \pm 12, \pm 24$ h in the excitation spectra. Bizouard et al. (1998) or Brzeziński et al. (2002) highlighted the considerable impact of atmospheric tides on the nutational motion of the Earth, demonstrating that geophysical excitation in this frequency range is largely amplified by the presence of the FCN resonance. Diurnal and semidiurnal atmospheric effects on polar motion and changes in LOD are below 10 μas or 10 μs, respectively, and thus by one order of magnitude smaller than the atmosphere-forced nutation amplitudes. Yet, the atmosphere certainly exerts an indirect influence on Earth rotation via the oceanic motion that is triggered by surface pressure and wind variations (de Viron and Dehant, 1999). The oceanic response to such an atmospheric forcing is, however, still poorly understood.

Two different but fundamentally equivalent methods can be applied in order to evaluate the effect of the atmosphere or, more generally, any mobile fluid on Earth rotation. The first method, the angular momentum approach, considers the system Earth + atmosphere + oceans as isolated, thus conserving angular momentum. In this case, any change of angular momentum in the atmosphere (AAM) is compensated by an opposite change of equal magnitude in the angular momentum of the system's remaining parts, which in turn can be observed as variation in the rotation of our planet. The second method, referred to as torque approach, requires the direct computation of the interaction torque between the atmosphere and the solid Earth + oceans ('solid Earth' is understood to comprise both mantle and core). The resulting time-dependent quantity is then introduced as forcing function in the equations of motion (Brzeziński et al. 2002), as shown, e.g, by Iskenderian and Salstein (1998) for the axial component of the Earth rotation vector and by de Viron and Dehant (1999) for the equatorial component. In the present review, emphasis is placed on the AAM approach, with the torque approach moderately further expounded in Sect. 2.6.

2 Modeling Geophysical Excitation of Earth Rotation

2.1 Liouville Equations

The dynamical equation of motion of a rotating body such as the Earth in a space-fixed reference system is (e.g. Moritz and Müller 1987)

$$\mathbf{L} = \frac{\mathrm{d}\mathbf{H}}{\mathrm{d}t}, \tag{3}$$

relating the torque $\mathbf{L}$ acting upon the body to the temporal change of its angular momentum $\mathbf{H}$. This is the basic relation for the development of (Newtonian) precession/nutation theories for astronomical Earth rotation. In order to characterize polar motion (or geophysical Earth rotation if referring to the traditional separation) and changes of LOD, Eq. (3) has to be rewritten in the rotating reference system that has been attached to the body (Munk and MacDonald 1960)

$$\mathbf{L} = \frac{\mathrm{d}\mathbf{H}}{\mathrm{d}t} + \boldsymbol{\omega} \times \mathbf{H}. \tag{4}$$

The time-dependent quantity $\boldsymbol{\omega}$ signifies the angular velocity vector of the body-fixed reference frame with respect to the space-fixed reference frame. Hence, $\boldsymbol{\omega}$ is also the angular velocity vector of the Earth with respect to inertial space (Gross 2007). Equation (4) is one form of Euler's dynamical equation for rigid body rotation. In case of rigidity, the angular momentum $\mathbf{H}$ can be basically expressed as the product of the inertia tensor $\mathbf{I}$ and $\boldsymbol{\omega}$. $\mathbf{I}$ is represented by a symmetric matrix containing the moments of inertia and the products of inertia of the rotating body, which characterize the internal mass distribution. In addition, the inertia tensor would be invariant for a rigid body, since single particles do not move with respect to the attached reference system. If deformations and fluid elements are allowed for, $\mathbf{I}$ becomes time-variable, the mass elements move with respect to the body-frame, introducing relative angular momentum $\mathbf{h}$. In this case, the angular momentum $\mathbf{H}$ of the entire, rotating, deformable body is composed of

$$\mathbf{H} = \mathbf{I}\boldsymbol{\omega} + \mathbf{h} \tag{5}$$

$$\mathbf{I}\boldsymbol{\omega} = \int_{Earth} \rho \mathbf{x} \times (\boldsymbol{\omega} \times \mathbf{x})\, \mathrm{d}V \tag{6}$$

$$\mathbf{h} = \int_{Earth} \rho \mathbf{x} \times \mathbf{v}\, \mathrm{d}V, \tag{7}$$

where both constituents $\mathbf{I}$ and $\mathbf{h}$ contain contributions of the solid Earth as well as the hydrosphere and the atmospheric effects of density and wind variations. The quantity $\mathbf{x}$ denotes the position of a mass element with material density ρ and $\mathbf{v}$ is its velocity relative to the terrestrial system. The first summand in Eq. (5) is generally referred to as *mass* or *matter term*, the second summand is labeled *motion term*. Moreover, Eq. (5) perfectly illustrates the idea of the angular momentum approach: mass displacements and fluxes in the different components of the Earth generate both variations of the inertia tensor and relative angular momentum. Since $\mathbf{H}$ remains constant in the absence of external torques ($\mathbf{L}$ will be set to zero in the following section as we do not consider astronomically-induced variations of Earth rotation), changes in the angular velocity vector balance the equation by altering its direction (polar motion) and magnitude (changes in LOD). Combination of Eqs. (4) and (5)

yields the *Euler-Liouville equations* or simply *Liouville equations*

$$\mathbf{L} = \frac{\mathrm{d}}{\mathrm{d}t}\left(\mathbf{I}\boldsymbol{\omega} + \mathbf{h}\right) + \boldsymbol{\omega} \times \left(\mathbf{I}\boldsymbol{\omega} + \mathbf{h}\right). \tag{8}$$

2.2 Excitation Functions

The basic task is now to decompose the Liouville equations into a mathematically practicable formulation that can be used for studying variations in Earth rotation in view of geophysical (and especially atmospheric) excitation. Basically, this can be accomplished by reverting either to a linear analytical approach or to a non-linear numerical approach. As sketched in Seitz and Schuh (2010), the numerical approach solves the differential equation system as an initial value problem via numerical integration. Further details on the implementation and sensitivity of this method are outlined in Seitz (2004). This review, though, focuses entirely on the conventional analytical approach, of which the initial derivations of Munk and MacDonald (1960) are still valid today. Yet, our formulation largely follows Gross (2007).

If we neglect secular effects like polar wander, Earth's rotation departs only slightly from uniform rotation. It is therefore justified to linearize Eq. (8) by considering only small deviations from an initial state of motion (subscript 0) in which the entire system Earth, including all solid and fluid portions, is rotating with constant angular velocity Ω around the polar axis $\mathbf{z}$ of the body-fixed reference system. The orientation of this frame is realized in such a manner that the inertia tensor of the Earth becomes diagonal and $\mathbf{z}$ coincides with the axis of figure $\boldsymbol{\pi}_{30}$ so that

$$\boldsymbol{\omega}_0 = \Omega\mathbf{z} \tag{9}$$

$$\mathbf{I}_0 = \begin{pmatrix} A & 0 & 0 \\ 0 & B & 0 \\ 0 & 0 & C \end{pmatrix}. \tag{10}$$

Here, A, B and C denote the equatorial and polar principal moments of inertia of the whole Earth. We now allow for slight perturbations of the defined reference state by mass redistribution and relative particle motion. The resulting incremental rotation can be described if a reference frame is appropriately attached to the disturbed Earth. Following Munk and MacDonald (1960), the body-fixed frame is defined so that $\mathbf{h}$ has contributions from the atmosphere, the oceans and the core, but not from relative motion in the deformable mantle. This is the 'Tisserand mean-mantle' frame of the perturbed Earth, its angular velocity with respect to inertial space equivalent to the mean rotation vector averaged through the mantle (Wahr 2005) being

$$\boldsymbol{\omega}(t) = \boldsymbol{\omega}_0 + \Delta\boldsymbol{\omega}(t) = \begin{pmatrix} \omega_1 \\ \omega_2 \\ \omega_3 \end{pmatrix} = \begin{pmatrix} m_1(t) \\ m_2(t) \\ 1 + m_3(t) \end{pmatrix} \Omega. \tag{11}$$

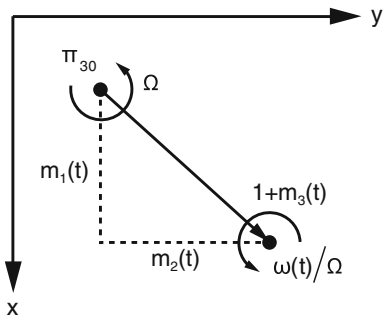

Fig. 3 Perturbations of the instantaneous rotation vector $\boldsymbol{\omega}(t)$ with respect to the state of uniform rotation around $\boldsymbol{\pi}_{30}$, the axis of figure of an undeformed Earth

The $m_i(t)$ are small dimensionless quantities describing excursions of the instantaneous rotation vector from uniform rotation. As is evident from Fig. 3, $m_1(t)$ and $m_2(t)$ can be interpreted as angular offsets that specify polar motion of the mantle's rotation axis, while $m_3(t)$ represents changes in the rate of rotation and thus LOD variations. The corresponding perturbations of Earth's angular momentum comprise $\mathbf{h}$ as well as time-variable increments in the inertia tensor

$$\mathbf{I}(t) = \mathbf{I}_0 + \Delta\mathbf{I}(t) = \mathbf{I}_0 + \begin{pmatrix} \Delta I_{11}(t) & \Delta I_{12}(t) & \Delta I_{13}(t) \\ \Delta I_{12}(t) & \Delta I_{22}(t) & \Delta I_{23}(t) \\ \Delta I_{13}(t) & \Delta I_{23}(t) & \Delta I_{33}(t) \end{pmatrix}. \tag{12}$$

For the sake of a simplified notation, the time-dependency of all quantities will be no more explicitly stated but borne in mind. The first time derivative shall be abbreviated by a dot above the character. Furthermore, it is recognized that the Earth is a nearly axisymmetric body and, hence, both A and B can be replaced by $A' = (A + B)/2$, the mean equatorial moment of inertia of the whole Earth. Substituting Eqs. (11) and (12) in the Liouville equations, and considering that $\Delta I_{ij} \ll C$, $h_i \ll \Omega C$ and $m_i \ll 1$, the equatorial and axial equations of motion (Eq. 8) can be linearized and rewritten as

$$\begin{aligned} \frac{\dot{m}_1}{\sigma_r} + m_2 &= \psi_2 \\ \frac{\dot{m}_2}{\sigma_r} - m_1 &= -\psi_1 \\ \dot{m}_3 &= \dot{\psi}_3, \end{aligned} \tag{13}$$

with $\sigma_r = \frac{(C-A')}{A'}\Omega$ being the Euler frequency, the frequency of resonance of a rigid axisymmetric Earth, see Sect. 1.3. While the m_i are quantities that may be principally inferred from astronomical or geodetic observations, the expressions on the right hand side of the system of first-order differential equations are geophysical measures, called *excitation functions* after Munk and MacDonald (1960). Neglecting external torques, the ψ_i read

$$\begin{aligned}\psi_1 &= \frac{\Omega^2 \Delta I_{13} + \Omega \Delta \dot{I}_{23} + \Omega h_1 + \dot{h}_2}{\Omega^2 (C - A')} \\ \psi_2 &= \frac{\Omega^2 \Delta I_{23} - \Omega \Delta \dot{I}_{13} + \Omega h_2 - \dot{h}_1}{\Omega^2 (C - A')} \\ \psi_3 &= \frac{-\Omega \Delta I_{33} - h_3}{\Omega C}.\end{aligned} \tag{14}$$

These expressions indicate that if the relative angular momentum components h_i and the changes of the inertia tensor ΔI_{ij} as well as their respective time derivatives are introduced as known quantities from models or observations, such as meteorological data in case of the atmosphere, the equation system (13) can be solved for m_i and thus $\boldsymbol{\omega}$. Apparently, the system's two equatorial components are coupled differential equations, and it is therefore convenient to define complex quantities according to (with $\mathrm{i} \equiv \sqrt{-1}$)

$$\begin{aligned}&\hat{m} = m_1 + \mathrm{i} m_2, \quad \hat{h} = h_1 + \mathrm{i} h_2, \quad \Delta \hat{I} = \Delta I_{13} + \mathrm{i} \Delta I_{23} \\ &\hat{\psi} = \psi_1 + \mathrm{i} \psi_2 = \frac{\Omega^2 \Delta \hat{I} - \mathrm{i} \Omega \Delta \dot{\hat{I}} + \Omega \hat{h} - \mathrm{i} \dot{\hat{h}}}{\Omega^2 (C - A')}.\end{aligned} \tag{15}$$

Thus, the bare analytical solutions of the Liouville equations for both equatorial and axial components are

$$\hat{m}(t) = \mathrm{e}^{i \sigma_r t} \left(\hat{m}(0) - \mathrm{i} \sigma_r \int_0^t \hat{\psi}(\tau) \mathrm{e}^{-\mathrm{i} \sigma_r \tau} \, \mathrm{d}\tau \right) \tag{16}$$

$$m_3 = \psi_3 + \text{const} \tag{17}$$

and describe the motion of the instantaneous rotation pole associated with a rigid axisymmetric body reacting to a small excitation. In the absence of any perturbing force, the only departure from uniform rotation would be the pole's free circular motion of period $\frac{2\pi}{\sigma_r} = 304\,\mathrm{sd}$ (sidereal days) and amplitude $\| \hat{m}(0) \|$ (Moritz and Müller 1987).

2.3 Angular Momentum Functions

Numerous authors have reformulated and modified the excitation functions in order to estimate the geophysical contributions to polar motion and changes in LOD, most notable Wahr (1982), Barnes et al. (1983) or Eubanks (1993), all highlighting a specific deficiency of the formulation given in Eq. (14): if the respective scaling factors in the denominators are disregarded, the axial excitation function ψ_3 can be interpreted as an angular momentum quantity, whereas the equatorial component $\hat{\psi}$ rather characterizes torque and contains time derivatives of inertia increments $\Delta \mathbf{I}$

and relative angular momentum **h**—quantities which cannot be accurately derived from geophysical models or observations. One possibility to overcome this difficulty would be to simply neglect the problematic terms, as done by Wahr (1982) under the severe restriction of allowing only perturbations with periods much greater than one day. Barnes et al. (1983) proceeded similarly and suggested partial integration of the equatorial excitation functions. These early studies, however, were referring the excitation equation to the instantaneous rotation axis instead of the actually observed axis—an adaption that could have eliminated the time derivatives in question. The present review will introduce the necessary adaptation in Sect. 3 and below we stick with the expressions in Eq. (14), albeit in a slightly rewritten form

$$\hat{m} + \frac{\mathrm{i}}{\sigma_r}\dot{\hat{m}} = \hat{\psi} = \hat{\chi} - \frac{\mathrm{i}}{\Omega}\dot{\hat{\chi}} \tag{18}$$

$$m_3 = \psi_3 = -\chi_3 + \text{const.} \tag{19}$$

Here, Eq. (18) has been inferred from the first two components of the Liouville equations by an adequate linear combination. $\hat{\chi}$ and χ_3 are the equatorial and axial *angular momentum functions* of the perturbing fluid (Barnes et al. 1983)

$$\hat{\chi} = \chi_1 + \mathrm{i}\chi_2 = \frac{\Omega \Delta \hat{I} + \hat{h}}{\Omega (C - A')} \tag{20}$$

$$\chi_3 = \frac{\Omega \Delta I_{33} + h_3}{C\Omega}. \tag{21}$$

The χ_i now uniformly relate to angular momentum and, as already anticipated in Sect. 2.1, they can be split into matter and motion terms, which depend on mass displacements ΔI_{i3} ($i = 1, 2, 3$) and relative angular momentum h_i, respectively. Note the differences in terminology and notation when comparing the given derivations to the formulations of other authors, e.g. Eubanks (1993) or Gross (2007), who designates the expressions in Eqs. (20) and (21) as excitation functions, too.

2.4 Effective Angular Momentum Functions

The presented solutions for wobble and changes in rotation rate are valid for a rigid, oblate but geometrically axisymmetric Earth which responds to small excitations described by the angular momentum functions in Eqs. (20) and (21). In view of Earth's fluid components and the elastic behavior of the solid Earth, perfect rigidity represents an inadequate assumption, though. It is thus necessary to systematically build a more realistic model of our planet and further develop the derived formalism for all effects which are caused by departures from rigidity. Our argumentation largely refers to Gross (2007):

- The solid portions of the Earth are elastic up to a limit. As a consequence, the mass displacement part of the excitation generates deformations which have to be treated as loading effects.
- The changing centrifugal forces accompanying variations of the rotation vector $\boldsymbol{\omega}$ lead to several indirect effects, which are relative angular momenta and changes of inertia in basically all subsystems of the planet. Added as increments to $\Delta\mathbf{I}$ and $\mathbf{h}$ in the rigid Earth solution, these contributions, along with the aforementioned loading effects, account for significant correction factors modifying the original matter and motion terms given in Eqs. (20) and (21).

Complementary to the second issue, incremental relative angular momentum $\Delta\mathbf{h}$ does not contain contributions from motions in the crust and the mantle due to the definition of the Tisserand mean-mantle frame. In addition, the oceanic response to polar motion is modeled as equilibrium tidal wave (*pole tide*). According to Wahr (2005), this approximation is sufficient for periods $\gg$ 1 d. The pole tide does not generate currents so that $\Delta\mathbf{h}$ will be void of any oceanic contributions, too. Owing to the small atmospheric mass, we can also neglect the relative motion of the atmosphere induced by perturbed centrifugal forces. Consequently, only Earth's core will contribute to $\Delta\mathbf{h}$.

Relative Angular Momentum of the Core

Following the fundamental study of Smith and Dahlen (1981) on the CW of a dynamically axisymmetric Earth, we now assume a fluid core of ellipsoidal shape. Only terms of first order in ellipticity are kept at frequencies $|\sigma| \ll \Omega$. In that case, the relative motion of the core resulting from a rigid rotation of the mantle reads

$$\begin{pmatrix} \Delta h_1 \\ \Delta h_2 \\ \Delta h_3 \end{pmatrix} = \begin{pmatrix} E & \mathrm{i}E' & 0 \\ -\mathrm{i}E' & E & 0 \\ 0 & 0 & \tilde{E} \end{pmatrix} \begin{pmatrix} m_1 \\ m_2 \\ m_3 \end{pmatrix} \tag{22}$$

$$E \approx \left(\frac{\sigma^2}{\Omega}\right) A_c, \quad E' \approx -\sigma(1-\varepsilon_c)A_c, \quad \tilde{E} = -\Omega C_c,$$

where A_c and C_c are the equatorial and polar principal moments of inertia of the core and ε_c denotes the eccentricity of the core-mantle boundary. The third equation of the given linear system implies that Earth's core is axially decoupled from the mantle and thus cannot follow changes in the mantle's rotation rate. This assumption has become the rule in excitation studies with publication of the works of Merriam (1980) or Wahr et al. (1981), and is more rigorously addressed by Dickman (2005). Besides, the assumption of dynamical axisymmetry rules out spin-wobble coupling (Smith and Dahlen 1981) so that there is no interdependency between the equatorial and axial components of the core's relative angular momentum response in Eq. (22).

Rotational Deformation

The contribution of spin and wobble to the inertia tensor via elastic yielding of the rotating Earth is denoted by $\Delta\mathbf{I}^r$. In the absence of oceans and secular effects like polar wander, the components of $\Delta\mathbf{I}^r$ can be obtained based on the assumption of an Earth model which responds to the changing centrifugal potential just in the same way as a non-rotating Earth would react to an external static potential of the same type and magnitude (Smith and Dahlen 1981, and references therein)

$$\begin{pmatrix} \Delta I^r_{13} \\ \Delta I^r_{23} \\ \Delta I^r_{33} \end{pmatrix} = \frac{a^5\Omega^2}{3G} \begin{pmatrix} k_2 & 0 & 0 \\ 0 & k_2 & 0 \\ 0 & 0 & n_0 + \frac{4}{3}k_2 \end{pmatrix} \begin{pmatrix} m_1 \\ m_2 \\ m_3 \end{pmatrix}. \tag{23}$$

Here, k_2 signifies the conventional body tide Love number relating the external potential of degree 2 to the evoked change of the Earth's potential. There have been ongoing geophysical discussions whether k_2 applies on the whole Earth (Smith and Dahlen 1981, p. 239) or on the mantle only (Dickman 2005). In this review, we shall choose the more traditional route of k_2 as a whole-Earth value. Additional parameters in Eq. (23) are a, the radius of the sphere having the same volume as the Earth (Smith and Dahlen 1981), and G, Newton's gravitational constant. The dimensionless quantity n_0 accounts for changes in Earth's mean moment of inertia associated with purely radial deformation (Gross 2007).

Equilibrium Pole Tide

The present Earth model can be augmented for the oceanic rotational response to the matter term by applying the results of Dahlen (1976) for the equilibrium pole tide. This basically requires rewriting the diagonal components of the tensor in Eq. (23) and considering small incremental quantities ΔD_{ij}

$$\begin{pmatrix} \Delta I^r_{13} \\ \Delta I^r_{23} \\ \Delta I^r_{33} \end{pmatrix} = \begin{pmatrix} D + \Delta D & \Delta D_{12} & \Delta D_{13} \\ \Delta D_{12} & D - \Delta D & \Delta D_{23} \\ \Delta D_{13} & \Delta D_{23} & \tilde{D} \end{pmatrix} \begin{pmatrix} m_1 \\ m_2 \\ m_3 \end{pmatrix}, \tag{24}$$

where

$$D = \left(k_2 + \Delta k_{ocn,w}\right) \frac{a^5\Omega^2}{3G} \tag{25}$$

$$\tilde{D} = \left[n_0 + \frac{4}{3}\left(k_2 + \Delta k_{ocn,s}\right)\right] \frac{a^5\Omega^2}{3G}. \tag{26}$$

Due to the irregular geographical distribution of the oceans, decoupling between polar motion and changes in LOD is not complete—a fact expressed in Eq. (24) by the

minute off-diagonal elements ΔD_{13} and ΔD_{23} (Smith and Dahlen 1981). However, as shown by Dahlen (1976), this effect is negligible, as is the coupling between both equatorial components conveyed by ΔD_{12}. The quantities of interest are the *oceanic Love numbers* $\Delta k_{ocn,w}$ and $\Delta k_{ocn,s}$ for the spin and wobble component in Eqs. (25) and (26). Superimposing them on the degree 2 body tide Love number increases D and $\tilde{D}$ by 16 % and 10 %, respectively. Hence, the pole tide correction is considerably smaller than the effect of rotational deformation.

Surface Loading Deformation

The matter term of the excitation process is associated with changes in the mass distribution of the geophysical fluid in question and thus represents a loading effect on the solid parts of the Earth. The resulting surface deformations partly compensate the influence of the direct mass effect of excitation on Earth's inertia tensor and are analytically accounted for by multiplying the matter terms of the angular momentum functions with a factor of $(1 + k_2')$ (for the equatorial component in Eq. 20) or $(1 + \alpha_3 k_2')$ (for the axial component in Eq. 21). Herein, k_2' denotes the load Love number of degree 2 and α_3 is a dimensionless coefficient that allows for axial core-decoupling (Merriam 1980).

The preliminary scheme for excitation studies established in Sect. 2.3 can now be updated for the described rotational and loading response of a more accurate Earth model by adding the components of $\Delta\mathbf{I}^r$ and $\Delta\mathbf{h}$, given by Eqs. (24)–(26) and (22), to the initial angular momentum functions in Eqs. (20) and (21). By substituting the so-corrected functions $\hat{\chi}$ and χ_3 into Eqs. (18) and (19), relative angular momentum of the core as well as rotational deformation of the Earth together with the passive response of equilibrium oceans are incorporated into the linearized Liouville equations. While the mathematical formulation in Eqs. (18) and (19) can be fully maintained, both the excitation terms as well as the resonance frequency of the (equatorial) system change as part of the necessary rearrangements. The updated angular momentum functions become

$$\hat{\chi} = \frac{\Omega(1 + k_2')\Delta\hat{I} + \hat{h}}{(C - A' - D)\Omega} \tag{27}$$

$$\chi_3 = k_r \frac{\Omega(1 + \alpha_3 k_2')\Delta I_{33} + h_3}{\Omega C_m}. \tag{28}$$

Clearly, the matter terms have now also been corrected for surface loading deformation. The leading factor k_r in Eq. (28) compactly describes the effect of axial rotational deformation. On the left-hand side of Eq. (18), the Euler frequency has to be expanded as $\sigma_r = \frac{(C-A')}{A'}\Omega$ and rewritten in order to yield the theoretical frequency of the CW, given also in Smith and Dahlen (1981) (p. 249)

$$\sigma_{cw} = \left(\frac{C - A' - D}{A'_m + \varepsilon_c A_c + D} \right) \Omega, \tag{29}$$

with A'_m being the mean equatorial moment of crust and mantle.

Mantle Anelasticity

Using the numerical values given in Table 1 of Gross (2007), the theoretical period of the CW calculated from Eq. (29) turns out to be about 7.5 sd smaller than the actually observed period of 434.3 ± 1.7 (1 σ) sd (Vicente and Wilson 1997). According to Smith and Dahlen (1981), such a discrepancy can largely be attributed to anelastic properties of Earth's mantle. Anelastic behavior, on the one hand, requires considering a complex increment $\hat{k}'_{an}$ on the load Love number k'_2, which is thereby modified by about 4 %. On the other hand, anelasticity also affects the body tide Love number k_2 and thus the frequency of the CW. Alas, at present there is no model that considers the impact of anelasticity on k_2, so that inclusion of this effect can only be achieved within a hybrid approach (Gross 2007), which consists of substituting the observed Chandler frequency $\hat{\sigma}_{cw}$ for its theoretical value σ_{cw} in the equatorial Liouville equation (18). The angular momentum functions have to be adapted accordingly. For this purpose, it is necessary to single out σ_{cw} in the denominator of Eq. (27) after eliminating the quantity D by aid of Eq. (29).

The resulting first-order differential equation system then reads

$$\hat{m} + \frac{\mathrm{i}}{\hat{\sigma}_{cw}} \dot{\hat{m}} = \hat{\chi} - \frac{\mathrm{i}}{\Omega} \dot{\hat{\chi}} \tag{30}$$

$$m_3 = -\chi_3 + \text{const}, \tag{31}$$

where

$$\hat{\sigma}_{cw} = \frac{2\pi}{T_{cw}} \left(1 + \frac{\mathrm{i}}{2Q_{cw}} \right) \tag{32}$$

is the complex Chandler frequency characterized by its period T_{cw} and quality factor Q_{cw}. The quantities $\hat{\chi}$ and χ_3 contain all previously stated corrections for a realistic model of our planet and, following Barnes et al. (1983), are called *effective angular momentum functions*. In this review, however, we shall keep the label *angular momentum functions*, since the initial angular momentum functions in Eqs. (20) and (21), set up for a rigid Earth, will not be needed anymore.

$$\hat{\chi} = \frac{\Omega(1 + k'_2 + \Delta\hat{k}'_{an})\Delta\hat{I} + \hat{h}}{(C - A' + A_m{}' + \varepsilon_c A_c)\hat{\sigma}_{cw}} \tag{33}$$

$$\chi_3 = k_r \frac{\Omega(1 + \alpha_3(k'_2 + \Delta\hat{k}'_{an}))\Delta I_{33} + h_3}{\Omega C_m}. \tag{34}$$

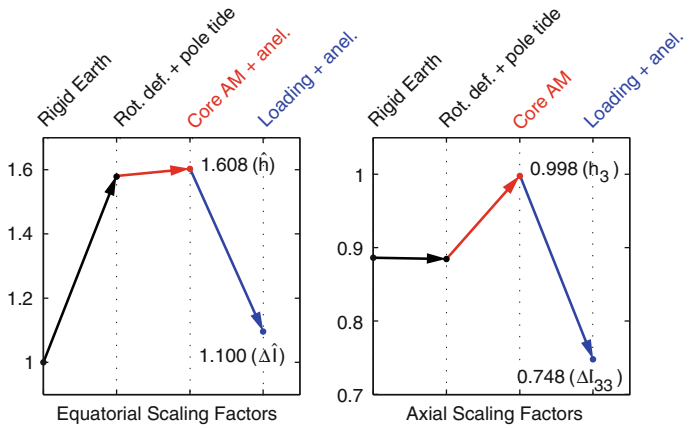

Fig. 4 Contributions of rotational deformation (including pole tide), relative angular momentum of the core, anelasticity and surface loading to the equatorial scaling factors (*left panel*, with respect to $(C - A')\Omega$ in the denominator of $\hat{\chi}$) and axial scaling factors (*right panel*, with respect to ΩC_m in the denominator of χ_3)

Introducing the numerical values specified in Table 1 of Gross (2007) for all geodetic parameters, rewriting the denominator of the angular momentum functions in terms of the traditionally used quantity $(C - A')\Omega$ and neglecting the small imaginary parts results in the final prefactors of matter and motion terms published by Gross (2007)

$$\hat{\chi} = \frac{1.100\,\Omega\,\Delta\hat{I} + 1.608\,\hat{h}}{(C - A')\Omega} \tag{35}$$

$$\chi_3 = \frac{0.748\,\Omega\,\Delta I_{33} + 0.998\,h_3}{\Omega C_m}. \tag{36}$$

Figure 4 illustrates the contributions of the various correction terms to the final equatorial and axial scaling coefficients. The displayed values have been inferred from setting the denominators in Eqs. (27)–(28) and Eqs. (35)–(36) in relation to the rigid Earth expressions, which are $(C - A')\Omega$ for the equatorial component and $\Omega C_m = 0.8864\,\Omega C$ for the axial direction, see Eqs. (20) and (21). Seemingly, surface loading acts to reduce the effects of rotational deformation, the equilibrium pole tide and relative angular momentum of the core. The impact of anelasticity on k_2 and core momentum are combined in Fig. 4 since their distinction is blurred in Eq. (35).

In Eqs. (30)–(31) and (35)–(36) we have now a mathematical tool to study relatively small geophysical excitation of polar motion variations and changes in rotation rate of a partially elastic, dynamically axisymmetric Earth equipped with a fluid, axially decoupled core and equilibrium oceans. The latter two components have been incorporated into the formulation by drawing on geophysical hypotheses valid only for frequencies $|\sigma| \ll \Omega$. As a result, the proposed scheme for excitation studies

Table 1 Comparison of the overall $\Delta\hat{I}$, $\hat{h}$, ΔI_{33} and h_3 coefficients as proposed by Gross (2007) and Barnes et al. (1983). The numerical results are based on the individual parameter values of either work

Model	$\Delta\hat{I}$ coefficient	$\hat{h}$ coefficient	ΔI_{33} coefficient	h_3 coefficient
Gross	$1.100/(C - A') = 4.1825 \cdot 10^{-36}$	$1.608/\left[(C - A')\Omega\right] = 8.3845 \cdot 10^{-32}$	$0.748/C_m = 1.0500 \cdot 10^{-38}$	$0.998/[\Omega C_m] = 1.9212 \cdot 10^{-34}$
Barnes et al.	$1.00/(C_m - A_m) = 4.2656 \cdot 10^{-36}$	$1.43/[(C_m - A_m)\Omega] = 8.3650 \cdot 10^{-32}$	$0.70/C_m = 0.9943 \cdot 10^{-38}$	$1/[\Omega C_m] = 1.9479 \cdot 10^{-34}$

is only applicable at periods significantly longer than 1 d. This restriction to the low-frequency band may also justify our tacit assumption of non-dispersive geophysical parameters such as the Love numbers, see Dickman (2005) for additional remarks on this topic. Moreover, it has to be pointed out, that the given set of correction factors is by no means unchallengeable, as it depends on the underlying geophysical models, the applied mathematical approach and the used numerical values. In detail, as shown by Gross (2007), the angular momentum functions in Eqs. (35)–(36) agree within 2 % with that of Wahr (2005) and reveal similar discrepancies compared to the approaches of Barnes et al. (1983), Eubanks (1993) or Zhou et al. (2006). A compilation and discussion of the various formulations in the spotlight of different amounts of core-mantle coupling is presented in Dickman (2003). Since the majority of previous investigations concerning geophysical effects on polar motion and LOD have used the angular momentum formulation of Barnes et al. (1983), we juxtapose in Table 1 the $\Delta\hat{I}$, $\hat{h}$, ΔI_{33} and h_3 coefficients of the latter study to the respective scaling factors of Gross (2007).

The two gravest approximations of the Barnes formulation—assuming an Earth model with a fully decoupled core and neglecting feedback features except rotational deformation plus crustal loading—are particularly apparent in the writing of the equatorial terms but numerically balance each other. As a result, the overall coefficients of $\Delta\hat{I}$ and $\hat{h}$ vary within 1–2 % across the two studies. For ΔI_{33} the discrepancy of about 5 % is down to the introduction of α_3, which has no correspondence in Barnes et al. (1983).

Considering the long-period limitations of the presented theory, it is clear, that investigation of geophysical excitation phenomena on short time scales, such as daily and subdaily atmospheric signals in ERP (or EOP, more generally), requires an adapted, frequency-dependent form of (effective) angular momentum functions. If models exist that account for relative angular momentum of the core and mass redistributions in the oceans—both engendered by the perturbing centrifugal forces due to spin and wobble—on short time scales, the derivations of Sect. 2.4 could be modified accordingly. However, this is not the case and hence, the creation of an accurate and consistent scheme for high-frequency excitation studies is still a pivotal topic of present Earth rotation research. The most remarkable effort in this field has been performed by Brzeziński (1994), who extended the original equatorial relationship of polar motion excitation, given in Eq. (30), for the FCN (Sect. 1.2). The

resulting formulation has been applied in numerous studies, most notably Brzeziński et al. (2002), Vondrák and Ron (2007) or Schindelegger et al. (2011), with the last one attempting to consistently account for a fully decoupled core. Refer to Gross (1993) for another frequently used expression of short-periodic polar motion excitation, incorporating the effects of the FCN. The present survey will expound upon the derivations of Brzeziński (1994) in Sect. 3.2 and will also discuss the model's deficits. For the major part of the review, though, the focus will be on the more established long-period formalism.

2.5 Evaluation of Angular Momentum Functions

In order to study geophysical excitation of Earth rotation, it is necessary to convert the angular momentum functions in Eqs. (35) and (36) into a practicable analytical form that is well-suited for numerical evaluation. In particular, this requires casting $\hat{\chi}$ and χ_3 in terms of certain parameters that represent the routine output of General Circulation Models (GCM), such as numerical weather or ocean models. In a first step, following Munk and MacDonald (1960), the components of the inertia tensor variations $\Delta\mathbf{I}$ and the relative angular momentum quantity $\mathbf{h}$ have to be written as volume integrals extended over the fluid considered. This conversion is accomplished by an appropriate modification of Eqs. (6) and (7), yielding

$$\hat{\chi}^{\,p} = \frac{1.100\Omega\,\Delta\hat{I}}{\Omega(C-A')} = \frac{-1.100}{C-A'}\int \rho(x_1x_3 + \mathrm{i}x_2x_3)\,\mathrm{d}V \tag{37}$$

$$\hat{\chi}^{\,w} = \frac{1.608\hat{h}}{\Omega(C-A')} = \frac{1.608}{\Omega(C-A')}\int (x_2\dot{x}_3 - x_3\dot{x}_2) - \mathrm{i}\,(x_1\dot{x}_3 - x_3\dot{x}_1)\,\mathrm{d}V \tag{38}$$

$$\chi_3^{\,p} = \frac{0.748\Omega\,\Delta I_{33}}{\Omega C_m} = \frac{0.748}{C_m}\int \rho(x_1^2 + x_2^2)\,\mathrm{d}V \tag{39}$$

$$\chi_3^{\,w} = \frac{0.998h_3}{\Omega C_m} = \frac{0.998}{\Omega C_m}\int \rho(x_1\dot{x}_2 - x_2\dot{x}_1)\,\mathrm{d}V, \tag{40}$$

where the separation into matter and motion terms is underlined by the superscripts p (for *pressure*) and w (for *wind*)—a labeling which originates from the meteorological parameters central to matter and motion terms of atmospheric angular momentum functions. An elegant formulation of pressure terms $\hat{\chi}^{\,p}$, $\chi_3^{\,p}$ and wind terms $\hat{\chi}^{\,w}$, $\chi_3^{\,w}$ can be obtained by transforming the position vector $\mathbf{x}$ into spherical coordinates and writing $\dot{\mathbf{x}} = \mathbf{v}$ in a suitable geographical coordinate system (e.g., Moritz and Müller 1987)

$$\mathbf{x} = r\begin{pmatrix}\cos\phi\cos\lambda\\ \cos\phi\sin\lambda\\ \sin\phi\end{pmatrix}$$

$$\mathbf{v} = u\mathbf{e}_{East} + v\mathbf{e}_{North} + w\mathbf{e}_{Vert}.$$

Here, ϕ and λ denote geocentric latitude and longitude, r is the geocentric radius of the mass element and the velocity components (u, v, w) are given in the direction of the unit vectors $\mathbf{e}_k$, $k \in \{East, North, Vert\}$. After some modifications, we find

$$\begin{aligned}\hat{\chi} &= \frac{-1.100}{C - A'} \iiint \rho r^4 \sin\phi \cos^2\phi \mathrm{e}^{\mathrm{i}\lambda} \,\mathrm{d}\lambda\mathrm{d}\phi\mathrm{d}r \\ &\quad + \frac{-1.608}{\Omega(C - A')} \iiint \rho r^3 (u \sin\phi + \mathrm{i}v) \cos\phi \mathrm{e}^{\mathrm{i}\lambda} \,\mathrm{d}\lambda\mathrm{d}\phi\mathrm{d}r \\ &= \hat{\chi}^p + \hat{\chi}^w \end{aligned} \tag{41}$$

$$\begin{aligned}\chi_3 &= \frac{0.748}{C_m} \iiint \rho r^4 \cos^3\phi \,\mathrm{d}\lambda\mathrm{d}\phi\mathrm{d}r \\ &\quad + \frac{0.998}{\Omega C_m} \iiint \rho r^3 u \cos^2\phi \,\mathrm{d}\lambda\mathrm{d}\phi\mathrm{d}r \\ &= \chi_3^p + \chi_3^w . \end{aligned} \tag{42}$$

Equations (41) and (42) represent the routine expressions for evaluating angular momentum functions. Pressure and wind terms are three-dimensional integrals accumulating the density distribution and velocity field over the volume of the perturbing fluid. Depending on the data available, though, it might be useful to employ slightly altered angular momentum functions formulae. We shall now give a brief compilation of the various calculation methods, with particular focus on atmospheric angular momentum (AAM) $\hat{H}^{(a)}$ and $H_3^{(a)}$

$$\begin{aligned}\hat{H}^{(a)} = H_1^{(a)} + \mathrm{i}H_2^{(a)} &= \Omega \Delta\hat{I} + \hat{h} \\ H_3^{(a)} &= \Omega \Delta I_{33} + h_3 .\end{aligned}$$

Integration Over Radial Increments

This computation variant fully corresponds to Eqs. (41) and (42), except for the scaling factors and geodetic parameters, which are not needed when considering raw angular momentum. The vertical integral extends from Earth's surface $r = r_s(\phi, \lambda)$ up to $r = \infty$, strictly speaking. In any practical application, the top border will be represented by a distinct layer (for instance the pressure level of 0.1 hPa), from which upwards density values ρ and wind velocities (u, v) have a negligibly small contribution to AAM. Equatorial and axial matter and motion terms read

$$\Delta\hat{I} = -\int_{r_s}^{\infty}\int_{-\frac{\pi}{2}}^{\frac{\pi}{2}}\int_0^{2\pi} \rho r^4 \sin\phi \cos^2\phi \mathrm{e}^{\mathrm{i}\lambda} \,\mathrm{d}\lambda\mathrm{d}\phi\mathrm{d}r \tag{43}$$

$$\hat{h} = -\int_{r_s}^{\infty}\int_{-\frac{\pi}{2}}^{\frac{\pi}{2}}\int_0^{2\pi} \rho r^3 (u \sin\phi + \mathrm{i}v) \cos\phi \mathrm{e}^{\mathrm{i}\lambda} \,\mathrm{d}\lambda\mathrm{d}\phi\mathrm{d}r \tag{44}$$

$$\Delta I_{33} = \int_{r_s}^{\infty}\int_{-\frac{\pi}{2}}^{\frac{\pi}{2}}\int_{0}^{2\pi} \rho r^4 \cos^3\phi \,\mathrm{d}\lambda\mathrm{d}\phi\mathrm{d}r \tag{45}$$

$$h_3 = \int_{r_s}^{\infty}\int_{-\frac{\pi}{2}}^{\frac{\pi}{2}}\int_{0}^{2\pi} \rho r^3 u \cos^2\phi \,\mathrm{d}\lambda\mathrm{d}\phi\mathrm{d}r. \tag{46}$$

Integration Over Pressure Increments

If a vertical atmospheric pressure gradient is assumed on the basis of the hydrostatic equation $\mathrm{d}p = -\rho g \mathrm{d}r$, the radial integral in the AAM formulae can be written in terms of pressure increments, see Barnes et al. (1983). $g = g(r)$ is the gravity acceleration and p_s, introduced in the integration limits, denotes the surface pressure.

$$\Delta\hat{I} = -\int_{0}^{p_s}\int_{-\frac{\pi}{2}}^{\frac{\pi}{2}}\int_{0}^{2\pi} \frac{r^4}{g} \sin\phi\cos^2\phi \mathrm{e}^{\mathrm{i}\lambda} \,\mathrm{d}\lambda\mathrm{d}\phi\mathrm{d}p \tag{47}$$

$$\hat{h} = -\int_{0}^{p_s}\int_{-\frac{\pi}{2}}^{\frac{\pi}{2}}\int_{0}^{2\pi} \frac{r^3}{g}(u\sin\phi + \mathrm{i}v)\cos\phi \mathrm{e}^{\mathrm{i}\lambda} \,\mathrm{d}\lambda\mathrm{d}\phi\mathrm{d}p \tag{48}$$

$$\Delta I_{33} = \int_{0}^{p_s}\int_{-\frac{\pi}{2}}^{\frac{\pi}{2}}\int_{0}^{2\pi} \frac{r^4}{g} \cos^3\phi \,\mathrm{d}\lambda\mathrm{d}\phi\mathrm{d}p \tag{49}$$

$$h_3 = \int_{0}^{p_s}\int_{-\frac{\pi}{2}}^{\frac{\pi}{2}}\int_{0}^{2\pi} \frac{r^3}{g} u\cos^2\phi \,\mathrm{d}\lambda\mathrm{d}\phi\mathrm{d}p. \tag{50}$$

Integration Over Pressure Increments, Constant Radius and Gravity

Given the relatively small extension of any surficial fluid layer compared to Earth's radius, it is justified to model the atmosphere as thin spherical shell with constant radius $\overline{r}$ and constant gravity acceleration $\overline{g}$. This thin layer approximation enables us to directly reduce the pressure integral of the matter terms in Eqs. (47) and (49) to the plain surface pressure p_s (Barnes et al. 1983)

$$\Delta\hat{I} = -\frac{\overline{r}^4}{\overline{g}}\int_{-\frac{\pi}{2}}^{\frac{\pi}{2}}\int_{0}^{2\pi} p_s \sin\phi\cos^2\phi \mathrm{e}^{\mathrm{i}\lambda} \,\mathrm{d}\lambda\mathrm{d}\phi \tag{51}$$

$$\hat{h} = -\frac{\overline{r}^3}{\overline{g}}\int_{0}^{p_s}\int_{-\frac{\pi}{2}}^{\frac{\pi}{2}}\int_{0}^{2\pi} (u\sin\phi + \mathrm{i}v)\cos\phi \mathrm{e}^{\mathrm{i}\lambda} \,\mathrm{d}\lambda\mathrm{d}\phi\mathrm{d}p \tag{52}$$

$$\Delta I_{33} = \frac{\overline{r}^4}{\overline{g}}\int_{-\frac{\pi}{2}}^{\frac{\pi}{2}}\int_{0}^{2\pi} p_s \cos^3\phi \,\mathrm{d}\lambda\mathrm{d}\phi \tag{53}$$

$$h_3 = \frac{\overline{r}^3}{\overline{g}}\int_{0}^{p_s}\int_{-\frac{\pi}{2}}^{\frac{\pi}{2}}\int_{0}^{2\pi} u\cos^2\phi \,\mathrm{d}\lambda\mathrm{d}\phi\mathrm{d}p. \tag{54}$$

Analogous expressions can be found for the purpose of calculating oceanic angular momentum (OAM). For example, the OAM matter terms follow from Eqs. (51) and (54) if p_s is substituted by $g\rho H$, where H represents the total height of the oceanic column and a constant density for sea water is used. Such variations in OAM are partly due to the effect of tidal displacements of water mass (Dehant and de Viron 2002), but are certainly also created by thermohaline processes and the oceanic response to atmospheric surface winds and pressure fluctuations (Wahr 1982). Whereas modeling wind-induced oceanic motion is a more complex problem, the pressure-based reaction on time scales longer than 5 d (Wunsch and Stammer 1997) can be easily taken into account by reverting to the IB (inverted barometer) model, see e.g. Munk and MacDonald (1960). This hypothesis is valid in deep water for most cases, whereas the response of shallow water requires separate treatment, refer to Wunsch and Stammer (1997) for a brief discussion. The IB model supposes the ocean surface to readjust to the spatial variation of atmospheric pressure, i.e. water is depressed (or lifted) by a local pressure increase (or decrease). Such a near-surface compensation of pressure variations implies that the bottom pressure at the bathymetry is constant in space but changes with time (de Viron and Dehant 1999). Hence, for the purpose of studying Earth rotation variations, the IB correction at a specific epoch consists of building the mean atmospheric pressure across the oceans

$$\bar{p}_o = \frac{1}{O} \iint p_o \, \mathrm{d}O$$

and adopting for each above-ocean data point the resulting value $\bar{p}_o$ in place of the actual surface pressure p_s in Eq. (51). As noted in Wahr (1982), this approach makes the oceanic contribution to χ_i^p compensate the corresponding contribution from the atmospheric portion above the oceans, so that in total the amplitude of the AAM matter term is reduced. At daily and subdaily time scales, though, the IB correction worsens the agreement of AAM functions with geodetic data (Brzeziński et al. 2002) and needs to be replaced by a sophisticated model that describes the dynamical response of the oceans to high-frequency atmospheric wind and pressure forcing.

We close this section with a brief investigation of axial AAM at the annual frequency. The significant dependency of this quantity on the strength and distribution of zonal winds $u\,(p, \phi, \lambda)$ is highlighted on the basis of monthly means of climatological data that have been generated by the ECMWF (European Centre for Medium-Range Weather Forecasts) within a 40-year reanalysis effort. Figure 5 displays the climatology of zonal winds, averaged over the full range of longitude and expressed as latitude-pressure cross-sections. From the available fields of $u\,(p, \phi)$ at monthly intervals, two mean fields have been extracted—one covering the period of December/January/February (labeled as *boreal winter*) and another one representing the average of wind speeds in June/July/August (*austral winter*). Data above the isobaric level of 10 hPa are neglected due to the small amount of total mass above that level ($\approx$1% of the total). This fact ensures that the contribution of upper atmospheric winds to relative angular momentum is small. Both hemispheres feature similar

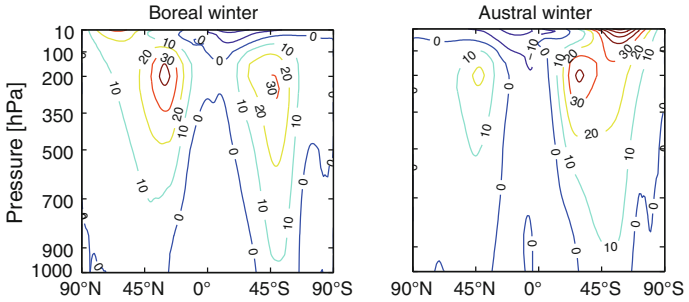

Fig. 5 Longitude-averaged cross sections of annual zonal winds as represented in ECMWF climatological data. The latitude-pressure fields of December/January/February (boreal winter, *left panel*) and June/July/August (austral winter, *right panel*) have been averaged to one respective cross section

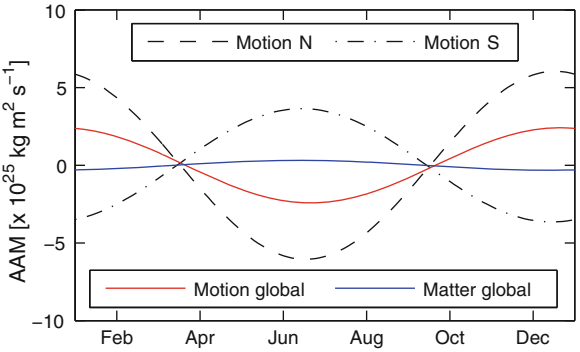

Fig. 6 Constituents of long-term axial atmospheric angular momentum at the annual frequency: motion term of each hemisphere (*dashed line* and *dotdashed line*), sum of hemispheric motion terms (*red line*) and global matter term (*blue line*). Underlying data: ECMWF climatological data at monthly intervals

signals: weak easterly winds (or negative u-values) prevail in the tropical regions, while westerly jet streams are found over most of the extratropics (Salstein 2002), centered at levels near 200 hPa. The jet stream phenomenon of each hemisphere is subject to an annual cycle and peaks in its respective winter months. As a result of the asymmetric global distribution of the continents, the signal in the Northern Hemisphere is of larger annual variability than that of the Southern Hemisphere. This difference in magnitude is also evident from Fig. 6, which depicts long-term mean axial AAM that has been obtained from the aforementioned climatological dataset. Obviously, the motion term of the Southern Hemisphere is only about 40 % that of the Northern, and of opposite sign, so that the annual amplitude of the global relative angular momentum does not exceed $25 \cdot 10^{24}\,\mathrm{kg\,m^2\,s^{-1}}$. Pressure fluctuations provide a relatively minor contribution of about 5–10 % to the annual cycle of axial AAM, see e.g. Gross et al. (2004).

2.6 An alternative Modeling Approach via Torques

Alongside the classical angular momentum method, the influence of Earth's fluid components on polar motion, nutation and changes in length of day can also be studied by considering atmospheric and oceanic effects as external torques acting on the mechanical system Earth (de Viron et al. 1999). Supposing the fluid layer to be outside the physical system contrasts with the angular momentum approach, which retrieves information about changes in Earth rotation from the abstract balance of angular momentum within the entire Earth-fluid system, cf. Sect. 1.5. Nonetheless, both methods are analytically and physically equivalent (de Viron and Dehant 1999) and should provide similar results when deployed for excitation studies. The relationship and numerical coherence between both approaches will be discussed in a later paragraph. We shall now focus on the analytical expressions that are central to the torque method.

Consider a fluid—the atmosphere in the following—surrounding and interacting with the solid Earth. In the light of basic Newtonian physics, any variation in the total angular momentum $\mathbf{H}^{(s)}$ of the solid body is equivalent to the total torque acting on the solid Earth due to the atmosphere (de Viron and Dehant 1999)

$$\mathbf{L}^{(a)\to(s)} = \frac{\mathrm{d}\mathbf{H}^{(s)}}{\mathrm{d}t}, \tag{55}$$

where $\mathrm{d}/\mathrm{d}t$ is the time derivative in an inertial reference system. By recognizing that

$$\mathbf{L}^{(a)\to(s)} = -\mathbf{L}^{(s)\to(a)} \tag{56}$$

$$\frac{\mathrm{d}\mathbf{H}^{(s)}}{\mathrm{d}t} = -\frac{\mathrm{d}\mathbf{H}^{(a)}}{\mathrm{d}t} \tag{57}$$

holds for an isolated Earth-atmosphere system in space, we obtain the angular momentum budget equation of the atmospheric layer in the celestial frame

$$\mathbf{L}^{(s)\to(a)} = \frac{\mathrm{d}\mathbf{H}^{(a)}}{\mathrm{d}t}. \tag{58}$$

As shown by de Viron et al. (1999) in a very general way, the torque exerted on the atmosphere can be computed directly from the integral of local forces at the bottom surface S of the atmosphere

$$\mathbf{L}^{(s)\to(a)} = \underbrace{\int \mathbf{r} \times (-p_s)\,\mathbf{n}\,\mathrm{d}S}_{\mathbf{L}^p} + \underbrace{\int \mathbf{r} \times p_s \mathbf{n}_g\,\mathrm{d}S}_{\mathbf{L}^g} + \underbrace{\int \mathbf{r} \times (\eta\mathbf{n}\cdot\nabla\mathbf{v}_r)\,\mathrm{d}S}_{\mathbf{L}^f}. \tag{59}$$

Herein, $\mathbf{r}$ is the position vector and $\mathbf{v}_r$ the relative velocity vector of the mass element with respect to the terrestrial frame. The quantity η represents the dynamic viscosity

of the fluid, while both $\mathbf{n}$ and $\mathbf{n}_g$ denote unit vectors orientated towards the center of the Earth, with $\mathbf{n}$ being orthogonal to the integration surface and $\mathbf{n}_g$ normal to the equipotential at S (de Viron et al. 2001a).

Obviously, the total interaction torque between the Earth and the atmosphere is composed of three parts, see e.g. de Viron and Dehant (1999): a pressure torque $\mathbf{L}^p$ acting on the topography, a gravitational torque $\mathbf{L}^g$ corresponding to the attraction of the atmospheric mass by Earth's nonspherical mass, and a friction torque $\mathbf{L}^f$ due to the local friction drag associated with atmospheric surface winds. We will now address those three components in more detail.

Pressure Torque

Speaking in terms of the atmospheric torque acting on the solid Earth (left-hand side of Eq. 56), the pressure torque is generated by the pressure forcing of fluid masses on the topography. As initially shown by Wahr (1982), the equatorial component of this torque has to be separated into two parts: a global pressure torque acting on the ellipticity of the Earth and a so-called *mountain torque* on the local topography. This local pressure torque arises from the differential action of surface pressure on the two faces of mountain ranges (de Viron et al. 2001b) as depicted in Fig. 7. Hence, it can be estimated by multiplying the gradient of $p_s = p_s(\theta, \lambda)$ with the radius arm $a + h(\theta, \lambda)$ at co-latitude θ and longitude λ. Herein, the quantity a denotes the radius of a mean spherical Earth, while h is the elevation of the topography bar the effect of ellipticity. The corresponding analytical expression is given by de Viron and Dehant (1999)

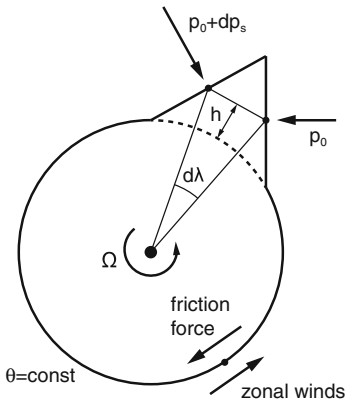

Fig. 7 Illustration of pressure torque and friction torque in the axial direction as seen from the north pole. An exaggerated topographic feature at co-latitude θ is subject to a zonal pressure gradient force of magnitude $\mathrm{d}p_s$. Local surface winds give rise to a zonal friction force, which in turn counters and reduces the depicted westerlies, i.e. the Earth gains angular momentum from the atmosphere (Salstein 2002). Figure modified from Wahr and Oort (1984)

$$\mathbf{L}^p = -a^2 \iint (a + h(\theta, \lambda)) \left(\frac{\mathrm{d}p_s}{\mathrm{d}\lambda} \begin{pmatrix} \cos\lambda\cos\theta \\ \sin\lambda\cos\theta \\ -\sin\theta \end{pmatrix} + \frac{\mathrm{d}p_s}{\mathrm{d}\theta} \begin{pmatrix} \sin\lambda\sin\theta \\ -\cos\lambda\sin\theta \\ 0 \end{pmatrix} \right) \mathrm{d}\theta\mathrm{d}\lambda. \tag{60}$$

Equivalent expressions for the equatorial and axial mountain torques can be derived from Feldstein (2008) and Iskenderian and Salstein (1998), respectively, after eliminating the pressure gradient in Eq. (60) using integration by parts. The latter study also demonstrates the significant contribution of the topographic pressure torque to the axial component of $\mathbf{L}^{(s)\to(a)}$, which may amount to 65 % at periods shorter than 15 d.

Gravitational Torque

By deploying the thin layer approximation in the set-up of Eq. (59), de Viron et al. (1999) showed that the analytical expression for the gravitational torque $\mathbf{L}^g$ is very similar to that of the $\mathbf{L}^p$. In fact, as it is the case for the pressure torque, the equatorial gravitational torque can also be divided into two constituents: a global portion arising from the flattening of the geopotential surface (expressed by Earth's form factor, J_2) and another portion due to the local anomalies of the geoid (comprising all degrees and orders except that of J_2). The contribution of this local gravitational torque to $\mathbf{L}^{(s)\to(a)}$ has been shown to be negligible at all frequencies (de Viron et al. 2001b) and will not be treated any further.

As noted in de Viron et al. (2005), the pressure torque on the Earth's bulge as well as the corresponding gravitational torque on the J_2 term are both caused by the pushing of atmospheric surface pressure distributed globally as spherical harmonic of degree 2 and order 1 (Fig. 8). A simple expression for this *ellipsoidal torque* $\mathbf{L}_E$ has been deduced by de Viron et al. (1999) after applying in Eq. (59) spherical harmonic expansions on the topography, the geopotential and the surface pressure field. Restricting the topography and geopotential to degree 2 and order 0, $\mathbf{L}_E$ can be expressed in terms of a torque acting on the atmosphere

$$\begin{aligned} \mathbf{L}_E &= \mathbf{L}^p_{20} + \mathbf{L}^g_{20} \\ &= \frac{12\pi}{5} a^3 \begin{pmatrix} u_{20}\tilde{p}_{21} \\ -u_{20}p_{21} \\ 0 \end{pmatrix} - \frac{12\pi}{5} a^3 \begin{pmatrix} -J_2\tilde{p}_{21} \\ J_2 p_{21} \\ 0 \end{pmatrix}, \end{aligned} \tag{61}$$

where $u_{20} = -2/3\,f$ and f represents the dynamical flattening of the Earth (de Viron and Dehant 1999). The real and imaginary parts of the degree 2 and order 1 coefficient in the spherical harmonic development of the surface pressure are labeled p_{21} and $\tilde{p}_{21}$. By substituting numerical values for f and J_2, it can be shown that the gravitational torque compensates about one half of the ellipsoidal pressure torque. Nonetheless, the sum of both effects is by far the largest signal in the equatorial part of the total torque.

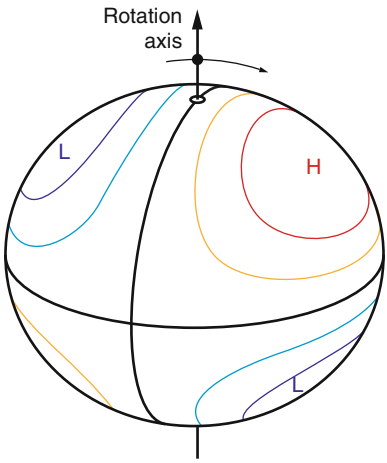

Fig. 8 Torque on the ellipticity of the Earth generated by the action of a global surface pressure field that corresponds to a spherical harmonic term of degree 2 and order 1

Friction Torque

The friction torque on the atmosphere depends on the local tangential wind stress $-\eta \mathbf{n}\cdot\nabla \mathbf{v}_r$, which is a common output of atmospheric models in the form of two scalar fields (f_θ, f_λ) representing the friction force on the topography in co-latitudinal and longitudinal direction, see Fig. 7. As shown by de Viron et al. (1999), the full friction torque vector is composed of

$$\mathbf{L}^f = -a^3 \iint \begin{pmatrix} -f_\theta \sin\lambda - f_\lambda \cos\theta \cos\lambda \\ f_\theta \cos\lambda - f_\lambda \cos\theta \sin\lambda \\ f_\lambda \sin\theta \end{pmatrix} \sin\theta \mathrm{d}\theta \mathrm{d}\lambda. \tag{62}$$

Feldstein (2008) gives an identical formulation for the equatorial part of the friction torque, which is very small except for subdaily frequencies (de Viron et al. 2001b). The axial friction torque, constituting 30–50 % of the total zonal Earth-atmosphere torque at different time scales, is treated intensively by Wahr and Oort (1984).

Having successfully evaluated the different constituents of the total atmospheric torque in Eq. (59), one might, in principle, deploy the integral quantity $\mathbf{L}^{(a)\to(s)} = -\mathbf{L}^{(s)\to(a)}$ as a forcing function in the Liouville equations. Since the atmosphere is modeled as external layer to the physical system, the interaction torque has to be considered in the vector $\mathbf{L}$ on the left-hand side of Eq. (8), see Seitz and Schuh (2010). Given this condition, it is clear that within the torque approach relative angular momentum vanishes from the Liouville equations. Likewise, there is also no contribution of the mass redistribution to the incremental tensor of inertia $\Delta\mathbf{I}$. Though, similar to what has been outlined in Sect. 2.4, inertia variations that are due to rotational perturbations and deformations related to the changing surface load have to be accounted for. Further details on the inclusion of the interaction torque in the Liouville equations are given by de Viron et al. (2005).

In literature, the direct determination of Earth rotation variations via torques has been approached only rarely, with most of the efforts being restricted to the axial component, see e.g. Salstein and Rosen (1994) or Wolf and Smith (1987). Wahr (1983), among other aspects, deployed the torque approach to study geophysical excitation of seasonal variations in polar motion, while Dehant et al. (1996) estimated the effect of the pressure torque on precession and nutation. The particular role of oceanic torques in inducing intraseasonal, seasonal and interannual polar motion variations has been addressed by Fujita et al. (2002). Refer to the last paper also for a practicable formulation of the equatorial excitation function based on torques.

The majority of related studies has brought the focus on the intercomparison of AAM and the Earth-atmosphere interaction torque. The analytical equivalence of those two quantities has already been notified in Eq. (58) in the form of the angular momentum budget equation, which states that the time derivative of AAM equals the total torque acting on the atmosphere. In order to obtain a practicable phrasing of this relationship, it is required to convert the AAM time series ($H_1^{(a)}$, $H_2^{(a)}$, $H_3^{(a)}$) from the terrestrial reference frame (see Sect. 2.5) to the space-fixed reference frame according to de Viron et al. (1999)

$$\begin{aligned} L_1^{(s)\longrightarrow(a)} &= \dot{H}_1^{(a)} - \Omega H_2^{(a)} \\ L_2^{(s)\longrightarrow(a)} &= \dot{H}_2^{(a)} + \Omega H_1^{(a)} \\ L_3^{(s)\longrightarrow(a)} &= \dot{H}_3^{(a)}. \end{aligned} \tag{63}$$

This vector-valued budget equation has been tested frequently within atmospheric models, showing that the time derivative of AAM can be indeed largely explained by the Earth-atmosphere interaction torque. Yet, such a numerical equivalence gradually vanishes at short time scales, i.e. periods smaller than 10 d, see de Viron and Dehant (2003). At the diurnal frequency in particular, the AAM budget equation remains unverified both in the axial and the equatorial component. Figure 9 illustrates the variable agreement between AAM and torques at different frequencies in terms of a coherence study for the equatorial part of Eq. (63). The observed discrepancies at short time scales are mainly due to some uncertainties in the torque formulations, numerical problems in the torque computation itself as well as deficiencies in the atmospheric models that provide the analysis fields of the underlying meteorological parameters. Unlike AAM, which stems from the calculation of one smoothed global value (Seitz and Schuh 2010), the total torque results from the cancellation of large numbers (see e.g. Eq. 61). This certainly fuels numerical instabilities and amplifies model errors. In fact, many of the quantities that are necessary for the torque determination are not well known, e.g. the friction drag and the surface pressure over regions of large altitude variations (de Viron and Dehant 2003). Furthermore, the coarse spatial resolution of topographic models poses limitations on the evaluation of the high-frequency pressure torque and requires considering subgrid scale processes, such as the *gravity wave drag*, of which the parameterization is still not fully solved (de Viron et al. 2001b).

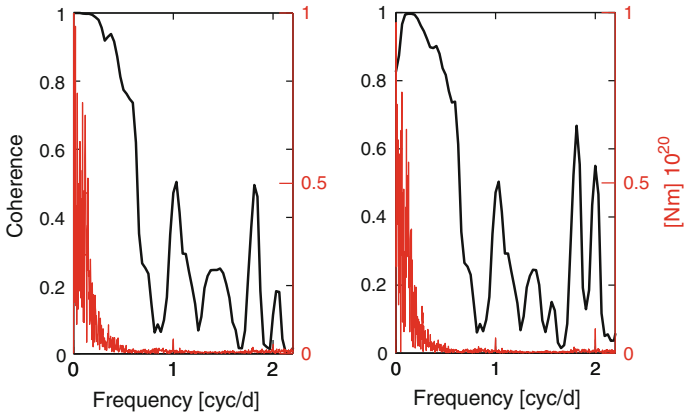

Fig. 9 Frequency-dependent magnitude-squared coherence (*black line*) between torques and the time derivative of atmospheric angular momentum as derived from Eq. (63) for the x-component (*left panel*) and the y-component (*right panel*). The amplitude spectrum of the torque signals (red line) indicates frequency bands (in cycles per day) of high signal-to-noise ratio. The underlying torques and AAM time series have been determined consistently from three-hourly forecast fields of the ECMWF for the time span of 2010. Ellipsoidal, pressure and friction torques have been derived from surface data, while the AAM values resort to pressure level data

A problem common to both modeling approaches is the consideration of the oceanic response to atmospheric forcing. This effect, already addressed in Sect. 2.5 is equivalent to the non-tidal part of OAM and may be regarded as indirect influence of the atmosphere on Earth rotation, which is non-negligible in the angular momentum budget of a system that comprises Earth, atmosphere and oceans. In an insightful study on this subject, de Viron et al. (2001a) examined the additional torques that have to be taken into account in the Earth's angular momentum balance as a result of the pressure, friction and gravitational forces exerted by the atmosphere on the oceans. As reported earlier, one may approach the issue of an oceanic response effect with either a static hypothesis (IB or non-IB) or a dynamic ocean model. The IB assumption can easily be incorporated in the torque formalism, though, it is only appropriate for low-frequency processes (de Viron and Dehant 1999). At periods shorter than 10 d, and for nutational motions in particular, complex ocean dynamics determine the indirect effect of the atmosphere on Earth rotation. However, dynamic ocean models that may account for such phenomena are still far from perfect.

Considering the presented difficulties, it is clear that the angular momentum method is generally more successful as far as a precise estimation of geophysical excitation of Earth rotation is concerned. As noted, the computation of angular momentum is an averaging operation, which is less sensitive to errors in the underlying data. The principal disadvantage of the angular momentum approach, however, is that it can only indicate the occurrence of angular momentum change in the fluid layer without being able to tell where and how momentum is transmitted to the solid Earth, see de Viron and Dehant (1999). Such understanding of the physical interac-

tion between Earth and atmosphere can only be provided by the torque approach. By explicitly looking at the normal and tangential surface forces, the torque method gives insight into the specific processes that lead to a change in angular momentum of the solid Earth (Seitz and Schuh 2010). In particular, it allows studying the origin and spatial location of those processes in an active way, noting how meteorological systems crossing particular mountain ranges effect the angular momentum exchange.

Consequently, when studying geophysically-induced variations of ERP, the torque approach represents a source of additional information, even though its actual rotation corrections are not as precise and less reliable than the corresponding estimates from the AAM method. Both approaches may be applied in parallel in order to also learn about their respective reliability and accuracy (de Viron et al. 1999). Finally, there is the prospect of improved circulation models in the future, which will be of great benefit for further advancing the value of torque estimates for Earth rotation studies.

3 Angular Momentum Functions and Earth Rotation Parameters

Comparison of numerically evaluated angular momentum functions and time series of Earth rotation (orientation) parameters is the core task of excitation studies and can be basically accomplished by means of the linearized differential equations system derived in Sect. 2.4. Equations (30) and (31) allow us to relate small changes in the angular momentum of a certain geophysical fluid to the associated equatorial and axial variations of Earth's rotation axis (Gross 2007). However, as already anticipated in Sect. 2.3, a practical application of the equation system requires incorporating the actually observed axis as reference direction. The following portions of the review will deal with this problem. For the case of polar motion studies, the conventional model will be introduced in Sect. 3.1, before being extended for the effects of the FCN in Sect. 3.2.

3.1 Polar Motion, Standard Model

The polar motion of Earth's instantaneous rotation axis $\hat{m} = m_1 + \mathrm{i}m_2$ is a relative quantity which requires specification of the underlying reference system. Within geodetic practice, this reference system is realized empirically by a network of globally distributed, rotating reference points, from which observations are made. As soon as such a body-fixed reference system (the TRS) is established, the instantaneous rotation pole cannot be defined freely but instead follows from kinematical considerations. Those considerations shall be the focal point of the present section. In particular, the motion of the instantaneous rotation axis will be related to that of the CIP, the position of which is usually reported by modern Earth rotation measurement

services and parameterized by the set of pole coordinates $\{x_p, y_p\}$. The prerequisite derivations have been published by Brzeziński (1992) or Gross (1992).

After finding the kinematical relationship between the TRS-based quantities $\{x_p, y_p\}$ and $\{m_1, m_2\}$, a link to the dynamical equations of rotation, such as Eq. (30), needs to be established, i.e. geophysical excitation and geodetic observation of Earth rotation have to be connected properly. This task appears to be straightforward since Eq. (30) incorporates the polar motion of Earth's instantaneous rotation axis. However, that equation has been deduced theoretically, based on the dynamical definition of a reference system (the Tisserand mean mantle frame). Hence, it has to be asked if it is legitimate to study polar motion with respect to the TRS by using formulae valid in the Tisserand mean mantle frame. Chao (1984) considered the evoked inconsistencies in the frequency band of the Chandler Wobble and found the resultant errors to be negligible. Moreover, current realizations of the TRS consider the concept of the mean crust (cf. Altamimi et al. 2003) and thus may provide an approximation to a Tisserand frame of the mantle. The validity of such an assumption is supported by the fact that motions in the mantle on time scales up to decades are concentrated in the upper layer of the astenosphere (A. Brzeziński, personal communication).

The considerations now closely follow Gross (1992), who assumes all celestial motions of the CIP to be perfectly accounted for by an appropriate precession-nutation model. The celestial reference is thus a modified (intermediate) form of the GCRS, rotated by the matrix $\mathbf{Q}(t)$, with its pole represented by the CIP. The TRS is rotating with respect to this GCRS and the motion is characterized by the angular velocity vector $\boldsymbol{\omega}_i$, where the subscript i labels quantities given in the inertial system. If the origins of both the TRS and GCRS coincide, the transformation of position vectors from one system to the other can be accomplished by aid of a time-dependent rotation matrix

$$\mathbf{x} = \mathbf{R}\mathbf{x}_i \tag{64}$$

$$\boldsymbol{\omega} = \mathbf{R}\boldsymbol{\omega}_i . \tag{65}$$

The velocity of a point that rests with respect to the GCRS follows from the derivative of Eq. (64)

$$\dot{\mathbf{x}} = \dot{\mathbf{R}}\mathbf{x}_i = \dot{\mathbf{R}}\mathbf{R}^{\mathrm{T}}\mathbf{x}$$

$$\dot{\mathbf{R}}\mathbf{R}^{\mathrm{T}} \equiv \mathbf{C}. \tag{66}$$

Considering that $\dot{\mathbf{x}}$ can be equivalently calculated from

$$\dot{\mathbf{x}} = -\boldsymbol{\omega} \times \mathbf{x}$$

the components of the rotation vector $\boldsymbol{\omega}$ can be associated with an antisymmetric matrix (Gross 1992)

$$\dot{\mathbf{R}}\mathbf{R}^{\mathrm{T}}\mathbf{x} = -\boldsymbol{\omega} \times \mathbf{x}$$

$$\Rightarrow \mathbf{C} = (-\boldsymbol{\omega}\times) = \begin{pmatrix} 0 & \omega_3 & -\omega_2 \\ -\omega_3 & 0 & \omega_1 \\ \omega_2 & -\omega_1 & 0 \end{pmatrix}. \tag{67}$$

In order to express $(\omega_1, \omega_2, \omega_3)$ in terms of the elements in $\mathbf{C}$, Eq. (66) requires us to find a representation of the rotation matrix $\mathbf{R}$. For this purpose, it is of benefit to introduce a body-fixed Intermediate Reference System [IRS, equivalent to the *nutation system* used by Moritz and Müller (1987)], characterized by its origin and reference axis being that of the GCRS. Thus, the pole of the IRS is the CIP. If we further suppose that the intermediate system is rotating about its reference axis at constant rate Ω, the transformation matrix $\mathbf{U}$, relating corresponding position vectors in the GCRS (subscript i) and the uniformly rotating IRS (subscript u), reads

$$\mathbf{x}_u = \mathbf{U}\mathbf{x}_i \tag{68}$$

$$\mathbf{U} = \begin{pmatrix} \cos\Omega t & \sin\Omega t & 0 \\ -\sin\Omega t & \cos\Omega t & 0 \\ 0 & 0 & 1 \end{pmatrix}, \tag{69}$$

see Fig. 10 for a graphical illustration of this relationship. Similar to the theoretical build-up of Sect. 2.2, the Earth's initial dynamical state, which is not perturbed by any time-dependent forces, is assumed to be that of uniform rotation with angular velocity Ω around the polar axis of the TRS (Gross 1992). In this initial state, the TRS perfectly coincides with the IRS. However, if dynamical processes, such as mass redistributions and relative motions within Earth's mobile fluids, are allowed for, the orientation and

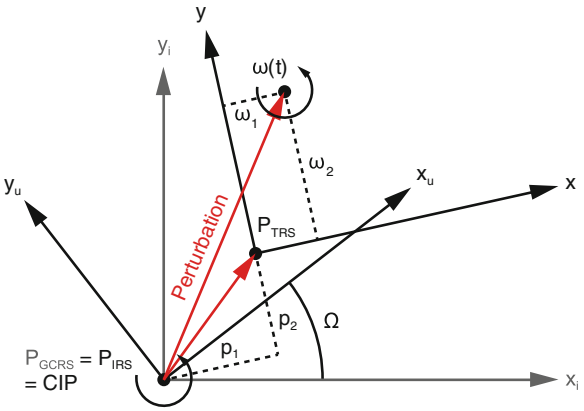

Fig. 10 Reference poles and axes in a tangential polar plane. The IRS (subscript u) rotates steadily with respect to the space-fixed GCRS (subscript i), while the TRS and the instantaneous rotation vector deviate from uniform rotation due to the presence of geophysical perturbations

motion of the TRS will start to deviate from the described initial state. Hence, the instantaneous rotation vector of the body-fixed reference system will exhibit changes in its magnitude and direction, denoted as 'Perturbation' in Fig. 10. In particular, the rotation axis will no longer coincide with the polar axis of either the TRS, the GCRS or the IRS, see Gross (1992). Provided the perturbing force is small, the induced rotational variations are small, too, and the coordinate conversion between the IRS and the TRS can be realized by employing an infinitesimal transformation matrix

$$\mathbf{x} = \mathbf{B}\mathbf{x}_u \tag{70}$$

$$\mathbf{B} = \begin{pmatrix} 1 & p_3 & p_1 \\ -p_3 & 1 & p_2 \\ -p_1 & -p_2 & 1 \end{pmatrix}. \tag{71}$$

Introducing in Eq. (70) the quantity $\mathbf{x}_u = (0, 0, 1)^{\mathrm{T}}$, which apparently represents the position vector of the CIP within the IRS, the corresponding vector in the TRS becomes $\mathbf{x} = (p_1, p_2, 1)^{\mathrm{T}}$. Thus, p_1 and p_2 locate the CIP with respect to the body-fixed rotating reference system and are equivalent to the routinely reported polar motion parameters x_p and y_p

$$p_1 = x_p, \quad p_2 = -y_p. \tag{72}$$

The negative sign in the second component considers that the y-coordinate is measured positively towards 90° W longitude, whereas the y-axis of the TRS, to which p_2 is referred to, points to 90° E. The quantity p_3 is associated with changes in the rotation rate of the Earth, see Sect. 3.3 for a detailed derivation.

Combining Eqs. (68) and (70) supplies

$$\mathbf{x} = \mathbf{B}\mathbf{U}\mathbf{x}_i = \mathbf{R}\mathbf{x}_i.$$

Both $\mathbf{B}$ and $\mathbf{U}$ are known matrices, so that their product yields the desired representation of the transformation matrix $\mathbf{R}$. Via Eq. (66), after neglecting second-order terms, the elements of $\mathbf{C}$ read

$$\mathbf{C} = \begin{pmatrix} 0 & \frac{\mathrm{d}p_3}{\mathrm{d}t} + \Omega & \frac{\mathrm{d}p_1}{\mathrm{d}t} - p_2\Omega \\ -\frac{\mathrm{d}p_3}{\mathrm{d}t} - \Omega & 0 & \frac{\mathrm{d}p_2}{\mathrm{d}t} + p_1\Omega \\ -\frac{\mathrm{d}p_1}{\mathrm{d}t} + p_2\Omega & -\frac{\mathrm{d}p_2}{\mathrm{d}t} - p_1\Omega & 0 \end{pmatrix}. \tag{73}$$

$$\Rightarrow \omega_1 = \Omega p_1 + \frac{\mathrm{d}p_2}{\mathrm{d}t} \tag{74}$$

$$\omega_2 = \Omega p_2 - \frac{\mathrm{d}p_1}{\mathrm{d}t}. \tag{75}$$

If Eqs. (11) and (72) are taken into account, the last two expressions can also be written as

$$m_1 = x_p - \frac{1}{\Omega}\dot{y}_p \tag{76}$$

$$m_2 = -y_p - \frac{1}{\Omega}\dot{x}_p \tag{77}$$

or in complex notation

$$\hat{m} = \hat{p} - \frac{\mathrm{i}}{\Omega}\dot{\hat{p}}, \tag{78}$$

where $\hat{p} = x_p - \mathrm{i}y_p$ characterizes terrestrial motion of the CIP in a tangential polar plane. Equation (78) represents the sought-for kinematical relation between the polar motion of the instantaneous rotation axis and that of the CIP. Considering the arguments brought forth in the first paragraph of Sect. 3.1, it is legitimate to combine this result with the dynamical theory of Earth rotation. Thus, the equatorial component of geophysical excitation in Eq. (30) referred to the actually observed axis (towards the time-variable CIP) reads

$$\begin{aligned} \hat{m} + \frac{\mathrm{i}}{\hat{\sigma}_{cw}}\dot{\hat{m}} &= \hat{\chi} - \frac{\mathrm{i}}{\Omega}\dot{\hat{\chi}}. \\ \Rightarrow \hat{p} - \frac{\mathrm{i}}{\Omega}\dot{\hat{p}} + \frac{\mathrm{i}}{\hat{\sigma}_{cw}}\frac{\mathrm{d}}{\mathrm{d}t}\left(\hat{p} - \frac{\mathrm{i}}{\Omega}\dot{\hat{p}}\right) &= \hat{\chi} - \frac{\mathrm{i}}{\Omega}\dot{\hat{\chi}} \\ \hat{p} + \frac{\mathrm{i}}{\hat{\sigma}_{cw}}\dot{\hat{p}} - \frac{\mathrm{i}}{\Omega}\frac{\mathrm{d}}{\mathrm{d}t}\left(\hat{p} + \frac{\mathrm{i}}{\hat{\sigma}_{cw}}\dot{\hat{p}}\right) &= \hat{\chi} - \frac{\mathrm{i}}{\Omega}\dot{\hat{\chi}}. \end{aligned}$$

By comparing terms on the left and right side of the latter equation, we arrive at the probably most vital relationship within Earth rotation excitation studies

$$\hat{p} + \frac{\mathrm{i}}{\hat{\sigma}_{cw}}\dot{\hat{p}} = \hat{\chi} \tag{79}$$

$$\hat{p}(t) = \mathrm{e}^{\mathrm{i}\hat{\sigma}_{cw}t}\left(\hat{p}(0) - \mathrm{i}\hat{\sigma}_{cw}\int_0^t \hat{\chi}(\tau)e^{-\mathrm{i}\hat{\sigma}_{cw}\tau}\,\mathrm{d}\tau\right), \tag{80}$$

represented either as differential equation (Gross 1992) or in integral form. Obviously, there are two main ways of comparing the reported values of polar motion $\hat{p}(t)$ and the associated geophysical excitation mechanisms in the context of the angular momentum approach. The first, more frequently applied method is a deconvolution problem (Brzeziński 1992) and consists of differentiating the complex series of observed polar motion (Eq. 79), see e.g. the study of fortnightly ocean tides by Gross et al. (1996). The second approach, on the contrary, requires convolution of the equatorial angular momentum function with the free Chandler mode (right-hand side of Eq. 80) in order to get an estimate of those polar motion variations that are induced by mass redistributions and relative motion in the fluid considered. This method, critically assessed by Chao (1985), is specifically sensitive to the initial conditions imposed on $\hat{\chi}(t)$ before integration.

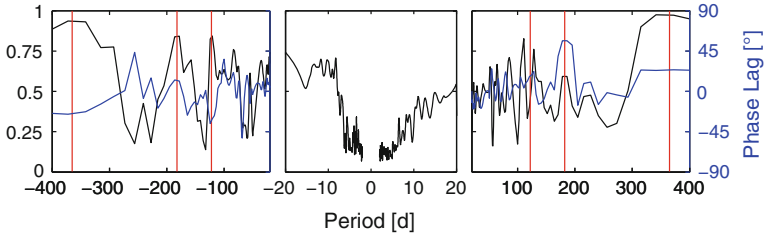

Fig. 11 Frequency-dependent magnitude-squared coherence c_{xy} (*black line*) and phase lag φ_{xy} (*blue line*) between observed polar motion excitation and equatorial angular momentum functions. Analyzed time span: 1980 to 2010. *Red vertical lines* (at annual, semiannual and terannual periods) indicate the prograde and retrograde seasonal bands. Spectral content at periods shorter than 100 d has been smoothed appropriately to underline the decrease of coherence at high frequencies. The phase lag information varies erratically at high frequencies and is thus not displayed in the *middle panel*

We complete the theoretical considerations of this section with additional remarks on Eq. (78), which suggests that full variability of $\hat{m}$ in the TRS is conveyed exclusively by $\hat{p}$. By definition, $\hat{p}$ characterizes all terrestrial perturbations of the CIP, i.e. that outside the retrograde diurnal band $\sigma_t \in (-1.5, -0.5)$ cpsd. However, the polar motion of the instantaneous Earth rotation axis is not subject to such a spectral separation and shows in fact substantial variations due to the celestial motion of the CIP, see Brzeziński and Capitaine (1993) for a rigorous treatment of the problem. The mean additional term to $\hat{m}$ ($\approx$28 mas) corresponds to the well-known analytical part of the precession-nutation model and is called *diurnal polar motion* (McClure 1973). Accordingly, the unpredictable portion of nutational motion, expressed by the celestial pole offsets $\{X', Y'\}$ (Sect. 1.2), is also affecting $\hat{m}$ but can be virtually omitted in view of the smallness of X' and Y'. A final contribution arises from the fact that the GCRS in the above derivations has been rotated by the precession-nutation model and thus is no more an inertial reference. As shown by Brzeziński and Capitaine (1993), the order of this effect is negligibly small ($2 \cdot 10^{-10}$ mas).

The application of the derived excitation relationships onto real data is straightforward. Figure 11 illustrates the differentiation approach of Eq. (79) in terms of a coherence study between geodetic polar motion and its geophysical excitation as modeled from atmospheric data. The observational time series have been extracted from the well-known EOP 05 C04 series (Bizouard 2011) at daily intervals from 1980 to 2010. The same sampling applies on the equatorial AAM function, which has been computed from pressure and wind analysis fields of the ECMWF. The response of the oceans to atmospheric perturbations at large time scales is assumed to be static, i.e. the IB-correction has been imposed on the matter term $\hat{\chi}^p$.

Numerical differentiation of the polar motion series yields the so-called *geodetic excitation function* (left-hand side of Eq. 79), a complex-valued signal that can be examined for linear dependency and phase differences with respect to the equatorial AAM function, e.g. within a two-sided magnitude-squared coherence plot, augmented by the corresponding phase lag information (Fig. 11). The displayed

functions c_{xy} and φ_{xy} are frequency-dependent and have been estimated from the spectra of the two input signals. Characteristically, geodetic and atmospheric excitation show a remarkably high coherence ($c_{xy} = 0.94 - 0.97$) and small phase lag values ($\varphi_{xy} = \pm 25°$) at $T \approx 365$ d, suggesting that the atmosphere is a major driving agent for the excitation of prograde and retrograde annual wobbles. Indeed, the amplitude of the observed prograde wobble excitation is in excellent agreement with that of the equatorial AAM, while there is more inconsistency in the retrograde band, see Gross et al. (2003). Significant values of c_{xy} are present at other spectral bands that feature high signal-to-noise ratios, such as semi- and terannual frequencies. The polar motion variations allocated to these bands can be explained to about 60 % by atmospheric pressure and wind fluctuations, as noted for instance in Eubanks (1993). Further intraseasonal wobbling motion is also partially driven by atmospheric processes, with surface pressure variations over Eurasia and North America of particular importance, see Nastula and Salstein (1999). At such time scales from several weeks to months, Fig. 11 reveals only minor phase lag values but limited coherences of about 0.5 at positive frequencies and 0.6 at negative frequencies. This implies that non-atmospheric processes such as oceanic excitation should be considered, too, see Sect. 3.4 for a short look at the angular momentum contributions of Earth's other subsystems. The invalidity of the inverted barometer approximation at very short periods is reflected in the substantial drop of coherence at about 10 d.

A brief illustration of the integration approach (Eq. 80) is given in Fig. 12. It employs the same geodetic and geophysical data as the previous example. The numerical integration required for convolution can be performed via Simpson's rule, and both the observed polar motion series as well as its corresponding atmospheric

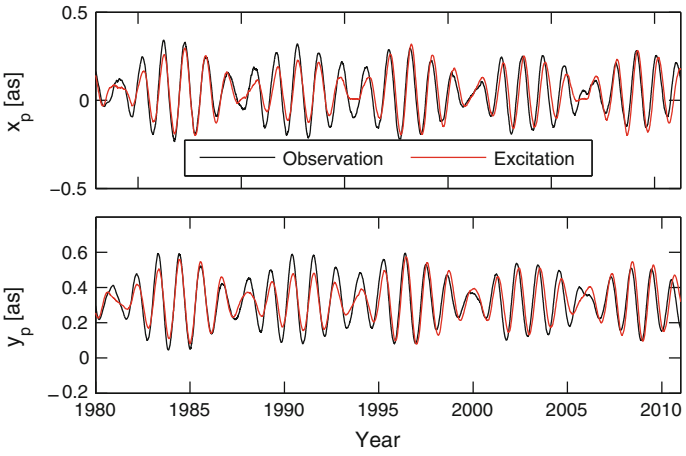

Fig. 12 Comparison of observed variations in polar motion (*black line*) and its corresponding atmospheric excitation (*red line*) obtained from convolution of the equatorial AAM function for the time span 1980–2010

excitation are stripped off their respective secular trends. Moreover, as an appropriate initial condition, the offset of $\hat{\chi}(t)$ before convolution is chosen to be identical with that of the geodetic excitation function determined in the foregoing example. As apparent from both components in Fig. 12, the analysis indeed recovers the beat-like signature of geodetic polar motion, since the annual signal component is well represented in the equatorial AAM. The largest discrepancies between observed and modeled pole curves persist at years of minimum amplitude. Moreover, throughout the second half of the analyzed time span, the atmospheric excitation features a considerable phase lag with respect to the geodetic series, whereas before 1995 the AAM data cannot fully account for the magnitude of the CW. Note, however, that within the integration approach, any resemblance between the observed and geophysically modeled pole curves does not allow drawing conclusions about the actual excitation of the CW, see Chao (1985) for a deeper discussion.

3.2 Polar Motion and Nutation: Extended Model

As a preparation for the argumentation and terminology used in the following, the reader is advised to recall the general parametrization of Earth rotation presented in Sect. 1. It is prerequisite to understand the frequency-based distinction between nutation and polar motion, and, in particular, the dualism of nutation and terrestrial perturbations of the CIP with nearly diurnal retrograde frequency $\sigma_t \in (-1.5, -0.5)$ cpsd. The extension of the equatorial excitation equation for high frequencies, which has been already indicated more generally in Sect. 2.4 (last paragraph), must be seen in the context of this discrimination. In detail, this section will echo the derivations of Brzeziński (1994), which specifically focus on the creation of an adequate model for studying geophysically-induced nutational variations. The extended formulation has also a marginal impact on modeling CIP variations outside the nearly diurnal frequency band, but basically represents only a partial solution of the requested thorough scheme for excitation studies at terrestrial frequencies of a few days or smaller, see the end of this section for further discussions.

The special significance of geophysical effects on Earth rotation in the nutation band [discussed e.g. by Dehant et al. (1999) in the frame of a non-rigid Earth nutation theory] is essentially down to the strong inertial coupling between the mantle and the liquid core in the vicinity of the diurnal retrograde frequency $-\Omega$ (Brzeziński et al. 2002). This coupling at the core-mantle-boundary (CMB) manifests itself in the rotational eigenmode of the FCN. According to Zürn (1997), the flattened shape of the CMB gives rise to restoring forces if the rotation axis of the core and the CMB's axis of symmetry do not coincide. Earth's reaction to the internal torque associated with those restoring forces is a diurnal retrograde oscillation of the rotation axis with respect to the body-fixed reference system. This oscillation is usually called *Nearly Diurnal Free Wobble* (NDFW), and its related space-referred motion is better known as FCN. Precession-nutation corrections that are estimated with respect to an

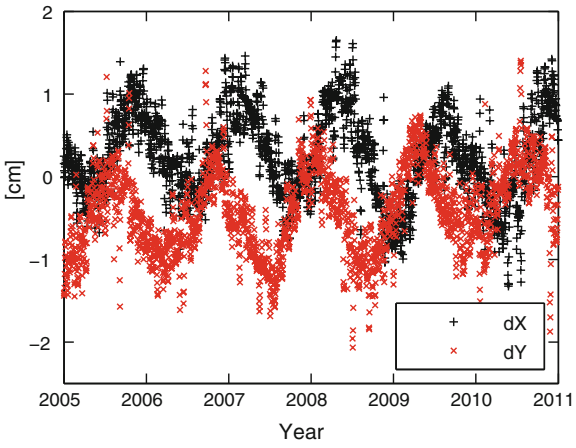

Fig. 13 Time series of the EOP 05 C04 precession-nutation residuals with respect to the conventional *a priori* model of Mathews et al. (2002). The daily corrections are projected to Earth's surface, thus 1 cm corresponds to ∼0.3 mas

a priori model provide observational evidence of the FCN but also reveal its temporal variability (Fig. 13).

Partly due to the presence of the NDFW/FCN eigenmode, different physical properties of the Earth are determinative when estimating excitation of nutation instead of slow polar motion variations (Brzeziński 1994). As already demonstrated, the assumption of a decoupled core (Sect. 2.4) is not tenable at retrograde diurnal frequencies and has to be refined by taking into account the effects of the FCN. Such an approach is also deeply required in view of steadily improving Earth rotation observations, that nowadays are available at high temporal resolution and at an accuracy that is sufficient to detect subdaily geophysically-induced variations in EOP.

As suggested e.g. in Schindelegger et al. (2011), the eigenfrequency $\hat{\sigma}_f$ of the NDFW resonance can be derived from T'_f, the period of the FCN in the celestial frame, and Q_f, its Earth-referred quality factor. Both values are taken from the conventional precession-nutation model (Mathews et al. 2002)

$$\hat{\sigma}_f = 2\pi \left(\frac{1}{T'_f} - \frac{1}{T_{sid}} \right) \left(1 - \frac{\mathrm{i}}{2Q_f} \right). \tag{81}$$

The numerical values are $T'_f = -430.2\,\mathrm{d}$, $Q_f = 20000$ and $T_{sid} = 0.9973\,\mathrm{d}$, describing the length of the sidereal day. Evaluation of Eq. (81) yields a frequency of resonance at $\sigma = -1.00232\,\mathrm{cpsd}$.

Given the introduction above, we can now devote ourselves to the derivations of Brzeziński (1994), which start from the frequency-dependent equation of motion of Sasao and Wahr (1981)

$$\hat{p}(\sigma) = \left[\frac{A}{A_m}(\tau-\mu)\frac{\Omega}{\sigma-\sigma_1} + \frac{A_f}{A_m}\eta\frac{\Omega}{\sigma-\sigma_2}\right]\hat{\Phi}_L - \left[\frac{A}{A_m}\frac{\Omega}{\sigma-\sigma_1} - \frac{A_f}{A_m}\frac{n_f}{\Omega}\frac{\Omega}{\sigma-\sigma_2}\right]\frac{\hat{h}}{A\Omega}. \tag{82}$$

Equation (82) describes polar motion at Earth-referred frequency σ generated by the complex-valued loading potential $\hat{\Phi}_L = \hat{\Phi}_L(\sigma)$ and the relative angular momentum $\hat{h} = h_1 + \mathrm{i}h_2 = \hat{h}(\sigma)$ of the perturbing fluid. The quantities A, A_f and A_m designate the equatorial moments of inertia of the Earth, the fluid core and the mantle, calculated from an underlying Earth model. τ, μ and η are dimensionless coefficients, while σ_1 and $\sigma_2 = -\Omega + n_f$ denote the theoretical frequencies of the CW and NDFW, respectively. Both σ_1 and σ_2 are valid for an oceanless Earth. However, it is not necessary to list any numerical values for the two parameters, since we will replace them by the corresponding observed values at the end of the present section.

Via MacCullagh's formula, as given for instance in Moritz and Müller (1987), the potential of the loading mass can be converted to the corresponding perturbation of the equatorial product of inertia

$$\hat{\Phi}_L = -\frac{\Delta\hat{I}}{A\tau}. \tag{83}$$

Using this relation in Eq. (82) and separating the effects of the CW and the FCN, we obtain

$$\hat{p}(\sigma) = -\frac{1}{\Omega A_m}\left[\left(1-\frac{\mu}{\tau}\right)\Omega\Delta\hat{I} + \hat{h}\right]\frac{\Omega}{\sigma-\sigma_1} - \frac{A_f}{\Omega A A_m}\left[\frac{\eta}{\tau}\Omega\Delta\hat{I} - \frac{n_f}{\Omega}\hat{h}\right]\frac{\Omega}{\sigma-\sigma_2}. \tag{84}$$

Equation (84) can be rewritten elegantly in terms of the matter and motion portions of the (effective) equatorial angular momentum function $\hat{\chi} = \hat{\chi}^p + \hat{\chi}^w$. In particular, it is possible to consistently incorporate the angular momentum function realization of Barnes et al. (1983), even though their derivations have to be considered critically to some extent, see e.g. Dickman (2003) or the brief discussion at the end of this section. One of the parameters central to the study of Barnes et al. (1983) is the Chandler frequency of an elastic Earth comprising crust and mantle

$$\sigma_e = \frac{k_s - k_2}{k_s}\frac{C_m - A_m}{A_m}\Omega, \tag{85}$$

with $k_s = 3(C-A)G/(\Omega^2 a^5)$ being the dimensionless 'secular' Love number of the whole Earth (Munk and MacDonald 1960). The equatorial angular momentum function, which is associated with the specific Earth model yielding Eq. (85), is corrected for rotational and loading deformation, see Barnes et al. (1983, pp. 46, 47). Expressed in the notation of the present review, matter and motion terms read

$$\hat{\chi}^p = \chi_1^p + \mathrm{i}\chi_2^p = \frac{\Omega\left(1+k_2'\right)\Delta\hat{I}}{\sigma_e A_m} \tag{86}$$

$$\hat{\chi}^w = \chi_1^w + \mathrm{i}\chi_2^w = \frac{\hat{h}}{\sigma_e A_m}. \tag{87}$$

Taking into account that, in principle, the identity

$$k_2' = -\frac{\mu}{\tau} \tag{88}$$

holds (Brzeziński 1994), we can appropriately modify Eq. (86) and insert the resulting matter term expression together with the motion term (Eq. 87) into Eq. (84). Thus, we obtain the following generalized, frequency-dependent equation, describing geophysical excitation of polar motion and nutation under consideration of both the CW mode and the FCN resonance

$$\hat{p}(\sigma) = \frac{\sigma_e}{\sigma_1 - \sigma}\left(\hat{\chi}^p + \hat{\chi}^w\right) + \frac{\sigma_e}{\sigma_2 - \sigma}\left(a_P\hat{\chi}^p + a_w\hat{\chi}^w\right) \tag{89}$$

$$a_p = \frac{A_f}{A}\frac{\eta}{\tau - \mu} = 9.509 \cdot 10^{-2}$$

$$a_w = -\frac{A_f}{A}\frac{n_0}{\Omega} = 5.489 \cdot 10^{-4}.$$

The given numerical values of the constants a_p and a_w are that of Brzeziński (1994) and depend on the applied structural model of the Earth. A recent reconsideration of Sasao and Wahr's theory by Koot and de Viron (2011) based on advanced geophysical models and data yielded $a_p = 9.200 \cdot 10^{-2}$ and $a_w = 2.628 \cdot 10^{-4}$, which is almost two times smaller than the value noted in the above equation. A detailed examination of the significance of both parameters can be found in Brzeziński (1994). Here, it only shall be stressed that a_p and a_w are purely theoretical quantities and have never been confirmed by any observation (Bizouard et al. 1998). Note also that the numerical values given in this section revert to the different Earth models applied by Sasao and Wahr (1981) and Barnes et al. (1983) and thus might be slightly inconsistent (1–3 % for the various Love numbers and Earth's moments of inertia). Besides, Sect. 2.4 makes use of another set of parameter values [following Gross (2007)], which are generally more up to date than those introduced here. This fact is not accounted for by a more distinguished notation, though.

The FCN term of Eq. (89) is resonant at $\sigma = \sigma_2 \approx \sigma_f$ and thus plays a pivotal role when studying diurnal retrograde perturbations of Earth rotation. However, in view of the numerical discrepancy between a_p and a_w of about two orders of magnitude, one has to treat matter and motion terms as two separate driving agents. On the contrary, the CW term, which especially reigns over slow polar motion variations, requires an equivalent weight on $\hat{\chi}^p$ and $\hat{\chi}^w$.

In order to improve the agreement of the formulation with the dynamical behavior of the real Earth, Brzeziński (1994) suggests to replace the theoretical frequencies

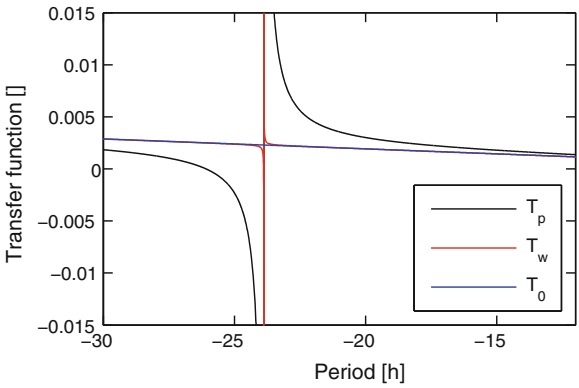

Fig. 14 Standard transfer functions $\hat{T}_p$ (*black line*), $\hat{T}_w$ (blue line) and simplified transfer function $\hat{T}_0$ without FCN term (red line). Only real parts are shown

of the CW and the NDFW by the corresponding observation-based values as defined in Eqs. (32) and (81). Equation (89) is modified accordingly, despite the fact that we evoke inconsistency with the theory of Sasao and Wahr (1981). The imaginary parts of the CW and NDFW eigenfrequencies account for damping and prevent singularities in the 'broad band' equation of polar motion (Brzeziński et al. 2002)

$$\hat{p}(\sigma) = \hat{T}_p(\sigma)\hat{\chi}^p(\sigma) + \hat{T}_w(\sigma)\hat{\chi}^w(\sigma). \tag{90}$$

Here, $\hat{T}_p(\sigma)$ and $\hat{T}_w(\sigma)$ are transfer functions used to accomplish the polar motion (nutation) contributions induced by pressure and wind excitation

$$\hat{T}_p(\sigma) = \hat{\sigma}_{cw}\left(\frac{1}{\hat{\sigma}_{cw} - \sigma} + \frac{a_p}{\hat{\sigma}_f - \sigma}\right) \tag{91}$$

$$\hat{T}_w(\sigma) = \hat{\sigma}_{cw}\left(\frac{1}{\hat{\sigma}_{cw} - \sigma} + \frac{a_w}{\hat{\sigma}_f - \sigma}\right). \tag{92}$$

Figure 14 displays the real parts of both $\hat{T}_p(\sigma)$ and $\hat{T}_w(\sigma)$ at $T = -24$ h and compares them with a simplified transfer function that neglects the FCN portions in Eqs. (91) and (92). On the one hand, due to the numerical discrepancy recognized between a_p and a_w, it is evident that the transfer function associated with the matter term is of stronger weight than its motion counterpart at diurnal retrograde frequencies. On the other hand, we can assume that an omission of the FCN term outside the nutation band does not lead to large errors in the excitation estimates. As illustrated by Brzeziński (1994), the ratio between the pure FCN transfer function and the plain CW term in Eq. (91) amounts to 0.19 and 0.05 at frequencies $\sigma = -2$ and 2 cpd (cycles per day), respectively. Hence, for applications that do not explicitly focus on the diurnal retrograde band, it is justified to neglect the effect of the FCN resonance by setting $a_p = a_w = 0$ and only deal with

$$\hat{p}(\sigma) = \frac{\hat{\sigma}_{cw}}{\hat{\sigma}_{cw} - \sigma}\hat{\chi}, \tag{93}$$

which is an equivalent representation of Eq. (79) in frequency domain. In turn, we can also give a time domain representation of the extended model in Eq. (90)

$$\begin{aligned}\left(\partial_t - \mathrm{i}\hat{\sigma}_{cw}\right)\left(\partial_t - \mathrm{i}\hat{\sigma}_f\right)\hat{p} = \\ -\mathrm{i}\hat{\sigma}_{cw}\left[\left(\partial_t - \mathrm{i}\hat{\sigma}_f\right)\left(\hat{\chi}^p + \hat{\chi}^w\right) + \left(\partial_t - \mathrm{i}\hat{\sigma}_{cw}\right)\left(a_p\hat{\chi}^P + a_w\hat{\chi}^w\right)\right].\end{aligned} \tag{94}$$

Alas, the practical implementation of this expression would require computing time derivatives of quickly-varying, empirical functions and thus might increase their initial inaccuracies (Moritz and Müller 1987).

Figure 15 portrays the application of the broadband frequency-domain formula (Eq. 90) onto the 30-year record of equatorial AAM values, which has already been utilized in Sect. 3.1. Complex-valued (non-IB) pressure and wind terms have been convolved with the corresponding transfer function, yielding Fourier coefficients of $\hat{p}(\sigma)$ at terrestrial frequencies σ_t in cycles per day. By aid of the basic relation in Eq. (2), the spectral content has been transfered to celestial frequencies σ_t in cpy (cycles per year). From the resulting amplitude spectrum one clearly recognizes the resonance peak at the FCN frequency located at $T'_f = {\sigma'_f}^{-1} = -430.2\,\mathrm{cpd}$. Moreover, large excitation amplitudes can be attributed to atmospheric tides which would be centered around the retrograde diurnal frequency in the terrestrial reference frame. Such global-scale atmospheric waves are chiefly of thermal origin, with their labeling identical to that of the coherent gravitational tides (Brzeziński et al. 2002): S_1 represents the main diurnal tidal component and contributes to the prograde annual nutational motion, while $\{\psi_1, K_1, P_1, \pi_1\}$ are side lobes that modulate S_1 and cause additional peaks in nutation at frequencies $\{-1, 0, 2, 3\}$ cpy. The amplitude values discernable from Fig. 15 may be compared to different findings in literature, e.g. with that of Brzeziński et al. (2002) or Vondrák and Ron (2010). Prerequisite for such cross checking is to analyze the same time span as in the comparative study, due to the fact that amplitude and phase values of atmospheric tides are time-variable quantities. Further discrepancies between the estimates of each study are basically down to insufficiencies in the underlying general circulation models for atmospheric and oceanic processes.

There are some critical issues to the presented extended model that need to be addressed more precisely. Firstly, the applied angular momentum function formalism of Barnes et al. (1983) is not consistent in its treatment of core-mantle coupling, see Dickman (2003). In detail, Eqs. (85)–(87) exclusively use the moments of inertia of the mantle, whereas all remaining parameters (k_2, k'_2 and k_s) are assigned values appropriate to the whole Earth, cf. the tabulations of Barnes et al. (1983, pp. 46, 71). Coincidentally, the free wobble frequency of the mantle σ_e, resulting from the theoretically erroneous Eq. (85), represents an exceptionally good estimate of the true Chandler frequency. Adapting the involved Love numbers to mantle-only quantities

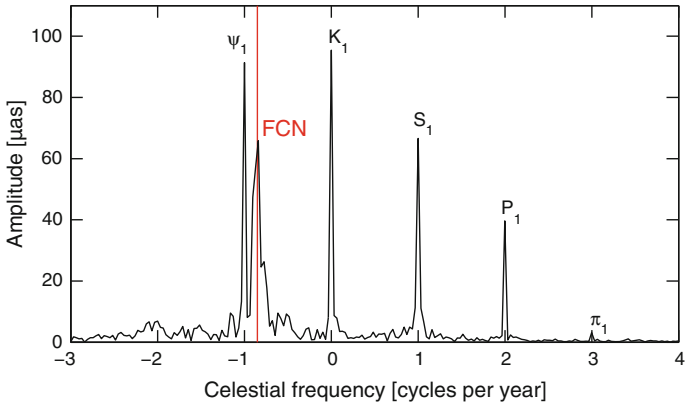

Fig. 15 Amplitude spectrum of long-periodic nutational motions associated with thermal tides in the atmosphere that can be allocated to the retrograde diurnal band in the terrestrial reference frame. The spectral content of S_1 (main sun-synchronous tide) and its side lobes $\{\psi_1, K_1, P_1, \pi_1\}$ has been obtained from six-hourly equatorial AAM function values for the time span 1980–2010

according to Dickman (2005) causes only marginal changes of σ_e (<0.5 %) and the resulting motion term coefficient in Eq. (87). However, the modification of the load Love number k_2' in Eq. (86) suggests a matter term coefficient of $1.09/(C_m - A_m)$ instead of $1.00/(C_m - A_m)$, cf. Table 1. This error is slightly larger than the level of inconsistencies we accept when replacing both $\sigma_1 = \Omega/402.6$ and $\sigma_e = \Omega/429.1$ by the observed Chandler frequency $\sigma_{cw} = \Omega/434.3$ (the difference in periods is about 7 %).

A further theoretical conflict emerges when realizing that $\hat{\chi}^p$ and $\hat{\chi}^w$, associated with an essentially core-less Earth model, relate via Eq. (90) to the NDFW/FCN resonance, which actually arises from the existence of Earth's oblate, liquid core. The numerical impact of this mismatch is small, though, and can be estimated by comparing the coefficients of $\Delta\hat{I}$ and $\hat{h}$ for the Barnes et al. (1983) formalism (see Table 1) and that inherent to Eq. (82). Both sets of scaling factors agree within 1.5 %.

Within the given limitations, the theory of Brzeziński (1994) accounts for rotational deformation and crustal loading, but being bound to the dynamical equation of Sasao and Wahr (1981), it does not include additional factors, such as mantle anelasticity or the wobble response of the oceans and the core. Theoretically, it should be possible to incorporate further rotational feedback phenomena into the extended polar motion equation by an appropriate change of its parameters. However, at present recognized models for those effects at diurnal time scales are not available (see also Sect. 2.4) and this adds to the absence of a dynamical model that accurately characterizes the response of the oceans to atmospheric forcing at short periods. There is a strong necessity to correctly model these indirect effects on Earth rotation in the diurnal frequency band, if a thorough verification of geophysical data versus geodetic observations is envisaged.

3.3 Length of Day Variations

The conversion of the axial angular momentum function χ_3 into variations of length of day and vice versa is derived following Barnes et al. (1983). At first, the third component of Eq. (11) is written explicitly

$$\omega_3 = \Omega\,(1 + m_3)\,. \tag{95}$$

Understandably, ω_3 relates to the actual length of the sidereal day Λ, which, in turn, is composed of the nominal length of the day Λ_0 plus a minute excess $\partial\Lambda$.

$$\begin{aligned}
\omega_3 &= \frac{2\pi}{\Lambda} = \frac{2\pi}{\Lambda_0 + \partial\Lambda} \\
&= \frac{2\pi}{\Lambda_0\left(1 + \frac{\partial\Lambda}{\Lambda_0}\right)} \\
&= \Omega\,\frac{1}{1 + \frac{\partial\Lambda}{\Lambda_0}} \\
\Rightarrow \omega_3 &\approx \Omega\left(1 - \frac{\partial\Lambda}{\Lambda_0}\right).
\end{aligned} \tag{96}$$

The ratio between $\partial\Lambda$ and the nominal length of day is sufficiently small to justify the employed approximation in Eq. (96). By comparing the obtained expression to Eq. (95) and recalling the axial solution of the Liouville equations, we find

$$\begin{aligned}
\chi_3 = -m_3 &= \frac{\partial\Lambda}{\Lambda_0} + \text{const} = \frac{\text{LOD}}{86400\,\text{s}} + \text{const} \\
&= -\frac{\text{d}}{\text{d}t}\,(\text{UT1} - \text{UTC}) + \text{const},
\end{aligned} \tag{97}$$

where LOD is the quantity conventionally reported by Earth rotation measurement services. It designates the excess length of day with respect to the mean solar day of length 86400 s. The absence of any frequency-dependent transfer function in Eq. (97) represents a certain advantage when studying the impact of geodynamical processes on Earth's rotation rate.

As an illustration, Fig. 16 compares daily values of observed variations in LOD from the EOP 05 C04 series (Bizouard 2011) with a 30-year record of axial atmospheric angular momentum that has been obtained from ECMWF data. As periods longer than two days are looked at, it is safe to revert to the IB-corrected matter term of AAM functions, χ_3^p. In order to facilitate the comparison with pure atmospheric excitation, the measured changes in LOD have to be cleared of a secular signal, decadal fluctuations due to angular momentum exchange between core and mantle, and pronounced harmonic variations induced by solid Earth tides. Refer to Sect. 1.4 and Seitz and Schuh (2010) for a further discussion on these effects.

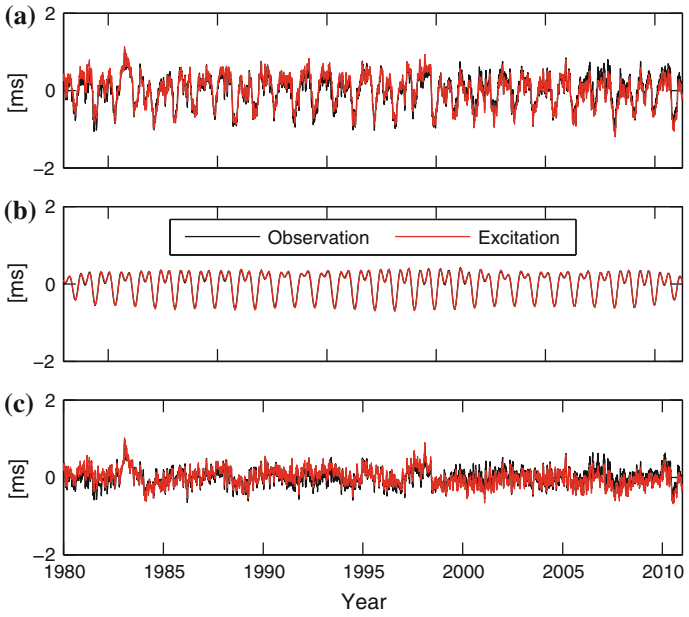

Fig. 16 Comparison of observed changes in length of day (*black line*) and axial atmospheric angular momentum (*red line*) for the time span 1980–2010. **a** Initial time series after elimination of secular trend, decadal variations and the effect of solid Earth tides. **b** Annual and semiannual signal components obtained by Wavelet filtering. **c** Residual time series (**a–b**)

The obtained residual signal, as depicted in Fig. 16a, is highly correlated with axial AAM fluctuations (correlation coefficient $\rho \approx 0.96$) that chiefly arise from strong zonal winds. At the frequency bands examined, both the contribution of atmospheric pressure variations and oceanic angular momentum are of minor extent.

The annual and semiannual signal components in LOD, in particular, are almost entirely driven by atmospheric processes. This remarkable correlation ($\rho \approx 1.00$) between geodetic observations and AAM is demonstrated in Fig. 16b, which displays the superposition of these two distinct spectral components. The time-variable amplitudes at $\sigma = 1$ cpy and $\sigma = 2$ cpy have been extracted from the respective Wavelet transforms of the initial LOD and AAM records. Mean magnitude values estimated from the utilized series amount to 0.36 ms for the annual oscillation and 0.27 ms for the semiannual oscillation. These two components can be reduced from the corresponding time series in Fig. 16a in order to shed light on the residual LOD and axial excitation signals. Figure 16c depicts those residuals, which are indicative of two prominent interannual atmospheric fluctuations, the El Niño-Southern Oscillation (ENSO) and a weak quasi-biennial oscillation (QBO), cf. Chao (1989). The QBO represents a regular alternation in the temperature regimes and zonal wind fields of the equatorial stratosphere (Holton and Lindzen 1972). Its period varies from 24 to 30 months, while the impact on LOD is about 0.1 ms as revealed by spectral analysis

of the displayed series. ENSO events, on the contrary, are significant anomalies in the usual annual seesawing of oceanic and atmospheric circulation over the entire eastern equatorial Pacific ocean region (Philander 1990). As apparent from Fig. 16c, such irregularities have been particularly strong during 1982–1983 and 1997–1998, normally lasting about 14–18 months. Since ENSO events originate from interactions in the atmosphere-ocean system, their impact on changes in LOD can only be studied properly if reverting to a coupled geophysical model that yields both atmospheric and oceanic angular momentum. However, Fig. 16c encompasses pure AAM, so that the correlation coefficient between the residual geodetic observations and AAM fluctuations is $\rho \approx 0.86$, only.

3.4 The Angular Momentum Budget

In accordance with the central theme of this review, the given comparisons of Earth rotation (orientation) parameters and physical model results have been solely based on atmospheric data. As suggested by Eqs. (5)–(7), a thorough application of the angular momentum approach would require to additionally consider the angular momentum portion of Earth's other subsystems in terms of variations of the tensor of inertia and relative angular momentum

$$\Delta\mathbf{I} = \Delta\mathbf{I}^{(a)} + \Delta\mathbf{I}^{(o)} + \Delta\mathbf{I}^{(c)} + \Delta\mathbf{I}^{(h)} \tag{98}$$

$$\mathbf{h} = \mathbf{h}^{(a)} + \mathbf{h}^{(o)} + \mathbf{h}^{(c)} + \mathbf{h}^{(h)}. \tag{99}$$

Herein, the contributions of the atmosphere (a), the oceans (o) as well as hydrological excitation (h), associated with land water, soil moisture and snow, and the effect of the core (c) have been linearly superposed. The resulting cumulative angular momentum of Earth's fluids has to be balanced by that of the solid Earth by means of small rotational fluctuations, which in turn can be monitored by high-accuracy space geodetic techniques. The underlying mathematical scheme capable of relating those observations to geophysical excitation in the form of angular momentum functions has been established and illustrated in the previous sections. Figures 11 and 16 reveal the large impact of atmospheric processes to polar motion and changes in length of day in different frequency bands, but also imply that full closure of the angular momentum budget has to likewise involve the contributions of other fluid layers. It is widely recognized that mass redistributions in the core are substantial for Earth rotation variations at decadal periods, see e.g. Dickey et al. (2010). The comprehensive studies of Ponte (1997) and Gross et al. (2003) point out the instrumental role of oceanic excitation mechanisms in balancing the equatorial angular momentum at seasonal, intraseasonal and interannual time scales. In detail, combined time series of atmospheric and oceanic excitation may account for up to 67 % of the variance in observed polar motion values at intraseasonal frequencies, while at longer periods the agreement between observed and modeled excitation function decreases (Gross

et al. 2003). The existing discrepancies may be further reduced if mass redistributions in the global hydrosphere are added to the analysis. As demonstrated by Chen and Wilson (2005) and Dobslaw et al. (2010), considering hydrological excitation can lead to an reasonably good closure of the angular momentum budget for the annual wobble.

Variations of length of day are primarily caused by the atmospheric wind term and also slightly affected by surface pressure fluctuations, see Fig. 16. Those small LOD residuals that are void of the influence of AAM have been successfully compared to oceanic bottom pressure and currents (Gross et al. 2004) as well as to combined time series of oceanic mass term and hydrological excitation (Chen et al. 2000). The latter study arrives at a particularly good agreement of modeled and observed excitation at the seasonal cycle.

Even though a complete closure of the angular momentum budget at different frequencies has hitherto been an elusive goal, relating Earth rotation parameters to the output of geophysical models remains a valuable field in view of several issues. In the first place, it allows assessing the quality of the applied models if observations of nutation, polar motion and changes of length of day are used as a reference (Seitz and Schuh 2010). The presented excitation scheme is also a perfect tool for interpreting time series of geodetic parameters with regard to distinct geophysical processes in all subsystems of our planet. In this context, the investigation of Earth's reaction to the manifold interactions between atmosphere, hydrosphere and solid Earth is an intriguing task. And finally, via inversion of the observed rotation signal, it is also possible to learn more about geophysically significant parameters and dynamic processes within the system Earth (Seitz and Schuh 2010). Such an approach is regarded as a highly promising challenge for future research in the field of Earth rotation.

Acknowledgments The authors would like to thank Prof. A. Brzeziński for his excellent review, which helped to improve this part of the book significantly and strengthened the major geophysical discussion of each section. Innumerable comments on the style and writing were provided by D. Salstein and are highly appreciated. The first author is particularly indebted to the Austrian Science Fund (FWF) for supporting his work within project P20902-N10.

References

Z. Altamimi, P. Sillard, and C. Boucher. The impact of a no-net-rotation condition on ITRF2000. *Geophys. Res. Lett.,* 30(2):1064, doi:10.1029/2002GL016279, 2003.

R. Barnes, R. Hide, A. White, and C. Wilson. Atmospheric angular momentum fluctuations, length-of-day changes and polar motion. *Proc. R. Soc. Lond.,* A 387:31–73, 1983.

C. Bizouard. Excitation of the polar motion and rotation rate. IERS EOP Product Center, Observatoire de Paris. http://hpiers.obspm.fr/eop-pc/, as at June 2011

C. Bizouard, A. Brzeziński, and S. Petrov. Diurnal atmospheric forcing and temporal variations of the nutation amplitudes. *J. Geod.,* 72:561–577, 1998.

A. Brzeziński. Polar motion excitation by variations of the effective angular momentum function: considerations concerning the deconvolution problem. *Manuscr. Geodaet.,* 17:3–20, 1992.

A. Brzeziński. Polar motion excitation by variations of the effective angular momentum function, II: extended-model. *Manuscr. Geodaet.,* 19:157–171, 1994.

A. Brzeziński and N. Capitaine. The use of the precise observations of the celestial ephemeris pole in the analysis of geophysical excitation of Earth rotation. *J. Geophys. Res.*, 98(B4):6667–6675, 1993.

A. Brzeziński, C. Bizouard, and S.D. Petrov. Influence of the atmosphere on Earth rotation: What new can be learned from the recent atmospheric angular momentum estimates? *Surv. Geophys.,* 23:33–69, doi:10.1023/A:1014847319391, 2002.

A. Brzeziński, H. Dobslaw, and R. Dill. Geophysical excitation of the Chandler wobble revisited. In Kenyon S.C., Pacino M.C., Marti U.J., editor, *Geodesy for Planet Earth, Proceedings of the 2009 IAG Symposium, Buenos Aires, Argentinia, 31 August - 4 September 2009*, pages 499–505. Springer, 2012.

B.F. Chao. On the excitation of the Earth's free wobble and reference frames. *Geophys. J. R. Astron. Soc.*, 79:555–563, 1984.

B.F. Chao. On the excitation of the Earth's polar motion. *Geophys. Res. Lett.,* 12(8):526–529, 1985.

B.F. Chao. Length-of-day variations caused by El Nino-Southern Oscillation and quasi-biennial oscillation. *Science*, 243:923–925, 1989.

B.F. Chao, R. Ray, J. Gipson, G. Egbert, and C. Ma. Diurnal/semidiurnal polar motion excited by oceanic tidal angular momentum. *J. Geophys. Res.,* 101(B9) (B9):20151–20163, doi:10.1029/96JB01649, 1996.

J.L. Chen and C.R. Wilson. Hydrological excitations of polar motion, 1993–2002. *Geophys. J. Int.,* 160:833–839, doi:10.1111/j.1365-246X.2005.02522.x, 2005.

J.L. Chen, C.R. Wilson, B.F. Chao, C.K. Shum, and B.D. Tapley. Hydrological and oceanic excitations to polar motion and length-of-day variations. *Geophys. J. Int.*, 141:149–156, doi:10.1046/j.1365-246X.2000.00069.x, 2000.

F.A. Dahlen. The passive influence of the oceans upon the rotation of the Earth. *Geophys. J. R. Astron. Soc.,* 46:363–406, 1976.

O. de Viron and V. Dehant. Earth's rotation and high frequency equatorial angular momentum budget of the atmosphere. *Surv. Geophys.,* 20:441–462, doi:10.1023/A:1006723924421, 1999.

O. de Viron and V. Dehant. Tests on the validity of atmospheric torques on Earth computed from atmospheric model outputs. *J. Geophys. Res.,* 108(B2):2068, doi:10.1029/2001JB001196, 2003.

O. de Viron, C. Bizouard, D. Salstein, and V. Dehant. Atmospheric torque on the Earth and comparison with atmospheric angular momentum variations. *J. Geophys. Res.,* 104(B3):4861–4875, doi:10.1029/1998JB900063, 1999.

O. de Viron, R.M. Ponte, and V. Dehant. Indirect effect of the atmosphere through the oceans on the Earth nutation using the torque approach. *J. Geophys. Res.,* 106(B5):8841–8851, doi:10.1029/2000JB900387, 2001a.

O. de Viron, S.L. Marcus, and J. Dickey. Diurnal angular momentum budget of the atmosphere and its consequences for Earth's nutation. *J. Geophys. Res.,* 106(B11):26747–26759, doi:10.1029/2000JB000098, 2001b.

O. de Viron, L. Koot, and V. Dehant. Polar motion models: the torque approach. In Plag H.P., Chao B.F., Gross R.S., van Dam T., editor, *Forcing of Polar Motion in the Chandler Frequency Band: A Contribution to Understanding Interannual Climate Change*, volume 24. Cahiers du Centre Européen de Géodynamique et du Séismologie, Luxembourg, 2005.

V. Dehant and O. de Viron. Earth rotation as an interdisciplinary topic shared by astronomers, geodesists and geophysicists. *Adv. Space Res.,* 30(2):163–173, doi:10.1016/S0273-1177(02)00281-8, 2002.

V. Dehant, C. Bizouard, J. Hinderer, H. Legros, and M. Greff-Lefftz. On atmospheric pressure perturbations on precession and nutations. *Phys. Earth Planet. Interiors*, 96:25–39, doi:10.1016/0031-9201(95)03112-X, 1996.

V. Dehant, F. Arias, C. Bizouard, P. Bretagnon, A. Brzeziński, B. Buffett, N. Capitaine, P. Defraigne, O. de Viron, M. Feissel, H. Fliegel, A. Forte, D. Gambis, J. Getino, R. Gross, T. Herring, H.

Kinoshita, S. Klioner, P.M. Mathews, D. McCarthy, X. Moisson, S. Petrov, R.M. Ponte, F. Roosbeek, D. Salstein, H. Schuh, K. Seidelmann, M. Soffel, J. Souchay, J. Vondrák, J.M. Wahr, P. Wallace, R. Weber, J. Williams, Y. Yatskiv, V. Zharov, and S.Y. Zhu. Considerations concerning the non-rigid Earth nutation theory. *Cel. Mech. Dyn. Astron.,* 72:245–310, 1999.

J.O. Dickey, S.L. Marcus, and O. de Viron. Closure in the Earth's angular momentum budget observed from subseasonal periods down to four days: No core effects needed. *Geophys. Res. Lett.,* 37:L03307, doi:10.1029/2009GL041118, 2010.

S.R. Dickman. Evaluation of 'effective angular momentum functions' formulations with respect to core-mantle coupling. *J. Geophys. Res.,* 108(B3):2150, doi:10.1029/2001JB001603, 2003.

S.R. Dickman. Rotationally consistent Love numbers. *Geophys. J. Int.*, 161:31–40, doi:10.1111/j.1365-246X.2005.02574.x, 2005.

H. Dobslaw, R. Dill, A. Grötzsch, A. Brzeziński, and M. Thomas. Seasonal polar motion excitation from numerical models of atmosphere, ocean, and continental hydrosphere. *J. Geophys. Res.,* 115:B10406, doi:10.1029/2009JB007127, 2010.

T.M. Eubanks. Variations of the orientation of the Earth. In Smith D.E., Turcotte, D.L., editor, *Contributions of Space Geodesy to Geodynamics: Earth Dynamics*, volume 24, pages 1–54. AGU, Washington, 1993.

S.B. Feldstein. The dynamics of atmospherically driven intraseasonal polar motion. *J. Atm. Sci.,* 65(7):2290–2307, doi:10.1175/2007JAS2640.1, 2008.

M. Fujita, B.F. Chao, B.V. Sanchez, and T.J. Johnson. Oceanic torques on solid Earth and their effects on Earth rotation. *J. Geophys. Res.,* 107(B8):2154, doi:10.1029/2001JB000339, 2002.

R.S. Gross. Correspondence between theory and observations of polar motion. *Geophys. J. Int.,* 109(1):162–170, doi:10.1111/j.1365-246X.1992.tb00086.x, 1992.

R.S. Gross. The effect of ocean tides on the Earth's rotation as predicted by the results of an ocean tide model. *Geophys. Res. Lett.,* 20(4):293–296, 1993.

R.S. Gross. The excitation of the Chandler wobble. *Geophys. Res. Lett.,* 27(15):2329–2332, doi:10.1029/2000GL011450, 2000.

R.S. Gross. Earth rotation variations - long period. In Herring T.A., editor, *Treatise on Geophysics*, volume 3, Geodesy, pages 239–294. Elsevier, 2007.

R.S. Gross, H.K. Hamdan, and D.H. Boggs. Evidence for excitation of polar motion by fortnightly ocean tides. *Geophys. Res. Lett.,* 23(14):1809–1812, doi:10.1029/96GL01596, 1996.

R.S. Gross, I. Fukumori, and D. Menemenlis. Atmospheric and oceanic excitation of the Earth's wobbles during 1980–2000. *J. Geophys. Res.,* 108(B8):2370, doi:P10.1029/2002JB002143, 2003.

R.S. Gross, I. Fukumori, D. Menemenlis, and P. Gegout. Atmospheric and oceanic excitation of length-of-day variations during 1980–2000. *J. Geophys. Res.,* 109(B01406), 2004.

T.A. Herring, C.R. Gwinn, and I.I. Shapiro. Geodesy by radio interferometry: Studies of the forced nutations of the Earth: 1. Data Analysis. *J. Geophys. Res.,* 91(B5):4745–4754, doi:10.1029/JB091iB05p04745, 1986.

J.R. Holton and R.S. Lindzen. An updated theory for the quasi-biennial cycle of the tropical stratosphere. *J. Atm. Sci.,* 29 (6):1076–1080, 1972.

IAU Resolutions, 2000. http://www.iau.org/static/resolutions/IAU2000_French.pdf

IAU Resolutions, 2006. http://www.iau.org/static/resolutions/IAU2006_French.pdf

H. Iskenderian and D.A. Salstein. Regional sources of mountain torque variability and high-frequency fluctuations in atmospheric angular momentum. *Mon. Wea. Rev.,* 126:1681–1694, 1998.

H. Jeffreys. Causes contributory to the annual variation of latitude. *Mon. Not. R. Astron. Soc.,* 76:499–525, 1916.

L. Koot and O. de Viron. Atmospheric contributions to nutations and implications for the estimation of deep Earth's properties from nutation observations. *Geophys. J. Int.,* 185:1255–1265, doi:10.1111/j.1365-246X.2011.05026.x, 2011.

K. Lambeck. *The Earth's Variable Rotation, Geophysical Causes and Consequences*. Cambridge University Press, 1980.

R. Madden and P. Julian. Detection of a 40–50 day oscillation in the zonal wind in the tropical Pacific. *J. Atmos. Sci.*, 28:702–708, 1971.

P.M. Mathews, T.A. Herring, and B.A. Buffett. Modeling of nutation and precession: New nutation series for nonrigid Earth and insights into the Earth's interior. *J. Geophys. Res.,* 104(B4):2068, doi:10.1029/2001JB000390, 2002.

D.D. McCarthy and B. Luzum. IERS Conventions 2010. *IERS Technical Note*, (36):179 pp., 2010.

P. McClure. Diurnal polar motion. GSFC document X-592-73-259, Goddard Space Flight Center, Greenbelt, Maryland, 1973.

P.J. Mendes Cerveira, J. Böhm, H. Schuh, T. Klügel, A. Velikoseltsev, U. Schreiber, and A. Brzeziński. Earth rotation observed by Very Long Baseline Interferometry and ring laser. *Pure Appl. Geophys.,* 166(8–9):1499–1517, doi:10.1007/s00024-004-0487-z, 2009.

J.B. Merriam. Zonal tides and changes in the length of day. *Geophys. J. R. Astron. Soci.*, 62:551–561, 1980.

H. Moritz and I.I. Müller. *Earth Rotation: Theory and Observation*. Ungar, New York, 1987.

L.V. Morrison and F.R. Stephenson. Historical eclipses and the variability of the Earth's rotation. *J. Geodyn.,* 32(1–2):247–265, doi:10.1016/S0264-3707(01)00024-2, 2001.

W.H. Munk and G.J.F. MacDonald. *The Rotation of the Earth: A Geophysical Discussion*. Cambridge University Press, New York, 1960.

J. Nastula and D. Salstein. Regional atmospheric angular momentum contributions to polar motion excitation. *J. Geophys. Res.,* 104(B4):7347–7358, doi:10.1029/1998JB900077, 1999.

S.G. Philander. *El Niño, La Niña, and the Southern Oscillation*. Academic Press, San Diego, 1990.

R.M. Ponte. Oceanic excitation of daily to seasonal signals in Earth rotation: results from a constant-density numerical model. *Geophys. J. Int.,* 130(2):469–474, doi:10.1111/j.1365-246X.1997.tb05662.x, 1997.

R.D. Ray, D.J. Steinberg, B.F. Chao, and D.E. Cartwright. Diurnal and semidiurnal variations in the Earth's rotation rate induced by oceanic tides. *Science*, 264(5160):830–832, doi:10.1126/science.264.5160.830, 1994.

D.A. Salstein. Angular momentum of the atmosphere. In J. Holton, J. Pyle, J. Curry, editor, *Encyclopedia of Atmospheric Sciences*, pages 128–134. Elsevier, 2002.

D.A. Salstein and R.D. Rosen. Topographic forcing of the atmosphere and a rapid change in the length of day. *Science*, 264:407–409, 1994.

T. Sasao and J.M. Wahr. An excitation mechanism for the free 'core nutation'. *Geophys. J. R. Astron. Soc.,* 64:729–746, 1981.

M. Schindelegger, J. Böhm, D. Salstein, and H. Schuh. High-resolution atmospheric angular momentum functions related to Earth rotation parameters during CONT08. *J. Geod.,* 8(7):425–433, doi:10.1007/s00190-011-0458-y, 2011.

H. Schuh and S. Böhm. Earth rotation. In H.K. Gupta, editor, *Encyclopedia of Solid Earth Geophysics*, pages 123–129. Springer, 2011.

H. Schuh, S. Nagel, and T. Seitz. Linear drift and periodic variations observed in long time series of polar motion. *J. Geod.,* 74(10):701–710, doi:10.1007/s001900000133, 2001.

F. Seitz. Atmosphärische und ozeanische Einflüsse auf die Rotation der Erde - Numerische Untersuchungen mit einem dynamischen Erdsystemmodell. C578, Deutsche Geodätische Kommission, München (in German), 2004.

F. Seitz and H. Schuh. Earth rotation. In G. Xu, editor, *Science of Geodesy I: Advances and Future Directions*, pages 185–227. Springer, 2010.

M.L. Smith and F.A. Dahlen. The period and Q of the Chandler wobble. *Geophys. J. R. Astron. Soc.,* 64:223–281, 1981.

R.O. Vicente and C.R. Wilson. On the variability of the Chandler frequency. *J. Geophys. Res.,* 102(B9):20439–20445, doi:10.1029/97JB01275, 1997.

J. Vondrák and C. Ron. Quasi-diurnal atmospheric and oceanic excitation of nutation. *Acta Geodyn. Geomater.,* 4(4):121–128, 2007.

J. Vondrák and C. Ron. Study of atmospheric and oceanic excitations in the motion of Earth's spin axis in space. *Acta Geodyn. Geomater.,* 7(1):19–28, 2010.

J.M. Wahr. The effects of the atmosphere and oceans on the Earth's wobble - I. Theory. *Geophys. J. R. Astron. Soc.,* 70:349–372, 1982.

J.M. Wahr. The effects of the atmosphere and oceans on the Earth's wobble and on the seasonal variations in the length of day - II. Results. *Geophys. J. R. Astron. Soc.,* 74:451–487, 1983.

J.M. Wahr. Polar motion models: Angular momentum approach. In Plag H.P., Chao B.F., Gross R.S., van Dam T., editor, it Forcing of Polar Motion in the Chandler Frequency Band: A Contribution to Understanding Interannual Climate Change, volume 24. Cahiers du Centre Européen de Géodynamique et du Séismologie, Luxembourg, 2005.

J.M. Wahr and A.H. Oort. Friction- and mountain-torque estimates from global atmospheric data. *J. Atm. Sci.,* 41(2):190–204, 1984.

J.M. Wahr, T. Sasao, and M.L. Smith. Effect of the fluid core on changes in the length of day due to long period tides. *Geophys. J. R. Astron. Soc.,* 64:635–650, 1981.

W.L. Wolf and R.B. Smith. Length-of-day changes and mountain torques during El Nino. *J. Atm. Sci.,* 44(24):3656–3660, 1987.

C. Wunsch and D. Stammer. Atmospheric loading and the oceanic 'inverted barometer' effect. *Rev. Geophys.,* 35(1):79–107, doi:10.1029/96RG03037, 1997.

Y.H. Zhou, D.A. Salstein, and J.L. Chen. Revised atmospheric excitation function series related to Earth's variable rotation under consideration of surface topography. *J. Geophys. Res.,* 111(D12108): doi:10.1029/2005JD006608, 2006.

W. Zürn. The Nearly-Diurnal Free Wobble-resonance. In Wilhelm H., Zürn W., Wenzel H., editor, *Tidal Phenomena*, pages 95–107. Springer, 1997.

Index

A
Angular Momentum Budget, 227
APL in Space Geodesy, 153
APL Services, 150
Atmosphere and Ocean, 178
Atmospheric Delays for SLR, 112
Atmospheric Layers, 17
Atmospheric Studies, 125
Atmospheric Tides, 15
Atmospheric Turbulence, 120

B
Basics, 75

C
Chapman Layer Profile, 21

D
3D Atmosphere, 174
Definition of Path Delay, 81

E
Earth's Variable Rotation, 182
Effective Angular Momentum Functions, 193
Eliminating TEC, 51
Empirical Model, 151
Estimating TEC, 58
Evaluating Angular Momentum Functions, 199

G
Gas Laws, 7
Geodetic Motivation, 2
Geopysical Approach, 142
Group and Phase Velocity, 36

H
Hydrostatic Delay, 83

I
Indirect Effect, 177
Influence of Atmosphere, 186
Inverted Barometer Hypothesis, 16
Ionization and Recombination, 19
Ionosphere Refractive Index, 38
Ionospheric Delay, 41

L
Length of Day Variations, 224
Long Period Excitation Formalism, 211

M
Mapping Functions and Gradients, 100
Meteorological Quantities, 5
Microwaves, 77
Modeling Delay, 92
Modeling Geophysical Excitation, 188
Modeling TEC, 46

N
Non-Tidal Displacements, 145

O
Optical Refractivity, 80

J. Böhm and H. Schuh (eds.), *Atmospheric Effects in Space Geodesy*,
Springer Atmospheric Sciences, DOI: 10.1007/978-3-642-36932-2,

P
Path Delays, 73
Pressure Variations, 169

R
Ray-Tracing, 93
Reference Pressure, 14

S
Satellite Gravity Missions, 169
Statics of the Atmosphere, 9
Sub-daily Excitation Formalism, 218
Surface Pressure Variations, 137

T
Theory of Gravity Field, 159
Thin Layer Approximation, 173
Tidal Displacements, 147
Torque Approach, 204
Total Mass of Atmosphere, 166

V
Variation in the Ionosphere, 24

W
Water Vapor Radiometry, 116
Wet Delay, 88